名古屋大学

Estimation of the neutron emissions during the large flares of solar cycle 24

by

NILTON DIEGO LOPEZ QUISPE

A thesis submitted in fulfillment of the requirements for the degree of Doctor of Phylosophy in the

Division of Particle and Astrophysical Science

Graduate School of Science

NAGOYA UNIVERSITY

February 2016

”Living on Earth may be expensive, but it includes an annual free trip around the Sun.”

Ashleigh Brilliant

Cosmic rays study is remarkable ”for the delicacy of the apparatus, the minuteness of the phenomena, the adventurous excursions of the experimenters and the grandeur of the inferences.”

Karl K. Darrow

Abstract

Solar flares are one of the most efficient particle accelerators that exist in the universe. In a solar flare, electrons and ions, which are accelerated in the solar corona, precipitate to the solar atmosphere where they deposit their energy in interactions with ambient gas. The emitted energy spans over the whole electromagnetic spectrum. The electron acceleration mechanism has been widely studied by the emission of X- and γ-rays, whereas the ion acceleration, especially the most energetic ones ($>$100 MeV), is still unknown. To understand how these ions are accelerated, it is important to study a variety of observations such as ions themselves and secondary γ-rays and neutrons. In order to avoid the complexity of the interplanetary magnetic fields, it is useful to examine solar neutrons, because they can travel directly to Earth without being affected by these fields. Moreover, these neutrons can carry crucial information regarding the acceleration process occurred at the solar flare.

During solar cycles 21, 22, and 23, ten solar neutron events were observed with high significance by ground-level detectors. The production time of the neutrons was associated to that of the X- and γ-rays. Those events were mostly found whenever a statistically significant excess was found in the data of Neutron Monitors (NM) and Solar Neutron Telescopes (SNT). Thus far, no systematic search for solar neutrons has been performed. Particularly, the relation between the solar neutron production and the scale of solar flares has not been discussed.

In the present work, a systematic method is developed to search for solar neutrons in association with large solar flares. The onset and maximum intensity time of soft X-rays observed by GOES (1-8Å) were used as the most probable production time of solar neutrons. The search was performed in two campaigns. In the first, three years (January 2010 to August 2013) of data collected by the Chacaltaya NM and twenty-eight M- and three X-class flares were used. The Chacaltaya NM has the highest efficiency to detect solar neutrons in the world. In the second, five years (January 2010 to December 2014) of data collected by the SNTs and the Chacaltaya NM were used. In this period thirty-five X-class flares were examined. In both campaigns, time profiles of the SNTs and the Chacaltaya NM were built for each studied flare. Based on these profiles, a statistical analysis was performed. A significance level of greater than 3σ was set to identify an enhancement. The result of both campaigns produced no significant and positive excess attributable to solar neutrons. Therefore, upper limits with the 90% C.L. on the $\geq$100 MeV of the solar neutron emission for the 35 flares of the second campaign were estimated. An impulsive emission following a power-law shaped neutron energy spectrum with power index equal to 3, 5 and 7 was assumed.

The estimated neutron emissions were compared with those of solar neutron events observed during solar cycles 21, 22 and 23. The obtained upper limits are consistent within the order of magnitude. The total energy release of solar neutrons was calculated for each of the 35 flares and compared with the radiated energy and the peak thermal energy of soft X-rays. The newest findings are: 1) in the most stringent upper limit, the total energy release of neutrons is at most two orders of magnitude lower than the peak thermal energy; 2) the least stringent upper limit is five orders of magnitude lower than the peak thermal energy; 3) the total energy release of neutrons for the successful detections observed during solar cycles 21, 22 and 23, range from 10^{-6} to 10^{-3} of the peak thermal energy. The major conclusions are: 1) the total solar neutron energy may not exceed more than 0.1% of the soft X-ray

radiated energy; 2) the total solar neutron energy may not exceed 0.01% of the peak thermal energy, if that is to be considered and 3) solar flares might have to produce at least 5×10^{30}[erg], so that a detectable neutron signal can be observed at the ground level.

To my parents,

Julio & Isabel.

Acknowledgments

First of all, I would like to thank the Ministry of Education, Culture and Sports of Japan for granting me the Monbusho Scholarship for five years. Next, I want to thank Prof. Yoshitaka Itow for giving me the possibility to attend the Graduate Program for the Master and Doctoral course of the Graduate School of Science of Nagoya University and also for reviewing the present work.
I am deeply indebted to my supervisor Prof. Yutaka Matsubara, whose help, stimulating suggestions and encouragement helped me in all the time of research for and writing of this thesis.
The present work would not be possible without the kind help and constant assistance of Prof. Yasushi Muraki, Prof. Kimiaki Masuda and Dr. Takashi Sako.
I want to also thank Prof. Jose F. Valdés-Galicia from the Instituto de Geofísica of the Universidad Nacional Autónoma de México (UNAM) for his kind help by reading the manuscripts and for providing helpful corrections and suggestions. I also acknowledge the members of the Cosmic-ray group of UNAM for their hospitality during my short stay in Mexico.
Sincere thanks are also addressed to Prof. Hiroyasu Tajima for reviewing the present work and for providing useful advice. I would also like to thank Prof. Satoshi Masuda for providing me good insights into the solar flare analysis, for kindly writing an IDL script and for teaching me the SSW (SolarSoftware) tool.
My colleagues, current and former, from our Cosmic Ray Group have created a pleasant working environment, and have been helpful in a large number of matters. I wish to express my gratitude to Ms. Tomoyo Kainai and Ms. Torii Tae for handling all the paperwork on my behalf.
I am deeply indebted to my family in La Paz, Bolivia who supports me in spite of the distance and helped me whenever things were not going as expected. Last but not least, I want to thank the friends I made during my long stay in Nagoya, specially Ms. Saori Suzuki, Mr. Ira Shefer and Mr. Yasuhisa Miyakoshi. The long talks and walks we had helped me to cope with home sickness.

Contents

Abstract **iii**

Acknowledgments **v**

1 Introduction **1**
1.1 Solar Flares . . . 1
1.2 Acceleration mechanisms . . . 3
1.2.1 Stochastic acceleration . . . 3
1.2.2 Shock acceleration . . . 4
1.2.3 Coherent acceleration . . . 5
1.3 Neutral emissions at a flare . . . 6
1.3.1 γ-rays . . . 6
1.3.2 neutrons . . . 6
1.4 Propagation of solar neutrons . . . 10
1.4.1 Propagation in the Interplanetary Space . . . 10
1.4.2 Propagation in the Earth's atmosphere . . . 11
1.5 Aim of this thesis . . . 13

2 Solar neutron detectors **15**
2.1 Ground-based observation . . . 15
2.1.1 The Neutron Monitor . . . 15
2.1.2 The Solar Neutron Telescope . . . 17
2.1.3 Performance of the SNT . . . 22
2.1.4 The Scintillation Bar Cosmic Ray Telescope - SciCRT . . . 24
2.2 Space observation . . . 27
2.2.1 SEDA-NEM . . . 27
2.2.2 MESSENGER . . . 29

3 Summary of solar neutron events in past cycles **31**
3.1 Solar neutron events between 1980-2005 . . . 31
3.2 The 1982 June 3 solar neutron event . . . 32
3.3 The 2005 September 7 solar neutron event . . . 33

4 Search for solar neutrons in association with M- and X-class flares **39**
4.1 GOES SXR Database . . . 39
4.2 Chacaltaya NM data . . . 40
4.3 Method . . . 40
4.4 Results . . . 44

5 Search for solar neutrons in association with X-class flares **49**
5.1 GOES SXR database 49
5.2 SNTs and Chacaltaya NM data 49
5.3 Validity 51
5.4 Results 51

6 Neutron emission during solar flares **61**
6.1 Method to calculate the upper limit of detection 61
6.1.1 The 2011 August 9 X6.9 solar flare 62
6.1.2 The other flares 63
6.2 Solar neutron emission 63
6.3 Discussion 66

7 Conclusions **79**

A Candidate events **81**
A.1 Search for solar neutrons during the maximum period of solar cycle 24 81
A.2 Possible solar neutron events 83
A.2.1 The solar flare on 2013 October 25 83
A.2.2 The solar flare on July 8, 2014 83
A.3 Discussion 89

B GOES Light-curves of thirty five X-class flares **91**

C Significance distributions of thirty-five flares **95**

Bibliography **129**

Chapter 1

Introduction

The study of cosmic rays is of great interest in astrophysics. Since their discovery more than 100 years ago, the mechanism of how these particles are accelerated is still not fully understood. There are several astrophysical phenomena which are thought to produce and accelerate cosmic rays. In the solar system, the Sun can accelerate particles up to a few GeVs via solar flares and coronal mass ejections. Outside the solar system, the candidates for the production of galactic and extra-galactic cosmic rays are via supernova remnants (SNR), neutron stars, active galactic nuclei, and gamma-ray bursts.

Cosmic rays are primarily composed of ionized nuclei: about 90% protons, 9% alpha particles and nearly 1% heavier nuclei. These numbers are estimated within the energy region where cosmic rays are observed directly. The information about the acceleration site (source location) is not immediately available from those ionized nuclei, because their paths are bent by the interplanetary magnetic fields. However, by the observation of secondary particles a part of these ionized nuclei can be understood. For instance by observing X- and γ-rays the electron acceleration has been understood rather well (via bremsstrahlung, Compton, and synchrotron process). It is left to understand how ions (protons, α, etc.), which are dominant in cosmic rays, are accelerated. Neutral particles, which are the by-product of primary particles, do not have their paths disturbed, therefore these particles can provide significant information regarding the acceleration site. From this point of view, X- and γ-rays are observed by different spacecrafts. Neutrinos are observed by underground experiments, such as Super-Kamiokande and IceCube among others. It is also useful to observe neutrons, the object of this thesis, in order to understand the acceleration mechanism of ions.

Bierman et al. (1951) proposed the possibility that protons, accelerated to the order of 100 MeV during solar flares, would interact with the solar photosphere to produce neutrons with energies above several MeV. These neutrons may be produced with energies great enough to reach the Earth before decay. Since neutrons are not influenced by the magnetic fields, they may provide direct information on the acceleration processes during solar flares, in contrast to the originally produced and emitted charged particles.

In this chapter, the production, the acceleration, the decay in the interplanetary space, the absorption in the Earth's atmosphere are briefly described.

1.1 Solar Flares

Solar flares are vast explosions of bursting material observed at the surface of the Sun. They were first observed by Carrington (1859) and R. Hodgson ca. 1859. They watched separately through a small telescope a brightening in the vicinity of a complex group of sunspots (shown in Figure 1.1) in the visible spectrum. In fact, what they actually observed is known nowadays as a *white-light flare*,

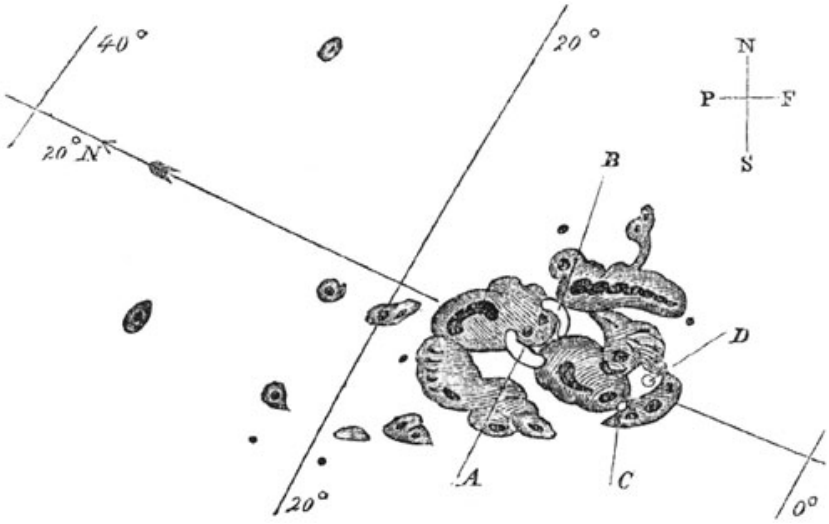

Figure 1.1: The sunspots of 1859 September 1st as sketched by Carrington (1859). A and B are the positions in which the flare appeared, while C and D are the place where it disappeared.

which is a very rare phenomenon.

Spacecrafts are used to better observe and track the Sun in these days. For example in Figure 1.2 the Hinode/SOT observations of an actual white-light flare occurred on 2006 December 14 (Watanabe et al., 2010) is shown. From these observations, it was found that highly accelerated electrons are responsible for the production of white-light emission.

More than 150 years have passed since the first observation of Carrington (1859), these days, it is widely accepted that the accumulation of sunspots will produce solar flares, this is due to the magnetic instability that exists in the collision and formation of magnetic loops. These flares can accelerate initially both electrons and ions to high energies. The by-product of these particles produce ions themselves and neutral radiations (radio waves, X-rays, γ-rays, neutrons, optical emissions) among others. In particular X-rays are a common indicator of the intensity of solar flares. They are mainly observed by spacecrafts, one of these is the Geostationary Operational Environmental Satellite (GOES-15), which records the soft X-ray flux (1-8Å) measured at 1 AU. GOES-15 or simply GOES classifies the X-ray flux intensity according to the flare size. This classification has five classes, A ($\geq 10^{-8}$ W/m^2), B($\geq 10^{-7}$), C($\geq 10^{-6}$), M($\geq 10^{-5}$) and X($\geq 10^{-4}$).

Heavier particles can also be released into the interplanetary space as secondary emission from the Sun. These highly energetic particles are usually released accompanied by a Coronal Mass Ejection (CME). A wide range of observations suggest that these solar energetic particles (SEP) are accelerated by shocks driven by CMEs (Gopalswamy et al., 2015). Those reaching the Earth are classified as Ground-level enhancements (GLE). They are produced when protons, with energies on the GeV order, create a nuclear cascade through the Earth's atmosphere that can be observed by detectors at ground level as an increase above the continuous background produced in a similar manner by galactic cosmic rays. Thus far, seventy-one[1] of these GLEs were successfully observed by ground-based detectors.

However, not all the solar flares will produce such SEPs. It is possible that their acceleration sometimes occurs at the flare site rather than in the CME. As an example, in the present solar cycle, the AR12192 which was one of the largest sunspot accumulations in the solar surface (in solar cycle 24), produced several solar flares catalogued as greater than X-class by GOES but few CMEs were observed (Sun et al., 2015). In Figure 1.3 it is possible to observe the sunspots of AR12192 registered

[1]The Neutron Monitor DataBase: www.nmdb.eu/nest/gle_list.php

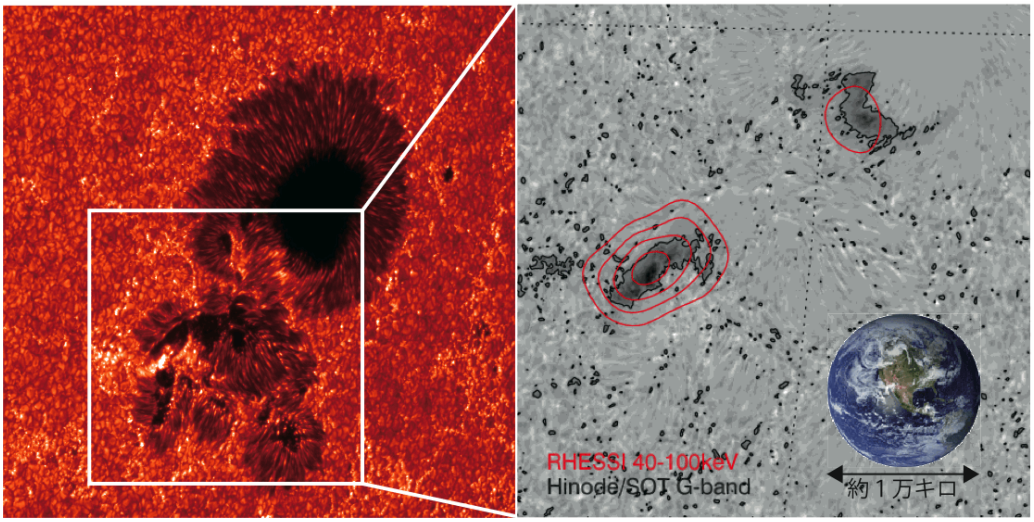

Figure 1.2: The Hinode/SOT G-band (left) and RHESSI 40-100keV (right) observations of a solar flare which occurred on 2006 December 14. Figure from Watanabe et al. (2010).

by SDO/HMI[2] and SDO/AIA[3] together with the record of GOES in October 2014.
According to Hudson (2011), the energy released during a solar flare spans many orders of magnitude, from the smallest microflares ($\sim 10^{24}$erg) to the highest ever recorded[4] by GOES SXR in the 1-8Å band, an X28.0-class observed on 2003 November 4 ($\sim 10^{35}$erg).

1.2 Acceleration mechanisms

In this section the mechanism of the particle acceleration in solar flares is discussed. There are many models that can explain this issue, the most important are: the first and second order acceleration models proposed by Fermi (1949) and the coherent acceleration. A brief description of each of them is provided. A full review of these three mechanisms is described in (Forman et al., 1986; Ramaty and Murphy, 1987).

1.2.1 Stochastic acceleration

In the environment of the solar atmosphere occurs turbulent processes in plasmas which cause particles to change their energy in a random way with many increases and decreases. When the random energy increments are small compared to the particle energy, stochastic acceleration can be described as diffusion in space phase.
Ramaty and Murphy (1987) (hereafter RM1987) constructed an acceleration model for the hard-sphere scattering diffusion. They considered a constant mean free path λ, a steady source of particles q per unit of time at an injection energy E_{inj}. In this model when the injection energy of the solar flare is in the non-relativistic regime, i.e. $E_{inj} << mc^2$, the number of particles $N(E)$ of the energy E is given as:

[2]Solar Dynamics Observatory/Helioseismic and Magnetic Imager `sdo.gsfc.nasa.gov`
[3]SDO/Atmospheric Imaging Assembly
[4]According to the ESA website: `http://www.esa.int/Our_Activities/Space_Science/The_biggest_solar_X-ray_flare_ever_is_classified_as_X28`

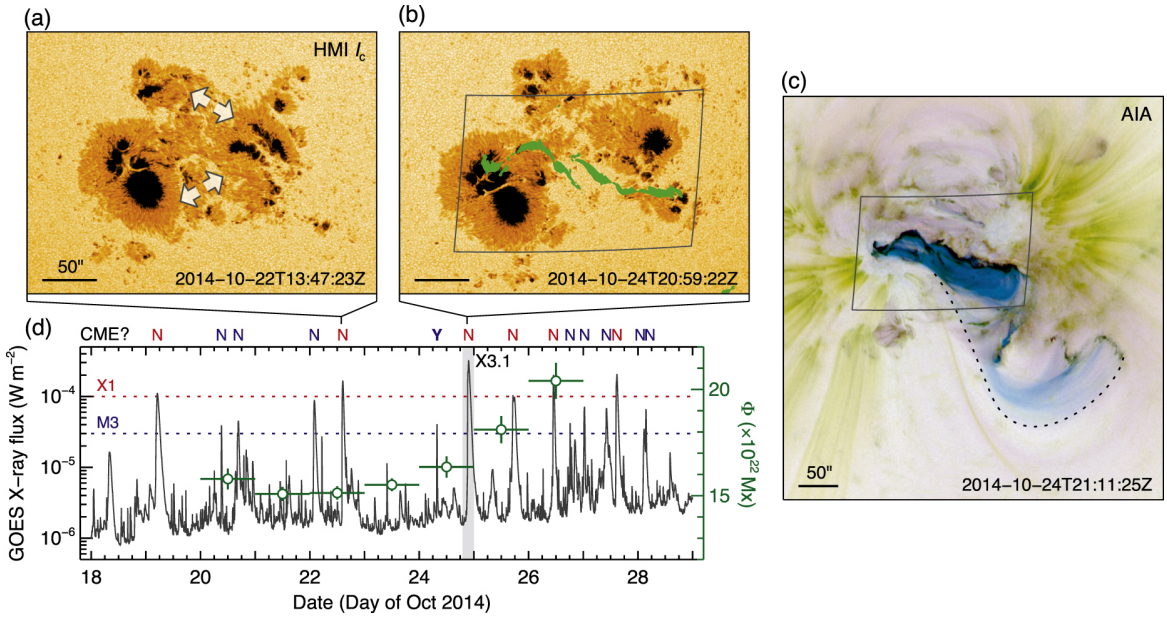

Figure 1.3: Overview of NOAA's AR12192 on October 24, 2014. (a) and (b) SDO/HMI continuum intensity before two X-class flares with scattered light removed. Arrows in (a) are the locations where significant sunspot separation took place. In (c) a negative composite SDO/AIA image during the X3.1 flare. The dotted curve outlines the hot 131Å loops connecting the main flaring situate the SW. In (d) the GOES 1-8Å SXR flux. According to Sun et al. (2015).

$$N(E) = \frac{6\,q}{p_{inj} c\alpha} I_2(x_{inj}) K_2(x), \tag{1.1}$$

where, $x = \sqrt{12pc/mc^2\alpha T}$; p, m, and T are the particle momentum, mass, and mean escape time respectively. α is the velocity of the scatterers divided by the mean free path and divided by the speed of light. K_2 and I_2 are Bessel functions.
Now, in the ultra-relativistic regime (E_{inj} >>mc^2) :

$$N(E) = \frac{3\,q}{\alpha E_{inj}} \left(\sqrt{9 + \frac{12}{\alpha T}}\right)^{-1} \left(\frac{E}{E_{inj}}\right)^{-s} \tag{1.2}$$

here, the spectral index $s = -1/2 + 1/2\sqrt{9 + 12/\alpha T}$. The non dimensional parameter αT in these solutions is important, because it characterizes the shape of the spectrum. The larger αT is, the smaller s is, which means the spectrum is harder. In Figure 1.4 the solution of the transport equations for the non relativistic, relativistic regime and a numerical fit for the energies in between is plotted. The blue curve corresponds to the stochastic calculation, where the αT parameter assumed is equals to 0.03, then s =9.61 in Equation 1.2. The red curve represents the non-relativistic regime given by Equation 1.1, while the dashed line is the ultra-relativistic spectrum denoted by Equation 1.2. Essentially the red and blue curves are similar, but at higher energies, the shape of the numerical solution differs from that given by the K_2 curve. According to RM1987, this has implications on nuclear reactions at energies above several GeV.

1.2.2 Shock acceleration

When a shock wave propagates through the corona, particles can be accelerated at its front. In front of and behind the shock a flux of charged particles is assumed to be present. There are basically

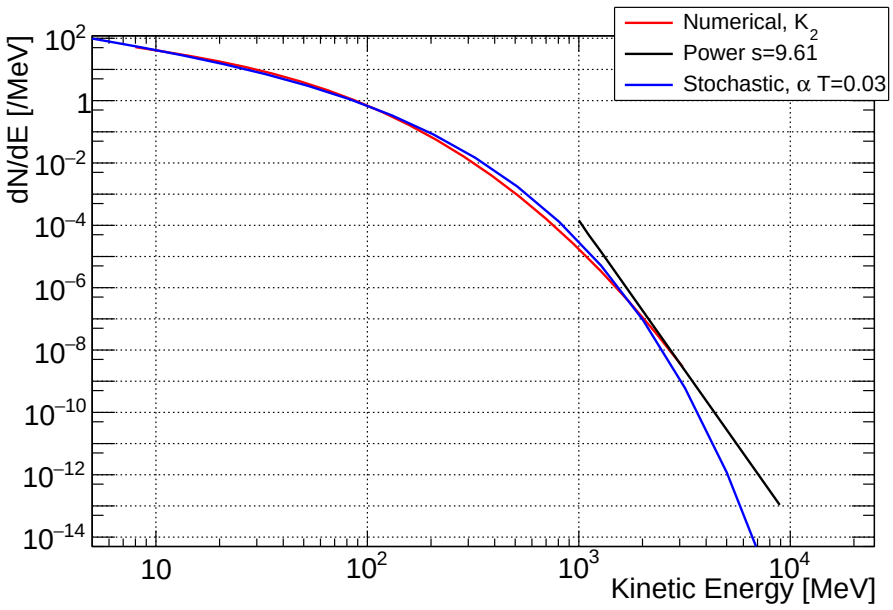

Figure 1.4: The solution for the transport equations in the ultra-relativistic and non-relativistic regime for particles that are accelerated in the solar atmosphere. A numerical calculation has been calculated for the in-between regime. The parameter that defines the spectra is αT =0.03. The dashed line is the unnormalized form for the ultra relativistic spectrum. Reproduced from Ramaty and Murphy (1987).

two types of shock acceleration: scatter-free and diffusive. In the first one, particles gain energy by reflection in a single shock encounter. In the second case, gain is obtained by multiple scattering with the plasmas on the sides of the shock front.
According to RM1987, the scatter-free mechanism can be enhanced by one order of magnitude if the shock front is almost perpendicular. In that case particles with speeds greater than the shock speed can be reflected, thus they are accelerated by multiple reflections. In restricted cases the particle density in phase space from shock acceleration is described by a power-law as,

$$\frac{\mathrm{d}N}{\mathrm{d}E} \propto p^{-z},$$

where the spectral index, z, is in the non-relativistic case, equals to $3V/\Delta V = 3r/(r-1)$. Here V is the shock speed, ΔV is the discontinuity in the plasma speed at the shock and r is the shock compression ratio. In the relativistic case, z increases by a factor of two.

1.2.3 Coherent acceleration

This type of acceleration model deals with a DC electric field in the solar atmosphere. Its origin and strength are still unknown. However, according to Vlahos (1989) there are two possible ways by which an electric field will appear in solar flares, 1) magnetic reconnection, and 2) double layers. These accelerating electric fields are called Direct Current (DC) and can be divided with respect to their orientation to the magnetic field into *parallel* and *perpendicular*. Acceleration by the first mode is further distinguished by the strength of the electric field in weak and strong. A critical level has been proposed by Dreicer (1960) and is known as the Dreicer field E_D and denoted by,

$$E_D = \frac{q_i \ln \Lambda}{4\pi\sigma_0\lambda_D^2}, \qquad \text{in SI units}$$

where $\ln \Lambda$ is the Coulomb logarithm and λ_D the Debye length. The process of electron acceleration ($q_i = e$) in weak ($E < E_D$, sub-Dreicer) electric fields is called runaway acceleration, which occurs for electrons that overcome the collisional friction between electrons and ions.
In the next section, an introduction of how solar neutrons are produced in solar flares and furthermore how they propagate in the interplanetary space and in the Earth's atmosphere is described.

1.3 Neutral emissions at a flare

Charged particles accelerated in a flare sometimes emit electromagnetic radiation and secondary particles when they interact with the solar atmosphere. Synchrotron emission is believed to produce around the corona electromagnetic waves at radio frequencies, whereas X-rays are produced by the interaction of accelerated electrons, which travel at speeds around one third of the speed of light in the corona, with the ambient protons. Energetic electrons also emit electromagnetic photons such as hard X-rays and γ-rays. Energetic neutral particles produced by energetic ions are γ-rays and neutrons. These two emissions provide the most unambiguous information regarding the acceleration of ions that occur at the Sun.

1.3.1 γ-rays

When accelerated protons encounter and collide with nuclei (C, O, Ne, etc.) in the solar atmosphere they produce excited nuclei (C,N,O,Ne,Mg,Si, and Fe) which rapidly deexcite, yielding observable gamma-rays with specific energies characteristic of the element involved. The associated gamma-ray emission during solar flares exhibits both line and continuum. In Figure 1.5 a theorethical spectrum which extends from 0.1 to 10^3 MeV energy range has been compiled to fit observations. The line emission starts to appear at energies from 0.5 to 8 MeV and result from the de-excitation of nuclei, the neutron capture and the annihilation of positrons. The continuum on the other hand, extends up to at least a few 10^2 MeV and is dominated by bremsstrahlung produced by the braking of the accelerated electrons in the Coulomb fields.
In Table 1.1 the energy of the strongest narrow de-excitation lines are described for ^{16}O, ^{12}C, ^{28}Si, ^{20}Ne, ^{24}Mg and ^{56}Fe. The strong very narrow line at 2.223 MeV is produced by thermal neutrons captured by the ambient hydrogen in the photosphere (neutron capture). Another strong narrow line is at 0.511 MeV which comes from positron annihilation. In the case protons are accelerated higher than 100 MeV, γ-rays are produced by the decay of pions ($\pi^0 \longrightarrow 2\gamma$). Additional information on the spectrum at high energies may be contained in high energy neutrons which can survive decay during their transit to Earth.
Since the 1980's, a number of spacecraft were dedicated to the observation of cosmic and solar γ-rays. Those dedicated to solar neutron observation are described in Chapter 2. In Table 1.2 a list of some of the most important missions for solar flare observations is given along with relevant instruments and their energy ranges.

1.3.2 neutrons

Solar neutrons are presumably produced by the interactions of ions with the solar atmosphere. These interactions are the following nuclear reactions: $p - p$, $\alpha - \alpha$, $p - \alpha$, $\alpha - p$ and interaction of p, α particles with heavier ambient nuclei and their inverse reactions. Table 1.3 lists the threshold energies for these various neutron-producing reactions according to Hua et al. (2002) which span a broad range of energies from about one MeV/nucleon for reactions involving heavy nuclei to several hundred MeV for $p - p$ reactions. Lingenfelter et al. (1965) also provided a list of the threshold

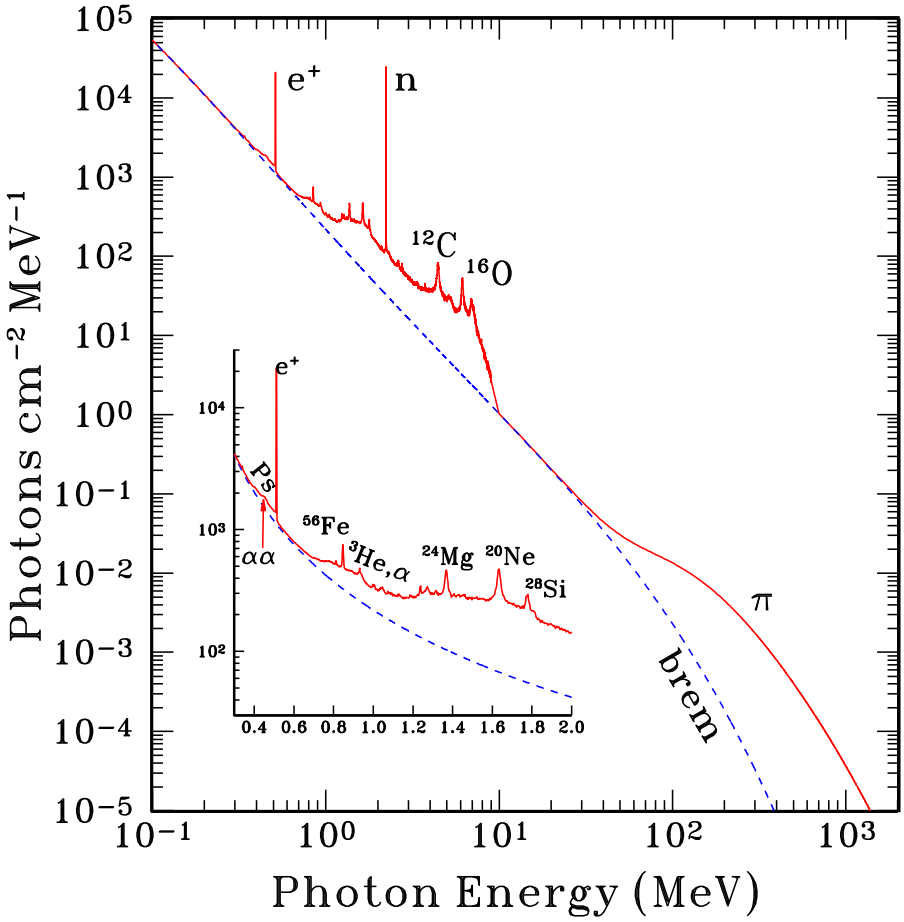

Figure 1.5: Theoretical solar flare gamma-ray sprectrum constructed to fit the observations. According to Ramaty and Manzhavidze (1998).

Table 1.1: The most strongest nuclear deexcitation lines from solar flares. According to Ramaty and Manzhavidze (1998).

Nucleus	γ-ray energy [MeV]
^{16}O	6.129
^{12}C	4.438
^{28}Si	1.779
^{20}Ne	1.634
^{24}Mg	1.369
^{56}Fe	0.847
^{7}Li	0.478
^{7}Be	0.429

Table 1.2: Recent and ongoing X-ray, γ-ray missions launched after 1980.

Mission	Lifetime	Instrument	Observed radiation	Energy range [MeV]	Website
SMM	1980-1989	GRS	γ-rays	0.3–20	go.nasa.gov/M52smd
			neutrons	>20	
GRANAT	1989-1998	PHEBUS	γ-rays	0.1–100	
CGRO	1991-2000	BATSE	γ-rays	0.02-0.6	cossc.gsfc.nasa.gov
		OSSE	γ-rays	0.05–10	
		COMPTEL	γ-rays	0.75–30	
		EGRET	γ-rays	50–3×10^4	
Yohkoh	1991-2001	HXT	X-rays	0.014–0.093	bit.ly/1NOOygs
		SXT	X-rays	0.25–4keV	
Geotail	Since 1992		X-rays	>0.05	stp.isas.jaxa.jp/geotail/
CORONAS-F	Since 2001	SONG	X-rays	0.05–100	go.nasa.gov/1P8HXTV
			electrons	12–100	
			proton	>75	
			neutrons	>20	
RHESSI	Since 2002	RHESSI	γ-rays	0.003–20	go.nasa.gov/1OrDvN8
INTEGRAL	Since 2002	SPI	γ-rays	0.02–8	
Hinode	Since 2006	XRT	X-rays	0.06–6.2keV	solarb.msfc.nasa.gov/
Fermi	Since 2008	LAT	γ-rays	>30 MeV	fermi.gsfc.nasa.gov/

energies for neutron-producing reactions which do not much differ from the ones provided by Hua et al..

The production cross-sections as a function of the kinetic energy per nucleon are shown in Figure 1.6, according to (Hua et al., 2002). Basically, four distinctive energy regions can be identified. The region E<1 MeV/nucleon is mostly dominated by α-initiated reactions with C, O, Ne, Mg. In the energy range 1<E<10 MeV/nucleon, the α-initiated reactions continue to dominate and the contribution of p-initiated reactions is small but significant. Even if the cross sections are small at low energies, because of a steep incident ion spectrum most of the solar neutrons are produced by these reactions. At E$\simeq$10-100 MeV/nucleon the reactions p-C,-N,-O and $\alpha - \alpha$ are the majority. In the high-energy region (E>100 MeV/nucleon) p-initiated reactions dominate, particularly $p - \alpha$ and from $\sim$500 MeV/nucleon $p - p$ reactions become available. At this level, cross sections of all the interaction processes involved remain almost constant.

The density distribution between the photosphere and chromosphere boundary (at height $h = -320$km) was recently re-calculated by Murphy et al. (2012), shown in Figure 1.7. These figures (panels (a) and (b)) show that neutrons are produced higher in the solar atmosphere, above 0 km ($\sim$<10g/cm^2). Hua and Lingenfelter (1987) showed that at these heights those neutrons initially directed upward have good chances of escaping from the solar atmosphere without scattering. A fraction of neutrons which were heading downward may be scattered upward and escape with reduced energy, but most will lose their energy in the atmosphere with some being captured on H from the $p(n,\gamma)d$ reaction. Neutrons that escape into the interplanetary medium can be detected in four ways, according to Miroshnichenko (2015, page 51):

1. Direct spacecraft detection,

2. detection of decay protons,

Table 1.3: Targets, projectiles and neutron-production threshold energies (MeV/nucleon) for proton- and α-particle-initiated reactions. According to Hua et al. (2002).

Isotope	Proton	α-particle
^{1}H	292.3	25.7
^{3}He	10.3	5.5
^{4}He	25.7	9.5
^{12}C	19.6	2.8
^{13}C	3.2	Exothermic
^{14}N	6.3	1.5
^{15}N	3.7	2.0
^{16}O	17.2	3.8
^{18}O	2.5	0.2
^{20}Ne	15.4	2.2
^{22}Ne	3.8	0.15
^{24}Mg	15.0	2.1
^{25}Mg	5.3	Exothermic
^{26}Mg	5.0	Exothermic
^{28}Si	15.6	2.3
^{29}Si	5.9	0.4
^{54}Fe	9.6	1.6
^{56}Fe	5.5	1.4

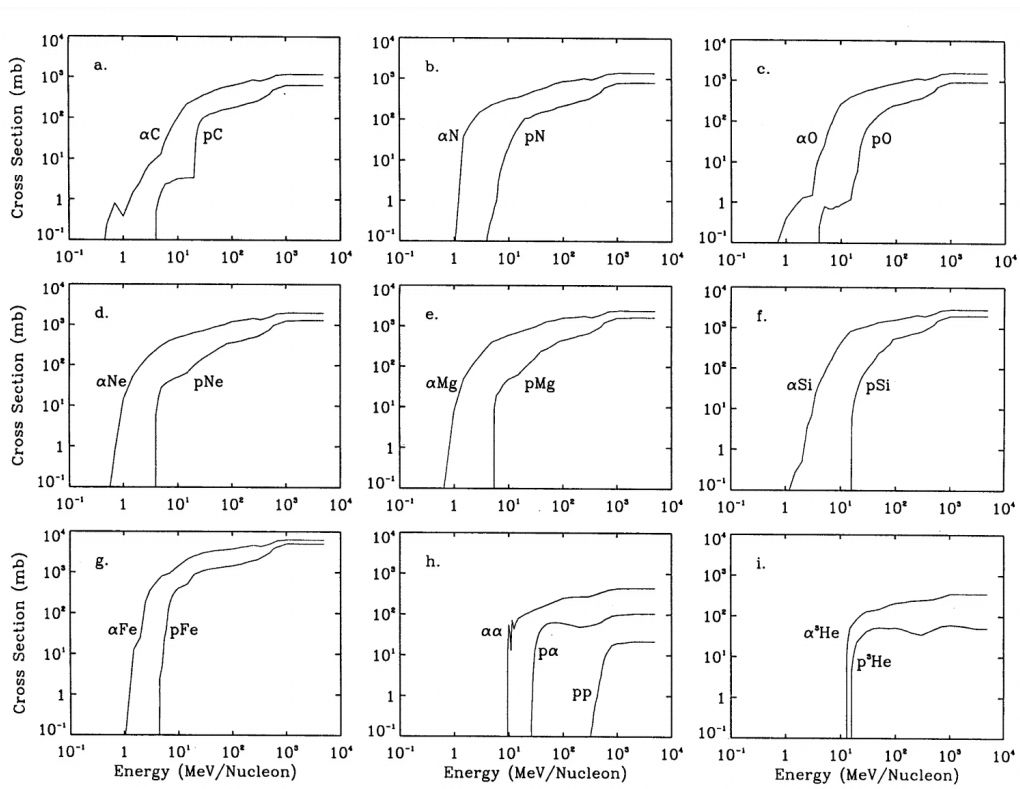

Figure 1.6: Total neutron production cross sections in proton- and α-particle-initiated reactions. According to Hua et al. (2002)

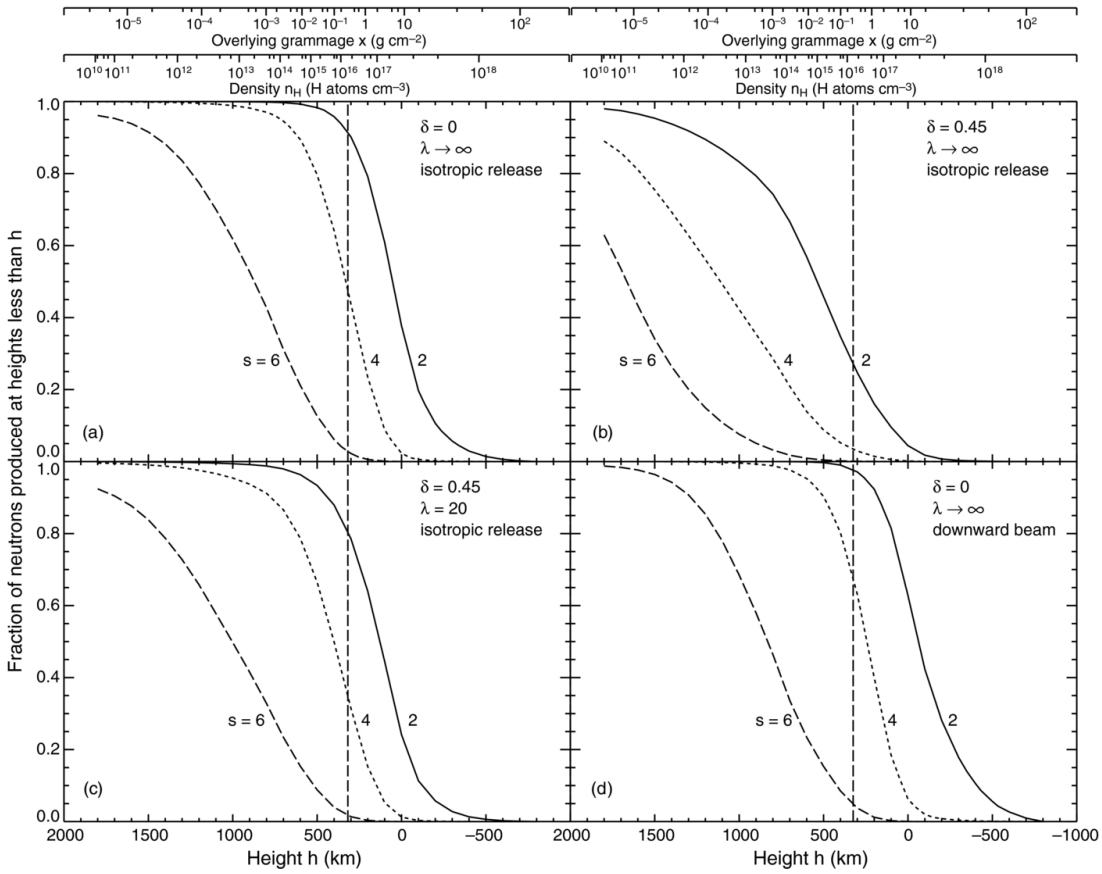

Figure 1.7: Dependence of the height distribution of neutron production on flare loop conditions. (a) isotropic accelerated-ion release and no magnetic convergence. (b) isotropic accelerated-ion release and strong magnetic convergence. (c) Same as (b) but with finite mean-free path. (d) downward-beam accelerated ions. The distributions are shown for accelerated-ion spectral indexes s of 2,4 and 6. The dashed vertical line represents the top of the photosphere (according to Murphy et al. (2012)).

3. detection of decay electrons,

4. direct ground-based detection by neutron monitors and solar neutron telescopes.

The measurements of neutron events observed at Earth (at high-altitude mountains) indicates that ions are accelerated nearly to GeV energies. The 2.223 MeV gamma-ray emission is an indicator of low-energy neutron generation, but these low-energy neutrons are also produced by more energetic neutrons in most cases. The π^0-generated gamma-ray emission could also be an indicator for these highly energetic particles.

1.4 Propagation of solar neutrons

1.4.1 Propagation in the Interplanetary Space

When solar neutrons escape from the solar atmosphere, they travel straightforward without being affected by the magnetic fields of the interplanetary space. Still, the expected spectrum of solar neutrons on the Earth's orbit will be changed from the spectrum at the solar surface, because neutrons are subjected to decay, which depends upon their kinetic energies E_n. This modification of the energy

spectrum is determined by the neutron's survival probability to reach the Earth without decaying and is given by the following equation,

$$P(E_n, r) = \exp\left(-\frac{t}{\gamma\tau}\right) \tag{1.3}$$

where t is the time of flight of the neutron, the lifetime of a neutron at rest[5] is $\tau = 880.3$s, and γ is the Lorentz factor.
The parameters to determine $P(E_n, r)$ are given by the following equations:

$$t = \frac{r}{c\beta} \tag{1.4}$$

$$E_n = M_n(\gamma - 1) \tag{1.5}$$

$$\gamma = \sqrt{\frac{1}{1-\beta^2}} \tag{1.6}$$

where r is the distance from the source, c is the speed of light in vacuum, β is the fraction of neutron's velocity to c, and $M_n = 939.56$ MeV is the neutron's rest mass[5].
For the case E_n =100 MeV, the probability of decay $P(E_n, r)$ at $r = 1.496 \times 10^{11} m = 1\ AU$ is given as:

$$P(100 \text{ MeV}, 1 \text{ AU}) = \exp\left(-\frac{t}{\gamma\tau}\right) \simeq 0.30$$

It means that a neutron with 100 MeV of kinetic energy has 30% of probability to reach the distance of 1 AU without decaying. In Figure 1.8 the survival probability and the travel time is plotted for different distances from the source (the Sun) in units of 1 AU and for different kinetic energies of neutrons.

1.4.2 Propagation in the Earth's atmosphere

After traveling the Sun-Earth distance, arriving neutrons at the Earth's atmosphere are strongly attenuated. According to Shibata (1994), the atmosphere prevents most of the high-energy primary neutrons from reaching ground level without interacting with atmospheric nuclei. Most of the particles reaching ground level are secondaries that no longer carry the original information about energy and arrival direction. Thus, this effect must be accounted when calculating the neutron spectrum. In the present work the nuclear interaction model proposed by Shibata (1994) (hereafter Shibata model) is used. To follow a brief description is introduced.
The Shibata model considers the interaction between a nucleon (neutron or proton) and an air nucleus (N, O, Ar, etc.) following the processes: a) elastic scattering; b) inelastic scattering; c) charge exchange and d) energy loss of protons by ionization. The calculation is started by injecting one neutron with incident energy E_0 vertically at the top of the atmosphere. Next, all collision processes of protons and neutrons with air nuclei are simulated by the Monte Carlo method taken into account the above mentioned processes. The incident neutron and all produced nucleons are followed until their energies drop to a given energy threshold E_{th}=20 MeV or until they arrive at a given limit of vertical atmospheric depth. Figure 1.9 shows the result of the calculation as a function of atmospheric depth and for different incident energies of neutrons at the top of the atmosphere. From this figure it can be understood that, if 10^6 neutrons with kinetic energies of 100 MeV and 900 MeV arrive at the top of the atmosphere, then the number of neutrons expected at the 1000 g/cm^2 level become 10 and 600 respectively.

[5]Particle Data Group (2014) `http://pdg.lbl.gov/2014/listings/rpp2014-list-n.pdf`

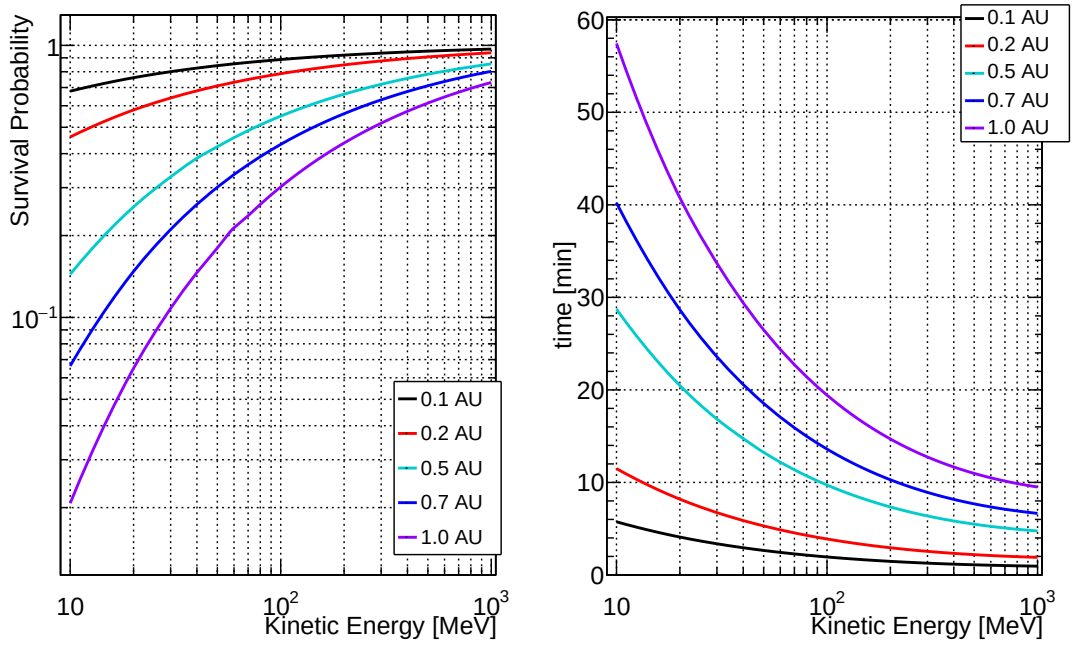

Figure 1.8: On the left, the neutron survival probability $P(E_n, r)$ to decay with different kinetic energies and at different distances from the source. On the right, the estimated arrival time of neutrons to the top of the Earth's atmosphere r =1 AU for different kinetic energies. For comparison, photons travel the Sun-Earth distance in ∼8 min.

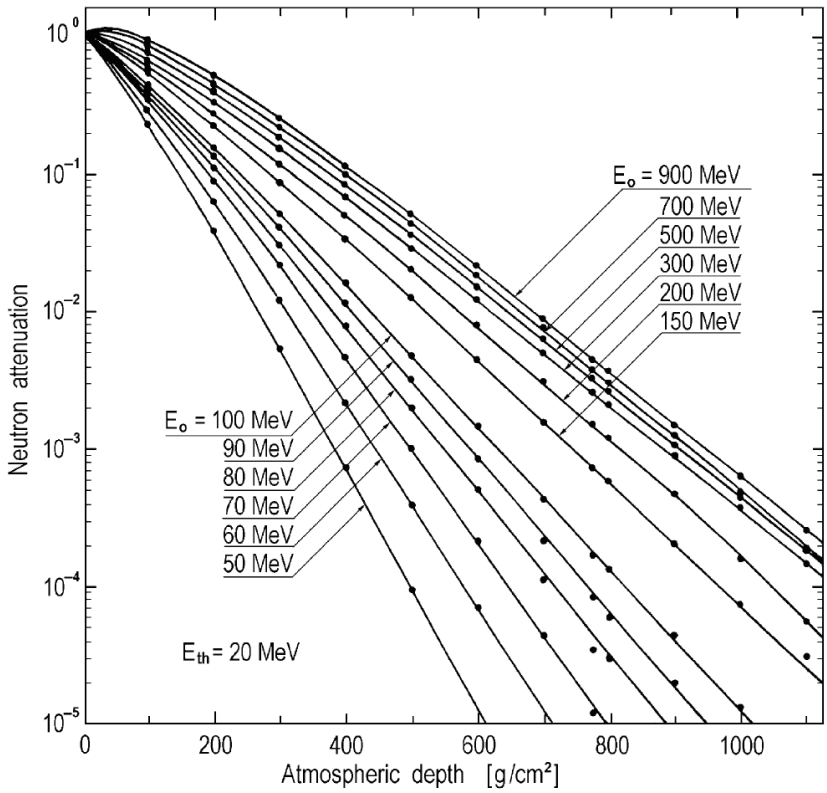

Figure 1.9: The attenuation of neutrons as a function of atmospheric depth for different incident energies (E_0) of neutrons at the top of the atmosphere. Calculation made by Dorman (2010) based on the Shibata Model.

1.5 Aim of this thesis

Thus far, 10 highly significant solar neutron events associated with large solar flares were successfully detected by ground-based detectors. However, they are not enough for clarifying the particle acceleration mechanism. Moreover, these events were searched whenever a very significant excess was seen in the data and then attributed to neutrons. Different criteria were applied to obtain these events, a systematic search for solar neutrons has not been executed so far. Additionally, an energy budget analysis between the associated soft X-ray (SXR) and the solar neutron emissions has not been performed yet.

In this thesis, there are three goals: the first is to search for solar neutrons applying the same criterion to all the candidate events; the second is to set upper limits in case no significant events are found in the data and the third is to compare the energy transferred to solar neutrons with the energy given to soft X-rays in large solar flares.

The search for solar neutrons in association with solar flares is performed in two campaigns. The GOES SXR onset and maximum intensity time are considered as indicators of solar neutron production. The first search is done with data collected by the Chacaltaya Neutron Monitor during the rising period of solar cycle 24 (January 2010 to August 2013). In this campaign, M- and X-class flares are considered. The second search is done with data collected by six detectors, the neutron monitor and the five solar neutron telescopes. Five years (January 2010 to December 2014) worth of data are analyzed. In this campaign, only X-class flares are considered.

The search returned no significant events which can be attributed to solar neutrons. Therefore, upper limits of detection are set in the 70-1000 MeV range for 35 X-class flares based on a statistical method and assuming impulsive emission. Next, the energy spectra of neutrons are built with these upper limits. A power-law shaped energy spectrum, which is theoretically expected from the shock acceleration process of ions in solar flares, was assumed. Here, the differential power law index is assumed to take values of 3, 5, and 7. Then, the neutron emissions are estimated between the energy range of 70-1000 MeV. The detection efficiency, the neutron attenuation in the atmosphere, the neutron survival probability, and the upper limit of detection of six detectors are considered.

Finally, three comparisons are made related to the energy budget: 1) the estimated neutron emissions of 35 X-class flares with that of the ten successful detections of solar neutrons; 2) the total energy release of neutrons with the soft X-ray radiated energy of those 35 flares and 3) the total energy release of neutrons with the peak thermal energy. The result of these comparisons give the amount of the needed energy to produce solar neutrons, which is on the order of 10^{30}[erg].

This thesis is organized in the following way. The characterization of the detectors: the neutron monitor and the solar neutron telescopes are described in Chapter 2. A summary of the ground-based detected solar neutron events is described in Chapter 3. The statistical analysis, method, data sample and results for the two search campaigns are described in Chapters 4 and 5. Then, the upper limits of detection and consequently the neutron emissions of the analyzed events of the second campaign are described in Chapter 6. Lastly, the conclusions and consequences of the upper limit are summarized in Chapter 7.

Chapter 2

Solar neutron detectors

As mentioned in the previous chapter, solar neutrons can travel from the Sun to the top of the Earth's atmosphere without suffering much attenuation other than decay. Thus, they can be detected both on the ground and in the space. On the ground, there are two traditionally operated kind of detectors, the Neutron Monitor and the Solar Neutron Telescope are used. In the space, there are solar-neutron specialized instruments such as the SEDA-AP/FIB instrument attached to the ISS (International Space Station) and the NS instrument onboard the MESSENGER spacecraft. In this chapter, these detectors are briefly described.

2.1 Ground-based observation

2.1.1 The Neutron Monitor

Neutron monitors were originally designed to continuously record the cosmic ray intensity. However, Chupp et al. (1987) proved that they can also observe solar neutrons. There are about 50 of these detectors which have been installed around the world. Recently, there is a movement to make a worldwide network of standardized neutron monitors (Mavromichalaki et al. (2011)). These neutron monitors are of two types, one is the IGY and other is the NM-64, both are currently in operation. The first one was designed by Simpson et al. (1953). The other was designed by Carmichael (1968) (see Figure 2.1a). The NM-64 (hereafter NM) is widely operated because of its higher efficiency compared to the IGY type. In Table 2.1 a comparison between these two types is given.
Neutron monitors are composed of four main parts (layers). They are, the reflector, the producer, the moderator and the counter. The detection method of the NM is as follows. First, incoming particles go through the most outer part of the detector (the reflector). Here, mostly low energy neutrons and environmental radiation (produced in the atmosphere) are rejected, only high energy nucleons (protons, neutrons, etc.) will go through the reflector to reach the producer. Next, at the producer, high energy nucleons via nuclear interactions with lead will produce evaporation neutrons. Then, these evaporation neutrons are slowed down at the moderator to nearly thermal energies to facilitate their capture by the proportional counter (containing BF_3 gas). In the counter, neutrons are captured by ^{10}B nucleons with the following exothermic reaction,

$$^{10}\mathrm{B} + n \rightarrow \begin{cases} ^{7}\mathrm{Li} + ^{4}\mathrm{He} & \text{Q=2.792MeV} \quad \text{(ground state)} \\ ^{7}\mathrm{Li}^{*} + ^{4}\mathrm{He} & \text{Q=2.310MeV} \quad \text{(excited state)} \end{cases}$$

A technical problem with the NM is the multiplicity effect which provides after the detection. Basically the particles are over counted at the moderator, then an statistical-based correction is necessary to compensate this over counting. In this thesis, this effect is considered in the analysis.

Table 2.1: Comparison between two types of Neutron monitors. According to Hatton (1971); Stoker (2009).

	IGY	NM-64
Reflector		
Material	Paraffin	Polyethylene
Average thickness[g/cm^2]	25.8	7.0
Producer		
Material	Lead	
Average Depth [g/cm^2]	153	156
Length parallel to counters [cm]	102	207
Moderator		
Material	Paraffin	Polyethylene
Average thickness [cm]	3.2	2.0
Counter		
Spacing[cm]	15.2	50.0
Active length [cm]	86.4	191
Diameter [cm]	3.8	14.8
Pressure [mmHg]	450	200

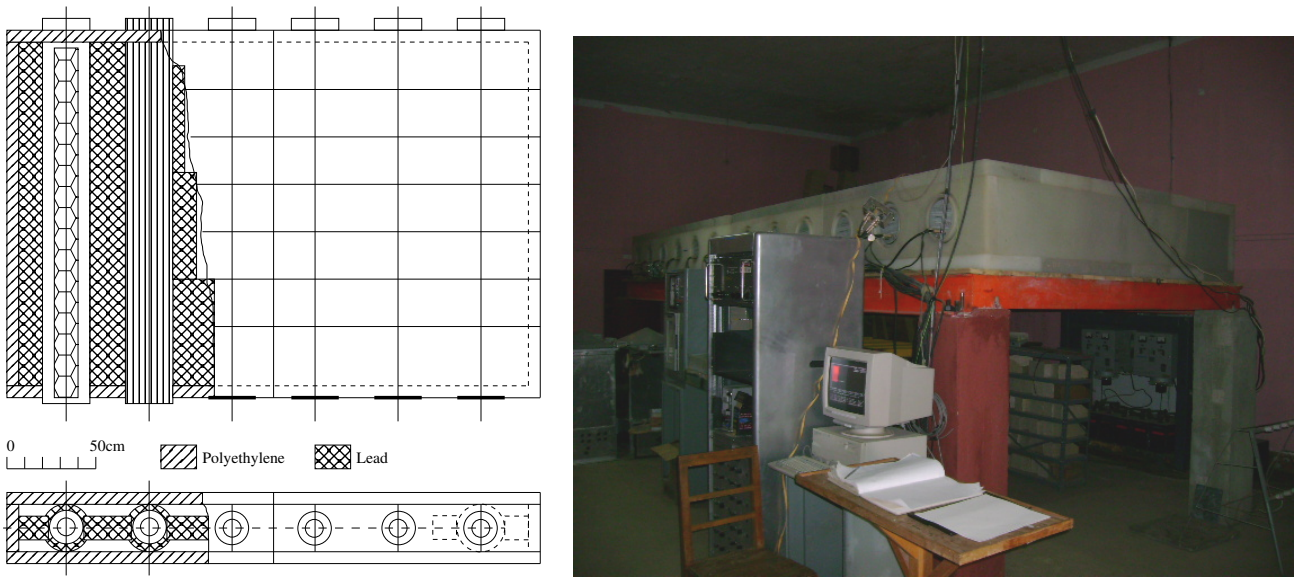

(a) (b)

Figure 2.1: (a) The 6NM-64 neutron monitor, shown diagrammatically (Reproduced from Carmichael (1968)), was designed for higher count rate and better statistics than the IGY neutron monitor, in particular for short-term events. (b) The Chacaltaya 12NM-64 installed at 5250 m in the Andes of Bolivia (Martinic et al., 1985).

The detection efficiency of the NM was first calculated by Hatton (1971), and later by Clem and Dorman (2000). This latter result is shown in Figure 2.12 together with the detection efficiency of the SNT.

Due to its simple structure, a NM can be easily constructed and installed. However, the NM cannot measure the energy and the arrival direction of the incoming particle. Such information are lost in the producer and the moderator. By assuming the production time of neutrons at the Sun, it is possible to

Table 2.2: The geographical locations of the detectors from the International Network of Solar Neutron Telescopes. A four-letter code has been assigned to each detector.

	Location	Long	Lat	Height [m]	Air mass [g/cm^2]	Operation
ARAM	Mt. Aragats, Armenia	40.5°E	44.2°N	3200	670	1997 Jun∼
GOSW	Gornergrat, Switzerland	7.8°E	46.0°N	3135	690	1998 Jan∼
MKUS	Mauna Kea, USA	156.3°W	19.8°N	4200	610	1997 Apr∼
CHBO	Mt. Chacaltaya, Bolivia	68°W	16.2°S	5250	540	1992 Sep∼
SNMX	Mt. Sierra Negra, Mexico	97.3°W	19.0°N	4580	575	2003 Jun∼
NRJP	Mt. Norikura, Japan	137.5°E	36.1°N	2770	730	1996 Oct∼
YACH	Yangbajing, China	90.5°E	30.0°N	4300	600	1999 Sep∼

infer the energy of neutrons. A detector which can accomplish such endeavors is required. It is the reason why the Solar Neutron Telescope was developed.

The Chacaltaya Neutron Monitor

The neutron monitor installed at Mount Chacaltaya (5250 m, 16°21′S, 68°08′W) in Bolivia is of the NM-64 type. It consists of 12 tubes, which are aligned horizontally. The area of the whole detector is 13.1 m^2. It has operated since 1966 (Martinic et al., 1985). A photograph of the detector can be seen in Figure 2.1b. The data collected by these detector are used in the search for solar neutrons.

2.1.2 The Solar Neutron Telescope

The Solar Neutron Telescope has the ability to:

1. Measure the energy of the incoming particle.
2. Discriminate between charged particles and neutral particles.
3. Determine the arrival direction of the incoming particle.

Seven detectors have been installed around the world forming the International Network of Solar Neutron Telescopes (SNT Network). In Table 2.2 the geographical position, height, vertical air mass, and start of operation of each SNT are listed. These detectors are installed at low-latitude and high-altitude locations. Both, low latitude and high altitude are required to reduce the attenuation of neutrons in the atmosphere. Because of their location, at least two neighboring detectors of this network can see the solar disc simultaneously as the Earth makes its 24h spin. This gives the possibility to examine the consistency of data at the time of observing solar neutrons.
The basic components of the SNT are the target, the photo-multiplier tube (PMT) and the proportional counters (PRCs). The target is made of plastic scintillator. The PRCs work both as directional counters and veto counters to charged particles. They are put before the incoming particles hit the target layer when they are used as veto counters. Underneath of some of the SNTs an array of PRCs is installed to determine the arrival direction.
The SNT has two operational modes to do the particle discrimination. The first one is called ”without_anti”. This mode is activated when an incident charged particle hits the veto counters, then an electronical signal is produced. In the case that signal is in electronical coincidence with the signal produced in the target, these signals will be recognized as charged particles. The other operational

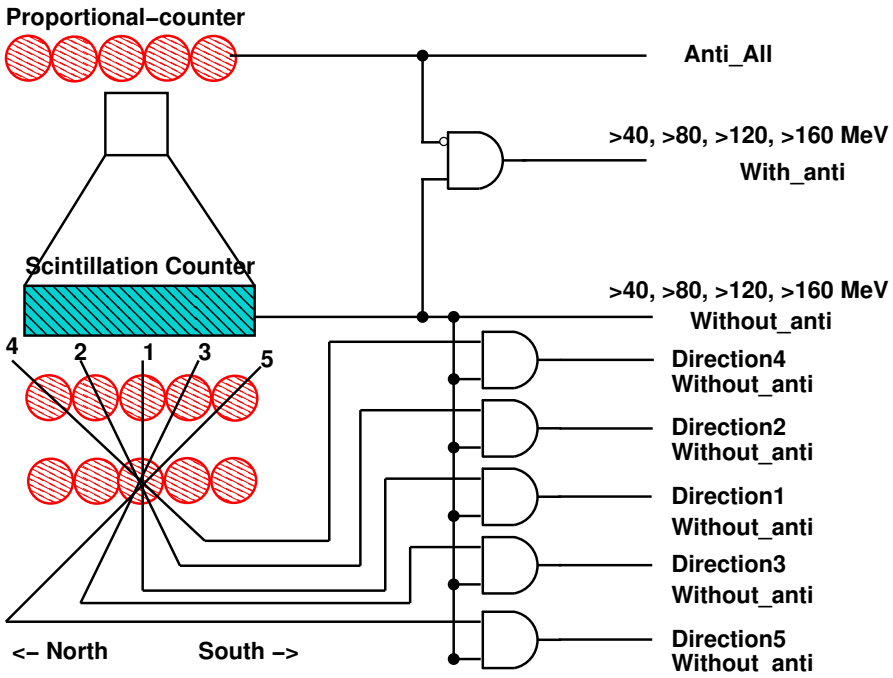

Figure 2.2: Schematic view of the electronic detection system of the Solar Neutron Telescope

Table 2.3: Characteristics of the SNTs

SNT	Area [m^2]	Target Thickness[cm]	Threshold level [MeV]				anti counter	directional mode
ARAM	4	60	>40	> 80	> 120	> 160	Top	Yes
CHBO	4	40	>40	> 80	> 160	> 240	Top + Side	No
GOSW	4	40	>40	> 80	> 120	> 160	Top + Side	5NS
MKUS[a]	8	20	>12	> 20			Top	3NS
NRJP	64	20	>40	> 80	> 120	> 160	Top + Side	5EW × 5NS
SNMX	4	30	>30	> 60	> 90	> 120	Top + Side	5EW × 5NS
YACH	9	40	>40	> 80	> 120	> 160	Top + Side	9EW × 9NS

[a] >12 MeV corresponds to PMT-L and >20 MeV to PMT-H.

mode "with_anti" is the anti-coincidence of the veto counter signals, hence they are identified as neutral particles. In Figure 2.2 a schematic view of the electronic system is shown.

The process that occurs inside the plastic scintillator is as follows. First, incoming neutrons are converted into protons by nuclear interactions in the target. Then, recoiled protons which are subjected to a charge exchange process tend to be scattered around the direction of incident neutrons, almost conserving its energy. The ionization energy loss of the protons is converted to scintillation lights and measured by PMTs located on top or side of the target. The number of signals exceeding the four different threshold levels are counted at each time interval. This gives information on the energy of the recoiled protons. In Table 2.3 the area of the SNTs, the thickness of the target, the discriminator thresholds of the PMTs, the location of the anti-counters and the size of the PRCs' array are shown for each SNT. Giving the fact that since 2007, ARAM (Aragats Solar neutron telescope) (Chilingarian 2003) operates independently from the SNT network, data from this detector are not considered in the analysis.

There are three stations where the SNTs have the ability to measure the local temperature and pres-

Table 2.4: Coefficients provided by Technoland.

Variable	Value	Variable	Value
$U_0[\mu s]$	5.759	$Y_1[^\circ/\mu s]$	-4039.117
$Y_2[^\circ C/\mu s^2]$	-10982.850	C_1[psi]	95.068
$C_2[psi/\mu s]$	4.487	$C_3[psi/\mu s^2]$	-108.638
D[psi]	0.035	$T_1[\mu s]$	27.915
$T_2[\mu s]$	0.739	$T_3[\mu s^{-1}]$	19.510
$T_4[\mu s^{-2}]$	7.408		

sure. A thermometer/barometer is installed within the electronic equipment and by a conversion, environmental information can be obtained.
The needed conversions are provided by the manufacturer[1] and given by,

$$\begin{aligned} X[\mu s] &= 10^6/f_T \\ U[\mu s] &= X - U_0 \\ T[^\circ C] &= Y_1 U + Y_2 U^2 \end{aligned} \tag{2.1}$$

$$\begin{aligned} V[\mu s] &= 10^6/f_p \\ C[psi] &= C_1 + C_2 U + C_3 U^2 \\ T_0[\mu s] &= T_1 + T_2 U + T_3 U^2 + T_4 U^3 \\ T_{par} &= \left(1 - \frac{T_0^2}{V^2}\right) \\ \frac{p[hPa]}{68.95} &= C\, T_{par}\, (1 - D\, T_{par}) \end{aligned} \tag{2.2}$$

In Eqs 2.1 and 2.2, $f_T[s^{-1}]$ and $f_p[s^{-1}]$ are the counting rates that are recorded together with the scintillator and the PRCs signals. In Table 2.4 the coefficients of Eqs 2.1 and 2.2 are listed. The capability to detect solar neutrons with the Solar Neutron Telescope (SNT) was confirmed when a 1-m^2 test prototype SNT installed on Mount Norikura, Japan in 1990 was able to detect solar neutrons associated with a large flare (X12.0) in 1991 June 4 (Muraki et al., 1992). The technique developed for the Mt. Norikura SNT has been improved and highly sophisticated versions have been developed. They are described in the following sections.

The Mount Norikura Solar Neutron Telescope - NRJP

The NRJP is installed at the Mount Norikura Cosmic Ray Observatory, Institute for Cosmic Ray Research, University of Tokyo, at 2770 m above sea level in Japan. It has an area of 64m^2 becoming the largest among the SNT Network. It has been operating since 1996 October (Muraki et al., 1997). In Figure 2.3 a schematic view of the NRJP is shown. In this SNT the scintillation counters are arranged in a 8×8 array. Each scintillator has a volume of 1m×1m×0.2m. Charged particles are rejected by the proportional counters which are on the top and the sides of the detector. γ-rays are converted to electron-positon pairs in the 0.5 cm lead plate located on the top of the PRCs and are rejected as charged particles. Underneath the detector an array of orthogonally-aligned PRCs is

[1]The manufacturer of the electronic component (NIM module) is Technoland Corporation (`http://www.tcnland.co.jp`)

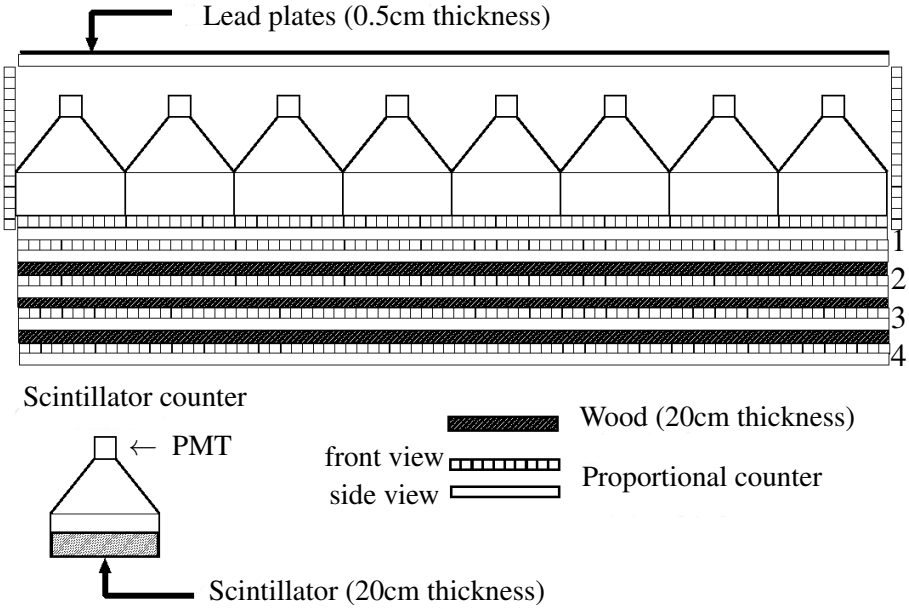

Figure 2.3: Schematic view of the Norikura Solar Neutron Telescope. Four layers of proportional counters, which are under the scintillators, are used to measure directions of recoil protons. PRCs 1 and 3 measure the North-South direction and PRCs 2 and 4 measure the East-West direction. Figure from `http://www.stelab.nagoya-u.ac.jp/CR/res02/observation/detection`

located in a 4-layer arrangement. This set is used to detect the direction of the recoiled proton. The method of detection is the same as shown in Figure 2.2. The North-South direction is measured by combining two PRCs of layers 1 and 3. The East-West direction is similarly measured by using layers 2 and 4. Each direction can be divided into five sections. In total, 25 directions can be measured. The threshold levels are the following: >40 MeV, >80 MeV, >120 MeV, and >160 MeV. The counting rate of these channels is recorded every 10 seconds. Giving that the Norikura NM also operates at the same Observatory, then its signal is recorded together with the signals of NRJP.

The Mount Chacaltaya Solar Neutron Detector - CHBO

The CHBO is installed at the Chacaltaya Cosmic Ray Laboratory at 5250 m above sea level. It has operated since September 1992 (Matsubara et al., 1993) and is maintained by the Instituto de Investigaciones Físicas, Universidad Mayor de San Andrés. The CHBO is a simple detector as seen on the left of Figure 2.4. It consists of four 1-m^2 plastic scintillators with a 40-cm thickness. The anti-counter consists of 17 scintillators, each with an area of 220cm$\times$46cm and a 1-cm thickness. The energies of the recoiled protons are discriminated by four threshold levels, >40 MeV, >80 MeV,>160 MeV, and >240 MeV. The counting rate is recorded every 10 seconds. As seen on the right of Figure 2.4, the CHBO does not have an array to determine the arrival direction of the recoiled proton.

The detection signal of the Chacaltaya NM which operates near the CHBO is sent via an optical fiber to the SNT site and recorded together with the CHBO signals. To have time accuracy, synchronization using a GPS is available and time data is recorded. Since March 2012 the data acquisition computer clock is synchronized, at least once a day, via internet with the NTP timeserver *south-america.pool.ntp.org*.

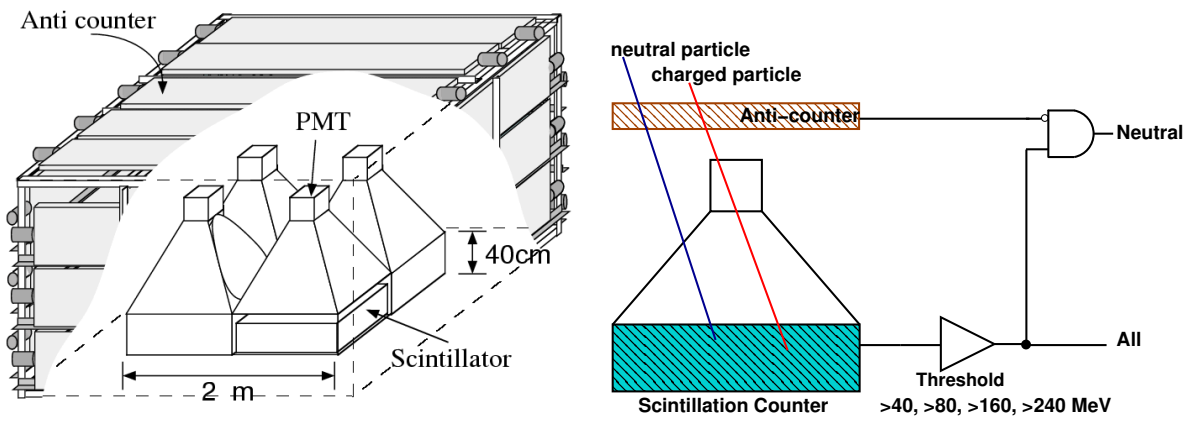

Figure 2.4: On the left, an schematic view of the Bolivia solar neutron detector is shown. The thickness of the plastic scintillator, the position of the PMT and the anti-counters are also shown. On the right, the detection logic showing the discrimination levels. The coincidence and anti-coincidence process is also shown.

The Gornergrat Solar Neutron Telescope - GOSW

The GOSW is located in Gornergrat, Switzerland at 3135 m above sea level. It has operated since 1998 (Flückiger et al., 1998). In Figure 2.5a a schematic view of this detector can be observed. GOSW has an area of 4 m^2 and consists of a horizontal array of four 1-m^2 plastic scintillators area with a thickness of 40 cm. Scintillation counters are covered with PRCs on top, side, and underneath the detector. The energies of the recoiled protons are measured by four threshold levels, >40 MeV, >80 MeV, >120 MeV, and >160 MeV. To determine the arrival direction of the recoiled proton, two layers of PRCs are set under the detector, hence, the North-South directions can be measured. The counting rate is recorded every 10 seconds. The data acquisition computer is synchronized with the NTP timeserver *sns2-tss2.unige.ch* once a day. This detector is maintained thanks to the help of the Cosmic Ray Group, Physikalisches Institut from the University of Bern. More details can be found in Moser (2002).

The Yangbajing Solar Neutron Telescope - YACH

The YACH is located in Yangbajing in the Tibet autonomous region of China at 4300 m above sea level. The detector was constructed in September 1998 (Katayose et al., 1999) and has been operated ever since. In Figure 2.5b a schematic view of this detector can be observed. YACH is structured in the same way as GOSW. However, nine instead of four scintillation counters are installed, giving an effective area of 9m^2. Under the detector four layers of PRCs aligned orthogonally are installed. Two 10-cm thick wood layers are installed in between the PRCs. Wood is used as an absorber of low energy particles. The North-South and East-West directions are divided into 9 sections, thus, the array can measure up to 81 directions. Since November 2002, the trigger rates of the scintillation counters, the PRCs and the 81 directions are recorded every second. Due to some power failures at the installation site, data acquisition stops occasionally.

The Mount Mauna Kea Solar Neutron Telescope - MKUS

The MKUS is located in Mauna Kea, Hawaii, inside the dome of the Subaru Telescope of the National Astronomical Observatory of Japan at 4200 m above sea level. It has operated since April 1997 (Matsubara et al., 1997). MKUS consists of four layers of scintillation counters. Each of these

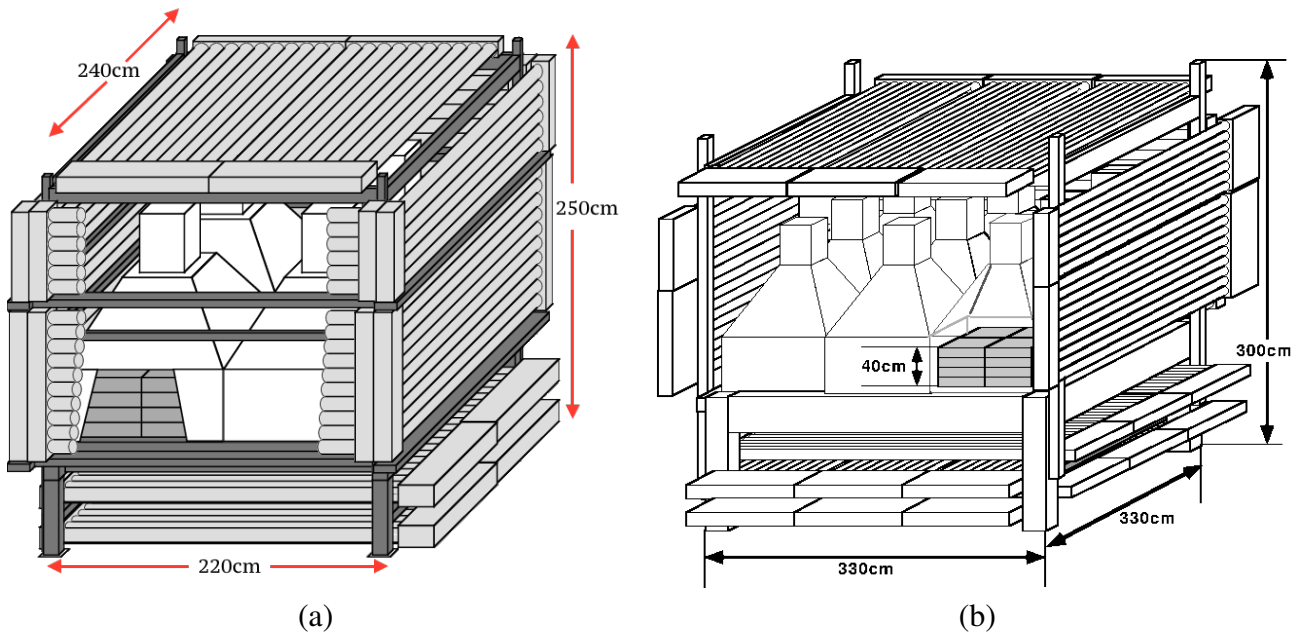

Figure 2.5: (a) Schematic view of the Switzerland SNT. (b) Schematic view of the Tibet SNT. Both schemes can be found at http://lhcfs1.stelab.nagoya-u.ac.jp/www-binary/Neutron/index.html

counters are formed by 16 plastic scintillators with a volume of 50cm×50cm×10cm. A wavelength shifter is inserted in the plastic scintillator. On top, a layer of 20 proportional counters are arranged, which work as an anti-counter to veto charged particles. In Figure 2.6 an overview of the detector is shown. The following layers are wood with thickness of 10 cm. The whole detector has an effective area of 8m^2. The counting rate is recorded every 10 seconds.

The Mount Sierra Negra Solar Neutron Telescope - SNMX

SNMX is located on top of Mount Sierra Negra in Mexico at 4580 m above sea level. It has been operated since June 2003 (Valdés-Galicia et al., 2004). On the site another detector has recently been installed (q.v. section 2.1.4). In Figure 2.7 a schematic view of SNMX is shown. This detector has the same structure as GOSW and YACH. The thickness of the plastic scintillator is different though. Four 30-cm-thick plastic scintillators are installed and surrounded by PRCs. The energies of the recoiled protons are measured by four threshold levels, >30 MeV, >60 MeV, >90 MeV, and >120 MeV. Under the detector, an array of four layers of PRCs is installed. The East-West and North-South directions are divided into 5 sections, obtaining 25 different directions. Above the PRCs which lay on top of the detector, a 0.5-cm lead plate has been put. This plate can convert incoming photons into electron-positron pairs, to be considered as charged particles. On the sides of the detector, iron plates have been placed to reduce the background. The data acquisition computer records trigger rates of the scintillation counters, the PRCs, the 25 directional channels and the recording time every 10 seconds. The system clock is synchronized via internet by an NTP timeserver. SNMX is regularly mantained by the Instituto de Geofísica from the Universidad Nacional Autónoma de México.

2.1.3 Performance of the SNT

The Solar Neutron Telescopes are plastic-scintillator based detectors, thus in this section their response to solar neutrons will be described. Several authors have examined the SNT performance. First, Tsuchiya et al. (2001) examined the detection efficiency of the SNT by performing an accel-

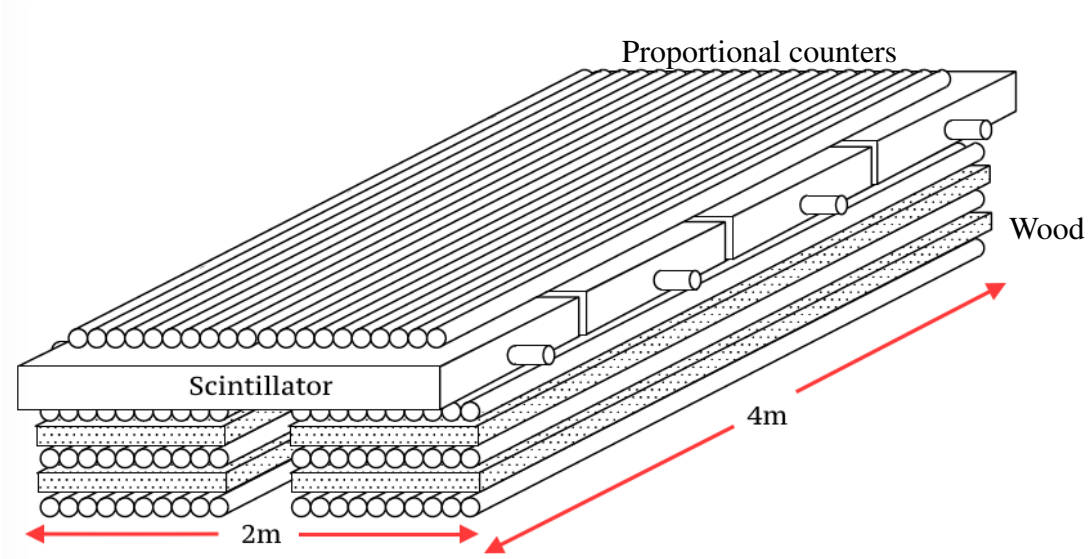

Figure 2.6: Schematic view of the Mauna Kea Solar Neutron Telescope. On the top layer, there are proportional counters, underneath is the scintillator box, and then the two layers of wood. Figure from Nagai (2014).

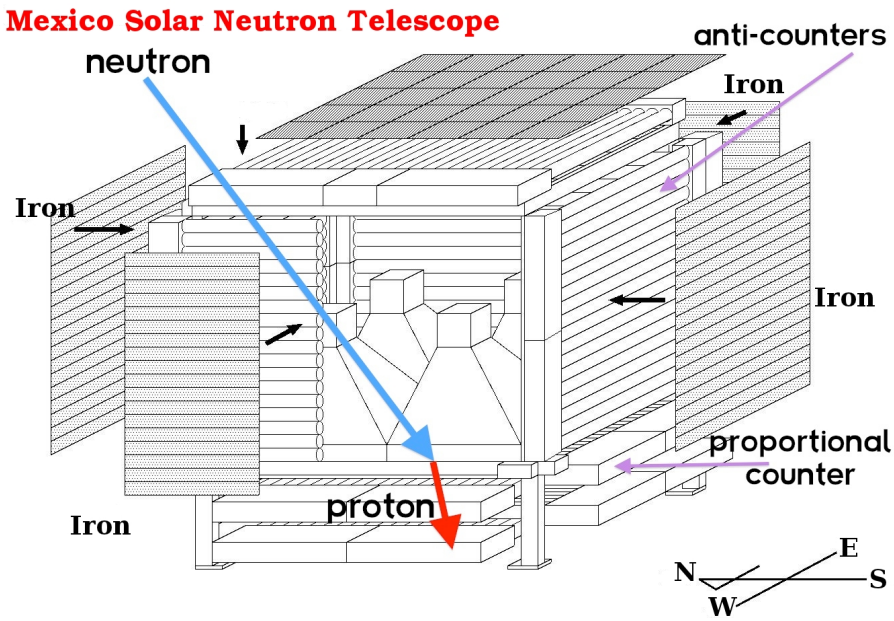

Figure 2.7: Schematic view of the Mexico Solar Neutron Telescope. Five arrays of proportional counters, located on top and sides, shield the plastic scintillators. Lead and iron plates (0.5 cm) located on top and sides are installed to convert background photons into electron and positron pairs (figure from Valdés-Galicia et al. 2004).

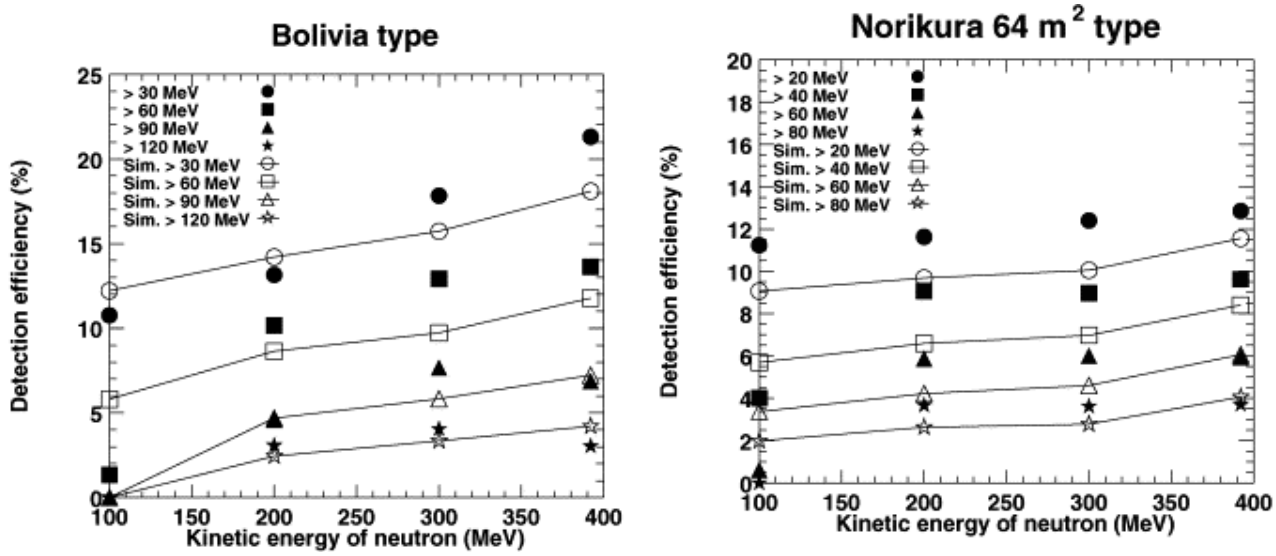

Figure 2.8: The experimental and Montecarlo simulation results for two SNTs. The ordinate gives the detection efficiency as a percentage and the abscissa gives the kinetic energy of neutrons in MeV. On the left, the results for the Bolivia detector and on the right the results for the Norikura detector. According to Tsuchiya et al. (2001).

erator experiment at the Research Center for Nuclear Physics of Osaka University. The experiment was performed with scaled versions of the SNTs which are installed in Gornergrat, Mauna Kea, Norikura and Chacaltaya. Due to limitations in the neutron beam, the neutron kinetic energy was set between 100 MeV and 392MeV. Additionally, Tsuchiya et al. calculated the SNT performance via Monte Carlo simulations. In Figure 2.8 the detection efficiencies for the Norikura and Chacaltaya SNTs are shown. Next, Moser (2002) examined the detection efficiency of the Gornergrat SNT via Monte Carlo simulations. He included the three modes of operation of the SNT, the with-anti, the without-anti and the directional mode. Moser's calculation considered the same kinetic energy of the threshold levels as of GOSW. In Figure 2.9 the results for the Gornergrat SNT are shown. In 2005, K. Watanabe performed a similar calculation to obtain the detection efficiency of the Mauna Kea SNT and the Yangbajing SNT. In Figure 2.10 the results of the simulation for both detectors are shown. Lastly, González et al. (2015), calculated the detection efficiency of the Sierra Negra SNT. In Figure 2.11 these results are shown. They calculated the performance of the plastic scintillator including the dependence on the incident angle and the probability of the incoming particle to produce protons.
Figure 2.12 shows the detection efficiencies of five SNTs for the lowest energy threshold and the with_anti operation mode. In spite that >30 MeV is the lowest energy threshold of SNMX, the >60 MeV channel is plotted here, because the >30 MeV channel was not properly working during the period of analysis. The detection efficiency for the NM adopted in this work is the calculated by Clem and Dorman (2000), added here just for comparison.

2.1.4 The Scintillation Bar Cosmic Ray Telescope - SciCRT

In 2003, Sako et al. proposed a new ground-based detector for solar neutrons to improve the current SNT. The detector uses scintillator bars, as shown in the left of Figure 2.13, and is much larger in volume than the traditional SNTs. This detector can measure the track of particles event by event, therefore the energy resolution and the directional determination are much improved. The new detector is called SciCRT (SciBar Cosmic Ray Telescope) and it was made possible thanks to the use of the SciBar detector, together with the scintillation bars, the optical sensors and the electronics, which

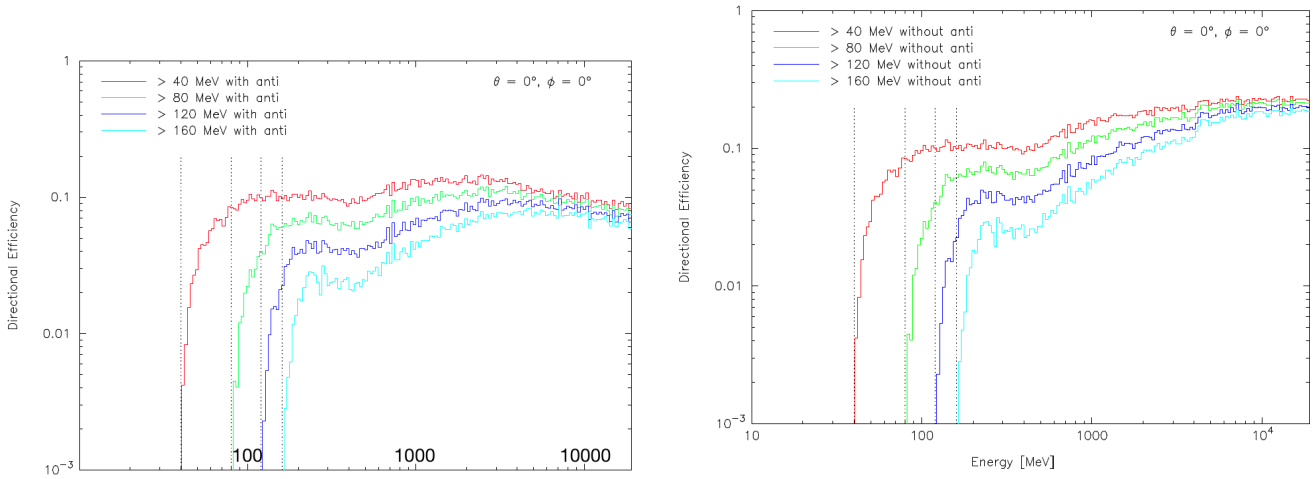

Figure 2.9: Simulated vertical directional efficiency for neutrons. Vertical dotted lines indicate the threshold energies of the four detection channels. On the left plot the four energy thresholds of the with-anti channels. On the right plot, the without-anti channels. According to Moser (2002).

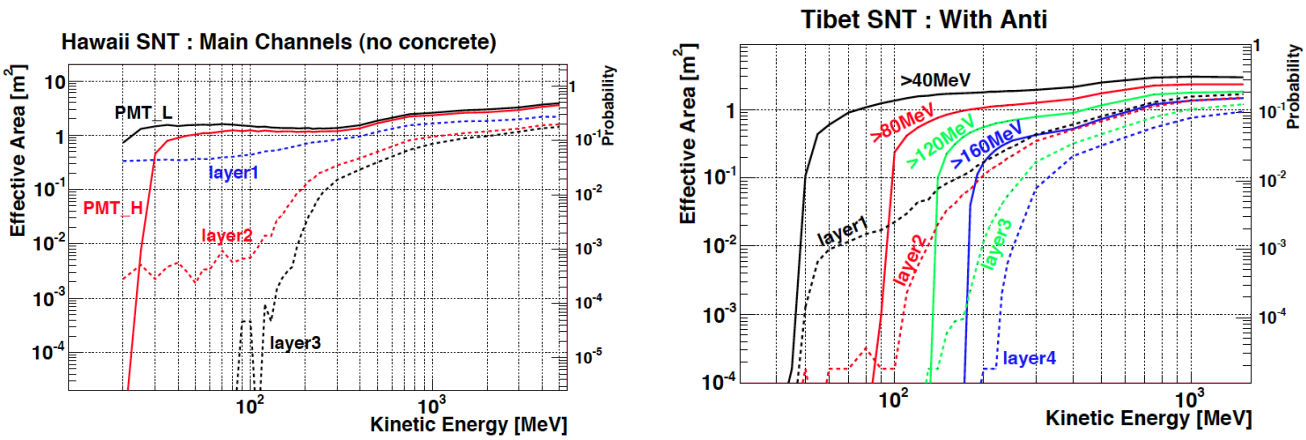

Figure 2.10: The detection efficiencies of two SNTs for neutrons according to K. Watanabe (2005). On the left for the Mauna Kea (MKUS) detector. Solid lines indicate the PMT-L and PMT-H scintillator channels. Dashed lines indicate those for the layer channels. On the right for the Tibet (YACH) detector. Efficiencies were calculated for the with-anti channel. Solid lines indicate the four different threshold levels. Dashed lines display the layer channels.

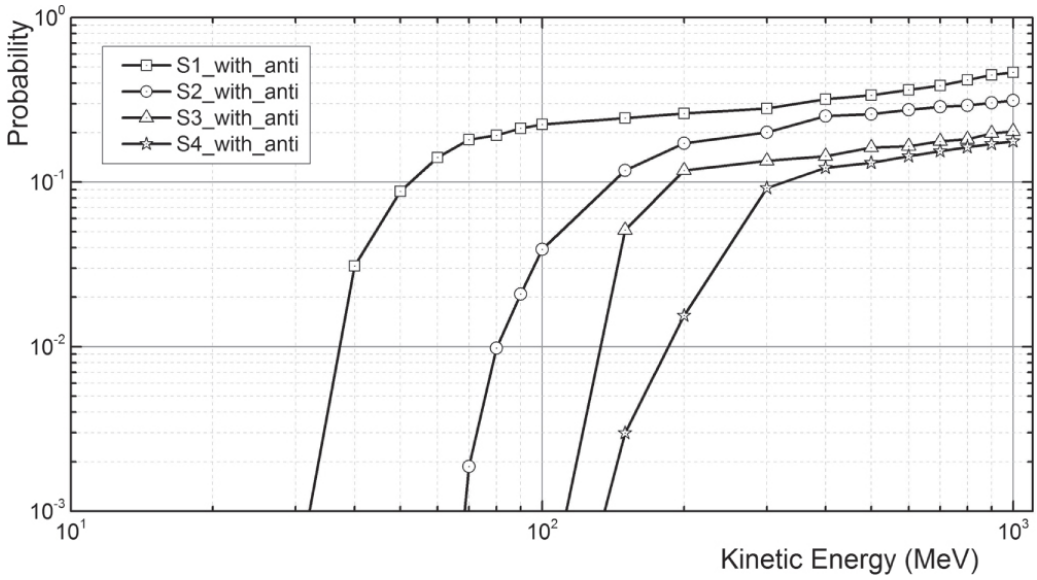

Figure 2.11: The detection efficiency for neutrons of the four with-anti channels of the Mexico Solar Neutron Telescope, according to González et al. (2015). In this Figure, "S1_with_anti" corresponds to the lowest energy threshold level (>30 MeV), "S2_with_anti" is for the >60 MeV and so on.

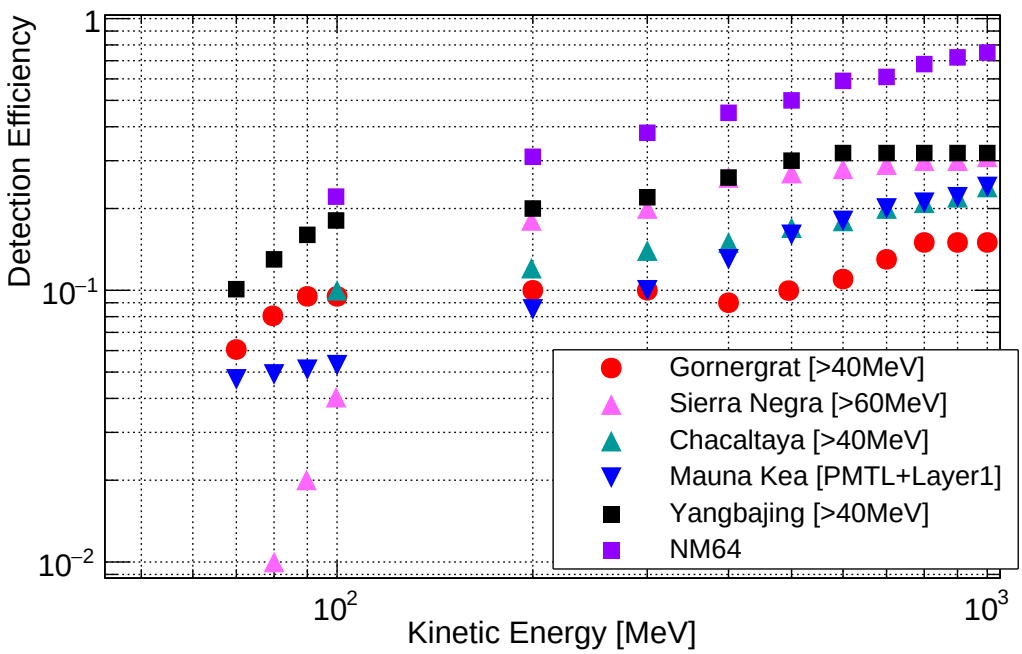

Figure 2.12: The detection efficiency for the lowest energy threshold of the SNTs and the NM is plotted as a function of the kinetic energy. In these calculations, neutrons were distributed evenly over the detector, with a vertical injection angle ($\theta_{\odot} = 0°$). Here are summarized the works made by H. Tsuchiya et al., 2001 (CHBO), M. Moser, 2002 (GOSW), K. Watanabe, 2005 (MKUS and YACH), L.X. González et al., 2015 (SNMX), and Clem & Dorman, 2000 (NM64 type).

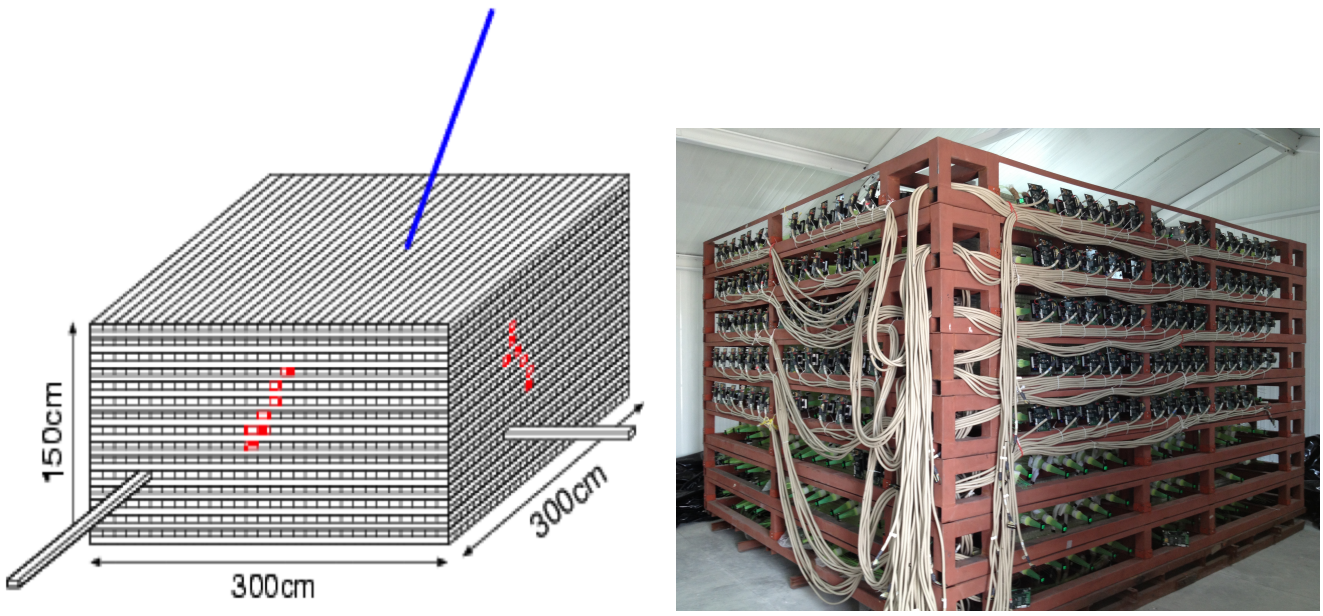

Figure 2.13: On the left, the SciCRT design proposed by Sako et al. (2003). On the right, the real detector installed at the top of Mt. Sierra Negra in Mexico at 4580 m

had been used at the accelerator experiment (Nitta et al., 2004).
The SciCRT consists of approximately 15000 plastic scintillator bars aligned orthogonally to form planes which are stacked up in blocks of eight. Each bar has a dimension of 1.3cm×2.5cm×300cm. The whole detector is currently installed at the top of Mount Sierra Negra in Mexico and started to operate and give its first results in 2013 (Nagai, 2014). On the right of Figure 2.13 a photograph of the real detector can be seen. This detector, up to now (February 2016), is not yet fully operational. There are several tasks that have to be completed before its full operation.
Since the original purpose of this detector was to operate at an accelerator experiment. Several tests are necessary before observing cosmic rays at high altitude. Before the actual installation of the SciCRT, a prototype (called mini-SciCR) was constructed to explore the operability of the components (Photo-Multipliers, Data Acquisition boards, Wave-Length Shifting fibers) at high altitudes. The performance of the mini-SciCR was examined by Nagai (2011) and Lopez (2012).

2.2 Space observation

Ground-based detectors have to deal with the attenuation of neutrons in the atmosphere. In space, detectors are free of such limitation. A very large detector, such as a NM cannot be installed in space, because of operational issues. Thus, space borne detectors are small in size, and their main purpose is to observe neutrons at the low energy range, less than 100 MeV. Most of those neutrons decay before reaching the Earth, but some signals of neutrons are still expected if the energy spectrum of neutrons is soft. To follow, two principal solar-neutron dedicated instruments are described.

2.2.1 SEDA-NEM

Imada et al. (1999) proposed a solar neutron detector that can operate at the International Space Station (ISS). This detector is called SEDA-AP (Space Environment Data Acquisition Equipment-Attached Payload) and its purpose is to measure the space environment along the orbit of ISS (Koga et al., 2011). SEDA-AP has eight instruments to accomplish its goal (see Figure 2.14a). These are:

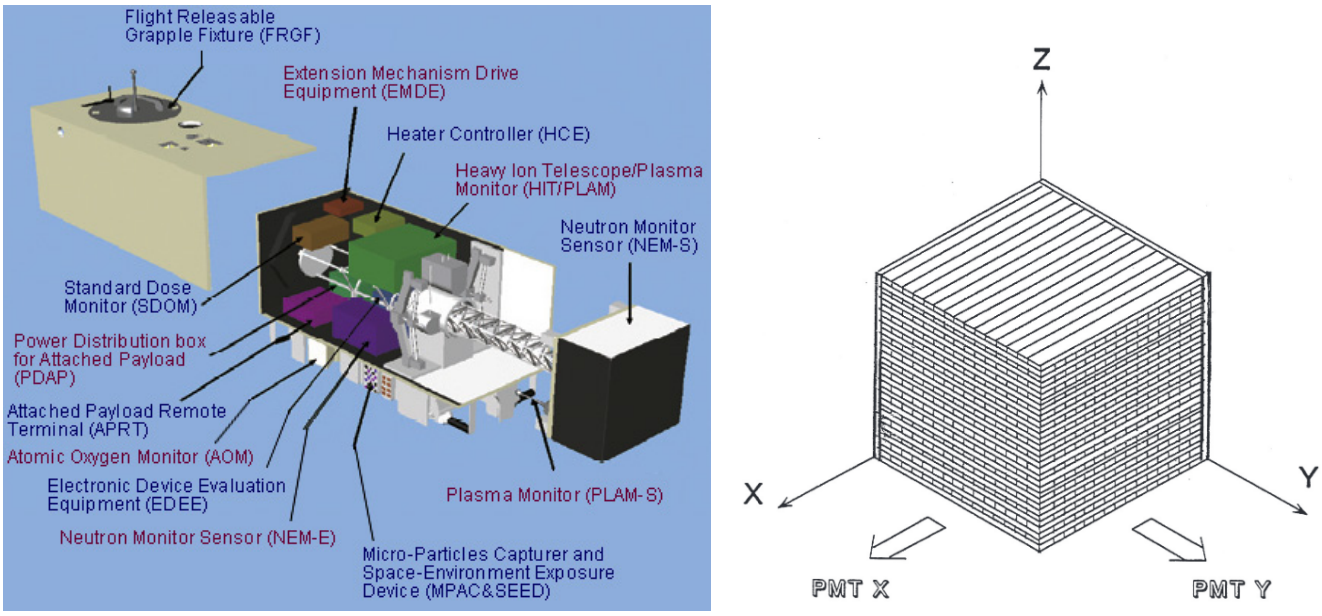

(a) (b)

Figure 2.14: (a)The SEDA-AP and its components. Figure from the JAXA website (`http://iss.jaxa.jp/en/kiboexp/theme/first/seda-ap/`). (b) The NEM instrument onboard SEDA-AP. Each layer of scintillation bars is located alternatively along the x-direction and y-direction. The two multi-anode photomultipliers are here denoted by PMT X and PMT Y. Figure from Koga et al. (2011)

1) Neutron Monitor (NEM), 2) Standard Dose Monitor (SDOM), 3) Heavy Ion Telescope (HIT), 4) Plasma Monitor (PLAM), 5) Atomic Oxygen Monitor (AOM), 6) Electronic Device Evaluation Equipment (EDEE), 7) Micro-Particle Capturer (MPAC) and 8) Space Environment Exposure Device (SEED). Detailed information of these instruments can be found at the JAXA website `http://iss.jaxa.jp/en/kiboexp/theme/first/seda-ap/`. To follow the NEM instrument is briefly described. The Neutron Monitor (NEM) measures the neutron energies from thermal to 100 MeV in real time using a Bonner Ball Neutron Detector (BBND) and a Scintillation Fiber Detector (FIB). The BBND discriminates neutrons from other charged particles by using He counters. It measures neutron energies from 0.025 eV to 15 MeV by using the relative response, which corresponds to the thickness of different polyethylene moderators.

The FIB has dimensions of 10cm$\times$10cm$\times$10cm and is assembled with mutually perpendicular scintillation bars (16$\times$16). Each bar has dimensions of 6mm$\times$3mm$\times$96mm. The whole detector can measure the tracks of recoil protons in each lot with a 256-channel multianode photomultiplier and estimates the energies and directions of incident neutrons by the amount of light emission and tracks. Discriminating neutrons from protons can be achieved by finding the anti-coincidence with light emissions from the scintillator at the outermost layer (a charged particle will emit light at the outermost scintillator). Discriminating neutrons from photons can be achieved by noting the difference in tracks (neutron: 1 track; photon: 2 tracks). The measured energy range is from 15 MeV to 100 MeV and 50 events can be recorded per second. In Figure 2.14b the alignment of the scintillation bars is shown. The capability of SEDA-FIB was confirmed in 2011 March 7 when solar neutrons where observed in association with an M3.7 class flare Muraki et al. (2013).

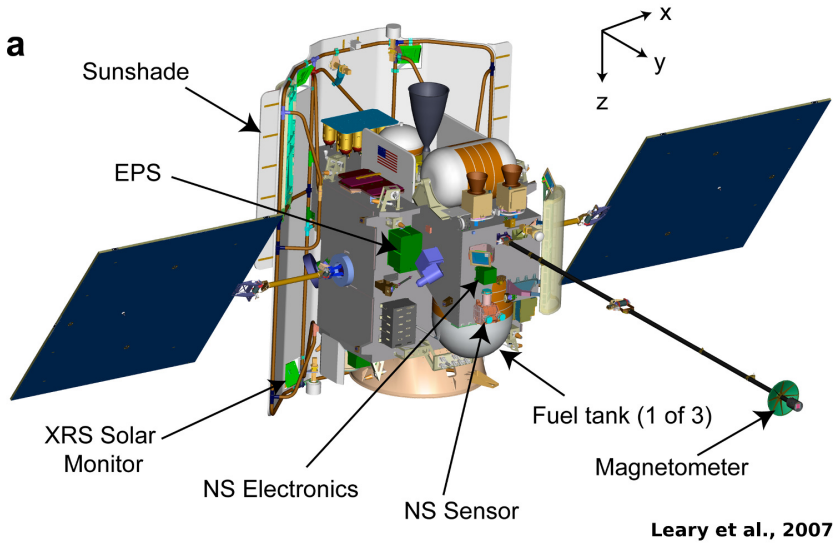

Figure 2.15: View of the MESSENGER spacecraft showing the location of the instruments. The NS is located near the base of the Magnetometer. Figure from the MESSENGER website `http://messenger.jhuapl.edu/instruments/index.html`.

2.2.2 MESSENGER

The closer to the Sun, the more likely of identifying neutrons that come directly from the Sun. This is because the survival probability of lower energy neutrons increase compared with the observation at the Earth. Therefore in 2011, the MESSENGER (MErcury Surface Space ENvironment Geochemistry and Ranging) spacecraft (see Figure 2.15) was inserted into the orbit of Mercury to carry out a comprehensive examination of the hosting planet and its space environment (Goldstein et al., 2007). One of the missions of this spacecraft is to detect solar neutrons. To accomplish such task an instrument called Neutron Spectrometer (NS) is onboard MESSENGER. In Figure 2.16b an schematic view of the NS detector is shown. The sensor element of the NS consists of three stacked scintillator sensors, each with an area of $\sim$100 cm^2. The two outside plates are 4mm thick lithium gas scintillators, and the middle sensor is a cubic borated plastic scintillator (see Figure 2.16c).
The NS can detect neutrons in the region between 0.3 to 0.85 AU. The detector is sensitive to neutrons with energies ranging from thermal ($<$0.4eV) up to fast (0.5–8 MeV) (Goldstein et al., 2007). It can be however, sensitive to energetic protons ranging in energy from 10 MeV to $>$120 MeV (Lawrence et al., 2014).

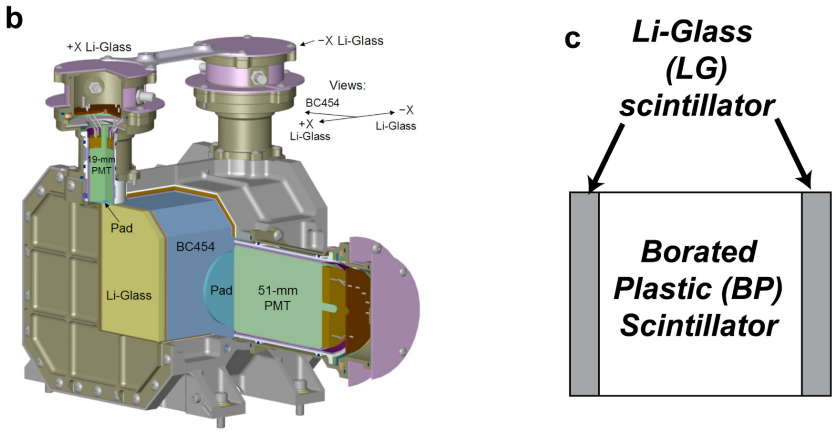

Figure 2.16: b) View of the NS detector. c) Schematic view of the sensor element of the NS. Figure from Goldstein et al. (2007).

Chapter 3

Summary of solar neutron events in past cycles

In the previous chapter, the detectors of solar neutrons were described. With these detectors solar neutrons were searched ever since Bierman et al. (1951) postulated its possibility of detection. However, no significant signal was observed on the ground-based and space-borne detectors for about 30 years. Then in 1980, solar neutrons were for the first time observed by the GRS (Gamma-Ray Spectrometer) instrument onboard the SMM (Solar Maximum Mission) spacecraft on June 21 (Chupp et al., 1982). Later, in the same decade on 1982 June 3 solar neutrons were detected for the first time by the ground-based neutron monitor installed in Jungfraujoch, Switzerland (Chupp et al., 1987). This event was also observed by the SMM/GRS instrument (Debrunner et al., 1983). Since then, a number of 10 solar neutron events were detected with high significance on the ground.
In this chapter, a brief description of the thus far, successfully detected solar neutron events on the ground during solar cycles 21, 22 and 23 is discussed.

3.1 Solar neutron events between 1980-2005

During solar cycles 21, 22 and 23 solar neutrons were searched by using different ground-based and space-borne instruments. Most of the observed solar neutron events were associated with large solar flares. Their details are described in Table 3.1. A majority of these events were detected only by neutron monitors (NM-64 and IGY) and two of them (Events 4 and 10) were simultaneously observed by two types of detectors, the NM-64 and the SNT (Muraki et al. (1992); Sako et al. (2006)). Event 10 was simultaneously detected at two locations. Event 5 shows the lowest flare class (X2.3). In this table are also listed the neutron emission at 100 MeV and the differential power index of the energy spectrum which spans from -3 to -7.
What is learned thus far are:

1. The energy spectrum of neutrons can be reproduced by assuming that neutrons are emitted with the same time profile as X- and γ-rays (Muraki et al., 2007; Watanabe, 2005).

2. The differential spectral indices of solar neutrons range between -3 and -7, thus they have a softer energy spectrum (Watanabe, 2005).

3. A correlation between the longitude of solar flares and solar neutrons is not found (Miroshnichenko, 2015).

4. The flare class is probably not an indicator of the magnitude of the ion acceleration.

Table 3.1: Successfully ground-based detected solar neutron events associated with large solar flares. Reproduced from Watanabe (2005), and Sako et al. (2006).

No	Date	Time UT	Flare Class	Location	Observatory	Power index	Flux @ 100 MeV $\times 10^{26}$/MeV/sr
1	1982 Jun 03	11:43	X8.0	S09E72	Jungfraujoch	-4.0±0.2	260±70
2	1990 May 24	20:48	X9.3	N36W76	Climax	-2.9±0.1	430±40
3	1991 Mar 22	22:44	X9.4	S26E28	Haleakala	-2.7±0.1	6.0±1.0
4	1991 Jun 04	03:37	X12.0	N30E70	Norikura	-4.9±0.6	19±2
5	2000 Nov 24	14:51	X2.3	N22W07	Chacaltaya	-4.2±0.5	4.0±1.3
6	2001 Aug 25	16:23	X5.3	S17E34	Chacaltaya	-3.1±0.4	2.4±1.3
7	2003 Oct 28	09:51	X17.4	S16E08	Tsumeb	-3.8±0.4	37±14
8	2003 Nov 02	17:03	X8.3	S14W56	Chacaltaya	-7.0±1.3	2.8±1.6
9	2003 Nov 04	19:29	X28.0	S19W83	Haleakala	-3.9±0.5	150 ±60
10	2005 Sep 07	17:17	X17.0	S06E89	Chacaltaya Sierra Negra	-3.8	61

5. According to the past observations, the production of solar neutrons is indifferent to the solar cycle activity.

From these information a conclusive view on the acceleration mechanism cannot be reached. Especially, the relation between the solar soft X-ray flux and the amount of produced neutrons is not clear.
In Table 3.2 solar neutron candidates observed between 1980 and 2005 are listed. According to Flückiger et al. (2005); Miroshnichenko (2015), these event candidates have registered a statistical significance between 2.7 to 4.9σ.
In the following sections the first and the most recent solar neutron events detected by ground-based instruments are described.

3.2 The 1982 June 3 solar neutron event

On 1982 June 3, the first ground-based detection of solar neutrons was observed. At 11:41UT an X8.0/2B white-light flare was observed at the S09E72 location. The flare was associated with emissions from meter radio waves to γ-rays. The GRS instrument onboard the SMM spacecraft recorded an intense solar γ-ray line event (Debrunner et al., 1983), which began at $\sim$11:43UT, followed by a $>$10 MeV γ-ray signal and solar neutrons at Earth. The NMs located at Jungfraujoch (46.5°N,8.0°E,3554 m), Lomnický Stít (49.2°N,20.2°E,2632 m) and Rome (41.9°N,12.5°E,60 m) registered significant increases over their background, ranging from 2.9 to 8.5σ, during the interval time 11:45–11:50UT (Chupp et al., 1987).
In Figure 3.1 the SMM/GRS and the Jungfraujoch NM 1-second count rate are shown. The bottom panel shows the 1- and 5-min data (solid and dashed) of the Jungfraujoch NM in comparison with the neutron counting rate by the SMM/GRS instrument. In the 5-minute data the two values at 11:45–11:50 UT and at 11:50–11:55 UT show an enhancement of 6.7σ and 4.0σ, respectively, over the average counting rate (gray solid line). The 1-min data locate the onset of the solar neutron event in the interval 11:44–11:45 UT (the following six minutes were increased by 1.8–3.8σ). After 11:50 UT, only the counting rate between 11:53 UT and 11:55 UT differs significantly from the average (5.0 σ). The upper scale of Figure 3.1 shows the expected neutron energy by assuming all neutrons are ejected

Table 3.2: Solar neutron events with level of significance from 2.7σ to 4.9σ. Reproduced from Flückiger et al. (2005); Miroshnichenko (2015).

No	Date	Flare Class	Location	Pions π^0 decay	Neutrons
1	1980 Jun 21		N20W90	-	SMM/GRS
2	1984 Apr 25	X13	S12E43	SMM/GRS	SMM/GRS, decay, protons (ISEE-3)
3	1988 Dec 16		N26E37	SMM/GRS	SMM/GRS, decay, protons (ISEE-3)
4	1989 Mar 06	X15	N35E69	SMM/GRS	SMM/GRS
5	1989 Oct 19		S25E09	-	Several NMs
6	1991 Jun 09	X10	N31E06	-	CGRO/COMPTEL, Norikura SNT
7	1991 Jun 11	>X12	N31W17	CGRO/EGRET	CGRO/COMPTEL, Japan SNT
8	1991 Jun 15	X12	N33W69	GAMMA-1/PHEBUS	CGRO/COMPTEL, Alma Ata NM
9	1997 Nov 06	X9.4	S16W43	-	Bolivia SNT
10	1998 Aug 17	X1.2		-	Hawaii SNT
11	1998 Aug 18	X4.9	N33E87	-	Hawaii SNT
12	2000 Jul 12	X1.9	N17E27	-	Swiss SNT, Armenia SNT
13	2001 Mar 29	X1.7	N20W19	-	Swiss SNT
14	2001 Apr 02	X1.4	N17W61	-	Swiss SNT
15	2001 Apr 09	M7.9	S21W04	-	Swiss SNT
16	2001 Apr 10	X2.3	S23W09	-	Armenia SNT
17	2001 Apr 12	X2.0	S19W43	-	Swiss SNT, Armenia SNT
18	2001 Apr 15	X14.4	S20W85	-	Swiss SNT

from the Sun at the moment of γ-ray (11:43:25 UT) as δ-function.
According to Chupp et al. (1987), the enhancement at the Jungfraujoch NM lasted for about 12 minutes. Therefore, neutrons were emitted with energies between 100 MeV to $\sim$2 GeV. Moreover, the majority of neutrons were produced after the impulsive phase. To determine the neutron production time profile at the Sun the pion γ-ray intensity from the SMM/GRS instrument was used. The energy spectrum follows a power-law form with differential index equals to -2.4. To summarize, it is possible to say that, in this event gradual production of high-energy neutrons might have occurred.

3.3 The 2005 September 7 solar neutron event

In 2005 September, the NOAA's AR 10808 produced several X-class flares. Among them, the X17.0 occurred on 2005 September 7 was the most energetic event according to GOES. The X-ray intensity started to increase at 17:17UT and reached a maximum at 17:40UT. According to Watanabe et al. (2007), the INTEGRAL spacecraft registered a strong 4.4 MeV γ-ray line at 17:36:40UT and a 2.223 MeV neutron-capture line. The Geotail spacecraft observed strong emissions of hard X-rays (>50 keV) also at 17:36:40UT. These are proof that particles were accelerated to very high energies during this flare.
Ground-based observation of neutrons was made at three locations, at Mount Chacaltaya in Bolivia, at Mount Sierra in Mexico and at Mexico city in Mexico. At these locations, the Sun was almost at its zenith. As seen on the left of Figure 3.2 the solar angle at Bolivia and Mexico were 28° and 17.5° respectively. At the right, of the same figure, the line-of-sight air mass is shown for each station of the SNT network. Clearly Chacaltaya in Bolivia and Sierra Negra in Mexico show the minimum air mass. Based on these numbers, it is possible to say that these two stations were the best locations to

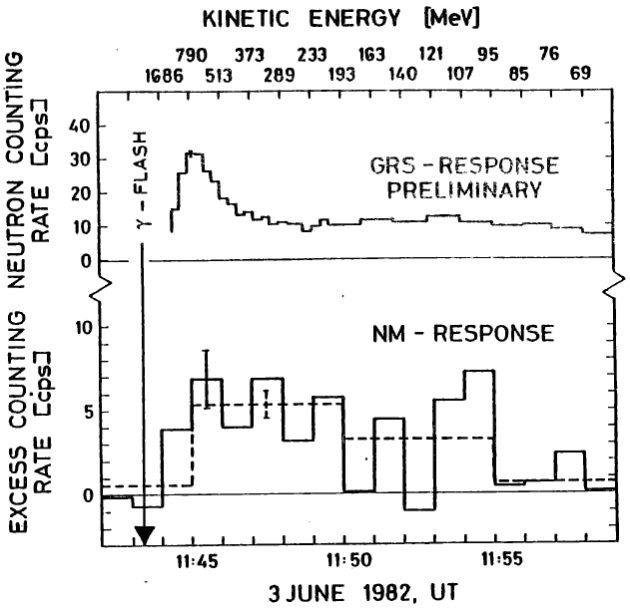

Figure 3.1: The counting rates for the SMM/GRS instrument and the relative excess count rate of the Jungfraujoch NM on 1982 June 3. Figure from Debrunner et al. (1983).

observe solar neutrons.

In Figure 3.3 the 5-minute time profile of the Mexico City NM and the 2-minute time profile of the Chacaltaya NM are shown. In Figure 3.4 the 2-minute time profile of the two lowest energy threshold channels of the Bolivia SNT and the Mexico SNT are shown. The four detectors show clear excesses after 17:36:40UT, when the peak of the γ-ray event was observed by INTEGRAL.

According to Sako et al. (2006) the largest statistical significance was observed by the Chacaltaya NM reaching $\sim 40\sigma$ between 17:40 and 17:45UT. The Mexico City NM reached a 9σ of significance. The >40 MeV channel of the Bolivia SNT registered 12σ of significance. Recently, González et al. (2015) re-evaluated the stadistical significance of the Mexico SNT. Their results are for the >30 MeV (15.8σ), >60 MeV (12.6σ), >90 MeV (9.6σ) and >120 MeV (7.8σ). These significances were calculated between 17:42 and 17:54UT.

In Figure 3.5(a), the inferred energy spectrum of solar neutrons produced at the solar surface is shown. According to Watanabe et al. (2007), this spectrum does not fit a single power-law. In fact, it shows a softer spectrum at lower energies (<100 MeV) and a harder spectrum at higher energies. They assumed a δ-function as the production time profile of solar neutrons. This spectrum is fitted by a power law with differential index -3.8. The neutron emission at 100 MeV is obtained as $6\times10^{2}7$[/MeV/sr].

In Figure 3.5(b), two panel are shown. The top panel shows the 1-minute counting rate (black line) observed by the Chacaltaya NM. The red dots represent the calculated result by using the Hua et al. (2002) transport and interaction model, Watanabe et al. (2009) considered the following parameters, that best fit the neutron profiles of the 2005 September 7 event: λ=2000, δ=0.12, and ion spectral index s=-4.42. The bottom panel shows the best fit (red dots) for the 2.2 MeV time profile of the neutron-capture line.

The main results of this event are summarized as follows. The data suggest that solar neutrons were produced for much longer time than the hard electromagnetic radiation (Sako et al. (2006)). According to Watanabe et al. (2007), it is evident from the INTEGRAL data that the γ-rays were observed continuously for $\sim$5 minutes. The highly statistical significances observed by the Chacaltaya NM can be explained by using the solar-flare magnetic-loop transport and interaction model of Hua et al. (2002), according to Watanabe et al. (2009). Their results indicate that solar neutrons were produced

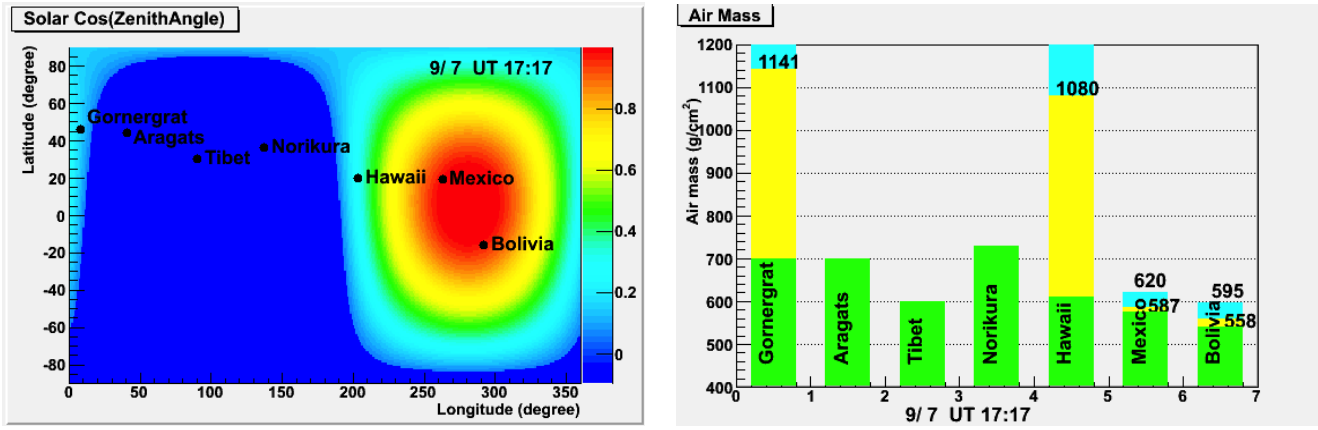

Figure 3.2: On the left, the zenith angle of the Sun at the onset time of X-ray flux on 2005 September 7 is shown. On the right, the line-of-sight air mass for each station of the SNT network is displayed. The green column shows the vertical air mass. The yellow column shows the air mass calculated considering the neutron refraction effect. The blue column shows the air mass calculated via geometrical approximation.

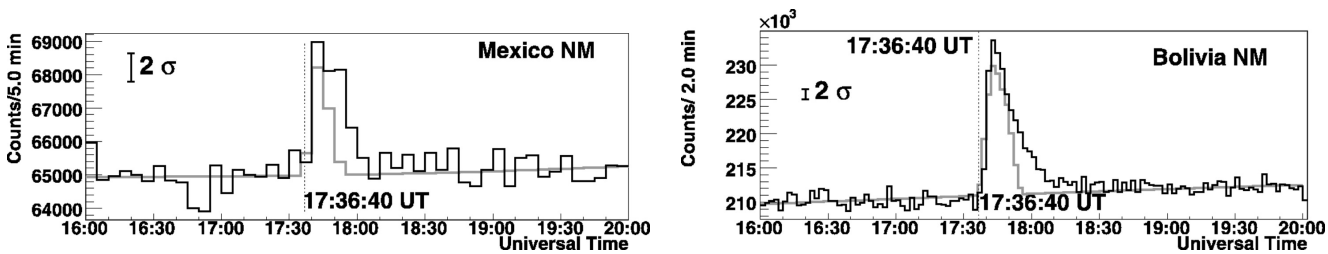

(a) (b)

Figure 3.3: (a) The 5-minute time profile of the Mexico NM located in Mexico city on 2005 September 7. (b) The 2-minute time profile of the Chacaltaya NM. The gray curves show expected counts assuming a neutron flux. In the top left is indicated the 2σ background fluctuation.

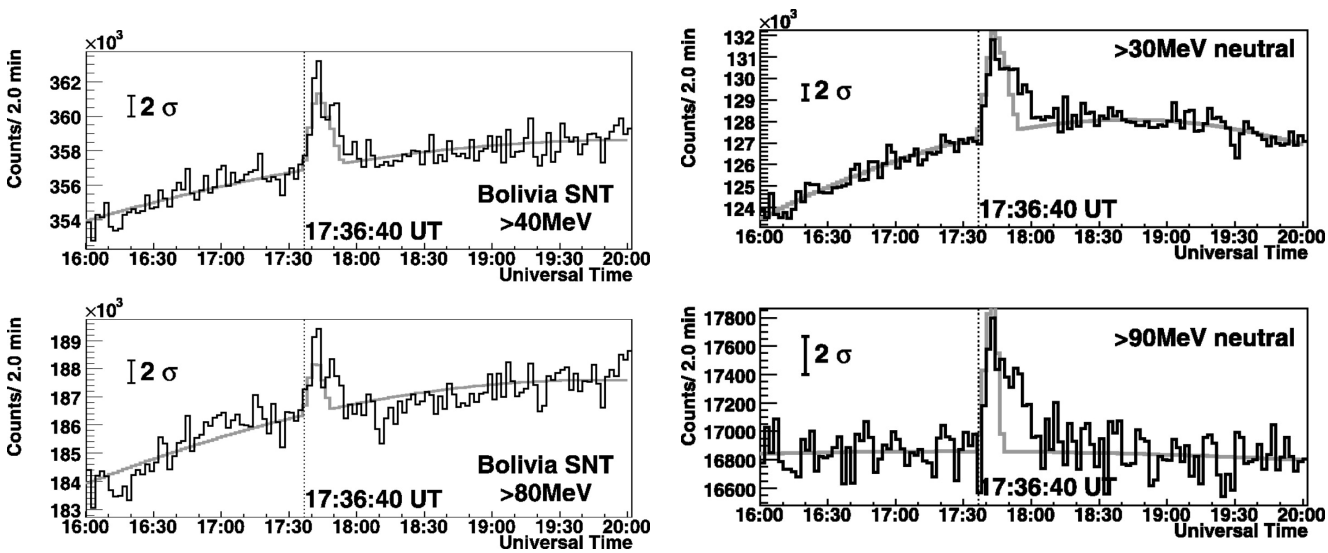

(a) (b)

Figure 3.4: (a) The 2-minute time profile of the Bolivia SNT (CHBO) and (b) the 2-minute time profile of the Mexico SNT (SNMX). The gray curve shows expected counts assuming a neutron flux. In the top left is indicated the 2σ background fluctuation.

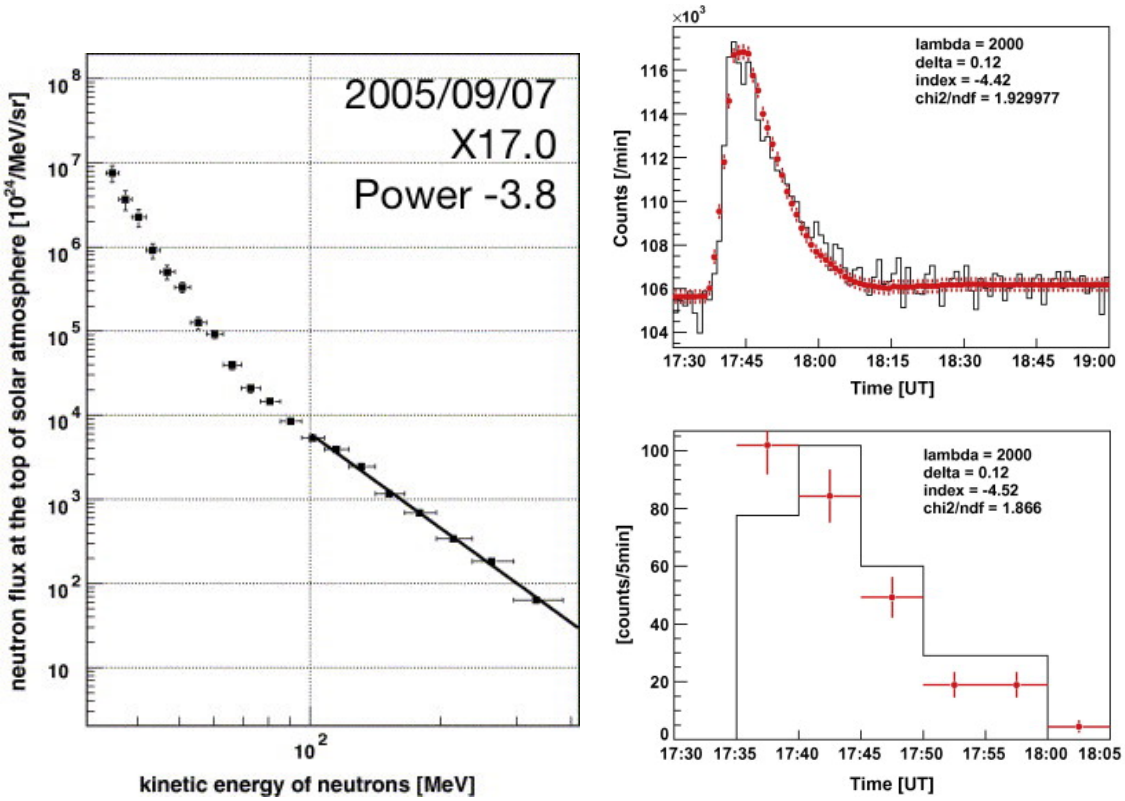

(a) (b)

Figure 3.5: (a) The inferred energy spectrum of solar neutrons on the solar surface for the X17.0 flare occurred on 2005 September 7, according to Watanabe et al. (2007). The fitting region is above 100 MeV. (b) The top panel shows the 1-minute time profile of the Chacaltaya NM on 2005 September 7. The red dots represent the calculated result by using the Hua et al. (2002) transport and interaction model, according to Watanabe et al. (2009). The bottom panel shows the observed (black line) and best fitting calculated (red dots) 2.2 MeV time profile of the neutron-capture line. Figures from Watanabe et al. (2009).

at the same time as the γ-ray emission and that ions were continuously accelerated at the emission site. Finally, based on a numerically calculated neutron energy deposition on the Mexico SNT (González et al., 2015) the detected neutrons might have reached the 1 GeV level of energy, implying that 10 GeV protons were probably produced. These protons could not have been observed at Earth, as the X17.0-flare was on the limb side of the Sun.

Chapter 4

Search for solar neutrons in association with M- and X-class flares

Thus far, 10 solar neutron events have been successfully detected with high statistical significance by ground-based detectors. These events were associated with the production of X- and γ-rays. Every successful detection has been done whenever an apparent and statistically significant excess was observed in the data. The positive excess was attributed to solar neutron detection. Therefore, a systematic search by applying the same criterion to all the event candidates has not been performed yet. Moreover, the kind of conditions on which solar neutrons are produced is still unknown.
In this Chapter, a method to search for solar neutrons in association with M- and X-class flares is discussed. The data collected by the Chacaltaya NM between January 2010 to August 2013 are used. There are two reasons why the Chacaltaya NM is used to search for solar neutrons: 1) The location: Mount Chacaltaya (5250 m, 16°21′S, 68°08′W) is one of the best places in the world to observe solar neutrons, because the air mass (540 g/cm^2) to the direction of the Sun is minimum on the average among all the other stations in the world. 2) The detector: the Chacaltaya NM is more sensitive to solar neutrons than that of the Bolivia SNT, because of its larger volume.
The onset time of thirty one M- and X-class flares observed during the rising period of solar cycle 24 are considered as the most probable production time of solar neutrons. The contents of this chapter are the following. First, the GOES SXR database and the constraints of the Chacaltaya NM data are introduced. Then, the method to search for solar neutrons is described. Next, the obtained results are shown.

4.1 GOES SXR Database

The search for solar neutrons in cycle 24 started by examining the GOES soft X-ray (SXR) database[1] during the period of January 2010 to August 2013. In that period 300 M-class and 19 X-class flares occurred. The onset time of the SXR light curves of these flares are considered. The database includes the following information (according to the GOES website `www.swpc.noaa.gov/products/goes-x-ray-flux`):

1. date of the flare.

2. begin time (of an X-ray event), is defined as the first minute, in a sequence of four, of steep monotonic increase in the 1-8Å flux. This time is commonly known as flare onset.

[1] Available at `ftp://ftp.ngdc.nasa.gov/STP/space-weather/solar-data/solar-features/solar-flares/x-rays/goes/`

3. maximum time, is taken as the minute of the maximum X-ray intensity.
4. end time, is the time when the flux level decays to a point halfway between the maximum flux and the pre-flare background level.
5. flare class, determined by the maximum time and related to GOES flare classification. In this Chapter >M1.0 flares are considered.
6. integrated flux, determined between the begin and end time, in units of J/m^2.
7. source location, if available the position where the flare occurred.
8. NOAA's active region number.

4.2 Chacaltaya NM data

Ground-based observation is done with the Chacaltaya NM. Data collected between January 2010 to August 2013 are used. Giving the local conditions of the detector, one restriction in the observation is considered. At the SXR flare onset, in local time (UT-4), the solar zenith angle should be less than 65° yielding a line-of-sight air mass of about 850 g/cm^2.
Taking into account the flare conditions, and the observation site restrictions, twenty-eight M- and three X-class flares are selected, which are summarized in Table 4.1. The table is divided into two groups, the first of which shows the data from GOES (flare conditions). The data included are the onset time, the peak time, the flare class, and the flare position. The second group shows the observational site conditions. These are, the onset in local time, the solar angle, the line-of-sight air mass and the correction factor. The latter is due to the multiplicity effect that the NM provides, which should be considered when the number of particles is compared.
In Figure 4.1 the positions of 28 M- and 3 X-class flares over the solar surface are shown. A majority of them are concentrated around the solar equator. The position of the M9.0 flare occurred on 2012 October 20 was not available in the GOES database.

4.3 Method

To search for solar neutrons within the Chacaltaya NM data a systematic method was employed. First, 3-minute time profiles are built for each event listed in Table 4.1. Next, a "work window" is set at $t_0 \pm 3$ hours. Here, t_0 represents the onset, in local time, of the SXR flare. This first interval includes the backgrounds and the possible excess due to solar neutrons. Then, a "signal window" is defined at $t_0 \pm 30$ minutes in which solar neutrons are searched. Even if solar neutrons are emitted at the same time as X-rays they will reach the Earth and the detectors delayed from them. This is known because neutrons have mass and cannot travel at the speed of light. Neutrons with energies of one GeV and 100 MeV require about 1.2 minutes and 11 minutes longer time than X-rays' travel time respectively to reach the top of the Earth's atmosphere. This is why the signal window has to be extended up to 30 minutes. The case when neutrons are produced for more than 20 minutes is covered as it occurred in the solar neutron event of 2005 September 7 (Sako et al., 2006). The case when neutron are produced earlier than soft X-rays by up to 30 minutes is also covered. The remaining two time intervals (2.5 hours before and after the onset) of the work window are used to estimate the background. The background is calculated by the running average (N_b) for 20 minutes with a 3-minute counting rate. To estimate the background at the signal window, a linear interpolation (B_s) between $t_0 - 30$ minutes and $t_0 + 30$ minutes is calculated.

Table 4.1: List of Soft X-ray flares observed by GOES and the local time of possible observation in Mt. Chacaltaya. At the top of the list, the solar neutron event reported by Sako et al. (2006) is included as a reference for calculations.

	Flare conditions					Observation Site			
No	Date (UT)	Start (UT)	$t_P{}^a$	Class	Position	$t_0{}^b$ (UT-4)	$\theta_\odot{}^\ell$ [deg]	Air Mass$^\jmath$ [g/cm^2]	$\alpha^\ddagger$ (NM-64)
	2005 Sep 07	17:17	17:40	X17.0	S06E89	13:17	28	612	1.7 ± 0.2
1	2010 Oct 16	19:07	19:12	M2.9	S20W26	15:07	42	724	1.7 ± 0.3
2	2010 Nov 06	15:27	15:36	M5.4	S19E58	11:27	12	551	1.8 ± 0.2
3	2011 Feb 13	17:28	17:38	M6.6	S20E04	13:28	10	541	1.6 ± 0.3
4	2011 Feb 14	17:20	17:26	M2.2	N56W18	13:20	9	540	1.8 ± 0.2
5	2011 Aug 03	13:17	13:48	M6.0	N16W30	09:17	60	773	1.9 ± 0.3
6	2011 Sep 24	12:33	13:20	M7.1	N14E45	08:33	59	792	1.4 ± 0.2
7	2011 Sep 24	17:19	17:25	M3.1	N15E56	13:19	21	547	1.3 ± 0.2
8	2011 Sep 24	19:09	19:21	M3.0	N15E54	15:09	43	627	1.6 ± 0.2
9	2011 Sep 24	20:29	20:36	M5.8	N16E54	16:29	62	786	1.6 ± 0.2
10	2011 Sep 25	15:26	15:33	M3.7	N16E43	11:26	21	552	1.5 ± 0.1
11	2011 Sep 25	16:51	16:58	M2.2	S28W75	12:51	17	543	1.7 ± 0.3
12	2011 Sep 26	14:37	14:46	M2.6	N14E30	10:37	30	580	1.6 ± 0.2
13	2011 Oct 02	17:19	17:23	M1.3	N09W56	13:19	19	570	1.6 ± 0.2
14	2011 Nov 03	20:16	20:27	X1.9	N22E63	16:16	58	716	1.5 ± 0.2
15	2012 Mar 02	17:29	17:46	M3.3	N16E83	13:29	14	543	1.7 ± 0.2
16	2012 Mar 05	19:10	19:10	M2.1	N14E44	15:10	37	617	1.9 ± 0.2
17	2012 Mar 10	17:15	17:44	M8.4	N18W34	13:15	15	543	1.9 ± 0.2
18	2012 Mar 13	17:12	17:41	M7.9	N17W60	13:12	16	543	1.7 ± 0.4
19	2012 Mar 14	15:08	15:21	M2.8	N14E05	11:08	27	558	1.8 ± 0.2
20	2012 Jun 03	17:48	17:55	M3.3	N16E38	13:48	43	638	1.8 ± 0.3
21	2012 Jun 06	19:54	20:06	M2.1	S19W05	15:54	63	824	1.2 ± 0.2
22	2012 Jul 08	16:23	16:32	M6.9	S17W74	12:23	39	615	1.7 ± 0.2
23	2012 Jul 12	15:37	16:49	X1.4	S15W01	11:37	41	624	1.6 ± 0.3
24	2012 Oct 20	18:05	18:14	M9.0	–	14:05	27	554	1.3 ± 0.1
25	2012 Oct 22	18:38	18:51	M5.0	S12E61	14:38	35	576	1.7 ± 0.2
26	2012 Nov 21	15:10	15:30	M3.5	N06E05	11:10	17	564	1.7 ± 0.2
27	2013 Abr 05	17:34	17:48	M2.2	N08E81	13:34	27	565	1.7 ± 0.2
28	2013 Abr 12	19:52	20:38	M3.3	N20E41	13:52	55	736	1.7 ± 0.2
29	2013 May 13	15:48	16:05	X2.8	N08E89	11:48	36	602	1.9 ± 0.2
30	2013 May 22	13:08	13:32	M5.0	N15W70	09:08	62	813	1.8 ± 0.2
31	2013 Aug 17	18:16	18:24	M3.3	S07W30	14:16	38	615	2.0 ± 0.3

^{a} GOES SXR maximum peak time. ^{b} Flare onset in local time. $^\ell$ Solar zenith angle at the onset time. $^\jmath$ Line-of-sight air mass at the onset time. ‡ Normalization factor for the NM-64.

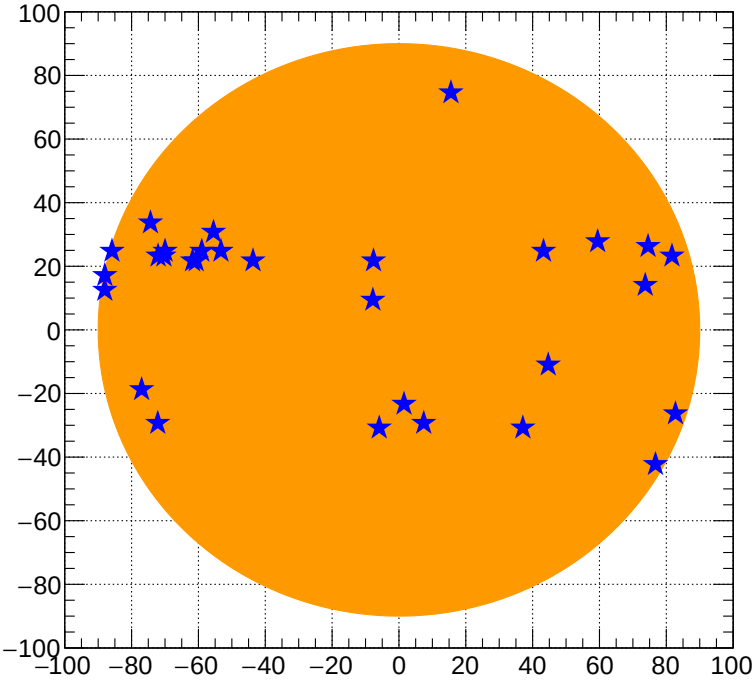

Figure 4.1: Source locations of the M- and X-class flares. Data available at ftp://ftp.ngdc.noaa.gov/STP/space-weather/solar-data/solar-features/solar-flares/x-rays/goes/

In Figure 4.2, the 3-minute time profiles for four of the studied events are shown. The signal window is enclosed by two violet vertical lines. In these Figures the whole interval corresponds to the work window. Similar time profiles were constructed for the other events listed in Table 4.2. To identify a solar neutron event, the statistical significance of the counting rate is examined and compared to the background rate.

Statistical significances are determined as follows. First, each point (3-minute bin) of the average background is subtracted from the data excluding the signal window. Subsequently, these data are normalized by the Poisson standard deviation ($\sqrt{N_b}$). Then, a background distribution is built with the resulted data. Next, a Gaussian function is fitted to this distribution. The resulting function, however, does not usually yield a normal distribution. Thus, to obtain a unitary standard deviation (std. dev.), the data are again normalized by the Gaussian standard deviation. This parameter is called, "normalization factor" and symbolized as "α". Its existence is attributed to the NM multiplicity effect as explained in Chapter 2. The resulting distribution is adjusted again by a Gaussian function. The individual α factor is applied to each signal window, and the significance distribution is calculated. This whole process can be expressed as,

$$\xi_{bi} = \frac{N_i - N_{bi}}{\alpha\sqrt{N_{bi}}} \qquad (i = t_0 \pm 3 \text{ hrs}) \tag{4.1}$$

$$\xi_{sj} = \frac{S_j - B_{sj}}{\alpha\sqrt{B_{sj}}} \qquad (j = t_0 \pm 30 \text{ mins}), \tag{4.2}$$

where N_i are the data from the Chacaltaya NM, N_{bi} is the averaged background, and α is the factor calculated from the first Gaussian fit. S_j and B_j represent the signal window and the interpolated background data.

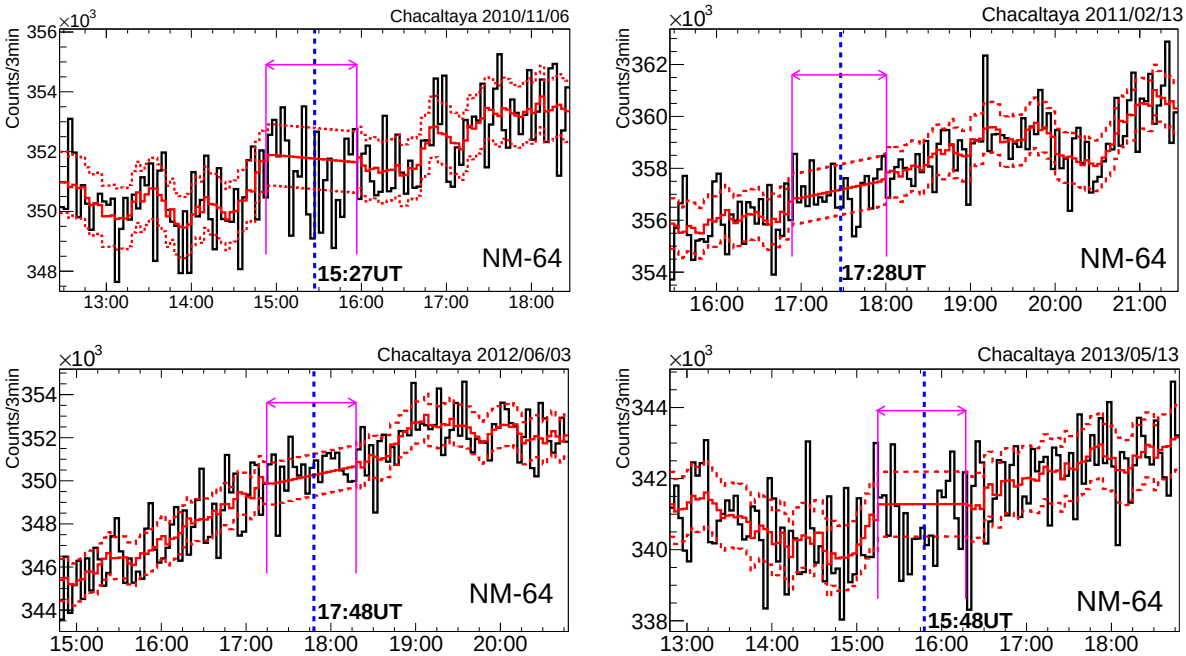

Figure 4.2: The 3-minute time profiles of the Chacaltaya NM for one X-class and three M-class flares. The left- and right-upper panels and the left-lower panel indicate those for the M5.4 (2010/11/06), M6.6 (2011/02/13) and M3.3 (2012/06/03) flares respectively. The right-lower panel corresponds to the X2.8 (2013/05/13) flare. The interval of the signal window is indicated by horizontal and vertical violet lines. The red thick line represents the average background for 20 minutes. The red dashed lines which follow the average background are $\pm 1\sigma$ curves. The dashed blue line and the label time show the flare onset (t_0) according to GOES. The abscissa in all plots represent the time in UT.

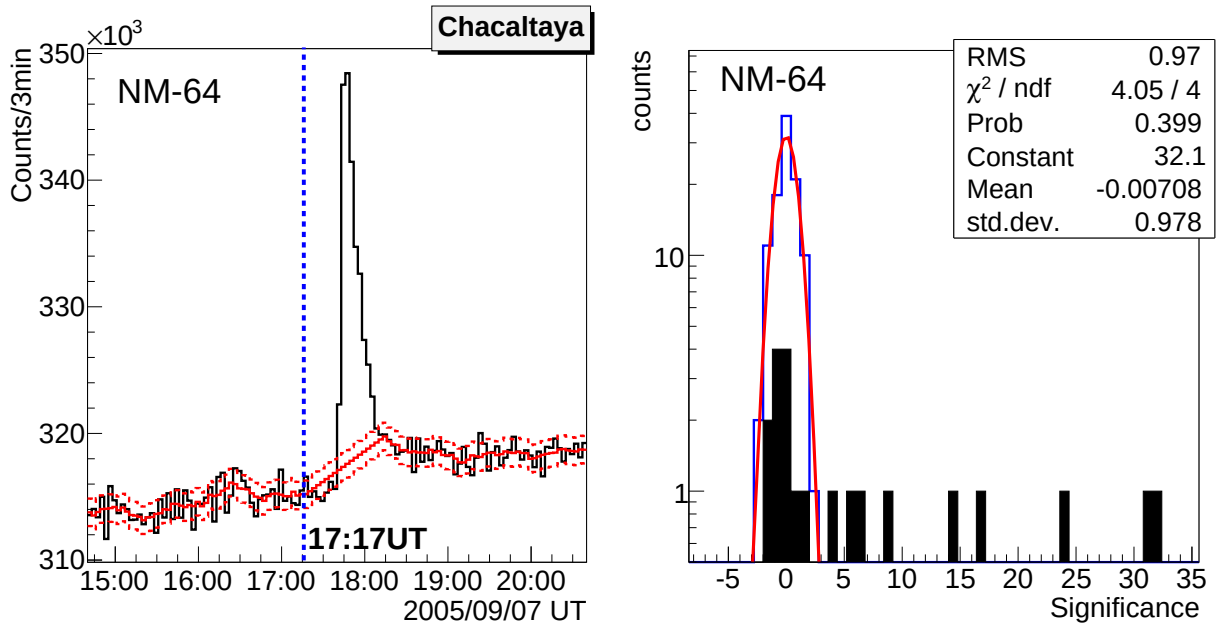

Figure 4.3: On the left, time profile of neutrons for the 2005 September 7 event observed by the Chacaltaya NM. The blue dashed line at 17:17 UT (13:17 local time) represents the time of the onset for the X-ray intensity recorded by GOES. The red thick line corresponds to the running average for 20 minutes. The red dashed lines are $\pm 1\sigma$ calculated without including the signal window. The abscissa corresponds to the time in UT. On the right, the statistical analysis following the same procedure described in this chapter. In this case, several excesses were observed, the most significant reached 32σ. More details can be found in Sako et al. (2006); Watanabe et al. (2007).

The criterion to get a significant signal is defined as: in the case an excess of events greater than "3σ" is seen at the signal window, it will be regarded as a candidate for a solar neutron event associated with the solar flare.

To test the method capability to determine a significant excess in the data, the 2005 September 7 solar neutron event which occurred in solar cycle 23 can be considered. This event was detected by the detectors (the NM and the SNT) installed in Bolivia and Mexico. The GOES X-ray flux started to increase at 17:17UT and reached its maximum intensity (X17.0) at 17:40UT. At the time of the maximum X-ray intensity, the solar zenith angle and the line-of-sight air mass at Chacaltaya, Bolivia were 28° and 612g/cm^2 respectively. On the left of Figure 4.3 a 3-minute time profile of the Chacaltaya NM is shown. The soft X-ray onset time (17:17UT) is represented by a dashed vertical line. At 17:40 UT the Chacaltaya NM started to increase its counting rate, which reached a maximum at $\sim$17:48UT and lasted for more than 20 minutes. On the right of this figure, the resulting significance distribution after being normalized by the α factor (shown in table 4.1) is shown. The black hatched skewed-right histogram which corresponds to the signal window, exhibits several positive excesses due to this event. The background is represented by a blue histogram exhibiting a Gaussian behavior.

4.4 Results

Having tested the analysis method with the 2005 September 7 solar neutron event, the same procedure is applied to the events listed in Table 4.1. As examples of the analysis method, in Figure 4.4 the statistical significances for four of the analyzed events are shown. The distributions show a normal

behavior. By observing the black hatched histogram it is clear that no positive enhancement greater than the threshold level (3σ) is observed in the signal window. Including those events shown in Figure 4.4 and the events listed in the Table 5.1, no statistically significant (and positive) excess was found. Based on the analysis method, the Chacaltaya NM data do not contain a solar neutron signal associated with solar flares.

Additionally, considering one particular bin per analyzed event, a significance distribution can be constructed. This result is shown in Figure 4.5. Therefore it is possible to say that no indication of the acceleration of ions was obtained during the onset emission time of soft X-rays exceeding the level of the criterion.

To further validate not finding any solar neutron event within the period of analysis, the probability of not obtaining any successful event can be calculated. By considering the number of solar neutron events detected in the last solar cycle compared with the number of solar flares which exceeded X2.3[2] class. In solar cycle 23 the number of solar neutron events detected in Chacaltaya is four, whereas the number of solar flares greater than X2.3 class is 43. In this analysis the number of solar flares greater than X2.3 class is six. Therefore the probability that a solar neutron event will not occur is 0.57, if GOES SXR classification is an indicator of solar neutron events.

Figure 4.6 shows the distribution of the "α" factor. It exhibits a Gaussian-like behavior with mean equals to 1.73 ± 0.03. This variation comes from the multiplicity effect that the NM provides.

[2]In solar cycle 23, the 2000 November 24 (Watanabe (2005)) solar neutron event detected by the Chacaltaya NM was the smallest X-class among the six successful detections in this solar cycle.

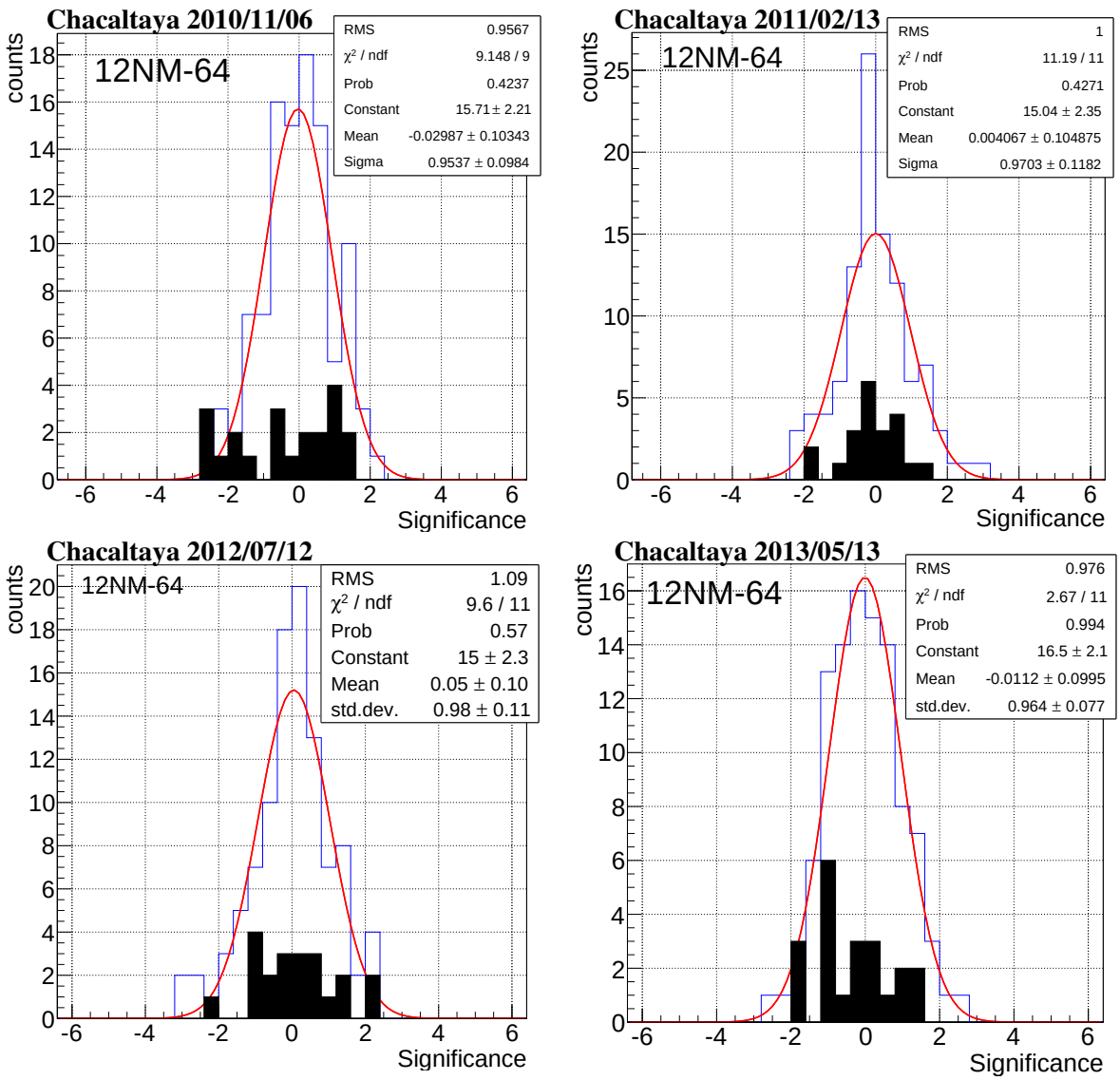

Figure 4.4: In the four figures the background histogram is well fitted by a Gaussian curve, represented here as a red thick line. The overlapped black-hatched area shows the significance distribution for the signal window. On top-left and -right, the results for the M2.9 (2010/11/06) and the M6.6 (2011/02/13) flares respectively. On the bottom-left and -right, the results for the X1.4(2012/07/12) and the X2.8(2013/05/13) flares respectively.

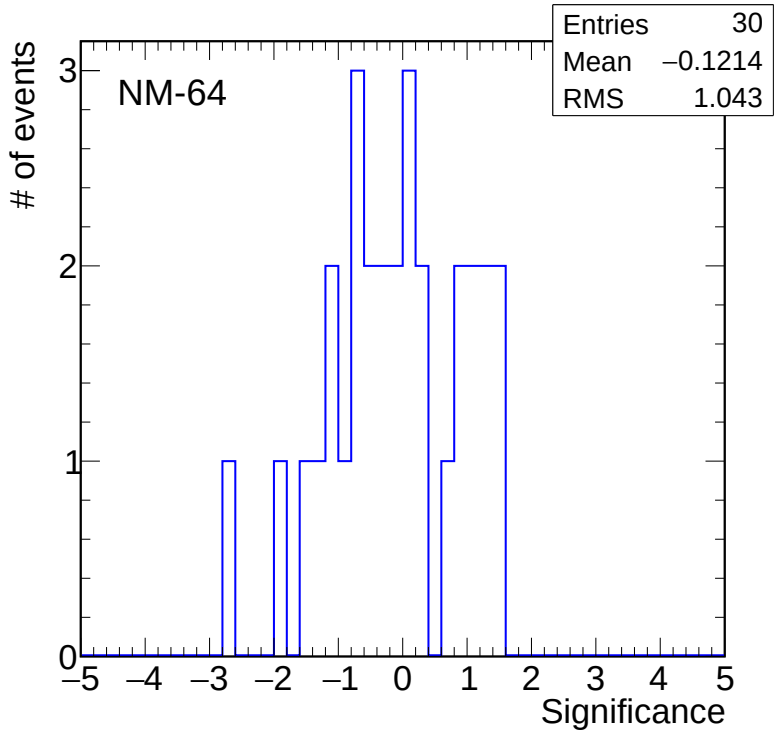

Figure 4.5: The significance distribution at the onset time is shown for all the analyzed events with the Chacaltaya NM.

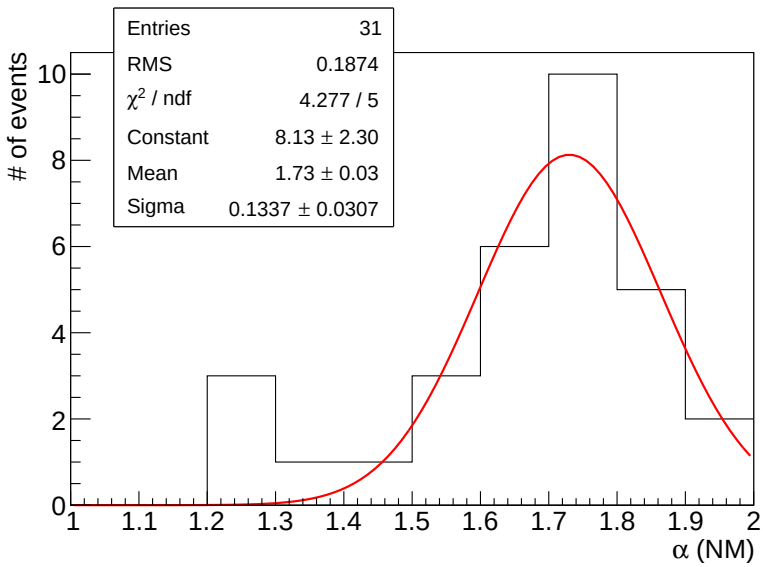

Figure 4.6: The distribution of the normalization factor (α), one per analyzed event for the Chacaltaya NM.

Chapter 5

Search for solar neutrons in association with X-class flares

In the previous Chapter, solar neutrons were searched by examining the Chacaltaya NM data. This single detector, in spite of its high efficiency, was limited to view more flares because the location of the detector cannot cover 24 hours of constant observation, thus it misses to observe some large flares. During the period of analysis (January 2010 to August 2013) 26 >X1.0 flares occurred. The 11% of these X-class flares were examined. The result of this first campaign was not positive, because no significant events were associated to X-ray flares.
In this Chapter, the intent is to apply the same structured method of the first campaign to search for solar neutrons in association with soft X-ray flares. In this time six detectors from the SNT network are used together with the Chacaltaya NM, extending the view for more solar flares. The period to search is also extended, from January 2010 to December 2014.

5.1 GOES SXR database

The period to search for solar neutrons comprehends five years of data, starting from January 2010 to December 2014. During this period a number of 105 flares classified as greater than M5.0 were recorded by GOES in the 1-8Å band. The focus of this search is flares classified as greater than X1.0 class. Reviewing the GOES database, 43 greater than X1.0 flares are found. The maximum intensity (peak) time of these 43 flares are considered as the most probable production time of solar neutrons.

5.2 SNTs and Chacaltaya NM data

Ground-based observation is done with the six detectors from the SNT network and the Chacaltaya NM. The data collected by the SNT detectors located at: Norikura, Japan; Sierra Negra, Mexico; Yangbajing, China; Gornergrat, Switzerland; Mauna Kea, USA and Chacaltaya, Bolivia are used. The four different threshold levels from the with_anti channel of those detectors are considered.
The same criteria applied to the previous search (Chapter 4) is adopted. The condition is that at the peak time the solar zenith angle and the line-of-sight air mass must be less than equal 60° and 950 g/cm^2 respectively. Considering the previous condition, data from the Norikura SNT was discarded because no flare sufficed the criteria. Hence, the final flare sample consist of thirty five greater than X1.0-class flares. They are summarized in Table 5.1. This list is divided in two groups, which are the flare conditions and the observation site. The first group shows from left to right, the date of the flare, the start time, the peak time, the flare class, the position on the solar surface, and the region where

it was originated. The second group shows, the SNT where neutrons associated with the flare could be observed, the peak SXR emission in local time, the zenith angle, and the line-of-sight air mass at the peak SXR emission. Some of the flare events can be observed by up to three stations. This is advantageous, since simultaneous observation can confirm the authenticity of a signal that is due to neutrons. In Figure 5.1 the positions of these 35 flares are shown. The left side indicates the East and the right side shows the West.

Table 5.1: List of soft X-ray class flares observed by GOES and the local peak time of possible observation.

		Solar Flare					Observation Site			
No	Date	Start (UT)	t_P[a] (UT)	Class	Position	Region	SNT[b]	t_0[c] (LT)	$\theta_\odot$[d] [deg]	Air Mass[e] [g/cm^2]
1	2011 Feb 15	01:44	01:56	X2.2	-	1158	MKUS	15:56	59	927
2	2011 Mar 09	23:13	23:23	X1.5	N08W09	1166	MKUS	13:23	27	638
3	2011 Aug 09	07:48	08:05	X6.9	N17W69	1263	GOSW	10:05	53	927
							YACH	14:05	31	643
4	2011 Sep 06	22:12	22:20	X2.1	N14W18	1283	MKUS	12:20	13	611
							SNMX	17:20	58	863
5	2011 Sep 07	22:32	22:38	X1.8	N14W28	1283	MKUS	12:38	15	612
6	2011 Sep 22	10:29	11:01	X1.4	-	1302	GOSW	13:01	46	843
7	2011 Sep 24	09:21	09:40	X1.9	N12E60	1302	GOSW	11:40	51	909
8	2011 Nov 03	20:16	20:27	X1.9	N22E63	1339	MKUS	10:27	42	722
							SNMX	14:27	48	728
							CHBO	16:27	60	850
9	2012 Jan 27	17:37	18:37	X1.7	N27W71	1402	CHBO	14:37	27	565
10	2012 Mar 05	02:30	04:09	X1.1	N17E52	1429	YACH	10:09	46	741
11	2012 Mar 07	00:02	00:24	X5.4	N17E27	1429	MKUS	14:24	37	684
12	2012 Mar 07	01:05	01:14	X1.3	N22E12	1430	MKUS	15:14	47	760
13	2012 Jul 06	23:01	23:08	X1.4	-	1515	MKUS	13:08	10	610
14	2012 Jul 12	15:37	16:49	X1.4	S15W01	1520	SNMX	11:49	25	595
							CHBO	12:49	38	616
15	2013 May 13	01:53	02:17	X1.7	-	1748	MKUS	16:17	56	877
16	2013 May 13	15:48	16:05	X2.8	N11E85	1748	SNMX	11:05	33	625
							CHBO	12:05	35	600
17	2013 May 15	01:25	01:48	X1.2	N12E64	1748	MKUS	15:48	49	786
18	2013 Oct 25	07:53	08:01	X1.7	S08E73	1882	YACH	14:01	54	830
19	2013 Oct 25	14:51	15:03	X2.1	S06E69	1882	SNMX	10:03	56	831
							CHBO	11:03	18	546
20	2013 Oct 29	21:42	21:54	X2.3	N08W71	1875	MKUS	11:54	34	665
21	2013 Nov 05	22:07	22:12	X3.3	S12E46	1890	MKUS	12:12	36	676
22	2014 Jan 07	18:04	18:32	X1.2	S15W11	1944	SNMX	12:32	41	674
							CHBO	14:32	27	567
23	2014 Feb 25	00:39	00:49	X4.9	S12E82	1990	MKUS	14:49	44	733

[a] GOES SXR maximum peak time (t_P). [b] SNT location where neutrons could be observed.
[c] t_P in local time. [d] Solar zenith angle at t_P. [e]Line-of-sight air mass at t_P.

Continued on next page

Table 5.1 – *Continued from the previous page*

No	Date	Solar Flare					Observation Site			
		Start (UT)	t_P[a] (UT)	Class	Position	Region	SNT[b]	t_0[c] (LT)	$\theta_\odot$[d] [deg]	Air Mass[e] [g/cm^2]
24	2014 Mar 29	17:35	17:48	X1.0	N11W32	2017	SNMX	11:48	19	582
							CHBO	13:48	26	564
25	2014 Apr 25	00:17	00:27	X1.3	S14W89	2035	MKUS	14:27	31	653
26	2014 Jun 10	11:36	11:42	X2.2	S19E81	2087	GOSW	13:42	23	706
27	2014 Jun 10	12:36	12:52	X1.5	S20E89	2087	GOSW	14:52	29	724
28	2014 Jun 11	08:59	09:06	X1.0	S18E66	2087	GOSW	11:06	37	767
29	2014 Sep 10	17:21	17:45	X1.6	N14E02	2158	SNMX	12:45	17	580
							CHBO	13:45	28	570
30	2014 Oct 22	14:02	14:28	X1.6	S14E13	2192	CHBO	10:28	27	566
31	2014 Oct 24	21:07	21:41	X3.1	S16W21	2192	MKUS	11:41	32	659
32	2014 Oct 25	16:55	17:08	X1.0	S16W31	2192	SNMX	12:08	35	635
33	2014 Oct 27	14:12	14:47	X2.0	S17W52	2192	SNMX	08:47	60	891
							CHBO	10:47	22	553
34	2014 Nov 07	16:53	17:26	X1.6	-	2205	SNMX	11:26	37	647
							CHBO	13:26	17	544
35	2014 Dec 20	00:11	00:28	X1.8	S21W24	2242	MKUS	14:28	53	837

5.3 Validity

The method to search for solar neutrons described in the previous chapter allows us: 1) to identify a significant and positive excess in the data of the signal window; and 2) to verify that the background-subtracted data follows a normal Gaussian function. Now, in order to find the same pattern in the data collected by the detectors, not only at the time an X-class flare occurs (center day), but also considering one day previous and one day after the flare occurrence. Therefore, the search for a positive excess is performed by using the data of the Switzerland SNT on 2011 August 9 (center day) and solar neutrons are searched on 2011 August 8 and 2011 August 10.
The same two-minute time profiles are built and then the background and signal windows are defined. Next, background and signal distributions are built. As usual, a Gaussian function is adjusted to the background distribution. In Figure 5.2 the results of this inspection are shown. Clearly the background distribution follows the shape of a Gaussian function (shown in red) and no significant excesses were found attributable to neutrons.

5.4 Results

Following the same method as the analysis made in Chapter 4, here 2-minute time profiles are built for each event listed in Table 5.1. The signal window, however, is slightly changed. It is defined between t_0-15 minutes and t_0+45 minutes. The work window follows the same way as in Chapter 4, i.e $t_0\pm3$ hours. The background is estimated by using a 15-minute running average. The linear interpolation is done between t_0-15 minutes and t_0+45 minutes. As examples of this analysis, in Figure 5.3 four

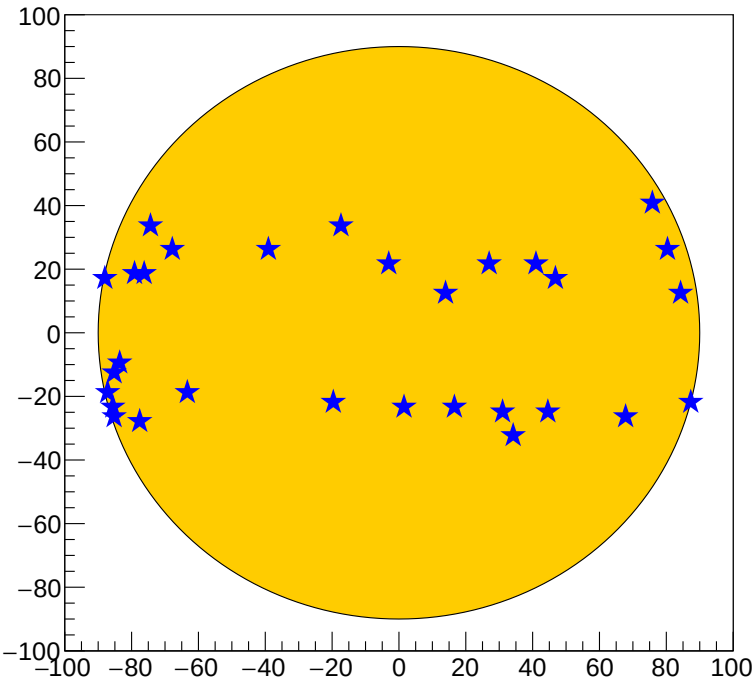

Figure 5.1: The positions of 35 X-class flares. The left side indicates the East and the right side shows the West. Data is available at ftp://ftp.ngdc.noaa.gov/STP/space-weather/solar-data/solar-features/solar-flares/x-rays/goes/

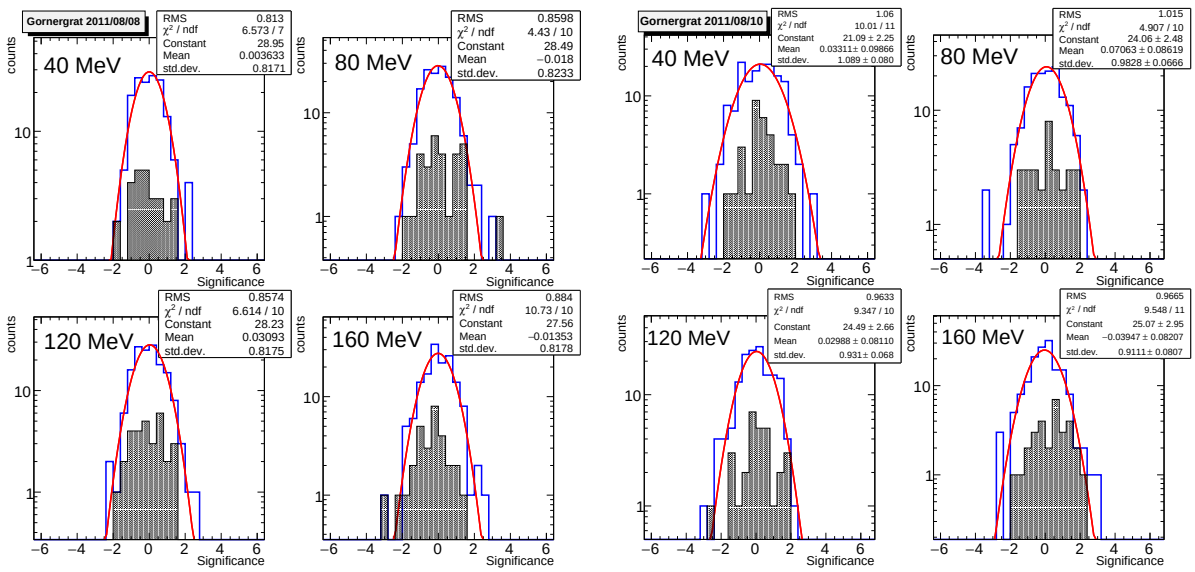

(a) (b)

Figure 5.2: Significance distributions for two days of the Switzerland SNT. The background distributions (shown in blue) are well adjusted by Gaussian functions (shown here as solid red lines). (a) The results for 2011 August 8 and (b) the results for 2011 August 10.

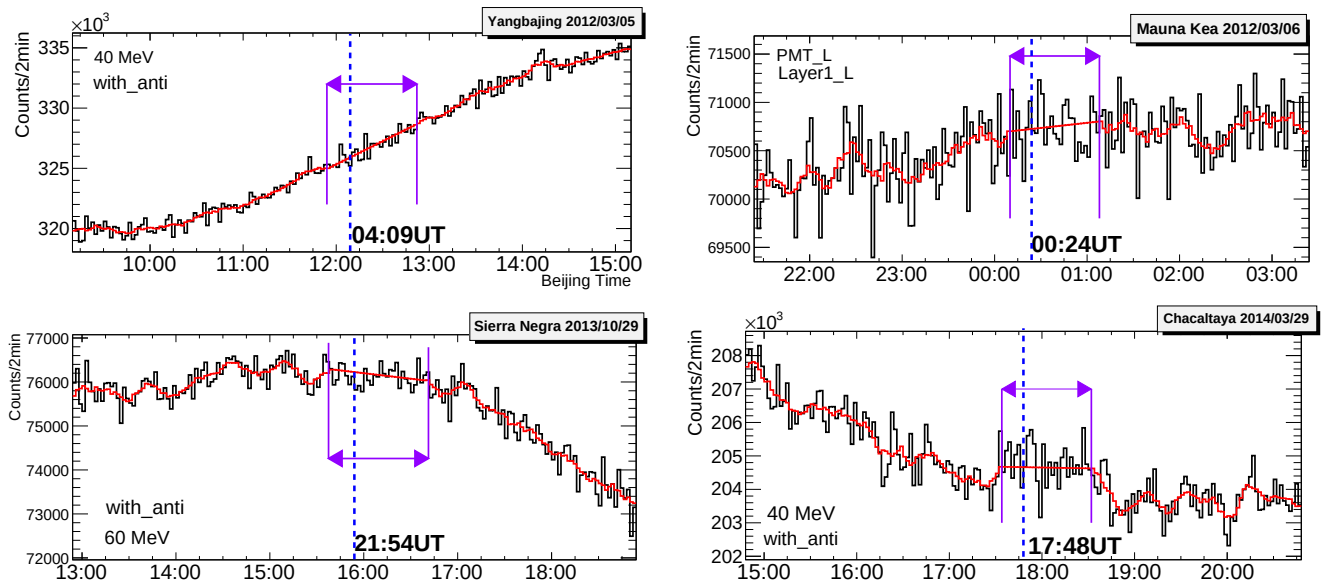

Figure 5.3: The 2-minute time profiles of four SNTs for four X-class flares. The top-left and -right panels indicate those for the X1.1 (2012/03/05) flares and the X5.4 (2012/03/07) flares respectively. The bottom-left and -right panels correspond to the X2.3 (2013/10/29) and the X1.0 (2014/03/29) flares respectively. The interval of the signal window is indicated by horizontal and vertical violet lines. The red thick line represents the average background for 15 minutes. The dashed blue line and the label time show the X-ray flare peak time (t_p) according to GOES. The abscissa in all plots represents the time in UT unless indicated.

of the studied events are shown. In these time profiles the whole interval corresponds to the work window. The signal window is enclosed by two vertical violet lines. Although the lowest threshold level of four SNTs are shown in the figure, time profiles were constructed also for the higher energy thresholds, which are shown in Appendix C.

Statistical significances were built for all the 35 events and for each of the threshold levels of the five SNTs. In Figure 5.4 four distributions are shown for each detector as examples of the analysis result. It is apparent that none of them passed the 3σ level. In addition, to inspect signal simultaneity, the significances of the four threshold levels of the Gornergrat SNT are plotted in Figure 5.5 as an example. These plots correspond to the largest solar flare in the period of analysis, the X6.9-class flare which occurred on 2011 August 9. The significance distributions for the other analyzed events are shown in Appendix C.

In Figure 5.6 four significance distributions have been built considering one particular bin (the peak time) of all the 35 studied events for 5 SNTs. In Figure 5.7 the same treatment is made for the Chacaltaya NM. Consequently, if the peak emission time alone is considered, an excess beyond the threshold level was not seen. Therefore, the evidences of the production of high-energy neutrons were not obtained at the same time as soft X-rays by using the current criterion.

The distributions of the α normalization factor for each detector are shown in Figures 5.8, 5.9, 5.10 and 5.11. For a majority of the SNTs detectors, the distribution fluctuates around the unity. Therefore a correction by this α factor is not necessary. However, for the Chacaltaya NM, as already explained in Chapter 4, the α distribution fluctuates between 1.4 and 2.2, thus correction is needed.

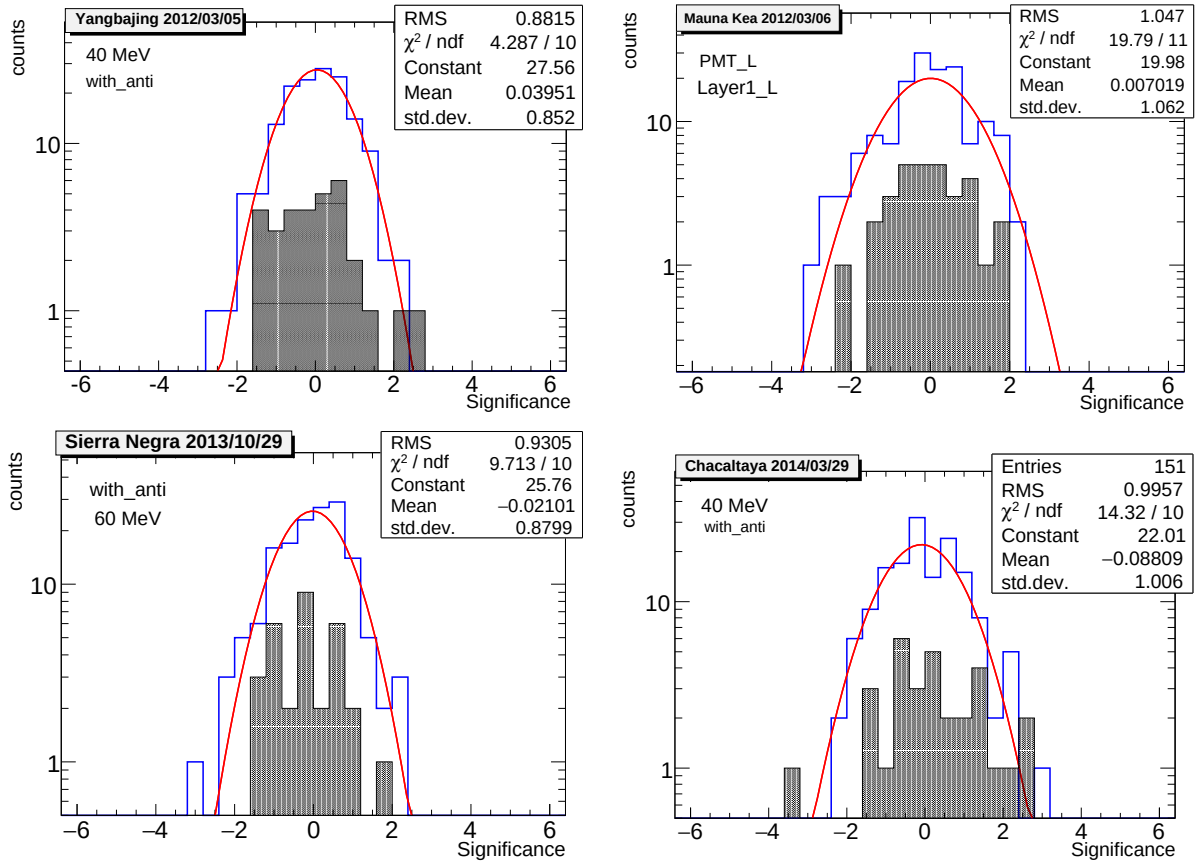

Figure 5.4: Statistical significances for four of the studied events. In all plots the overlapped black-shadowed area corresponds to the signal distribution. On the top-left and -right panels, the results for the >40 MeV with-anti channel YACH for the X1.1 (2012/03/05) flare and for the PMT-L+Layer1 channel of MKUS for the X5.4 (2012/03/07) flare. On the bottom-left and -right panels, the distributions for the >60 MeV with-anti channel of SNMX for the X2.3 (2013/10/29) flare and the >40 MeV with-anti channel of CHBO for the X1.0 (2014/03/29) flare.

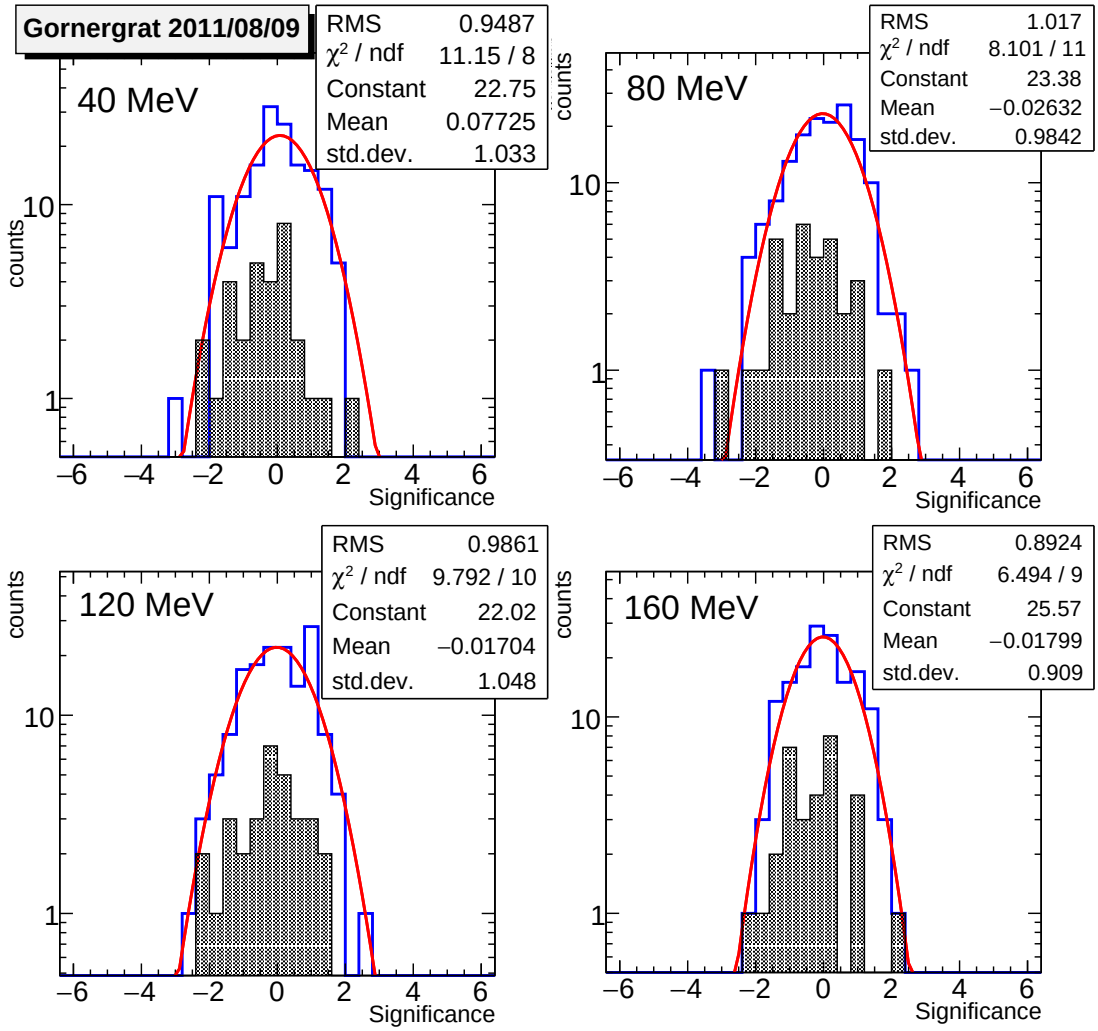

Figure 5.5: Statistical significances for four different threshold levels of GOSW for the X6.9 (2011/08/09) flare. In all plots the overlapped black-shadowed area corresponds to the signal distribution. On the top-left and -right layers, the results for the >40 MeV and >80 MeV with-anti channel respectively. On the bottom-left and -right, the distributions for the >120 MeV and >160 MeV with-anti channel respectively.

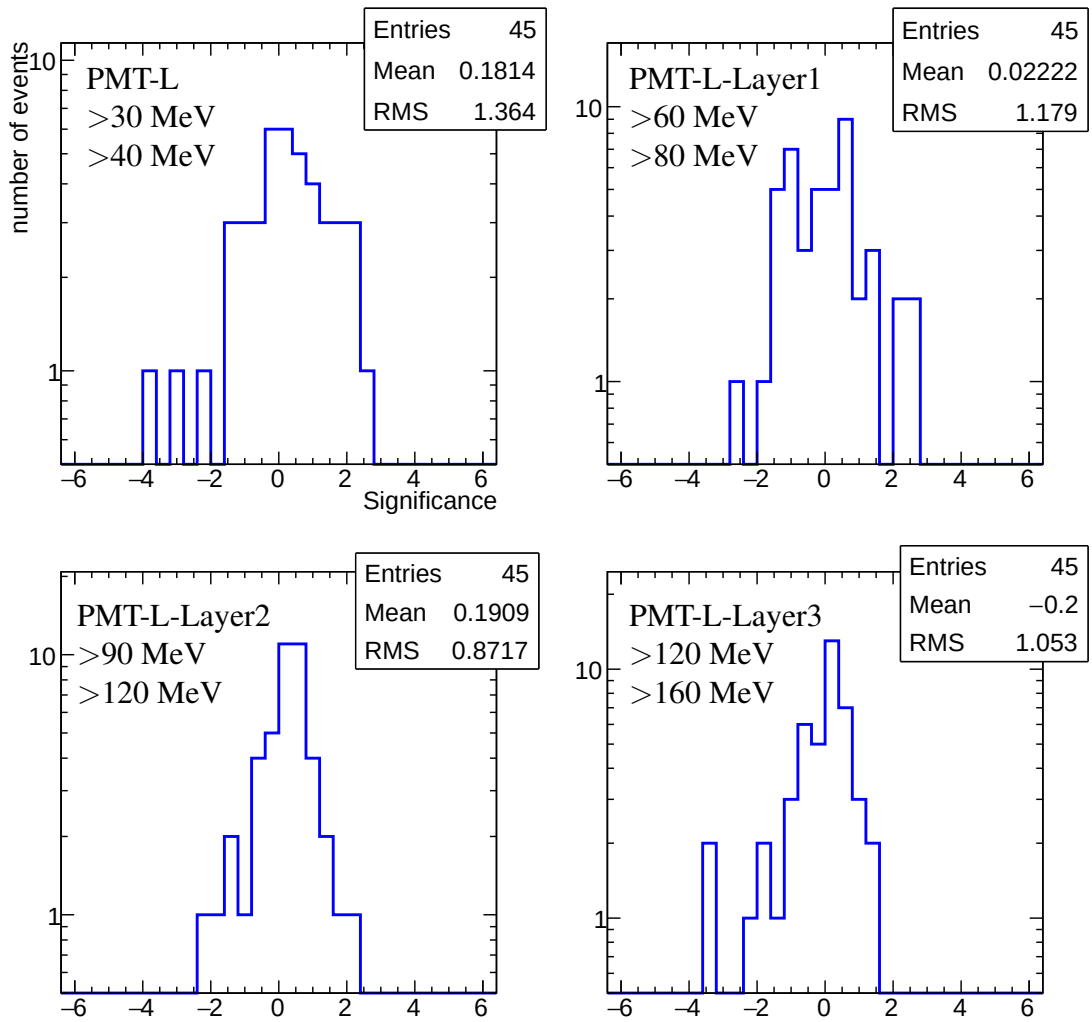

Figure 5.6: Significance distributions at the peak time of the X-ray intensity for five SNTs. The energy threshold levels are indicated at each panel.

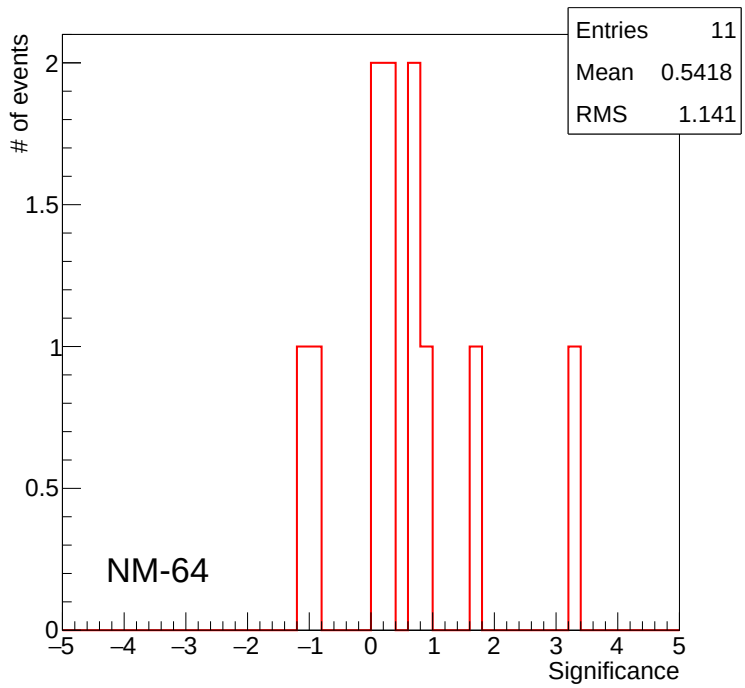

Figure 5.7: Significance distribution at the peak time of the X-ray intensity for the Chacaltaya NM.

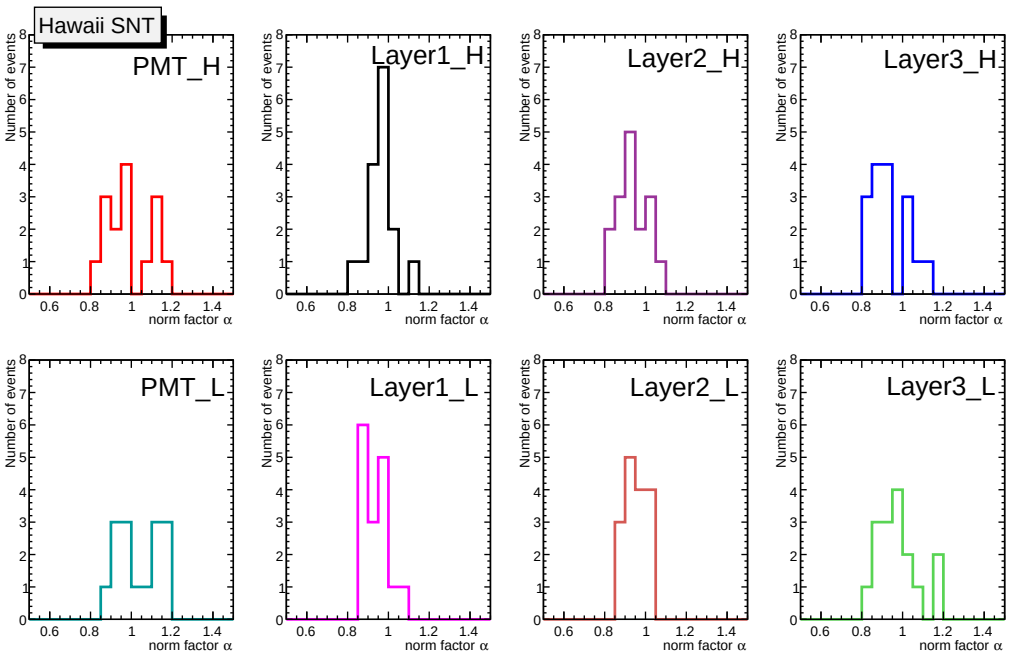

Figure 5.8: The distribution of the normalization factor α for the eight threshold channels of the Hawaii SNT.

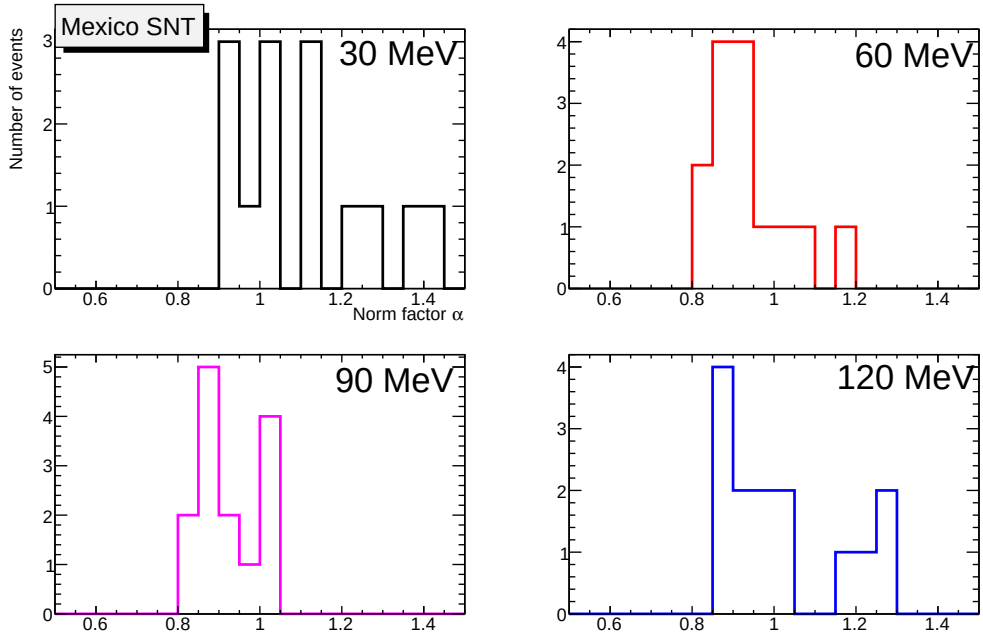

Figure 5.9: The distribution of the normalization factor α for the four threshold channels of the Mexico SNT.

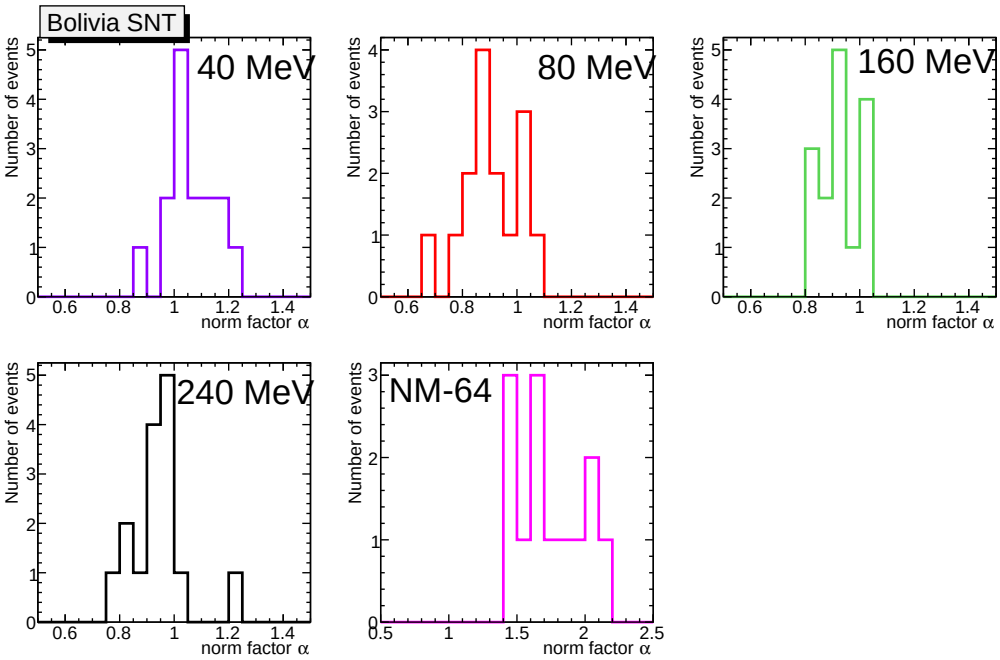

Figure 5.10: The distribution of the normalization factor α for the four threshold channels of the Bolivia SNT.

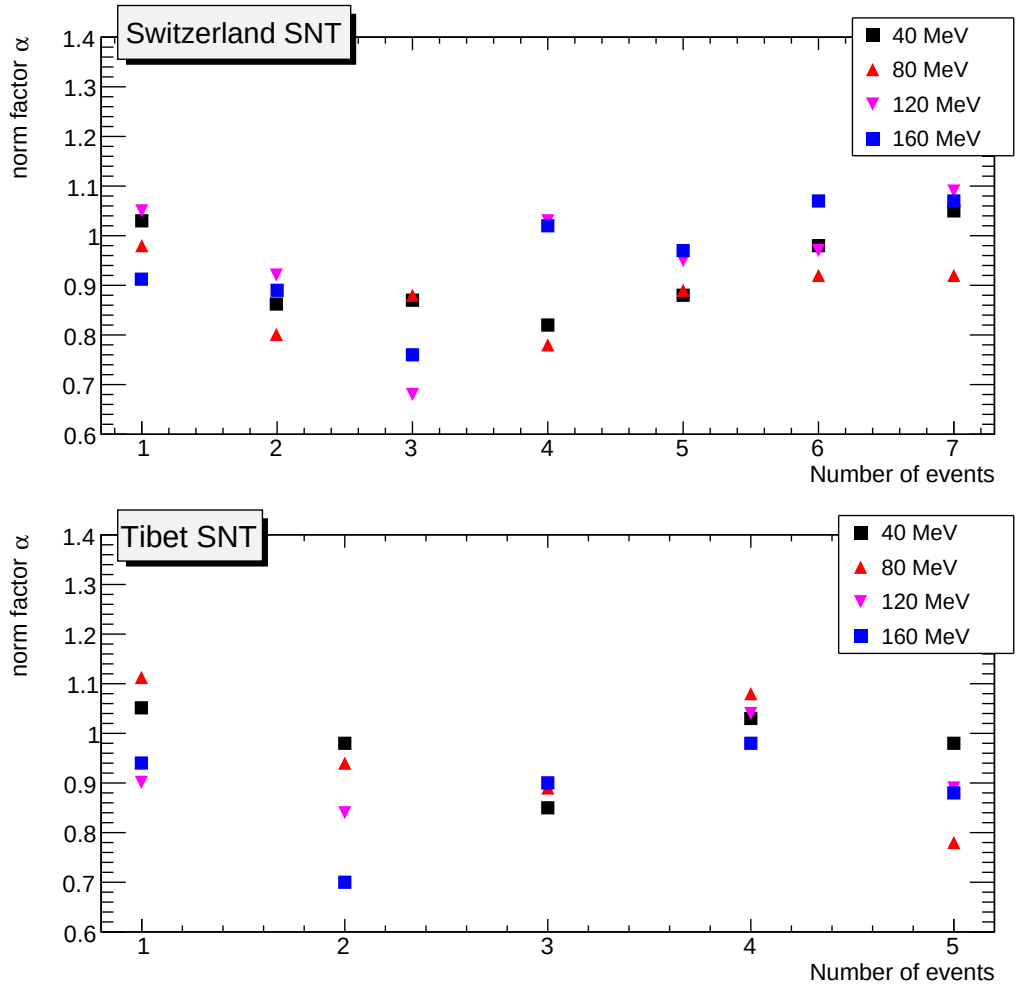

Figure 5.11: Scatter plot showing the normalization factor α for the four threshold channels of the Switzerland and Tibet SNT.

Chapter 6

Neutron emission during solar flares

During the rising and maximum activity of solar cycle 24 (January 2010 to December 2014) a systematic search for solar neutrons in association with X-class flares was performed. The data collected during these five years by the SNTs and the Chacaltaya NM were used. No statistically significant signals due to solar neutrons were found. However, these data can be used to derive the maximum neutron emission during solar flares.
In this chapter, a method to calculate the upper limit of detection is introduced. Next, the neutron emissions are estimated for each of the studied events in Chapter 5. Then, they are compared with that of the successful detections made in solar cycle 23. Additionally, the estimated neutron emissions are compared with the associated soft X-ray fluxes.

6.1 Method to calculate the upper limit of detection

Before describing the method to calculate the upper limit, the following considerations are needed. First, the time profile of the neutron emission is assumed as a δ-function. That is, when a solar flare occurs, neutrons are emitted from the Sun instantaneously at the same time as the maximum intensity of the soft X-ray emission. Second, the correction factor "α"(=$1\sigma/\sqrt{N_0}$) introduced in Chapter 4 is considered. Lastly, the 3σ threshold level to identify solar neutrons adopted in the previous two Chapters is also taken into account.
Considering all the above described, the upper limit of the excess signal which was actually not detected can be defined as the number which gives lower than the counts given by the detector plus the 3σ excess within the 90% of C.L. This condition is shown by:

$$(N_0 + N^* - 1.64\sigma^*) < N_0 + 3\sigma$$

Here, the upper limit is represented as N^*. The term $N_0 + N^*$ represents the background counts plus the excess due to an apparent solar neutron signal. There are two standard deviations in this expression. The first one, σ^*, corresponds to the fluctuation of signal plus background considering the 90% C.L. The second one, σ, is the Poisson standard deviation used to define the threshold level for a signal. Now, replacing variables, the next equation is obtained:

$$(N_0 + N^*) - 1.64\sqrt{N_0 + N^*} < N_0 + 3\alpha\sqrt{N_0} \tag{6.1}$$

This equation is understood as, the fluctuation of the signal and the background wishing the 90% of CL should be lower than the 3σ excess. Solving Equation 6.1 for N^*, the upper limit of detection can

Table 6.1: Example of data from the Gornergrat SNT for the >40 MeV with-anti channel.

X-rays delay	Time [UT]	Range [MeV]	>40 MeV (N_0) Counts/2min
08:05+70s	08:06	1000–446	174381
+180s	08:08	446–263	173767
+300s	08:10	263–179	174245
+420s	08:12	179–132	174146
+540s	08:14	132–101	173182
+660s	08:16	101–81	173510
+780s	08:18	81 – 66	174509
$\sum$(15min)	08:06 - 08:20	1000∼70	1217740

be found.

$$\begin{aligned} z &= N_0 + N^* \\ \ell &= N_0 + 3\alpha\sqrt{N_0} \\ x^2 &= z \\ x^2 - 1.64x - \ell &< 0 \end{aligned}$$

The last expression is an equation with two solutions, where the positive one is considered as the upper limit.

6.1.1 The 2011 August 9 X6.9 solar flare

To better illustrate the method to obtain the upper limit, the data obtained by the GOSW detector on 2011 August 9 can be used as an example. This is the largest solar flare observed thus far in solar cycle 24 and classified as X6.9. The NOAA region of this flare was 1263 and its position was N 17°, W 69°. According to GOES in the 1-8Å band, the soft-X-ray intensity started at 07:48UT and reached its maximum at 08:05UT. During this period there were two SNTs that had the possibility, giving their location, to observe solar neutrons. They were, GOSW in Switzerland and YACH in Tibet, China. At the time of the maximum SXR intensity it was 10:05:00CEST in Gornergrat, Switzerland. Then, the zenith angle and the line-of-sight air mass were 53° and 927g/cm^2 respectively. Starting from 10:06:11CEST, assuming δ-emission, 1 GeV neutrons are expected to arrive to the SNT installed at Gornergrat (3150m). However, as discussed in Chapter 5 no significant signal was observed. Thus, the upper limit can be calculated for the energy range between 70 MeV to 1 GeV which corresponds approximately to the first 15 minutes after the maximum soft X-ray intensity. In Figure 6.1 a 2-minute time profile is plotted for the > 40MeV with-anti channel of the Gornergrat SNT. In Table 6.1 the counting rate per 2 minutes is shown. There are seven bins (1bin=2-minute counts) listed.
Now, with the 15-minute integrated data one single upper limit can be calculated. For this case the correction factor was α=1.03. Solving Equation 6.1 for N^*, one can get,

$$\begin{aligned} N_0 &= 1217740 \\ N_0 + 3\alpha\sqrt{N_0} &= 1221149.85 \\ N_0 + N^* &= 1223694 \\ N^* &= 5223.57 \text{ counts} \end{aligned}$$

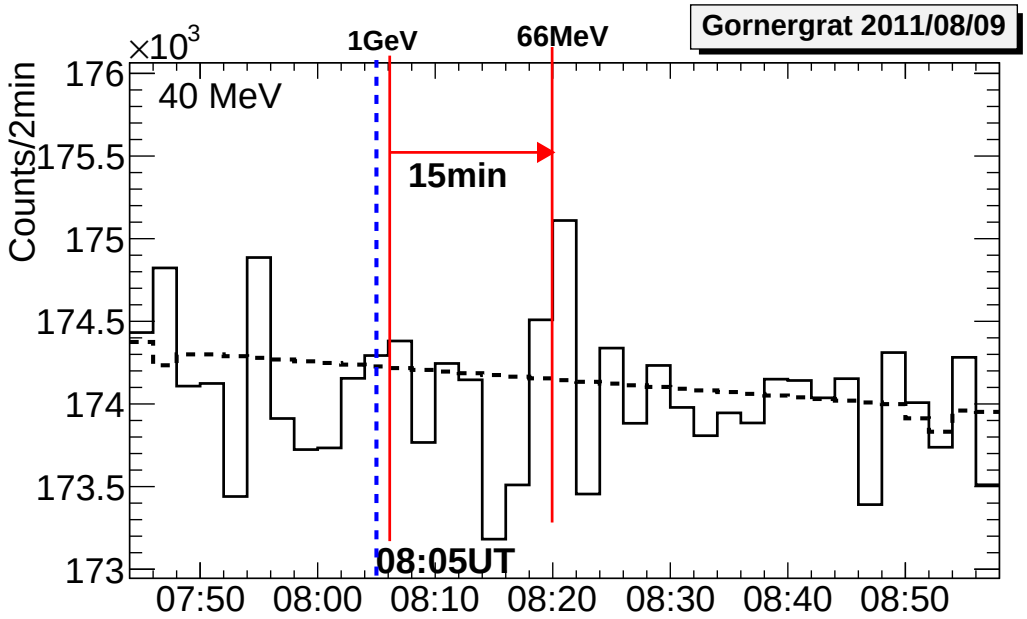

Figure 6.1: An example of how the upper limit was calculated. The whole interval corresponds to the signal window. The segmented black curve is the interpolated data between 07:50 to 08:50UT. The vertical blue dashed line is the peak time of SXRs (here shown by a time label). The red lines enclose the used data to calculate the upper limit.

N^* is the upper limit for this single event. The other upper limits for all the analyzed events in the second campaign are calculated in the same way.

6.1.2 The other flares

Proceeding in the same way as the example in the previous section, the upper limits of detection for the other analyzed events can be obtained. The calculation is done for the lowest threshold level of each SNT detector. Although, >30 MeV is the lowest threshold level of the SNMX detector, the next threshold level (>60 MeV) was considered. The reason is that the >30 MeV with-anti channel during the period of analysis suffered from the temperature effect which could not be corrected during the second campaign.
In Figure 6.2 the upper limits for the 35 analyzed solar flares are shown. The abscissa shows the number of analyzed events at each detector. The ordinate shows the upper limit (N^*) calculated via the method described in this section.

6.2 Solar neutron emission

Assuming that the number of solar neutrons arriving at the detector is the same as the upper limits calculated in the previous section, then the number of neutrons that should have been released from the Sun to produce these upper limits can be estimated. To calculate this, a power-law shaped neutron energy spectrum and an impulsive emission profile at the Sun are assumed. Thus,

$$\frac{\mathrm{d}f(\mathrm{E})}{\mathrm{d}E} \propto \mathrm{E}^{-\beta},$$

is the differential energy spectrum of neutrons, which is theoretically expected from the shock acceleration process of ions in solar flares (Hua et al., 2002). Here β is the differential power-law index.

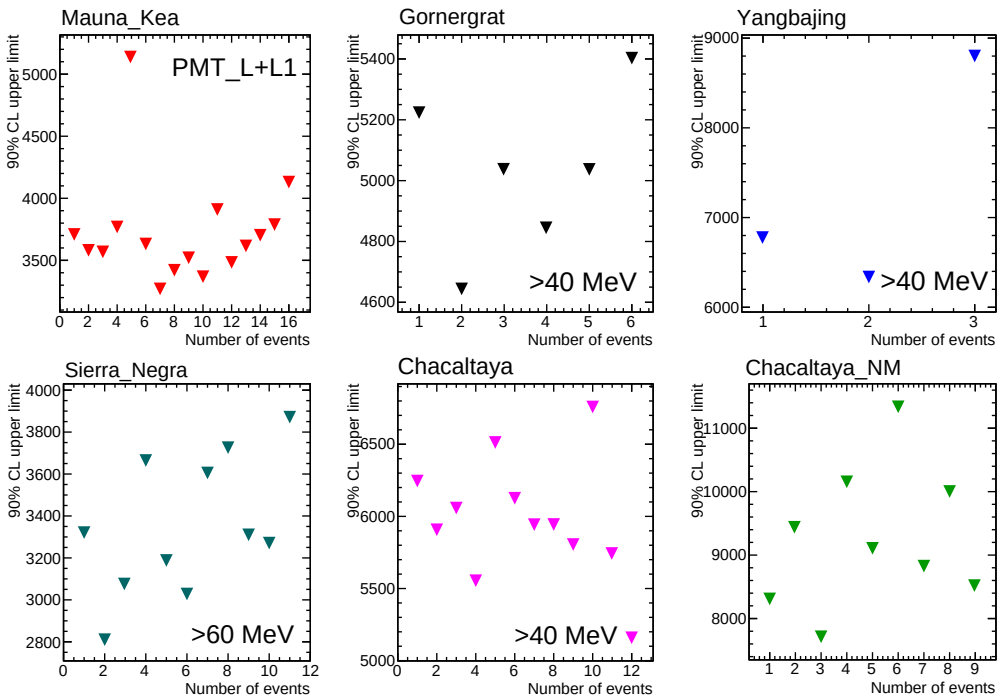

Figure 6.2: The upper limits of detection calculated for the lowest energy threshold level of the SNT detectors and the Chacaltaya NM.

The energy spectrum of neutrons is modified due to the decay of neutrons in the interplanetary space as,

$$F(\mathrm{E}) = \Omega\, P(\mathrm{E})\, C \left(\frac{\mathrm{E}}{100\ [\mathrm{MeV}]}\right)^{-\beta} \tag{6.2}$$

$$\Omega = \frac{\text{area of the detector}}{4\pi(1[\mathrm{AU}])^2}$$

Here, Ω is the solid angle. P(E) is the neutron survival probability, t is the time of flight of neutrons and τ the half-life of neutrons to decay. The Lorentz factor is $\gamma = ((E/M_n) + 1)$, M_n being the neutron's rest mass. The energy term is conveniently divided by a reference energy of 100 MeV.
Equation 6.2 is further modified by the attenuation of neutrons in the atmosphere λ(E) and the detector's response to neutrons ϵ(E′). After the atmospheric propagation the primary energy "E" and the energy at the detector level are not identical. Therefore, λ(E,E′) is introduced as the probability that the primary energy E changes into E′ at the detector level. Hence, the final expression of the flux is of the form,

$$\mathcal{F}(\mathrm{E}) = \epsilon(\mathrm{E}')\ \lambda(\mathrm{E}, \mathrm{E}')\ F(\mathrm{E}) \tag{6.3}$$

The detection efficiency, ϵ(E′), of the SNTs and NM were already discussed in Chapter 2. In this Chapter, the results of those calculations are taken into account. The neutron attenuation in the Earth's atmosphere is calculated based on the nuclear interaction model postulated by Shibata (1994) (hereafter Shibata model). The zenith angle and the incident neutron's kinetic energies between 70 to 1000MeV are considered. By integrating Equation 6.3 and comparing with the upper limit of detection, the neutron emission can be obtained.
As an example, the case for the X6.9 flare occurred on 2011 August 9 is examined. This flare was already considered to calculate the upper limit in the previous section. The data collected by the GOSW detector (effective area equals to 4 m^2) are considered.

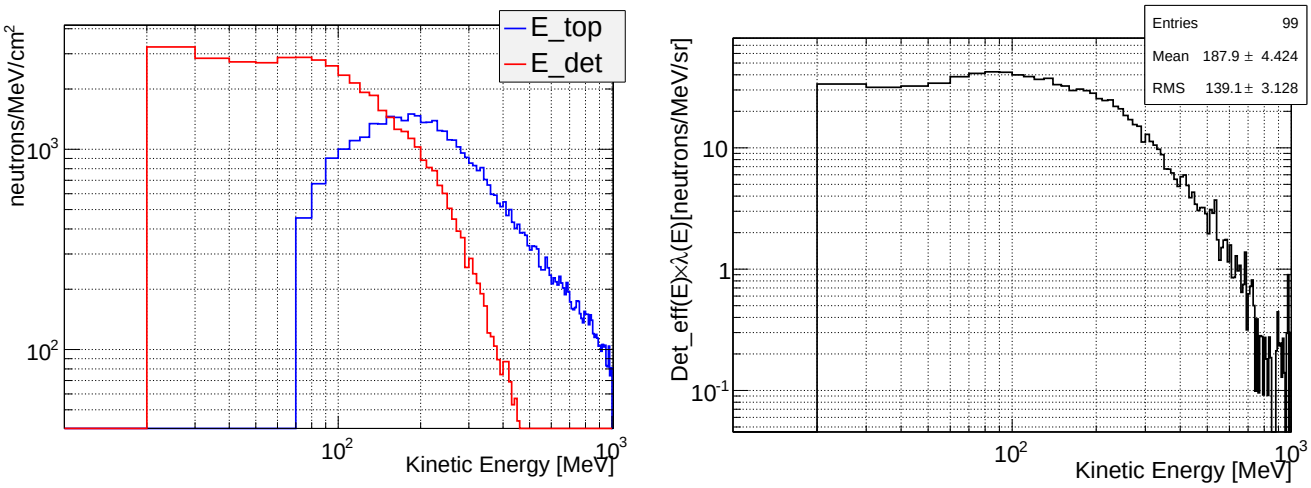

Figure 6.3: On the left, the energy spectra of neutrons obtained via the Shibata model. Considering the height of Gornergrat, Switzerland and the zenith angle of observation. E-top is the curve for the neutrons reaching the top of the Earth's atmosphere and E-det is the curve for neutrons reaching the detector level. On the right, the multiplication of the detection efficiency of the Gornergrat SNT with the neutron attenuation in the atmosphere at the detector level is shown.

The Shibata model is used to calculate the attenuation of neutrons in the atmosphere. In the simulation, 10^8 neutrons are assumed to reach the top of the atmosphere with zenith angle equal to 53°. These neutrons are followed until they reach the line-of-sight air mass of 690 g/cm^2 or until they reach the 20 MeV energy threshold. In Figure 6.3 the results of the simulation are represented. On the left, two curves are shown, one is indicated as "E_top" and the other as "E_det". They represent the kinetic energies of neutrons at the top of the atmosphere and at the detector level respectively.
To estimate the neutron emission, two calculations are necessary. In the first one, Equation 6.2 is integrated between 70MeV to 1000MeV, assuming the power law index equal to 3 and the effective area of the Gornergrat SNT. The result is:

$$F_0 = \frac{10^8 \text{ neutrons}}{4.82 \times 10^{-21}} = 2.07 \times 10^{28} [\text{neutrons/MeV/sr}]$$

The second calculation considers the detection efficiency and the neutron attenuation. On the right of Figure 6.3 the multiplication between these two variables is shown as one single curve. Thus, by integrating this histogram between 70 MeV and 1000 MeV, it is possible to obtain $N_S = 989$ counts. Then comparing with the calculated upper limit, $N^* = 5223.57$ counts, one can get,

$$n^* = \frac{N^*}{N_S} = \frac{5223.57}{989} = 5.28$$

Thus, the neutron emission at 100 MeV is:

$$\begin{aligned} C &= n^* \times F_0 \\ &= 109.44 \times 10^{27} [\text{neutrons/MeV/sr}] \end{aligned}$$

Then, the neutron energy spectrum is given as,

$$F(\text{E}) = 109.44 \times 10^{27} \left(\frac{\text{E}}{100 \text{ MeV}} \right)^{-3} [\text{neutrons/MeV/sr}] \tag{6.4}$$

Finally, the total energy release of solar neutrons can be obtained by integrating Equation 6.4 (multiplied by the energy term E) in the same energy range (70 MeV to 1 GeV). Thus, the energy release is:

$$f(E) = EF_n = C \int_{70\ \mathrm{MeV}}^{1\ \mathrm{GeV}} E \left(\frac{E}{100\ \mathrm{MeV}} \right)^{-3} \mathrm{d}E \tag{6.5}$$

$$EF_n = 232.93 \times 10^{25} [\mathrm{erg/sr}] \tag{6.6}$$

The results shown here are for the 2011 August 9 X6.9-class flare and the >40 MeV with-anti channel of the GOSW detector. The same calculations are performed for the other analyzed events of the second campaign. The results are listed in Table 6.3. Columns 2, 3 and 4 come from the GOES soft X-ray database. Columns 2 and 3 show the date and the class of the flare. Column 4 shows the soft X-ray integrated flux in units of J/m^2. Column 5 shows the SNT or NM detector. Column 6 shows the zenith angle at the time of maximum intensity of the X-ray flux. Column 7 shows the normalization factor, described in Chapter 4. The estimated upper limit based on the method described in section 6.1 is in Column 8. Columns 9 and 10 are the neutron emission at 100 MeV and the total neutron energy release respectively.
The results of the upper limit calculation show a strong dependence with respect to the incident zenith angle. This is expected because neutrons have to travel through a thicker atmosphere, hence their emission will be reduced when they reach the ground-based detectors. In Figure 6.4 this tendency can be observed.
In Figure 6.5 the estimated upper limits of the neutron emission at the Sun for five SNTs and the Chacaltaya NM are shown as black triangles. For comparison, the successful detections (colored squares) observed in solar cycles 21, 22 and 23 listed in and obtained by Watanabe (2005) for the X8.0(1982/06/03), X9.3(1990/05/24), X9.4(1991/03/22), X12.0(1991/06/04), X2.3 (2000/11/24), X5.3 (2001/08/25), X17.0 (2003/10/28), X8.3 (2003/11/02), X28.0 (2003/11/04) flares and by Sako et al. (2006) for the X17.0 (2005/09/07) flare are also shown. In Figures 6.6 and 6.7 show the upper limits when the differential power index is $\beta = 5$ and $\beta = 7$.

6.3 Discussion

Thus far the upper limit of the neutron emission has been calculated for different conditions of solar activity and by several authors. To follow, three of them are mentioned. Forrest and Chupp (1969) used a balloon experiment and searched for solar neutrons on 1967 November 2. Having not observed any positive detection, they estimated the solar neutron flux in the energy interval of 20-120 MeV to be $\sim 2 \times 10^{-2}$neutrons cm^{-2} s^{-1}. Kirsch (1973) used the data collected by fours NMs located in Chacaltaya (Bolivia), Mina Aguilar (Argentine), Pic-du-Midi (France) and Jungfraujoch (Switzerland) to search for solar neutrons, but no significant event was found. Therefore, he estimated the upper limit by the Chree method of epoch superposition. He obtained for the Chacaltaya NM: 2.8×10^{-3}neutrons cm^{-2} s^{-1} and for Pic-du-Midi NM: 1.4×10^{-2}neutrons cm^{-2} s^{-1}. Tsuchiya et al. (2007) have also performed the upper limit calculation making use of the data collected by the Yangbajing NM during the rising period of solar cycle 23. They considered three different types of emission and also three power-law index spectra. The onset time of flares detected by BATSE[1] were considered as the best production time of neutrons. Their flare sample included two X- and 16 M-class flares. Their results are in good correlation with the flux of GOES soft X-rays.

[1]The Burst and Transient Source Experiment on board the Compton Gamma Ray Observatory (CGRO).

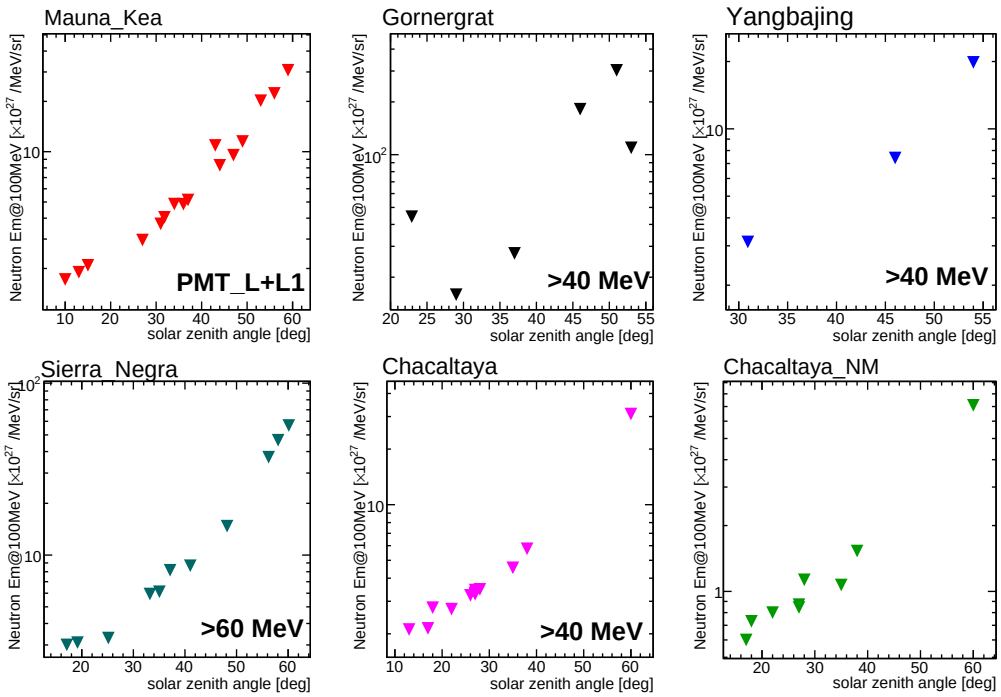

Figure 6.4: Relation between the zenith angle of observation and the estimated neutron emission.

In this chapter the upper limit of the neutron emissions was calculated considering a sample of 35 X-class flares during the period of January 2010 to December 2014. The maximum intensity time (peak) of the soft X-ray emission was assumed as the most probable production time of solar neutrons. The energy spectrum of neutrons was assumed as a power law with indices equal to 3, 5 and 7 as conventional values. The calculation of the neutron emission was limited to only the lowest energy threshold energy of the SNTs, it is expected the upper limits of the neutron emissions of the other high-energy threshold levels will be higher because their sensitivity to neutrons is lower.

Three aspects can be inferred from the results of the upper limit calculation which are shown in Figure 6.5. The first aspect is that, the neutron emissions for the 35 studied flares are in the range between 10^{26}–10^{29}[/MeV/sr], the ten successful detections of solar neutrons in solar cycles 21, 22 and 23 are also in the range between 10^{26}–10^{29}[/MeV/sr]. In a majority of the upper limits the order of magnitude is consistent with that of when a solar neutron event is observed. The consistency is observed when an energy spectrum with power law index equal to 3 is considered. In the other two cases (β=5 and 7) the results are also within the order of magnitude of the solar neutron events. In spite of the softer spectrum shape. These comparisons are listed in Table 6.2.

The second aspect, the results of integrating the neutron energy spectrum (Equation 6.4) are compared with the total radiated energy of soft X-rays. In Figure 6.8 the total energy release of solar neutrons as a function of the total radiated energy of X-rays (measured by GOES) is shown. The abscissa represents the total soft X-ray radiated energy (E_{SXR}) in the 1-8Å band. The ordinate represents the total energy release of neutrons (EF_n) emitted from the Sun in the energy range between 70–1000 MeV. Since the SXR integrated flux for the solar neutron events before 2000 was not available in the GOES database, an energy budget analysis is made only with the successful detections made in solar cycle 23.

Four zones are defined in Figure 6.8, these are: EF_n[erg/sr] $= 10^{-2}E_{SXR}$[erg], $EF_n = 10^{-3}E_{SXR}$ and $EF_n = 10^{-4}E_{SXR}$. Counting the number of upper limit (the most stringent) events and solar neutron events that are included at each zone (fraction energy zone), it is possible to obtain the following: In the first and second zones, 7 and 16 upper limit events (UL) respectively but no successful

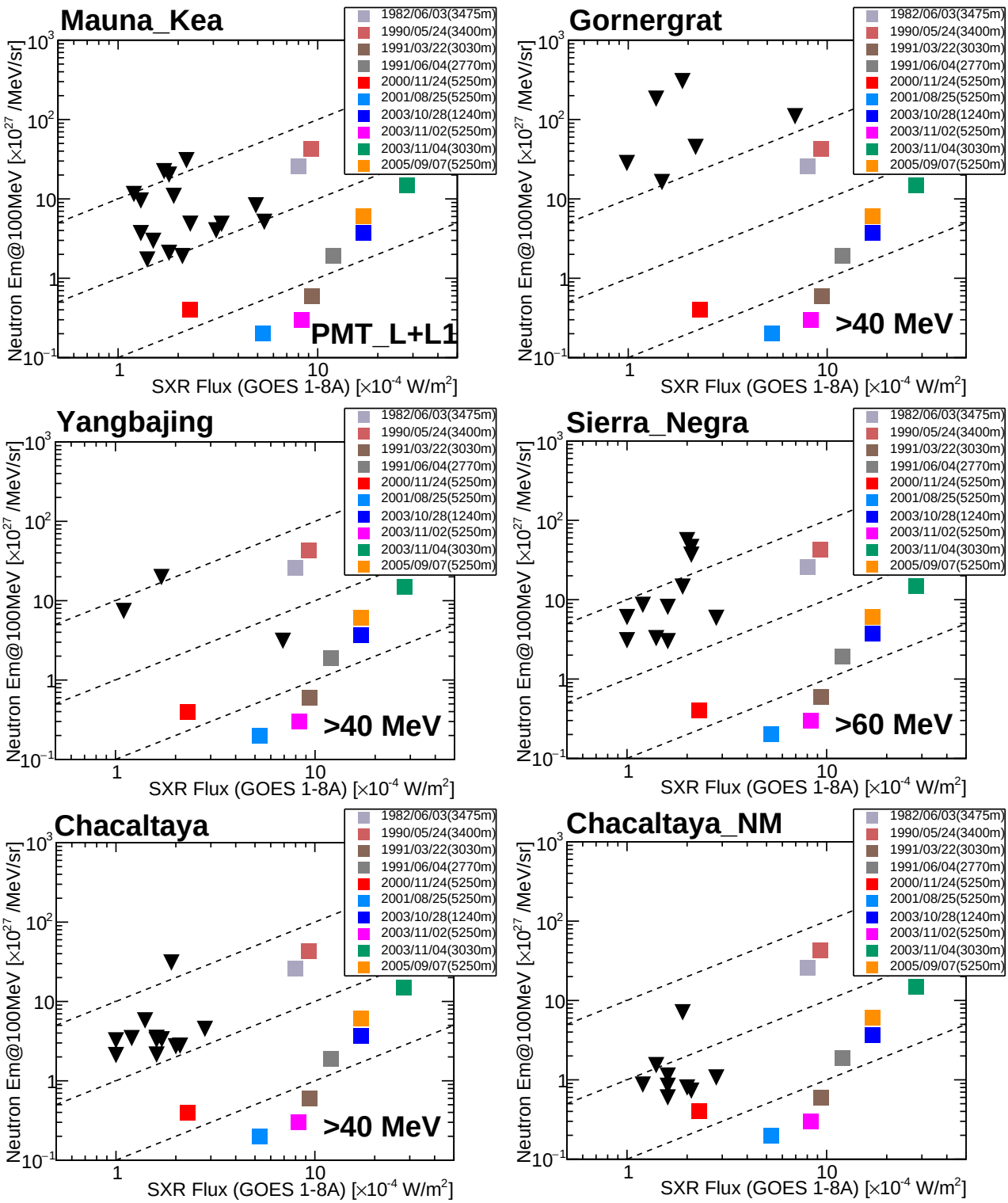

Figure 6.5: The 90% CL upper limits at the 100 MeV (shown as black triangles) solar neutron emission estimated for five SNTs (lowest threshold level) and one NM. Previous successful detections observed in solar cycles 21, 22 and 23 are also plotted (colored squares). The abscissa represents the SXR flux measured by GOES in units of W/m^2. Top-left, -right display upper limits for MKUS, GOSW respectively. The middle-left and -right display upper limits for YACH and SNMX respectively. The bottom-left, and -right display upper limits for CHBO and CHNM respectively.

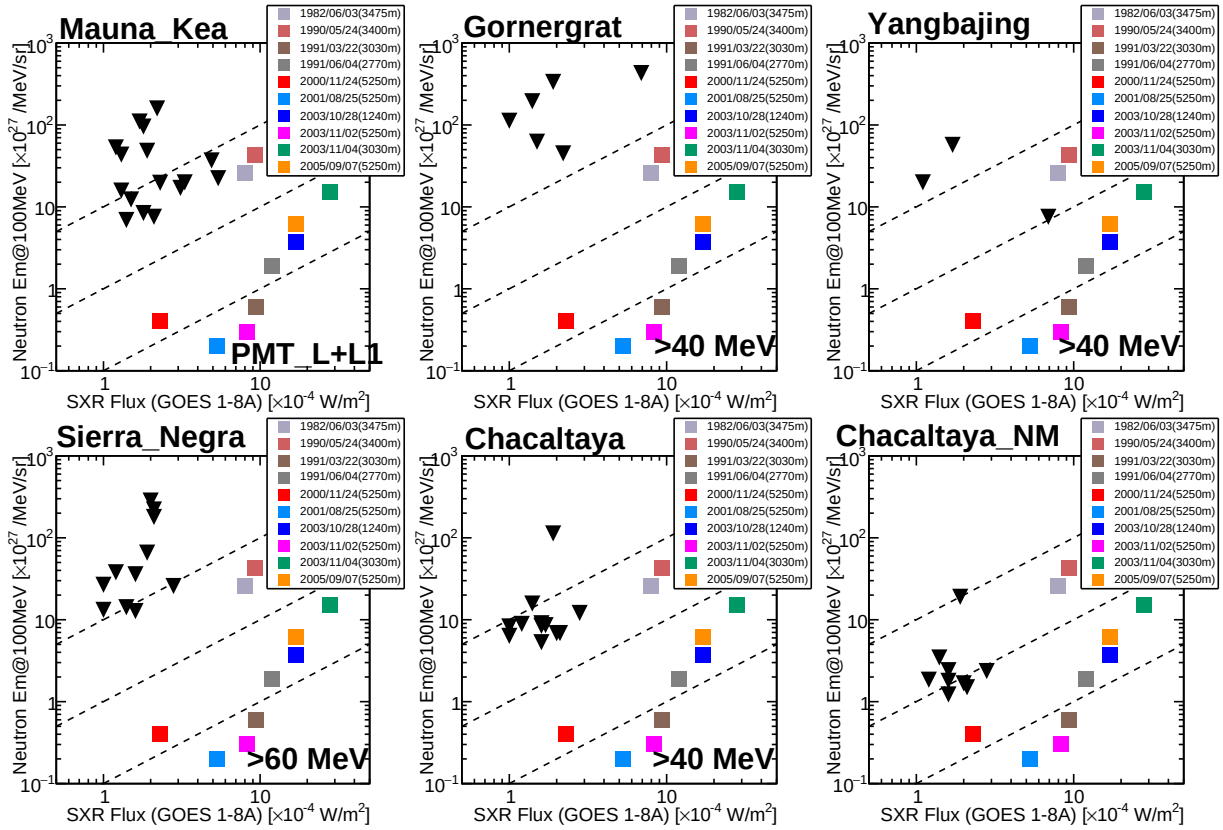

Figure 6.6: Same as Figure 6.5 but considering $\beta = 5$.

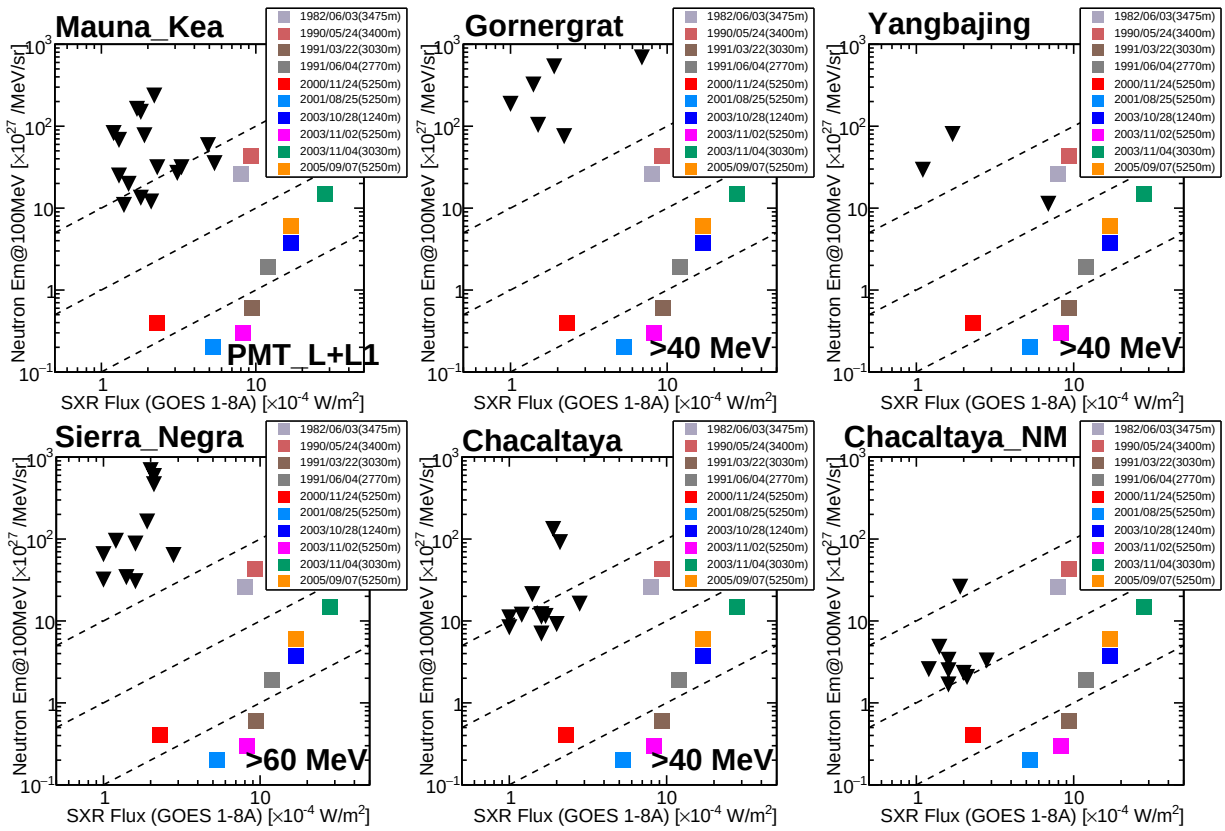

Figure 6.7: Same as Figure 6.5 but considering $\beta = 7$.

Table 6.2: The least and most stringent upper limits on the neutron emission and the total energy release of solar neutrons.

Power law index	Neutron Emission $C^a \times 10^{27}$[/MeV/sr]		Energy Release $EF_n^b \times 10^{25}$[/erg/sr]	
β	least	most	least	most
3	302.71	0.60	644.27	1.27
5	429.96	1.22	915.10	2.60
7	690.70	1.68	1470.00	3.60
2.9	43.00[c]		140.00[c]	
3.1		0.24[d]		0.64[d]

[a] Neutron emission at 100 MeV
[b] Total energy release of solar neutrons between 70 MeV and 1GeV.
[c]Solar neutron event of 1990 May 24.
[d]Solar neutron event of 2001 August 25.

detections. In the third zone, 12 UL events and 3 successful detections. Lastly, in the fourth zone, no UL events and 3 successful detections. In Figure 6.9 it is graphically represented as a function of fractional energy these zones and the corresponding number of events in percentage.
According to Figure 6.9, it is possible to infer: 1) the solar neutron energy may not exceed 0.1% of the SXR energy and 2) between EF_n/E_{SXR}=10^{-4} and 10^{-3} most (45.7%) solar flares are concentrated, but none of them were associated with the production of solar neutrons.
As the third aspect of this discussion, a comparison between the total energy release of solar neutrons and the radiated energy of soft X-rays was considered. However, the latter term might not be suited to make a correct evaluation of the SXR energy released during solar flares. The radiated energy in the 1-8Å band is the integrated energy over the flare duration (from the onset of the GOES soft X-ray emission until this decreased to 10% of its peak value). This value may be underestimated and does not focus on the important part of the SXR emission, which is the peak area. The peak thermal energy can be calculated to better understand the energetics of the plasma released at the time the solar flare occurred.
To calculate the peak thermal energy (U_{th}), the GOES IDL class available in SSW[2] is used. Two necessary variables are calculated in advance, these are, the average temperature and the emission measure (EM= $\int n^2$dV [cm^{-3}]) of the thermal plasma considering a constant density of electrons and ions $n = 10^{11}$[cm^{-3}]. V is the emitting volume and determined via:

$$V = \frac{10^{49} EM}{n^2}$$

Finally, the peak thermal energy will be:

$$U_{th} = nkVT, \tag{6.7}$$

where $k = 1.380 \times 10^{-23}$[J K^{-1}] is the Boltzmann's constant.
Notice that the peak thermal energy calculation involves the 0.5-4Å and 1-8Å bands of the GOES soft X-ray emission.
An IDL script kindly prepared by Prof. S. Masuda, allow us to estimate the thermal energy and moreover, plot the light curve of the 35 studied flares. The script in question considers the IDL

[2]SSW: SolarSoftware, `http://hesperia.gsfc.nasa.gov/rhessidatacenter/complementary_data/goes.html`

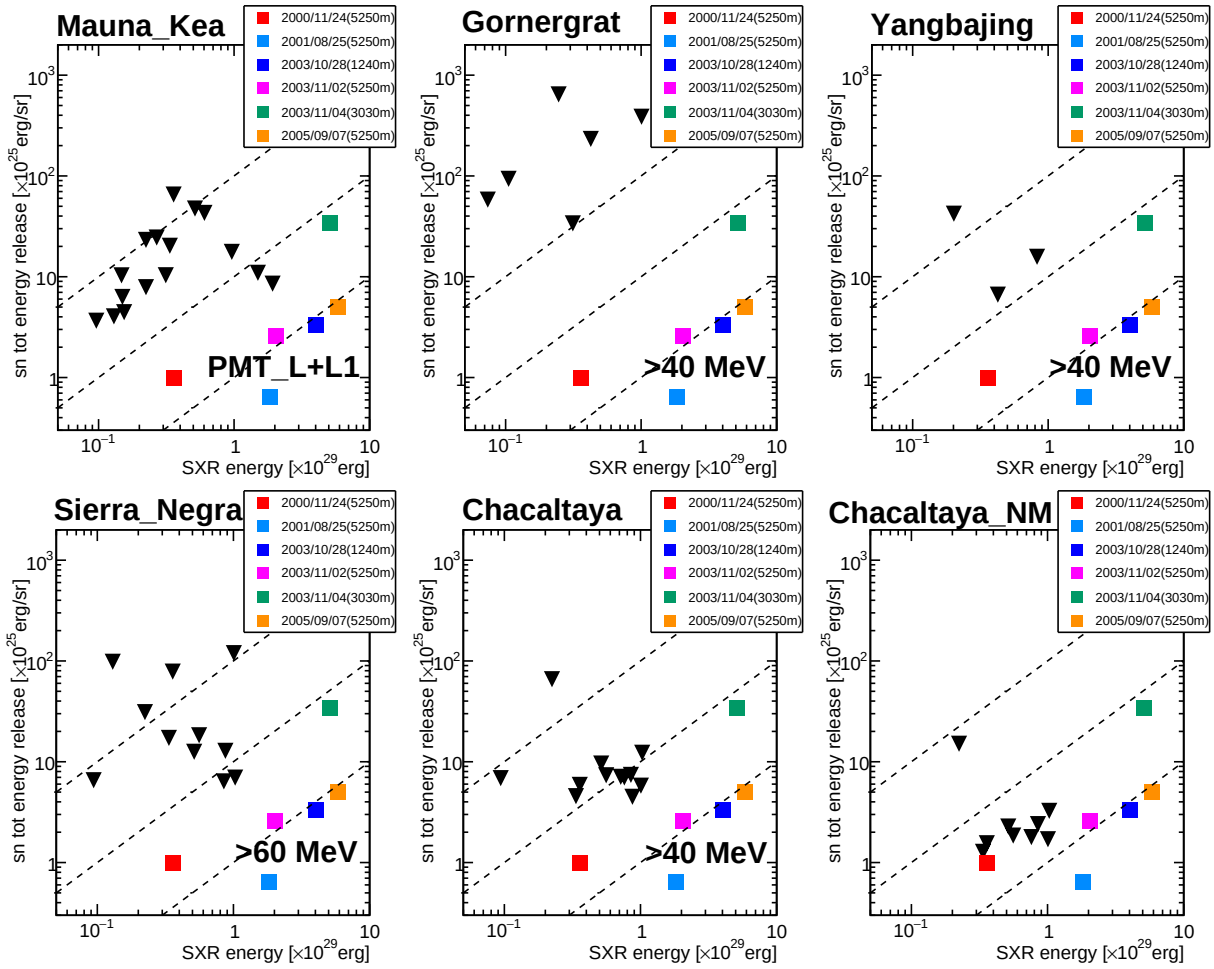

Figure 6.8: The total energy release of solar neutrons (sn) which were emitted from the Sun (ordinate) in the energy range between 70 – 1000 MeV was estimated for five SNTs (lowest threshold level) and one NM. Previous successful detections done by Watanabe (2005) and Sako et al. (2006) are also plotted (colored squares). The abscissa represents the SXR radiated energy measured by GOES in the 1-8Å band. In all the plots three segmented lines can be observed. These relations are: EF_n[erg/sr] $= 10^{-2}E_{SXR}$[erg], $EF_n = 10^{-3}E_{SXR}$ and $EF_n = 10^{-4}E_{SXR}$. Top-left, -center and -right display energy intensities (EF_n) for MKUS, GOSW and YACH respectively. The bottom-left, -center, and -right display energy intensities for SNMX, CHBO and CHNM respectively.

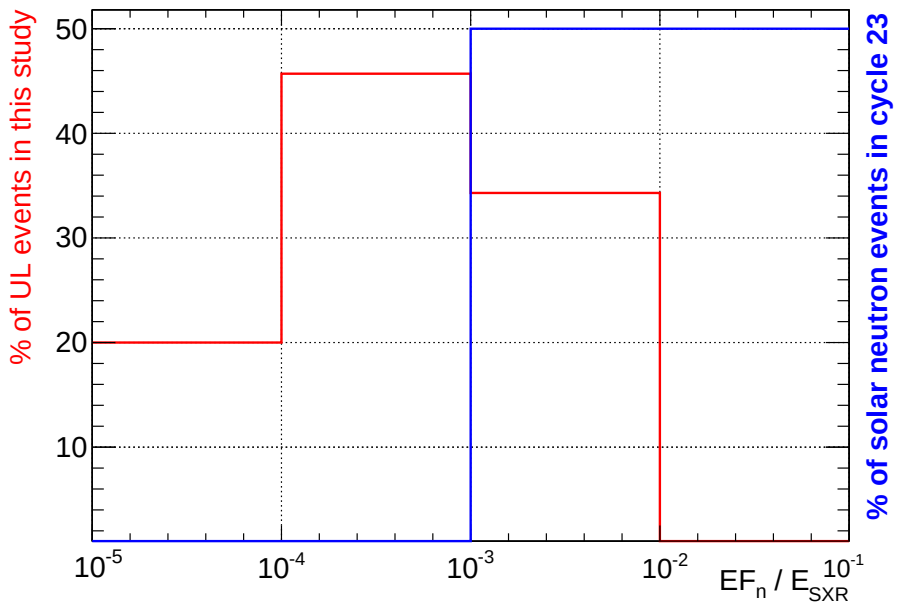

Figure 6.9: The red histogram is the number [%] of calculated upper limits (UL), excluding multiple detections, in this study. The blue histogram represents the number [%] of solar neutron events (successful ground-based detections).

procedure *goes_chianti_tem* to calculate the thermal energy, temperature and emission measure of the soft X-rays. The results of this calculation are shown in Table 6.4. In that list the Columns 2, 3 and 4 are provided directly from the GOES database. Columns 6, 7, and 8 are calculated by using the SSW tool. Additionally, the peak thermal energy, temperature and energy emission were calculated for the solar flares which produced solar neutrons. They are listed in Table 6.5. The peak thermal energy of the X12.0(1991/06/04) and the X28.0 (2003/11/04) flares could not be estimated because of the limitations of the GOES IDL procedure.

Figure 6.11 shows the scatter plots of the total energy release of solar neutrons and the peak thermal energy of soft X-rays. In all the plots four segmented lines are drawn. These relations are: EF_n[erg/sr] $= 10^{-3}U_{th}$[erg], $EF_n = 10^{-4}U_{th}$, $EF_n = 10^{-5}U_{th}$ and $EF_n = 10^{-6}U_{th}$. It is possible to define five zones, in which the upper limits (UL) are included, from the four segmented lines drawn. Hence, it is possible to count, the number of successful solar neutron events and the number of UL events in this study at each zone. In the first zone, 2 (5.7%) UL events but no successful detections are found. In the second zone, 16 (45.7%) UL events and one (10%) successful detection. In the third zone, 17 (48.6%) UL events and 2 (20%) successful detections. In the fourth zone, no UL events and 6 (60%) successful detections. Lastly, in the fifth zone, no UL events and 1(10%) successful detection. Notice that in the case where UL events are observed at more than one location, only the most stringent UL event is considered. The number of events (in percentage) is shown as a function of fractional energy corresponding to the zones defined above.

According to Figure 6.10 it is possible to infer the following. First, the neutron energy (EF_n) may not exceed 0.01% of the soft X-ray peak thermal energy (U_{th}). Second, between $EF_n/U_{th}=10^{-5}$ and 10^{-3} most (94%) solar flares are concentrated, but none of them were associated with the detection of solar neutrons.

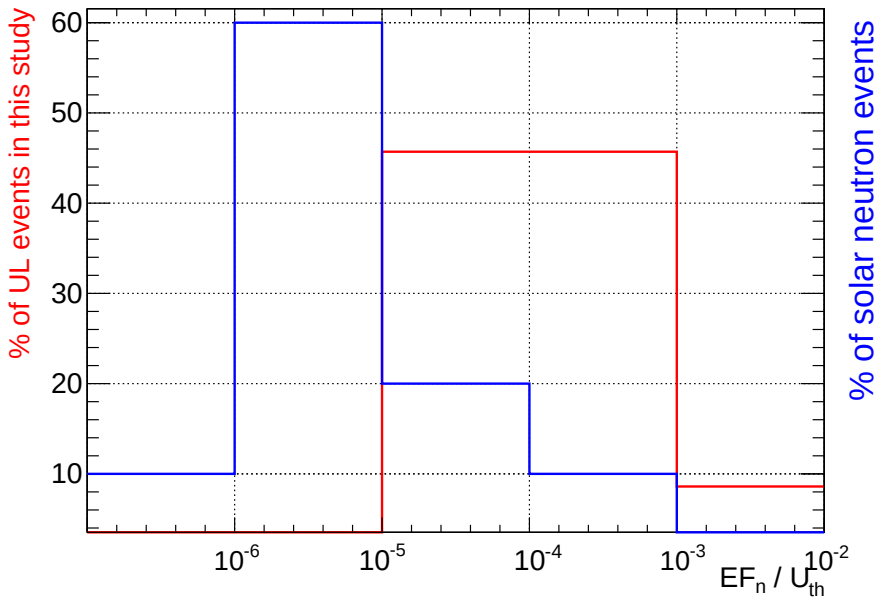

Figure 6.10: The red histogram is the number [%] of calculated upper limits (UL), excluding multiple detections, in this study. The blue histogram represents the number [%] of solar neutron events (successful ground-based detections).

Table 6.3: Upper limits for thirty-five solar flares.

No	Date	Class	Intg. Flux† [J/m^2]	SNT	$\theta_{\odot}$ [a] [deg]	α [b]	N*	C$^{\ell}$ $\times 10^{27}$ [/MeV/sr]	EF$_n^{\ddagger}$ $\times 10^{25}$ [erg/sr]
1	2011 Feb 15	X2.2	0.16	MKUS	59	0.97	3708.75	30.72	65.38
2	2011 Mar 09	X1.5	0.067	MKUS	27	0.92	3580.97	2.96	6.30
3	2011 Aug 09	X6.9	0.19	GOSW	53	1.03	5223.57	109.44	232.93
				YACH	31	1.05	6767.61	3.12	6.65
4	2011 Sep 06	X2.1	0.058	MKUS	13	0.89	3568.61	1.90	4.04
				SNMX	58	0.93	3320.72	46.11	98.15
5	2011 Sep 07	X1.8	0.069	MKUS	15	0.97	3769.11	2.09	4.44
6	2011 Sep 22	X1.4	0.45	GOSW	46	0.86	4644.17	181.72	386.78
7	2011 Sep 24	X1.9	0.11	GOSW	51	0.87	5035.76	302.71	644.27
8	2011 Nov 03	X1.9	0.1	MKUS	43	1.18	5129.14	10.90	23.20
				SNMX	48	0.85	2810.25	14.59	31.05
				CHBO	60	1.20	6244.99	30.96	65.90
				CHNM	60	1.65	8309.53	7.09	15.10
9	2012 Jan 27	X1.7	0.32	CHBO	27	1.09	5907.33	3.33	7.09
10	2012 Mar 05	X1.1	0.37	YACH	46	0.85	6337.39	7.41	15.78
11	2012 Mar 07	X5.4	0.67	MKUS	37	1.06	3631.89	5.15	10.95
12	2012 Mar 07	X1.3	0.15	MKUS	47	0.90	3270.23	9.53	20.29
13	2012 Jul 06	X1.4	0.043	MKUS	10	0.94	3420.49	1.72	3.67
14	2012 Jul 12	X1.4	0.46	SNMX	25	0.95	3075.58	3.27	6.96

† GOES SXR Integrated Flux. [a] Solar zenith angle. [b] Normalization factor.
N* Upper limit of detection. [ℓ] Neutron Emission at 100 MeV. [‡] Total Neutron Energy Release

Continued on next page

Table 6.3 – *Continued from previous page*

No	Date	Class	Intg. Flux† [J/m^2]	SNT	$\theta_{\odot}{}^{a}$ [deg]	α^{b}	N*	$C^{\ell} \times 10^{27}$ [/MeV/sr]	$EF_n^{\ddagger} \times 10^{25}$ [erg/sr]
				CHBO	38	1.04	6057.77	5.77	12.28
				CHNM	38	1.77	9436.00	1.53	3.26
15	2013 May 13	X1.7	0.23	MKUS	56	0.87	3521.05	22.32	47.51
16	2013 May 13	X2.8	0.23	SNMX	33	1.16	3664.47	5.90	12.57
				CHBO	35	1.00	5554.13	4.51	9.60
				CHNM	35	1.49	7713.02	1.06	2.27
17	2013 May 15	X1.2	0.12	MKUS	49	0.90	3368.40	11.50	24.49
18	2013 Oct 25	X1.7	0.09	YACH	54	1.03	8800.94	19.83	42.21
19	2013 Oct 25	X2.1	0.16	SNMX	56	0.92	3187.91	36.83	78.40
				CHBO	18	1.14	6512.31	2.77	5.90
				CHNM	18	1.97	10155.00	0.73	1.56
20	2013 Oct 29	X2.3	0.14	MKUS	34	0.99	3909.77	4.86	10.34
21	2013 Nov 05	X3.3	0.066	MKUS	36	0.92	3483.57	4.85	10.32
22	2014 Jan 07	X1.2	0.25	SNMX	41	0.85	3028.01	8.60	18.30
				CHBO	27	1.16	6125.88	3.45	7.36
				CHNM	27	1.86	9107.13	0.87	1.86
23	2014 Feb 25	X4.9	0.43	MKUS	44	0.98	3616.42	8.30	17.66
24	2014 Mar 29	X1.0	0.042	SNMX	19	0.98	3605.05	3.08	6.54
				CHBO	26	1.00	5942.75	3.22	6.87
25	2014 Apr 25	X1.3	0.1	MKUS	31	0.90	3702.54	3.70	7.88
26	2014 Jun 10	X2.2	0.047	GOSW	23	0.82	4841.79	43.98	93.60
27	2014 Jun 10	X1.5	0.14	GOSW	29	0.88	5037.06	15.90	33.83
28	2014 Jun 11	X1.0	0.033	GOSW	37	0.98	5402.73	27.35	58.21
29	2014 Sep 10	X1.6	0.38	SNMX	17	1.09	3725.66	3.00	6.384
				CHBO	28	1.11	5943.8	3.48	7.40
				CHNM	28	2.14	11337	1.12	2.40
30	2014 Oct 22	X1.6	0.34	CHBO	27	0.97	5804.9	3.28	6.97
				CHNM	27	1.59	8826.26	0.84	1.80
31	2014 Oct 24	X3.1	0.86	MKUS	32	0.87	3788.1	4.01	8.54
32	2014 Oct 25	X1.0	0.39	SNMX	35	0.81	3310.12	6.03	12.84
				CHBO	13	1.30	6758.08	2.10	4.49
33	2014 Oct 27	X2.0	0.45	SNMX	60	0.91	3270.68	56.15	119.50
				CHBO	22	1.05	5735.76	2.72	5.80
				CHNM	22	2.02	10002.7	0.80	1.71
34	2014 Nov 07	X1.6	0.15	SNMX	37	1.03	3871.15	8.10	17.23
				CHBO	17	0.92	5158.75	2.14	4.55
				CHNM	17	1.62	8500.67	0.60	1.27
35	2014 Dec 20	X1.8	0.27	MKUS	53	0.98	4130.8	20.19	42.97

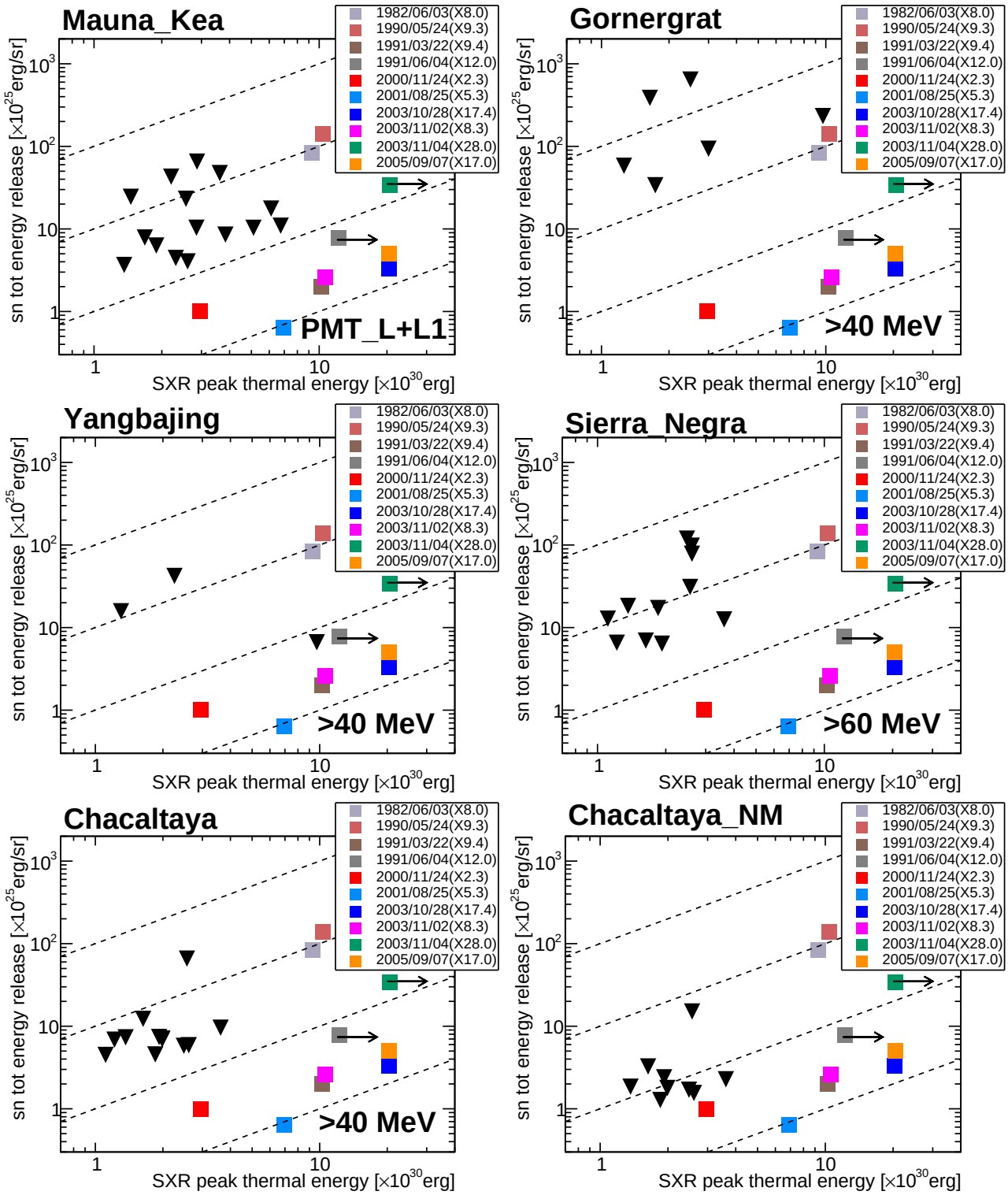

Figure 6.11: The total energy release of solar neutrons (shown here as black triangles) which were emitted from the Sun (ordinate) in the energy range between 70 – 1000 MeV was estimated for five SNTs (lowest threshold level) and one NM. Previous successful detections listed in and done by Watanabe (2005) and Sako et al. (2006) are also plotted (colored squares). The abscissa represents the peak thermal energy of soft X-rays. Top-left, -center and -right display energy intensities (EF_n) for MKUS, GOSW and YACH respectively. The bottom-left, -center, and -right display energy intensities for SNMX, CHBO and CHNM respectively. The two arrows ($\rightarrow$) show the flares for which the peak thermal was not estimated because of the limitations of the SSW tool.

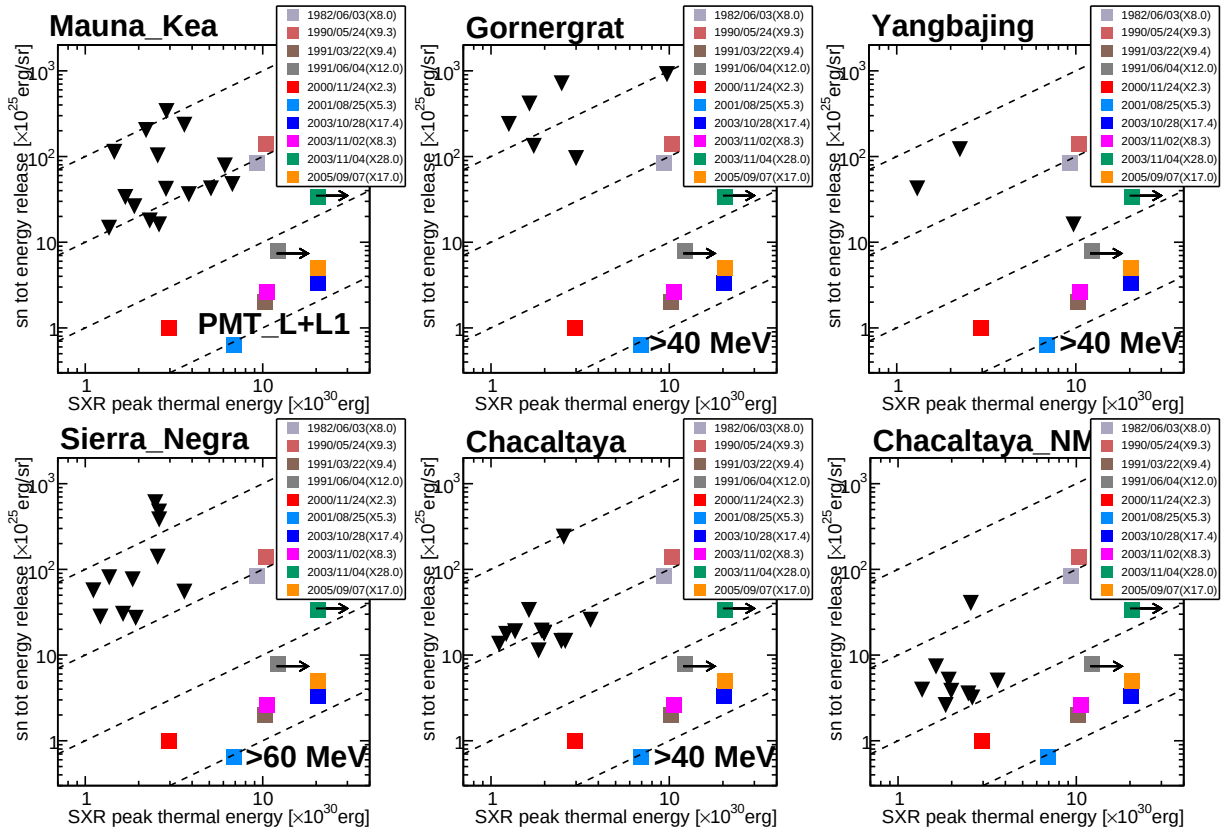

Figure 6.12: Same as Figure 6.11 but the differential power law index is β=5.

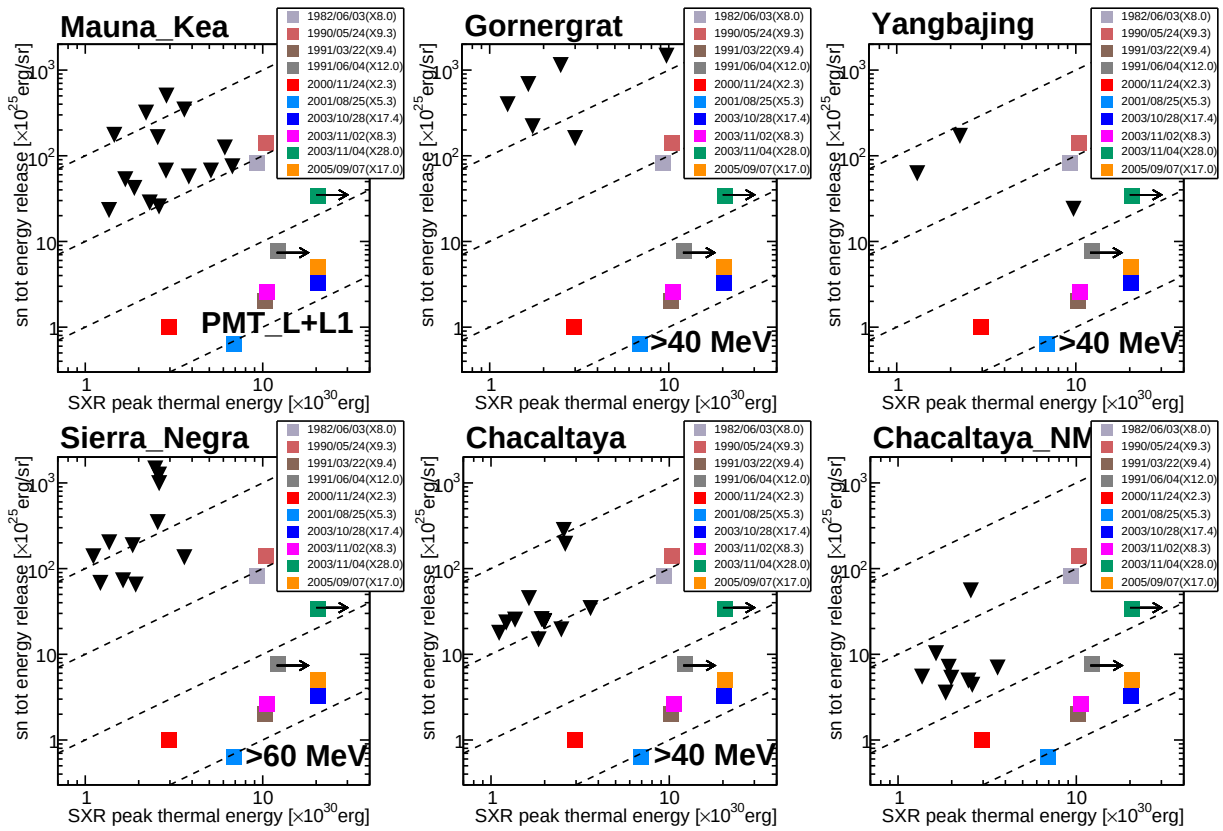

Figure 6.13: Same as Figure 6.11 but the differential power law index is β=7.

Table 6.4: Characteristics of thirty-five solar flares.

No	Date	Class	Intg. Flux[a] [J/m^2]	Rad. energy [$\times 10^{29}$erg]	Temperature[b] [$\times 10^6$ K]	EM[c] [10^{49}cm^{-3}]	U_{th}[d] [$\times 10^{30}$erg]
1	2011 Feb 15	X2.2	0.16	0.36	20.59	10.09	2.87
2	2011 Mar 09	X1.5	0.067	0.15	19.35	7.08	1.89
3	2011 Aug 09	X6.9	0.19	0.42	24.47	28.74	9.71
4	2011 Sep 06	X2.1	0.058	0.13	19.36	9.75	2.60
5	2011 Sep 07	X1.8	0.069	0.15	21.25	7.87	2.31
6	2011 Sep 22	X1.4	0.45	1.00	17.39	6.85	1.64
7	2011 Sep 24	X1.9	0.11	0.24	24.47	7.38	2.49
8	2011 Nov 03	X1.9	0.1	0.22	21.73	8.53	2.56
9	2012 Jan 27	X1.7	0.32	0.72	15.20	9.45	1.98
10	2012 Mar 05	X1.1	0.37	0.83	16.79	5.61	1.30
11	2012 Mar 07	X5.4	0.67	1.50	21.02	23.25	6.74
12	2012 Mar 07	X1.3	0.15	0.33	18.17	0.34	0.08
13	2012 Jul 06	X1.4	0.043	0.10	19.90	4.96	1.36
14	2012 Jul 12	X1.4	0.46	1.03	17.34	6.82	1.63
15	2013 May 13	X1.7	0.23	0.51	18.71	8.08	2.08
16	2013 May 13	X2.8	0.23	0.51	21.56	12.16	3.62
17	2013 May 15	X1.2	0.12	0.27	16.39	6.44	1.46
18	2013 Oct 25	X1.7	0.09	0.20	23.21	7.03	2.25
19	2013 Oct 25	X2.1	0.16	0.36	21.01	9.00	2.61
20	2013 Oct 29	X2.3	0.14	0.31	19.39	10.65	2.85
21	2013 Nov 05	X3.3	0.066	0.15	25.57	14.47	5.11
22	2014 Jan 07	X1.2	0.25	0.56	14.86	6.65	1.36
23	2014 Feb 25	X4.9	0.43	0.96	20.03	22.12	6.12
24	2014 Mar 29	X1.0	0.042	0.09	18.89	4.67	1.22
25	2014 Apr 25	X1.3	0.1	0.22	19.38	6.28	1.68
26	2014 Jun 10	X2.2	0.047	0.10	24.68	8.81	3.00
27	2014 Jun 10	X1.5	0.14	0.31	16.42	7.67	1.74
28	2014 Jun 11	X1.0	0.033	0.07	20.80	4.39	1.26
29	2014 Sep 10	X1.6	0.38	0.85	17.58	7.93	1.92
30	2014 Oct 22	X1.6	0.34	0.76	18.91	7.62	1.99
31	2014 Oct 24	X3.1	0.86	1.92	19.11	14.53	3.83
32	2014 Oct 25	X1.0	0.39	0.87	18.74	4.30	1.11
33	2014 Oct 27	X2.0	0.45	1.00	19.38	9.27	2.48
34	2014 Nov 07	X1.6	0.15	0.33	17.54	7.64	1.85
35	2014 Dec 20	X1.8	0.27	0.60	17.50	9.11	2.20

[a] GOES SXR Integrated Flux. [b] Average temperature at the peak of emission of soft X-rays.
[b] Emission measure of the thermal plasma. [d] Peak thermal energy of the plasma.

Table 6.5: Characteristics of solar neutron events and the associated solar flares.

No	Date	Class	T[a] [$\times 10^6$ K]	EM[b] [10^{49}cm^{-3}]	U_{th}[c] [$\times 10^{30}$erg]	C[d] $\times 10^{27}$ [/MeV/sr]	EF_n[e] $\times 10^{25}$ [erg/sr]
1	1982 Jun 3	X8.0	15.90	42.40	9.30	26.0	83.0
2	1990 May 24	X9.3	12.43	60.42	10.37	43.0	140.0
3	1991 Mar 22	X9.4	12.50	59.34	10.24	0.6	2.0
4	1991 Jun 4	X12.0	>11.57	>76.60	>12.23	1.9	7.8
5	2000 Nov 24	X2.3	17.52	12.22	2.95	0.4	1.0
6	2001 Aug 25	X5.3	19.11	26.28	6.93	0.2	0.64
7	2003 Oct 28	X17.4	18.10	81.67	20.38	3.7	3.3
8	2003 Nov 2	X8.3	22.10	34.76	10.60	0.3	2.6
9	2003 Nov 4	X28.0	>18.0	>82.74	>20.54	15.0	34.0
10	2005 Sep 7	X17.0	18.10	82.0	20.43	6.1	4.98

[a] Average temperature at the peak of emission of soft X-rays.
[b] Emission measure of the thermal plasma. [c] Peak thermal energy of the plasma.
[d] Neutron emission at 100 MeV. [e] Total energy release of solar neutrons.

Chapter 7

Conclusions

Solar neutrons have been detected on the ground by the traditional Neutron Monitor (NM) and the Solar Neutron Telescope (SNT). The former records the cosmic ray intensity and the latter is dedicated to detect solar neutrons. Thus far, 10 solar neutron events associated with large solar flares have been successfully observed with high statistical significance by these detectors. These events were detected whenever significant enhancements were observed in the data and then they were attributed to solar neutrons. Different criteria were applied to obtain these events, therefore a systematic search for solar neutrons has not been executed so far.

In this work a systematic method was developed to search for solar neutrons associated with the emission of soft X-rays during solar cycle 24. The search was performed in two campaigns. The first campaign considered three years of observation (January 2010-August 2013) of the Chacaltaya NM. This detector is more efficient to detect solar neutrons among the other detectors considered in this study. In this campaign the onset of solar flares classified as greater than M1.0 was considered as the most probable production time of solar neutrons. The second campaign considered the Chacaltaya NM and the detectors from the SNT network. Solar neutrons were searched with the collected data by these detectors during five years (January 2010-December 2014). The maximum intensity time (peak time) of solar flares classified as greater than X1.0 was considered as an indicator of solar neutrons. In both campaigns, a criterion to determine a significant signal was set at the 3σ level. In both searches no statistically significant and positive excesses attributable to solar neutrons were found.

Although no solar neutron event was obtained, the upper limit of detection was determined for 35 X-class flares. As the production tendency of solar neutrons, a power-law shaped energy spectrum with differential power law indices of 3, 5 and 7 was assumed. The upper limits were compared with the neutron emissions of the past successful detections done in cycles 21, 22 and 23. The soft X-ray integrated flux for the flares which produced solar neutrons during solar cycles 21 and 22 was not available in the GOES database. Therefore, the six solar neutron events of solar cycle 23 are only considered. In addition, the total energy release of neutrons was calculated for each of the studied events. The soft X-ray radiated energy (1-8Å) and the peak thermal energy, which is the total energy content at the peak area of the soft X-ray emission in the 1-8Åand 0.5-4Å bands, were determined to make energy budget comparisons between these two types of emission.

A re-calculation of the neutron emission for the 2005 September 7 solar neutron event by using the Chacaltaya NM data was performed. The obtained result is 7.33×10^{27}[/MeV/sr]. The result calculated by Sako et al. (2006) is 6.1×10^{27}[/MeV/sr]. The first calculation involved an integration between 70 MeV to 1 GeV ($\sim$15 min of data) and power law index equal to -3, whereas the latter considered an integration between 100 MeV to 400 MeV, the first 7 minutes after the peak time of the soft X-ray flux and power law index of -3.8. This calculation was performed to test the analysis method in the case a real signal due to solar neutrons were detected.

To follow, the consequences of the estimated upper limits are summarized in two groups:

1. Consistency of the results:
   - The solar neutron emissions of the 35 studied flares are consistent, within the order of magnitude, with that of the successful detection of solar neutrons obtained in solar cycles 21, 22 and 23.
   - In the most stringent upper limit, the total energy release of solar neutrons is at most two orders of magnitude lower than the peak thermal energy.
   - In the least stringent upper limit, the total energy release of solar neutrons is at most five orders of magnitude lower than the peak thermal energy.
   - The total energy release of solar neutrons for the successful detections observed during solar cycles 21, 22 and 23 range from 10^{-6} to 10^{-3} of the peak thermal energy.
2. Energy budget of the considered emissions:
   - The total energy release of solar neutrons may not exceed the 0.1% of the radiated energy of soft X-rays.
   - The total energy release of solar neutrons may not exceed the 0.01% of the peak thermal energy.
   - To produce a solar neutron signal, solar flares might have to generate at least 5×10^{30}[erg] of peak thermal energy.

These results are subjected to the sensitivity of the detectors (SNTs and NM). More efficient detectors might modify the scenario.

Appendix A

Candidate events

In Chapter 5 solar neutrons were searched by using the SNTs and the Chacaltaya NM. The search was performed during the rising and maximum intensity period of solar cycle 24. Based on the statistical analysis no significant and positive excess was attributed to solar neutrons. However, one of the SNTs, the Yangbajing SNT (YACH) registered significant enhancements at four of its energy threshold levels.
In addition to the searches described in Chapters 4 and 5, a search for solar neutrons was performed during the maximum period of solar cycle 24, i.e. 2013 October to 2014 October. This search was performed assuming that during the maximum activity, solar flares will occur more frequently. In this case flares classified by GOES as greater than M5.0 were examined. The same method of analysis described in Chapter 4 is considered. One of the detectors (the Bolivia SNT) registered a statistical significance greater than the significance level in all of its energy threshold levels.
In this Chapter, an statistical analysis of the Yangbajing and the Chacaltaya candidate events is described. A possible explanation is also provided.

A.1 Search for solar neutrons during the maximum period of solar cycle 24

The search for solar neutrons is focused during the period of maximum activity of solar cycle 24, which runs from October 2013 to October 2014. During this period a search for solar neutrons associated with M- and X-class flares is performed. According to the GOES database, more than 41 solar flares classified as greater than M5.0 were recorded. The maximum intensity time (peak time) of those flares are considered as the most probable time for neutron production.
Ground observation was carried by the SNTs and the Chacaltaya NM. Due to the location of each SNT, some limitations are considered. These are, at the peak time, the zenith angle and the line-of-sight air mass to the Sun must be less than 65° and 1000 g/cm^2 respectively. With these considerations, the final flare sample consists of 13 M-class (>M5.0) and 16 X-class flares.
In table A.1 the analyzed events are listed. In columns 2, and 3 describe the onset and the peak time of the X-ray intensity respectively. In column 4, the flare class according to GOES. Columns 5 and 6 describe the flare position and region respectively. Column 7 shows the SNT location, column 8 displays the peak time (t_0) of the X-ray intensity in local time. Columns 8 and 9 show the zenith angle and the line-of-sight air mass to the Sun respectively.
Two- and three-minute time profiles of each detector were constructed for each of the flares listed in Table A.1. The Work window and signal window were set following the same procedure of Chapter 4. Significance distributions were constructed by following the method described in Chapter 4.

Table A.1: List of Soft X-ray flares observed by GOES (1-8Å) and the local time of possible observation.

	Solar Flare					Observation Site			
Date	Start (UT)	t_P[a] (UT)	Class	Position	Region	SNT[b]	t_0[c] (LT)	$\theta_\odot$[d] [deg]	Air Mass[e] [g/cm^2]
2013 Oct 24	00:21	00:30	M9.3	S10E08	1877	MKUS	14:30	47	766
2013 Oct 25	07:53	08:01	X1.7	S08E73	1882	YACH	14:01	54	830
2013 Oct 25	14:51	15:03	X2.1	S06E69	1882	SNMX	10:03	56	831
						CHBO	11:03	18	546
2013 Oct 28	04:32	04:41	M5.1	N08W71	1875	YACH	10:41	46	737
2013 Oct 29	21:42	21:54	X2.3	N08W71	1875	MKUS	11:54	34	665
2013 Nov 01	19:46	19:53	M6.3	S11E03	1884	SNMX	1353	42	678
						CHBO	15:53	52	733
2013 Nov 05	22:07	22:12	X3.3	S12E46	1890	MKUS	12:12	36	676
2013 Dec 31	21:45	21:58	M6.4	S16W35	1936	MKUS	11:58	43	729
2014 Jan 1	18:40	18:52	M9.9	S14W47	1936	SNMX	12:52	42	681
						CHBO	14:52	33	587
2014 Jan 07	18:04	18:32	X1.2	S15W11	1944	SNMX	12:32	41	674
						CHBO	14:32	27	567
2014 Jan 30	15:48	16:11	M6.6	S13E58	1967	CHBO	12:11	8	540
2014 Feb 25	00:39	00:49	X4.9	S12E82	1990	MKUS	14:49	44	733
2014 Mar 12	22:28	22:34	M9.3	N15E78	1996	MKUS	12:34	23	625
2014 Mar 29	17:35	17:48	X1.0	N11W32	2017	SNMX	11:48	19	582
						CHBO	13:48	26	564
2014 Apr 2	13:18	14:05	M6.5	N14E53	2027	GOSW	16:05	53	925
2014 Apr 18	12:31	13:03	M7.3	S20W34	2036	GOSW	15:03	40	794
2014 Apr 25	00:17	00:27	X1.3	S14W89	2035	MKUS	14:27	31	653
2014 May 08	09:59	10:07	M5.2	N08E54	2056	GOSW	12:07	33	746
2014 Jun 10	11:36	11:42	X2.2	S19E81	2087	GOSW	13:42	23	706
2014 Jun 10	12:36	12:52	X1.5	S20E89	2087	GOSW	14:52	29	724
2014 Jun 11	08:59	09:06	X1.0	S18E66	2087	GOSW	11:06	37	767
2014 Jul 08	16:06	16:20	M6.5	N12E56		SNMX	11:20	31	617
						CHBO	12:20	39	620
2014 Aug 24	12:00	12:17	M5.9	S07E75	2151	GOSW	14:17	36	764
2014 Sep 10	17:21	17:45	X1.6	N14E02	2158	SNMX	12:45	17	580
						CHBO	13:45	28	570
2014 Oct 02	18:49	19:01	M7.3	S17W82	2192	SNMX	14:01	25	596
						CHBO	15:01	41	633
2014 Oct 22	14:02	14:28	X1.6	S14E13	2192	CHBO	10:28	27	566
2014 Oct 24	21:07	21:41	X3.1	S16W21	2192	MKUS	11:41	32	659
2014 Oct 25	16:55	17:08	X1.0	S16W31	2192	SNMX	12:08	35	635
2014 Oct 27	00:06	00:34	M7.1	S14W44	2192	MKUS	14:34	49	781
2014 Oct 27	14:12	14:47	X2.0	S17W52	2192	SNMX	08:47	60	891
						CHBO	10:47	22	553

[a] GOES SXR maximum peak time. [b] Observatory where neutrons have greater possibilities.
[c] Peak time in local time. [d] Solar zenith angle at the peak time.
[e] Line-of-sight air mass at the peak time.

The Bolivia SNT registered a significant excess at four of its energy threshold levels. The implications of that enhancement are described in following sections.

A.2 Possible solar neutron events

A.2.1 The solar flare on 2013 October 25

On 2013 October 25 an X1.7-class flare was observed at S08E73 of the solar surface. According to GOES, the SXR intensity started at 07:53UT and reached a maximum at 08:01UT. At the GOES soft X-ray maximum intensity time (08:01UT), Tibet, China was suitable place to observe solar neutrons in the SNT network. The solar zenith angle and the line-of-sight air mass were 54° and 830 g/cm^2 respectively.
The same procedure described in Chapter 4 is followed to search for solar neutrons in the Tibet SNT data. Two-minute time profiles were build for the four energy threshold levels of the Tibet SNT. These are shown in Figure A.1. The work window is set between 05:52 and 10:52UT. The signal window is set between 07:45 and 08:45UT.
Significances were also determined using the same method of Chapter 5. In Figure A.2 four panels for each of the energy threshold level of the Tibet SNT are shown. In this figure, the blue histogram corresponds to the background (work window) and the black-hatched area corresponds to the signal window. Some enhancements are seen on the positive side. At the same time, there are also significant deficits on the negative side. Therefore, no further discussion is done for this event.

A.2.2 The solar flare on July 8, 2014

On 2014 July 8 an M6.5-class flare was observed at N12E56 of the solar surface. According to GOES, the soft X-ray intensity started at 16:06UT and reached a maximum at 16:20UT. The RHESSI spacecraft could not observe this flare, because it suffer from annealing, however, the SEDA-AP/FIB instrument observed a significant excess after the peak time of the SXR flux.
At the GOES SXR onset time (16:06UT), the Sun was almost at its zenith over the American continent, thus Sierra Negra, Mexico and Chacaltaya, Bolivia were suitable places to observe solar neutrons in the SNT network. The solar zenith angle and the line-of-sight air mass were 34° and 698 g/cm^2 respectively at Sierra Negra, Mexico. In Chacaltaya, Bolivia, they were 40° and 700 g/cm^2.
Following the same procedure described in Chapter 4, 2-minute time profiles are built for the Bolivia SNT and the Chacaltaya NM. Then, the work window and signal window are set at 14:36-20:36UT and 15:46-16:46UT respectively. A 15-minute moving average is calculated in the work window. Whereas, a linear interpolation is calculated in the signal window. In Figures A.3 and A.4 these profiles are shown.
The statistical significances were also calculated based on the method of Chapter 4. In Figure A.6 the significance distributions for the four energy threshold levels of the Bolivia SNT are shown. In this figure, the blue histogram corresponds to the background (work window) and the black-hatched area corresponds to the signal window. Some minor enhancements are seen on the positive side. These enhancements are also seen in the significance time profile per 2 minutes (Figure A.5). An excess greater than 3σ can be seen between 16:10 and 16:12UT in the >40 MeV with_anti channel.
In Table A.2 the statistical significances are calculated for each bin (2-minute) between 16:06 and 16:14UT. The largest enhancements are seen between 16:08 and 16:12UT, these are highlighted in blue. Assuming neutrons are produced at the onset time of soft X-rays (δ-emission), then these neutrons have energies between $\sim$446 to 179 MeV.

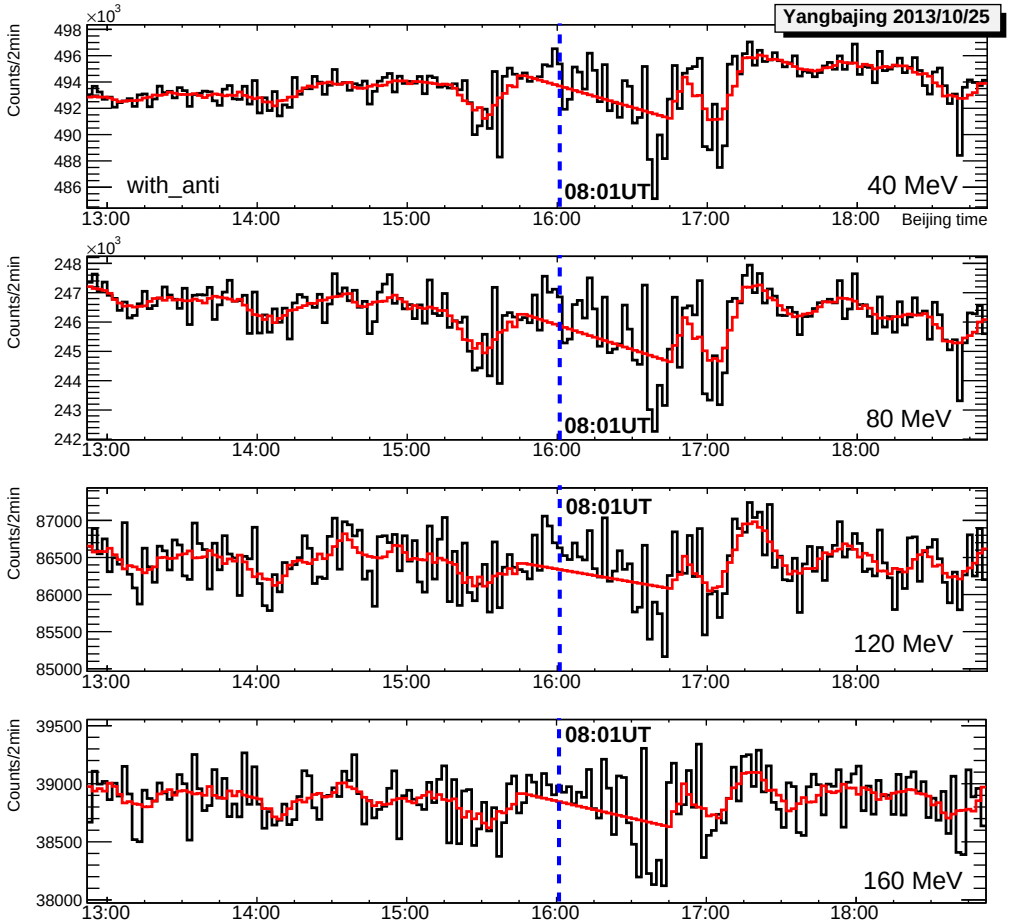

Figure A.1: 2-minute time profile of the Tibet SNT. From top, the lowest energy threshold (>40 MeV) to bottom, the highest (>160 MeV) are shown. The red solid line shows the 15-minute moving average. The blue dashed line indicates the maximum intensity time of soft X-rays observed by GOES. A linear interpolation is calculated between 07:45 and 08:45UT, which in Beijing time are 15:45 and 16:45 respectively.

Table A.2: Statistical significances for the 2014 July 8 candidate event observed by the with_anti channel of the Bolivia SNT and the Chacaltaya NM.

2-minute bin	>40 MeV	>80 MeV	>160 MeV	>240 MeV	NM-64
	enhancement in units of σ				
16:06-16:08	0.1	-1.1	-0.9	-1.0	-3.4
16:08-16:10	2.5	1.9	2.5	2.4	1.3
16:10-16:12	3.9	2.1	1.7	1.3	-0.5
16:12-16:14	1.9	0.5	1.7	1.2	1.0

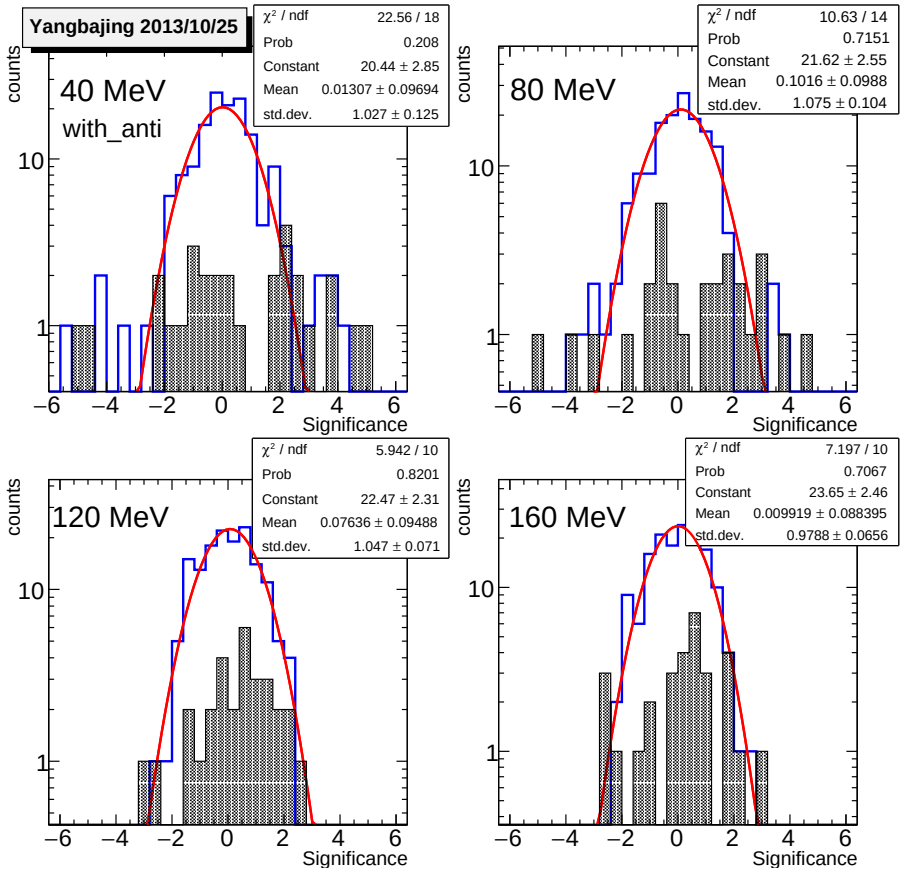

Figure A.2: Significance distributions of the Tibet SNT. The red solid line shows the adjusted Gaussian function to the background (blue solid line). The black hatched area indicates the signal window significance.

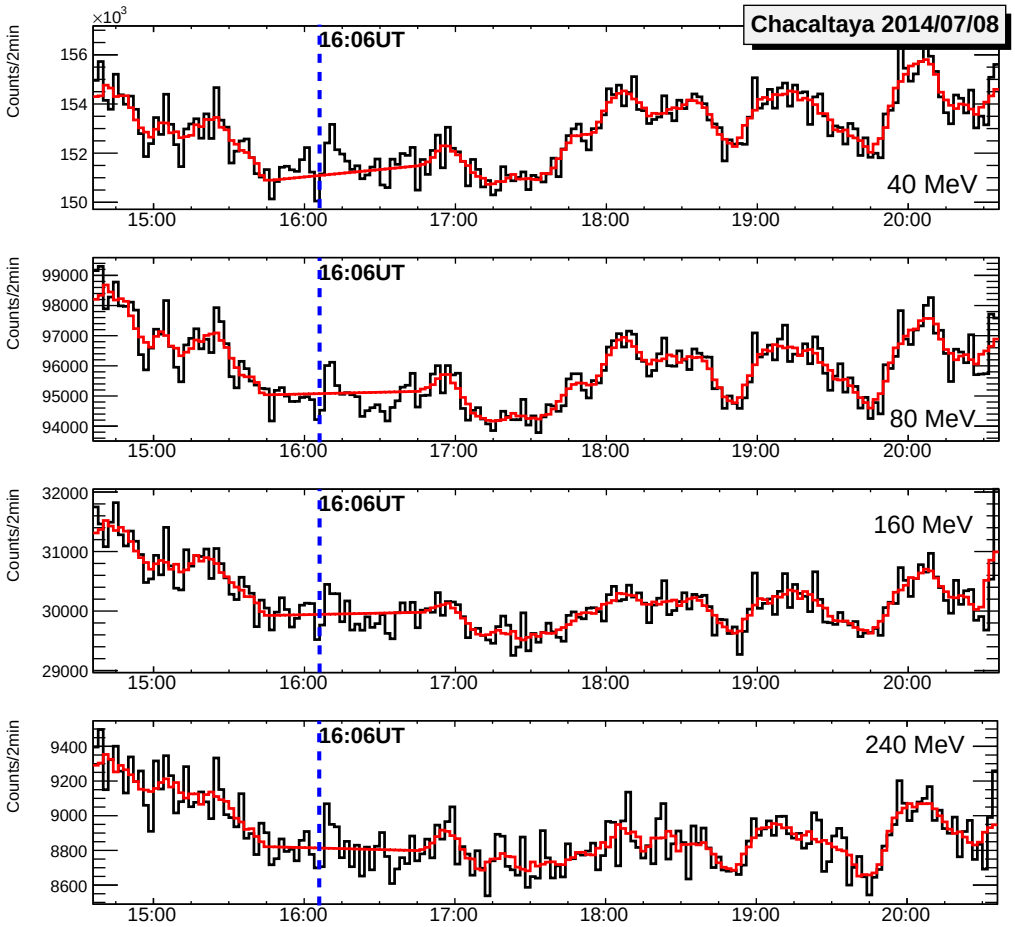

Figure A.3: 2-minute time profile of the Bolivia SNT. From top, the lowest energy threshold (>40 MeV) to bottom, the highest (>240 MeV) are shown. The red solid line shows the 15-minute moving average. The blue dashed line indicates the onset time of the X-ray intensity observed by GOES. A linear interpolation is calculated between 15:46 and 16:46UT.

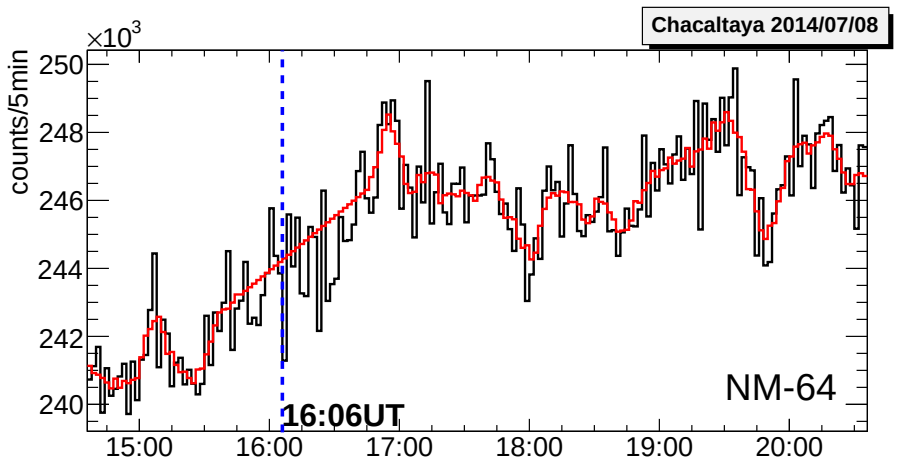

Figure A.4: 2-minute time profile of the Chacaltaya NM. The red solid line shows the 15-minute moving average. The blue dashed line indicates the onset time of the X-ray intensity observed by GOES. A linear interpolation is calculated between 15:46 and 16:46UT.

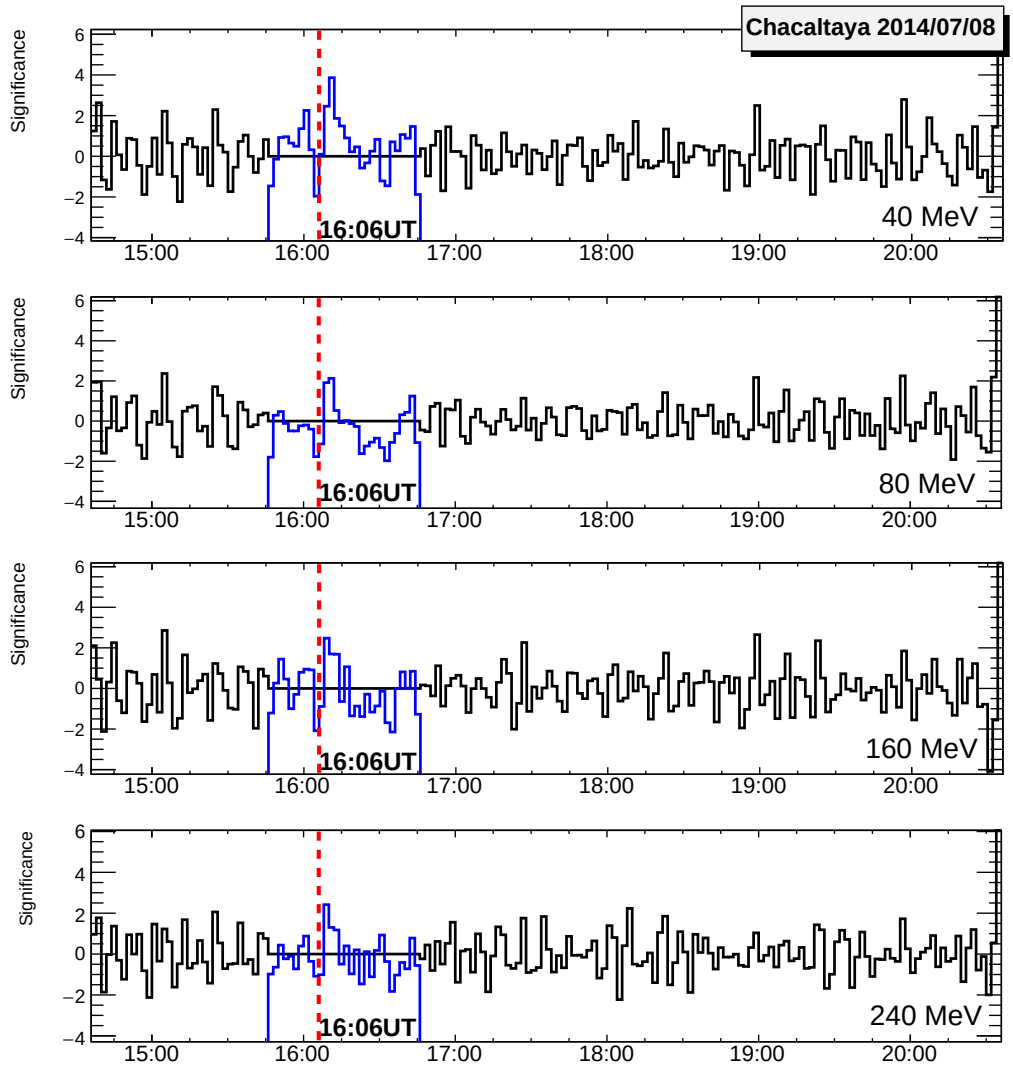

Figure A.5: 2-minute significance profile of the Bolivia SNT. From top, the lowest energy threshold (>40 MeV) to bottom, the highest (>240 MeV) are shown. The blue solid line shows the 1-hour signal window. The red dashed line indicates the onset time of the X-ray intensity observed by GOES.

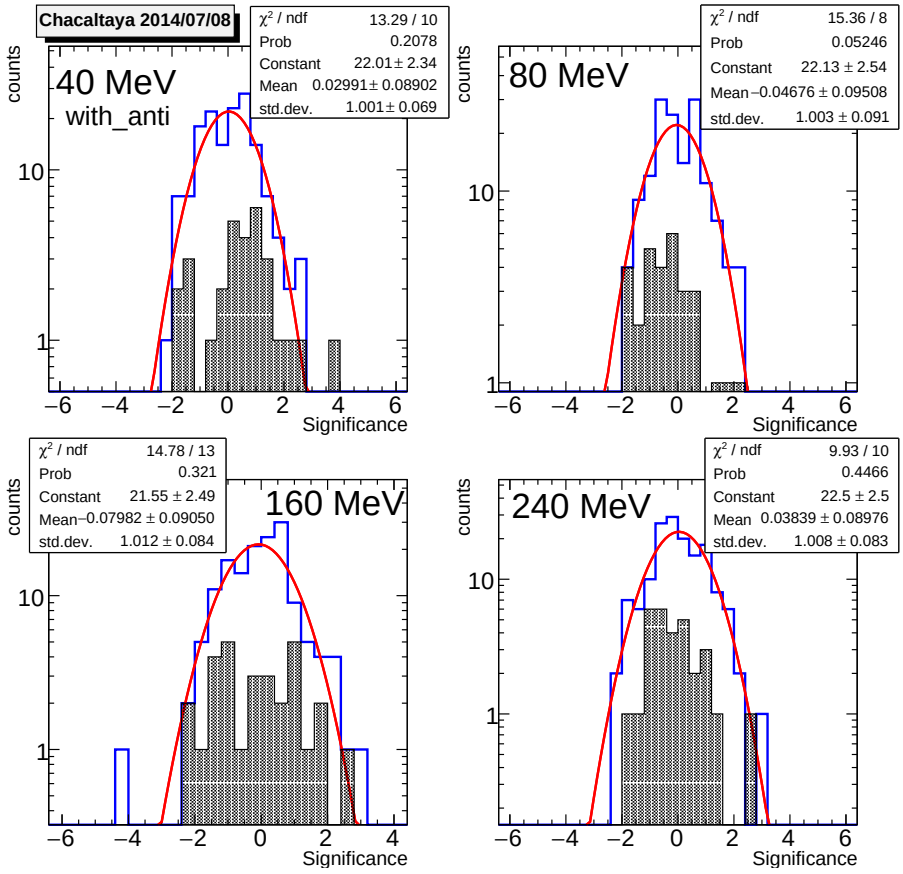

Figure A.6: Significance distributions of the Bolivia SNT. The red solid line shows the adjusted Gaussian function to the background (blue solid line). The black hatched area indicates the signal window significance.

Muraki et al. (2016) also examined this event. They considered not only the ground-based detectors (Sierra Negra, Mexico and Chacaltaya, Bolivia) but also the data from the SEDA-AP/FIB instrument attached to the ISS. To determine the significance of the Bolivia SNT, they considered the without_anti channel as background. The results are summarized in Table A.3.

Table A.3: Statistical significances for the 2014 July 8 candidate event observed by the Bolivia SNT. Adapted from Muraki et al. (2016).

Time	>40 MeV	>80 MeV	>160 MeV	>240 MeV
	enhancement in units of σ			
16:07-16:13	6.2	7.2	6.0	4.9
16:37-16:43	2.4	4.9	3.8	1.6
16:45-16:57	4.9	8.1	5.8	5.5

A.3 Discussion

In this Chapter an initial analysis of the two candidate events found in two search campaigns was discussed. Significances greater than the 3σ, the criterion to identify a solar neutron signal, were found. However, this significances are not consistent in all the energy threshold levels of the Tibet SNT and the Bolivia SNT. It is clear a further rigorous analysis and Montecarlo simulation are needed to completely assess the significance of the apparent enhancement observed in both events. Nevertheless, for this two candidate events, upper limits were determined based on the method described in Chapter 6. These numbers are shown in Table A.4.

Thus far, the successfully detected solar neutron events in solar cycles 21, 22 and 23 were associated with large solar flares, >X1.0-class. The 2014 July 8 solar neutron event could be the first of its kind which is associated to an M6.5-class flare. If this is right, then the flare intensity would not be related to the possibility to produce solar neutrons. Although this event and the associated M6.5-flare could be exceptional.

Table A.4: Estimated neutron emissions for two candidate events.

Date	Flare class	SNT location	Threshold energy	Upper Limit‡	$C^{\ell}\times10^{27}$ [/MeV/sr]
2013 October 25	X1.7	Tibet	>40 MeV	8800.94	19.83
2014 July 8	M6.5	Chacaltaya	>40 MeV	7776.00	6.90

‡ Upper limit of detection. $^{\ell}$ Neutron emission at 100 MeV.

Appendix B

GOES Light-curves of thirty five X-class flares

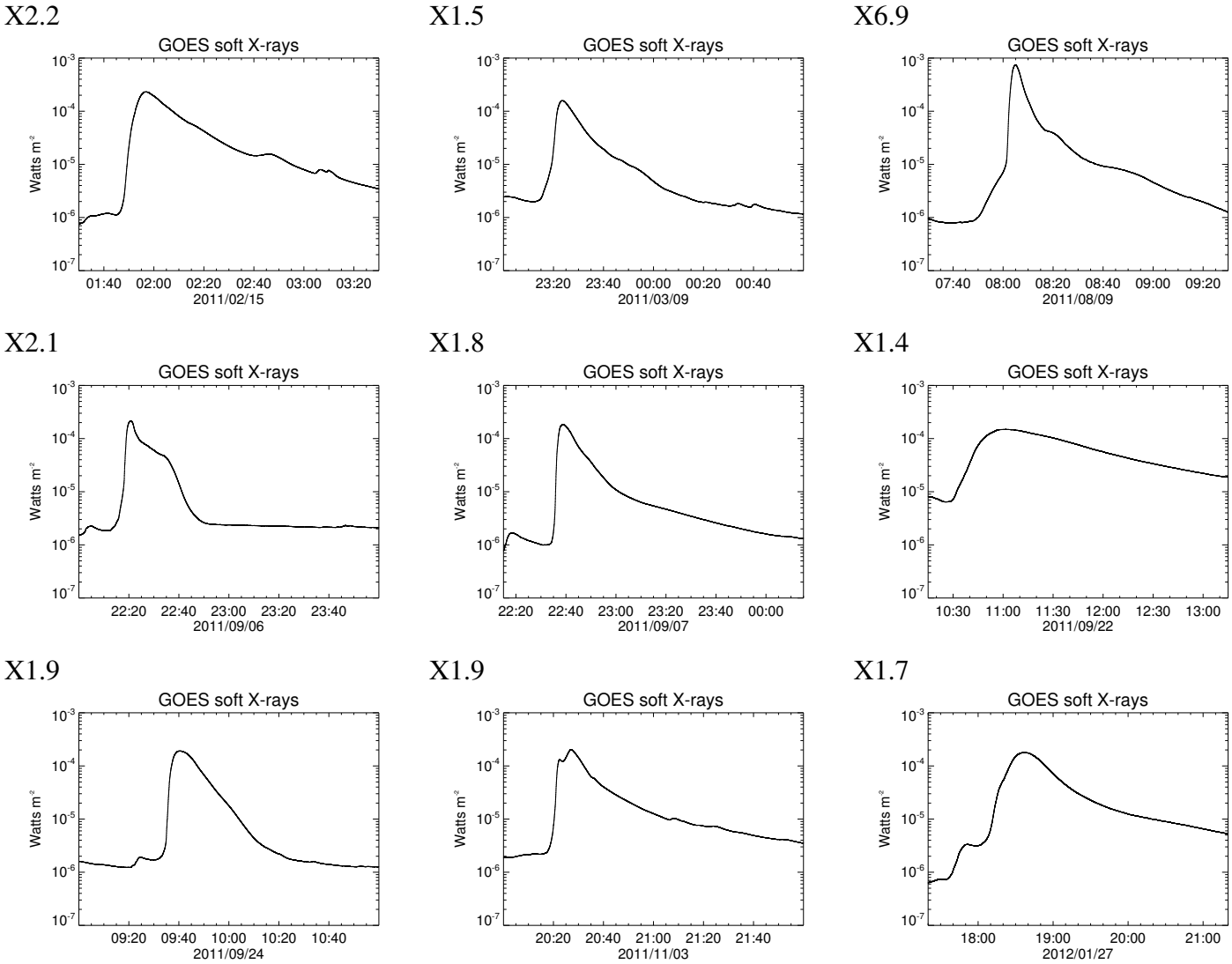

Figure B.1: Solar flares

X1.1

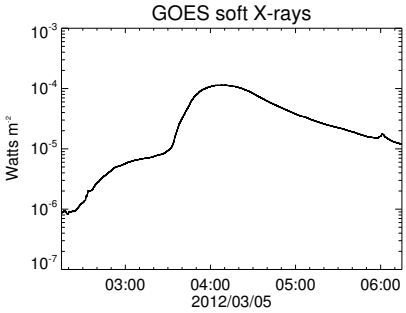

X5.4 and X1.3

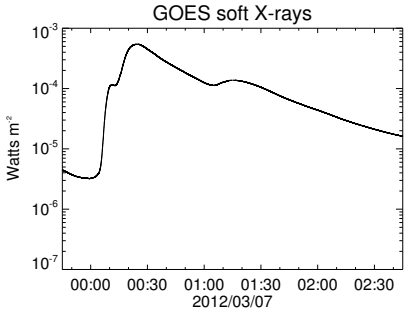

X1.4

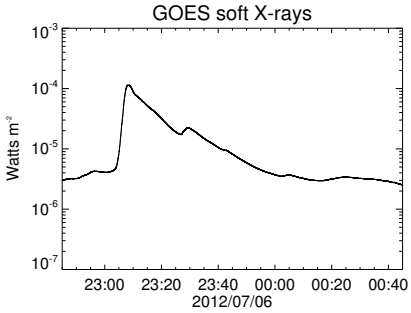

X1.4

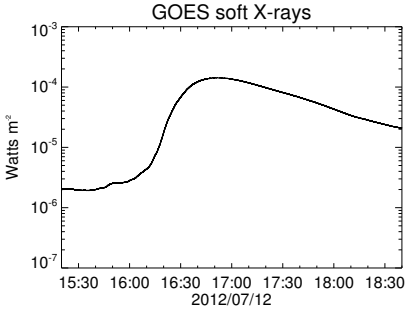

X1.7

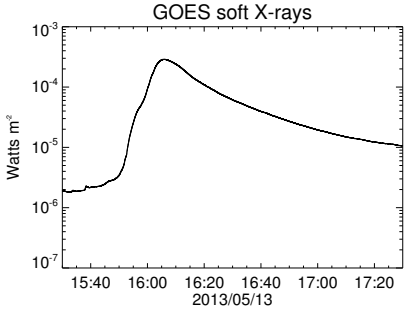

X2.8

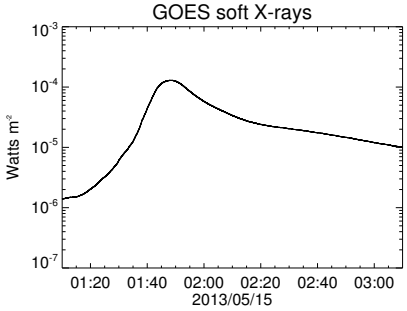

X1.7

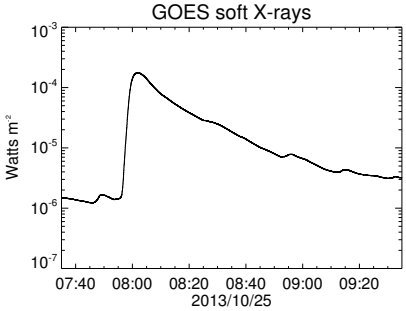

X2.1

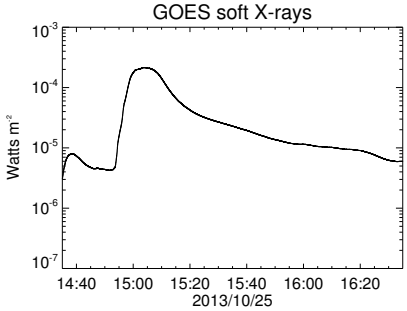

X2.3

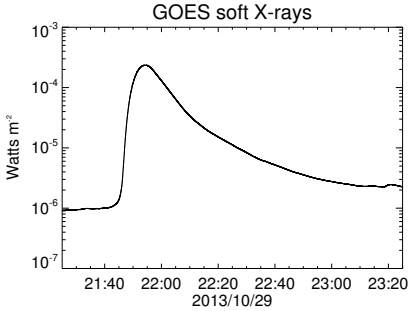

X3.3

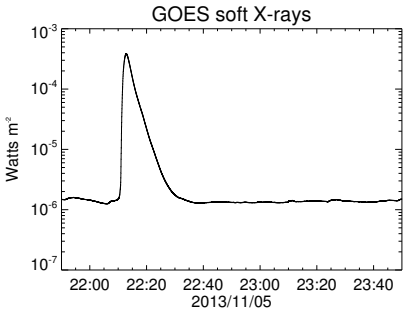

X1.2

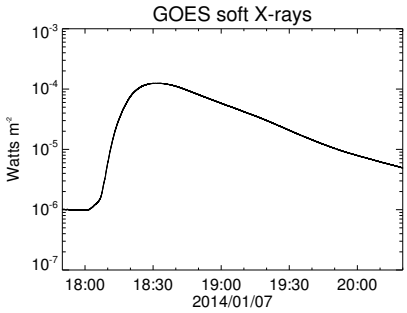

X4.9

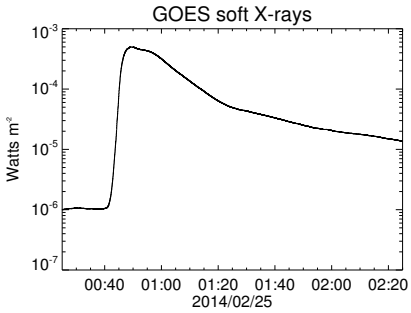

X1.0

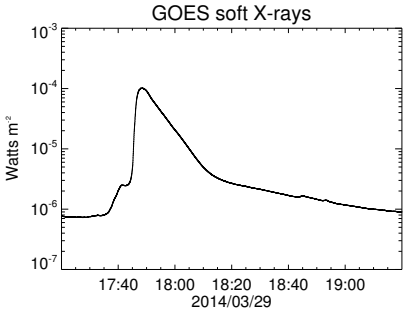

X1.3

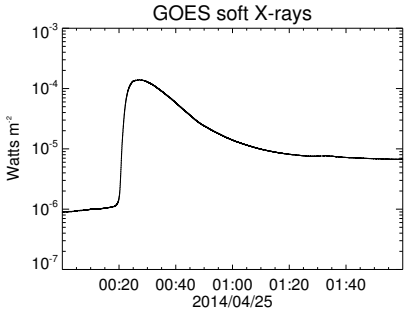

X2.2 and X1.5

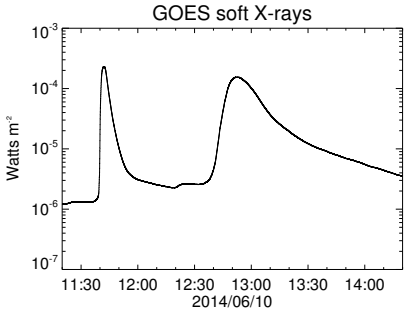

X1.0

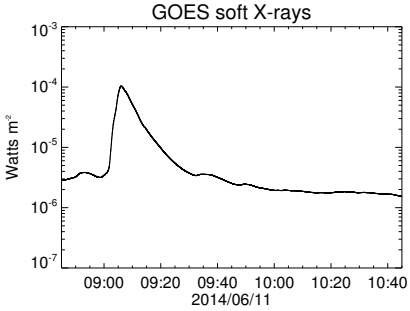

X1.6

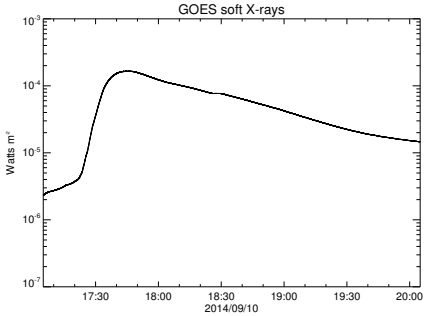

X1.6

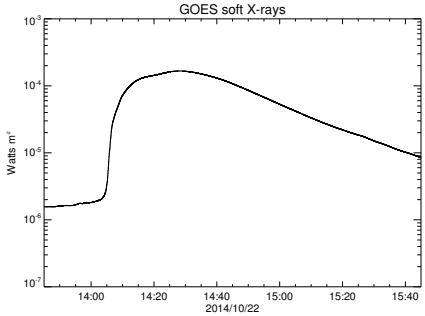

X3.1

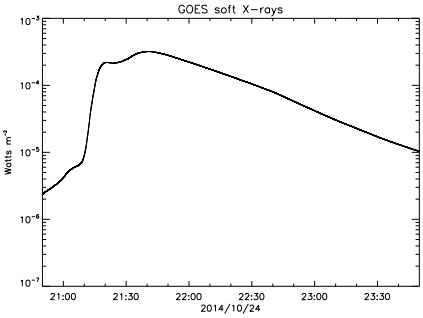

X1.0

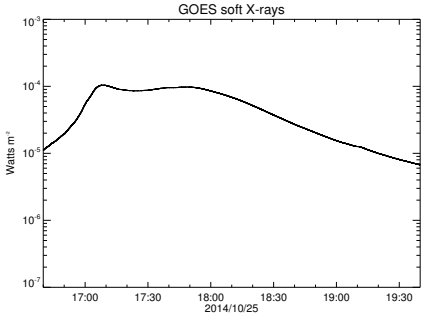

X2.0

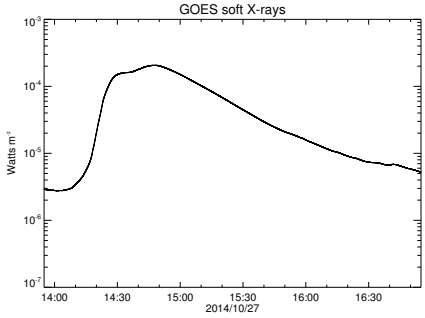

X1.6

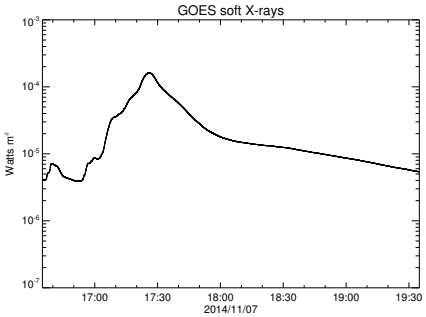

X1.8

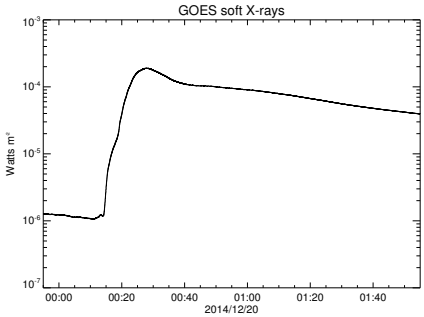

Appendix C

Significance distributions of thirty-five flares

In this chapter, the time profile and significance distributions for the thirty-five studied X-class flares are shown. The soft X-ray light-curves for these flares are also shown.

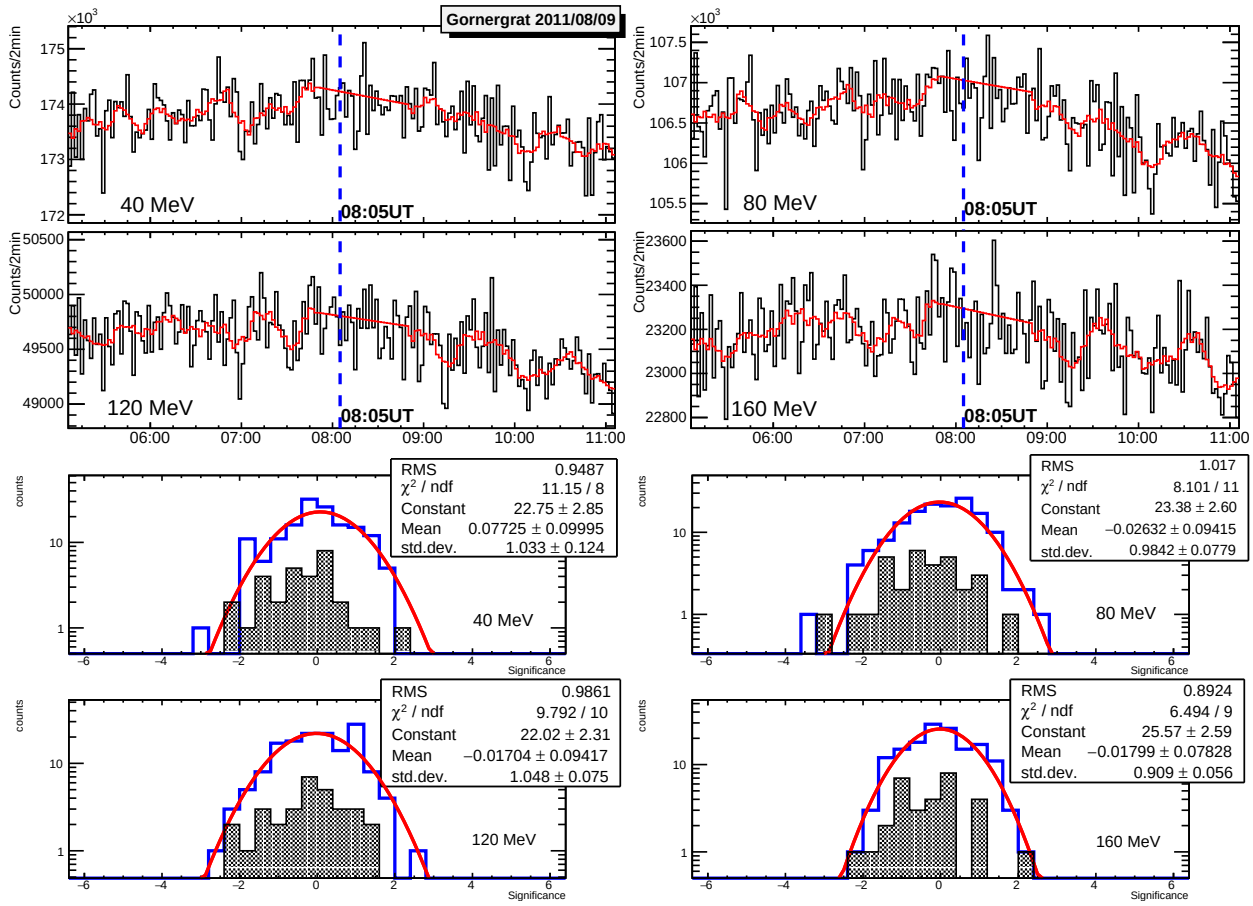

Figure C.1: 2-min time profiles and statistical significances for the four different channels of GOSW for the X6.9 (2011/08/09) flare.

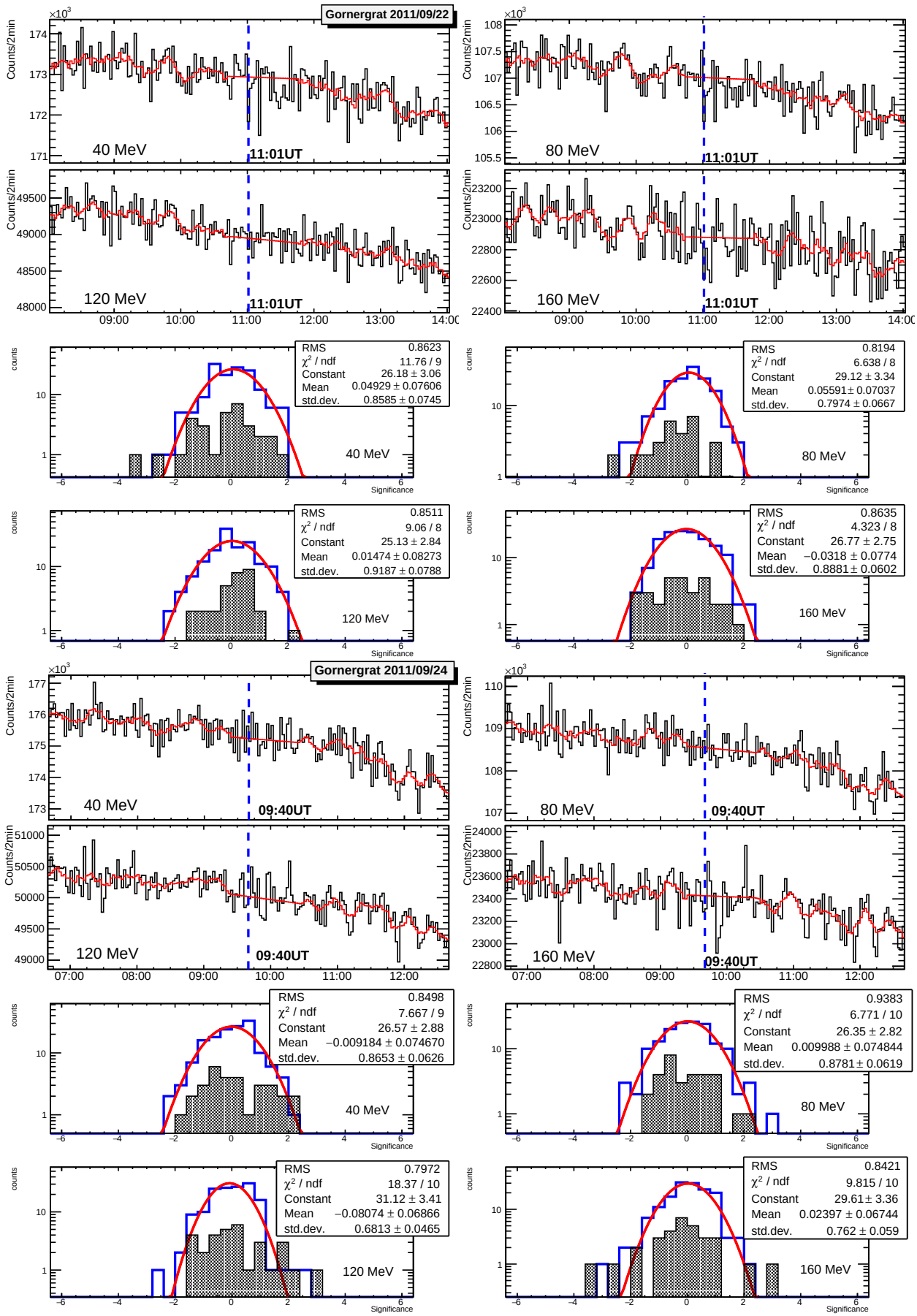

Figure C.2: 2-min time profiles and statistical significances for the four different channels of GOSW for the X1.4 (2011/09/22) and X1.9 (2011/09/24) flares.

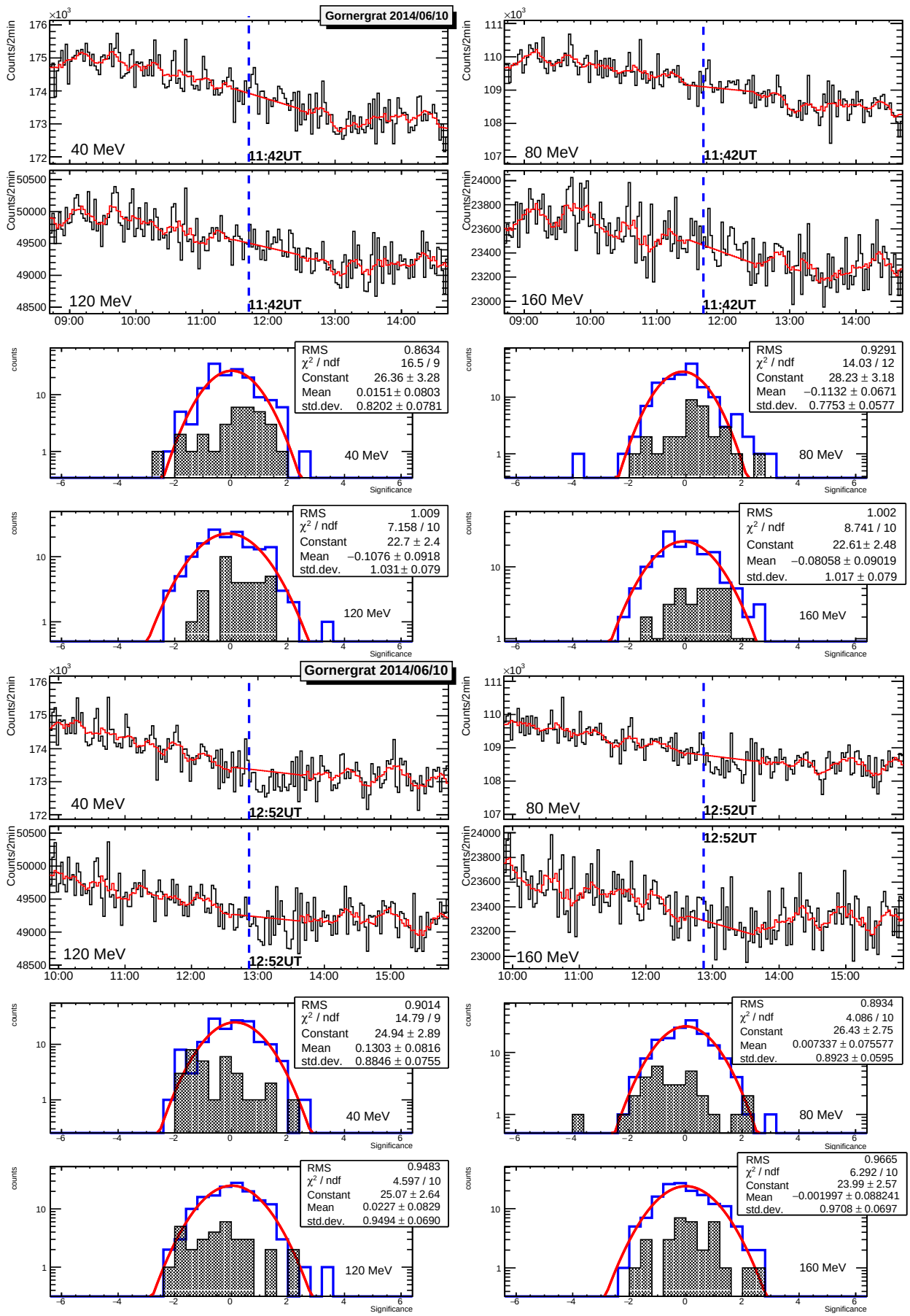

Figure C.3: 2-min time profiles and statistical significances for the four different channels of GOSW for the X2.2 (2014/06/10) and X1.5 (2014/06/10) flares.

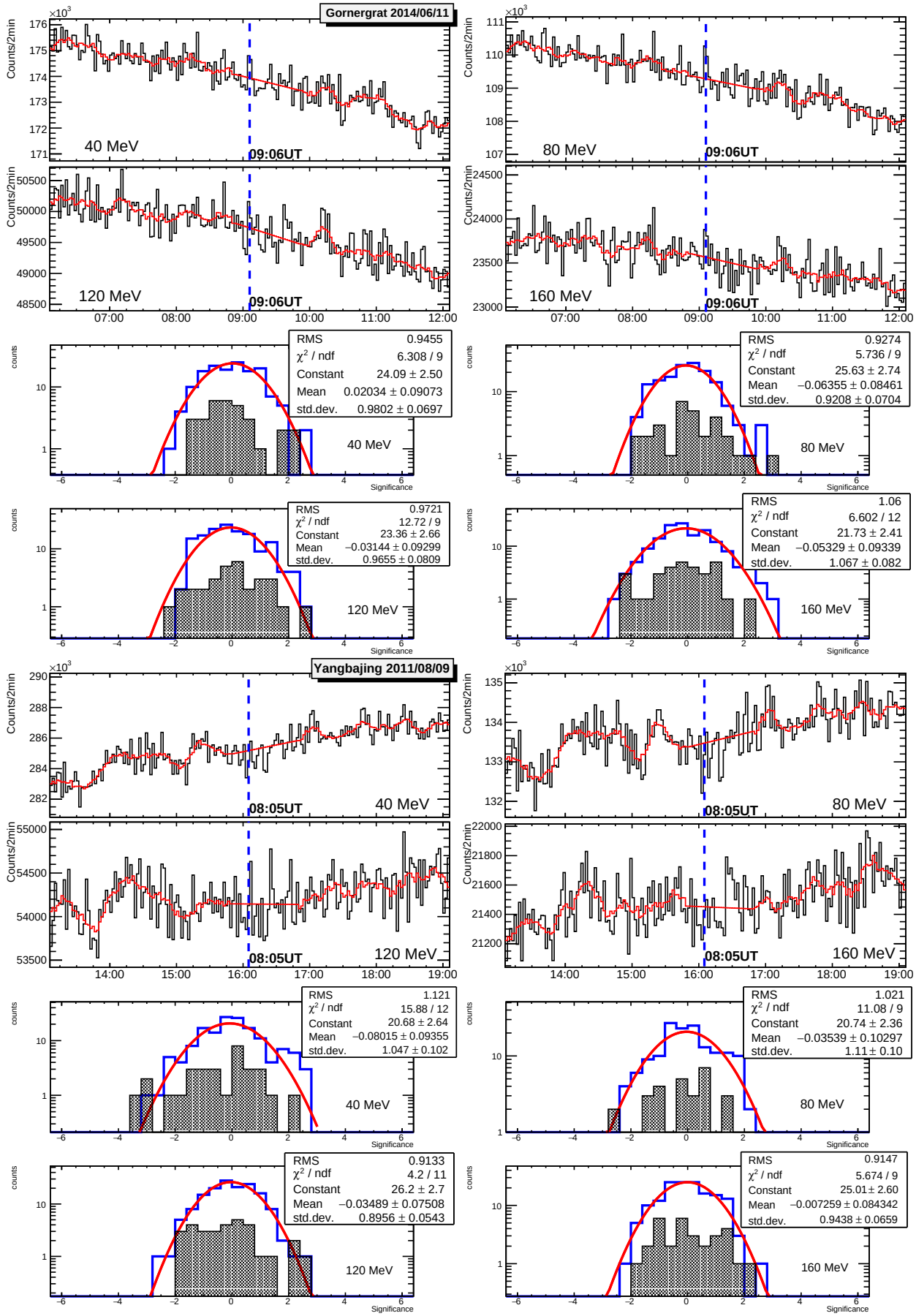

Figure C.4: 2-min time profiles and statistical significances for the four different channels of GOSW and YACH for the X1.0 (2014/06/11) and the X6.9 (2011/08/09) flares respectively.

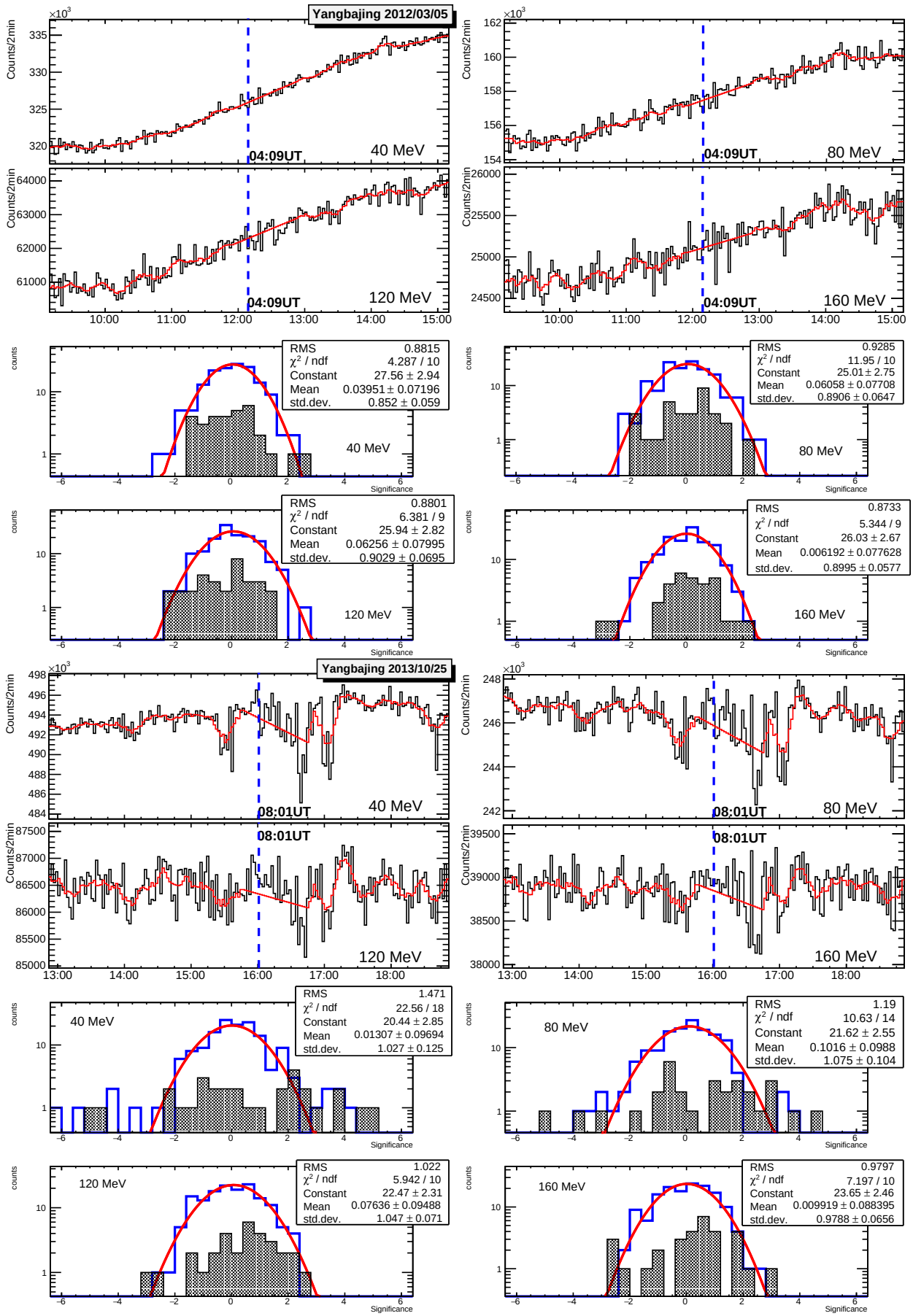

Figure C.5: 2-min time profiles and statistical significances for the four different channels of YACH for the X1.1 (2012/03/05) and X1.7 (2013/10/25) flares.

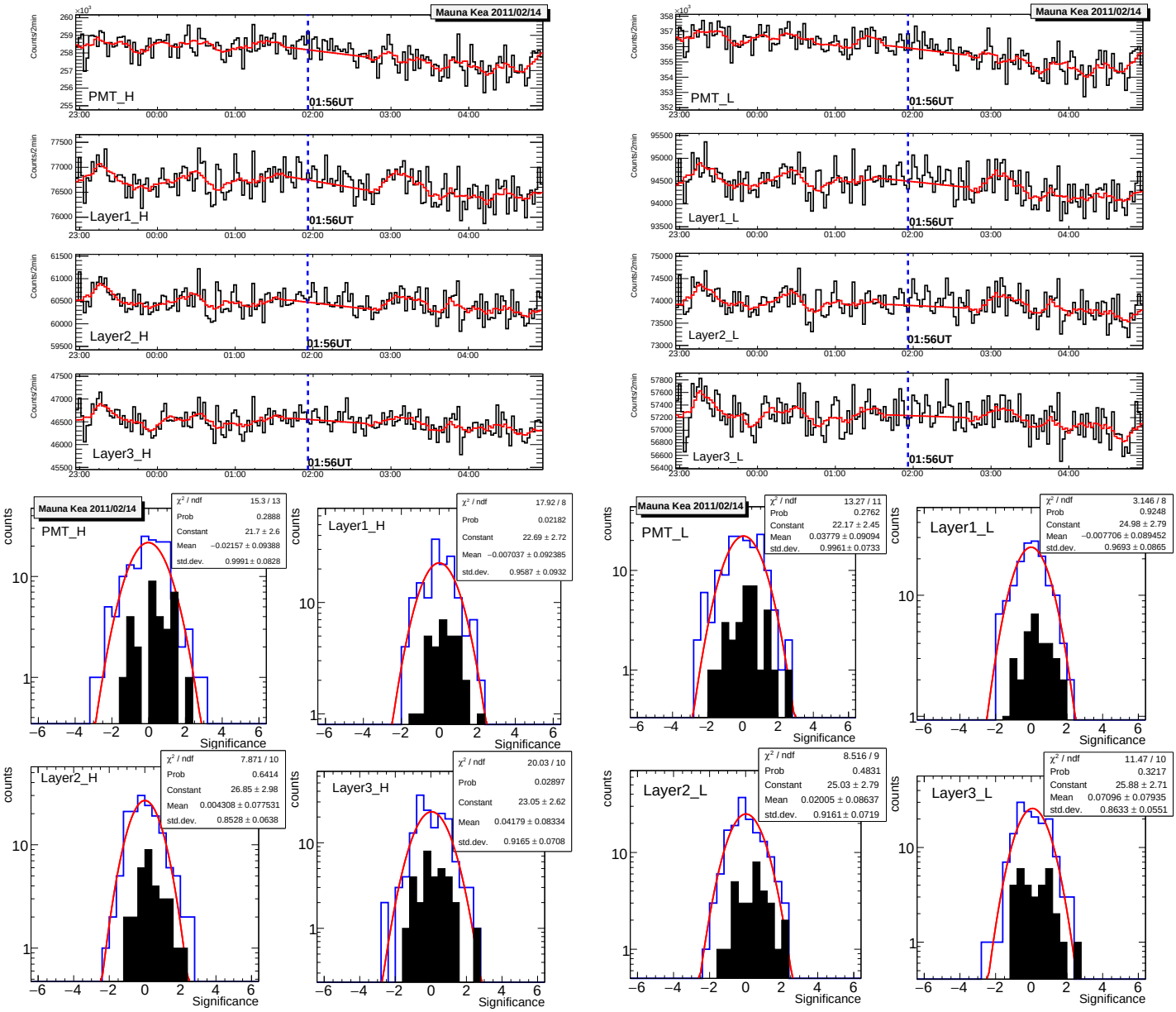

Figure C.6: 2-min time profiles for the MKUS detector on 2011 February 15

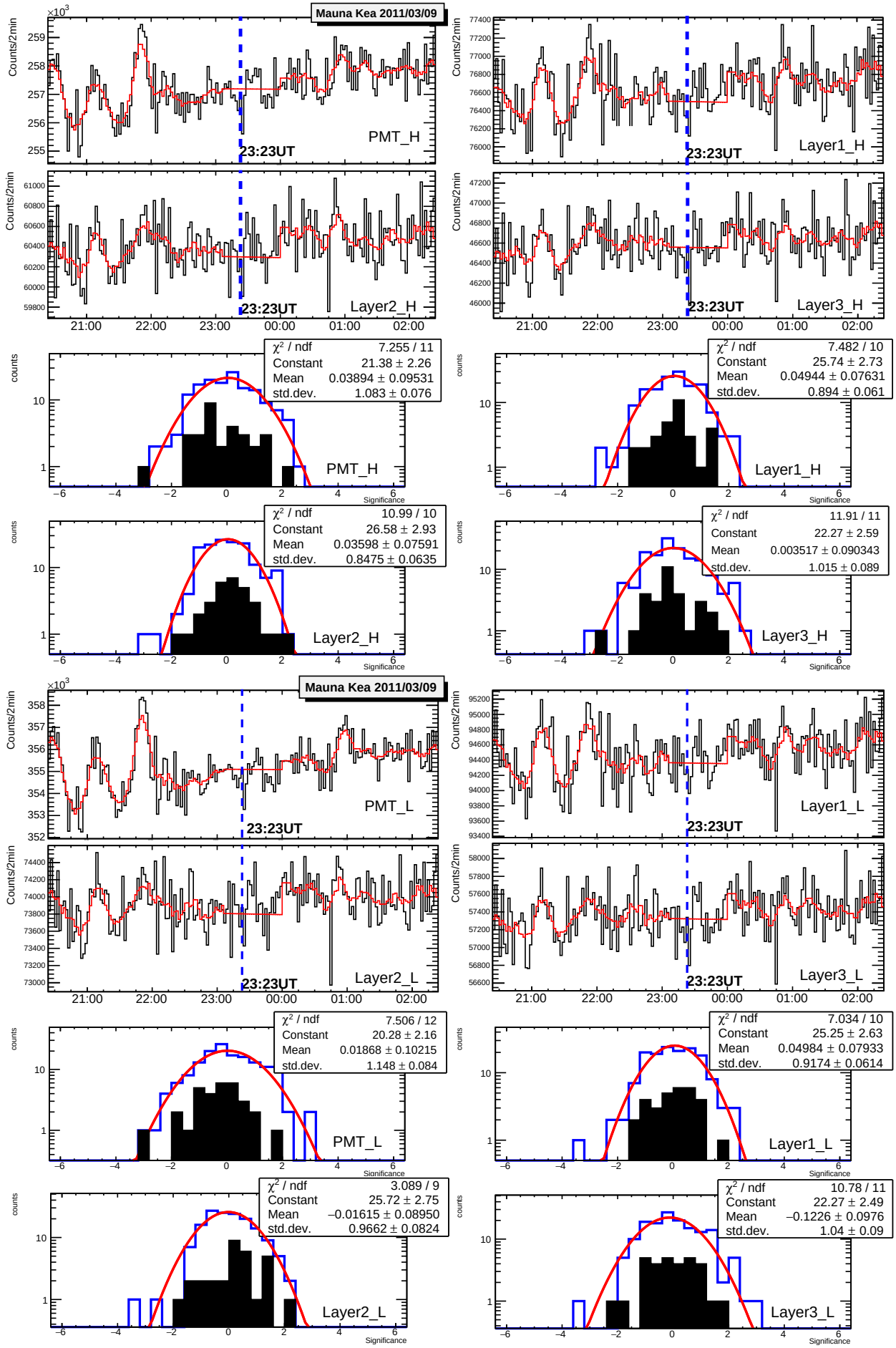

Figure C.7: 2-min time profiles and statistical significances for the eight different channels of MKUS for the X1.5-class flare on 2011 March 9. The top 8 panels correspond to the highest energy threshold (>20 MeV). The bottom 8 panels correspond to the threshold energy of >12 MeV.

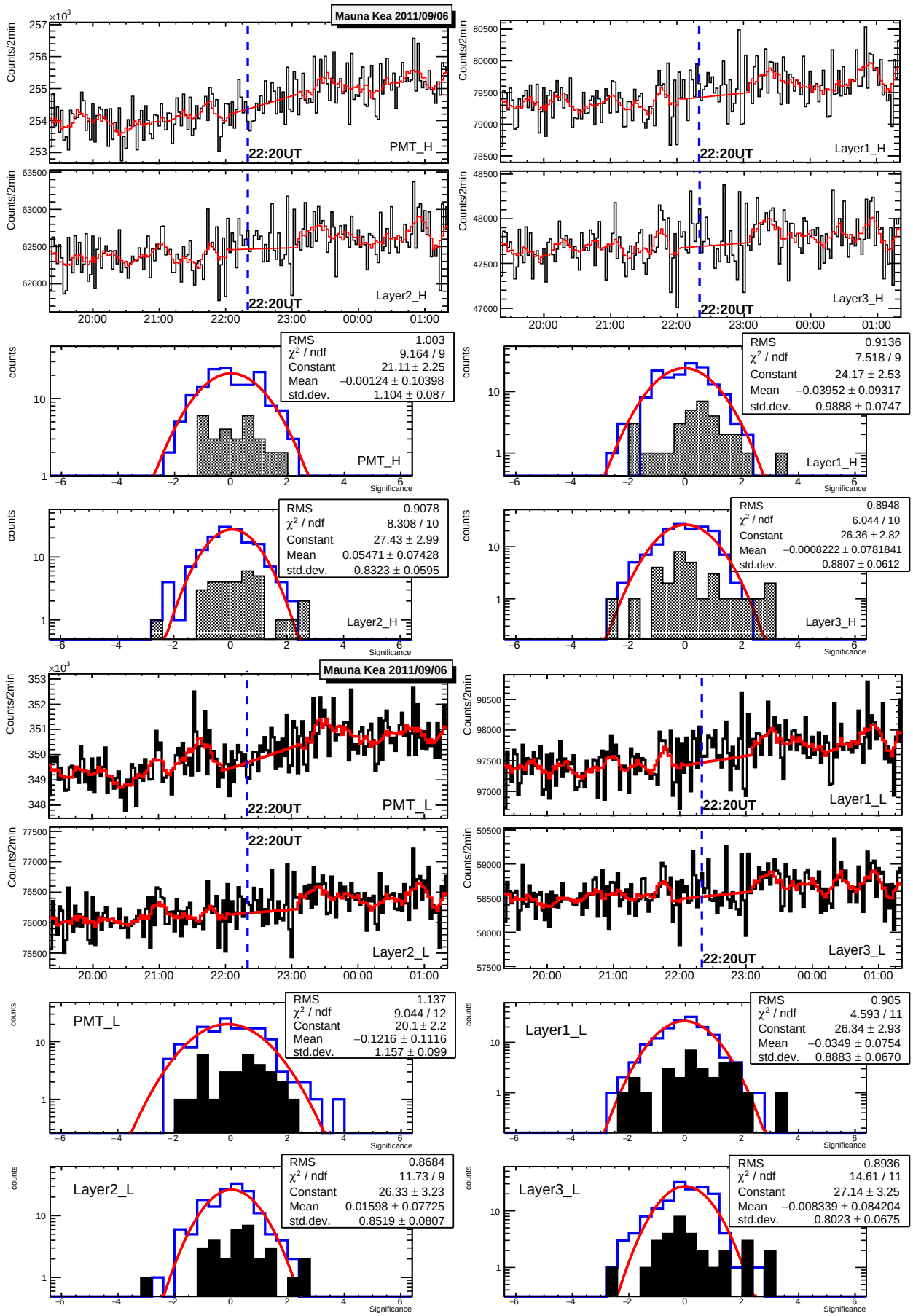

Figure C.8: 2-min time profiles and statistical significances for the eight different channels of MKUS for the X2.1-class flare on 2011 September 6. The top 8 panels correspond to the highest energy threshold (>20 MeV). The bottom 8 panels correspond to the threshold energy of >12 MeV.

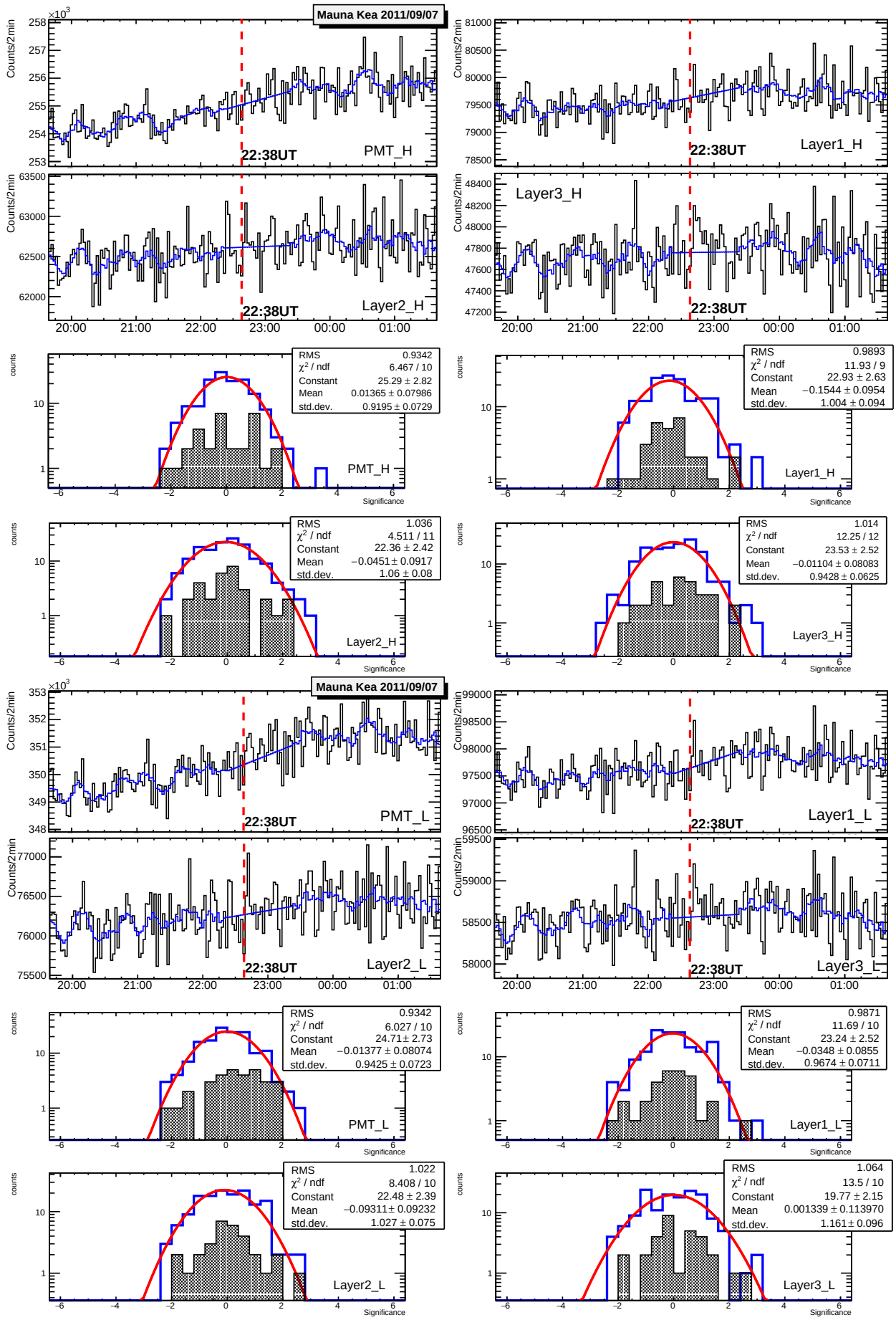

Figure C.9: 2-min time profiles and statistical significances for the eight different channels of MKUS for the X1.8-class flare on 2011 September 7. The top 8 panels correspond to the highest energy threshold (>20 MeV). The bottom 8 panels correspond to the threshold energy of >12 MeV.

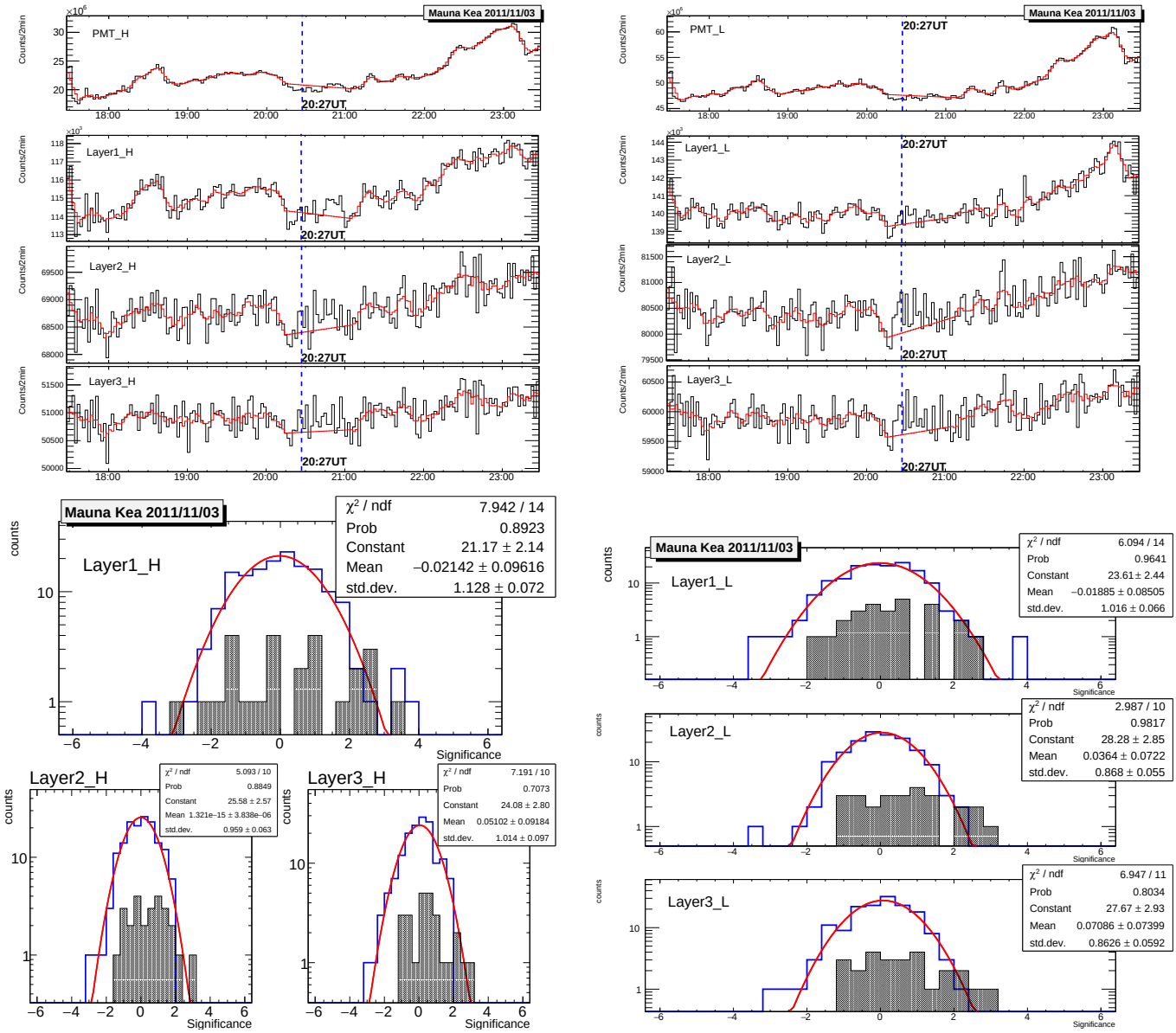

Figure C.10: 2-min time profiles for the MKUS detector on 2011 November 3

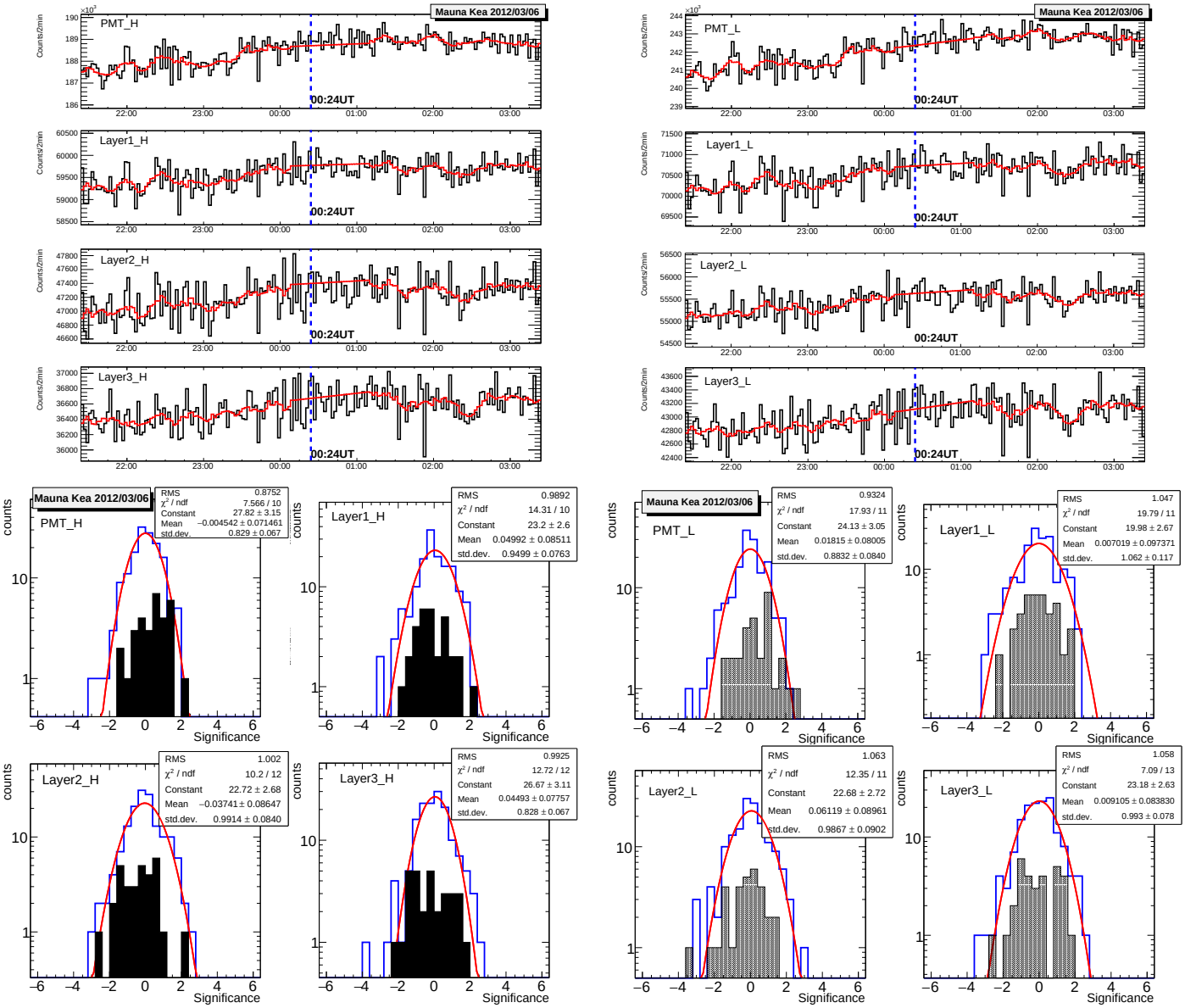

Figure C.11: 2-min time profiles for the MKUS detector on 2012 March 7

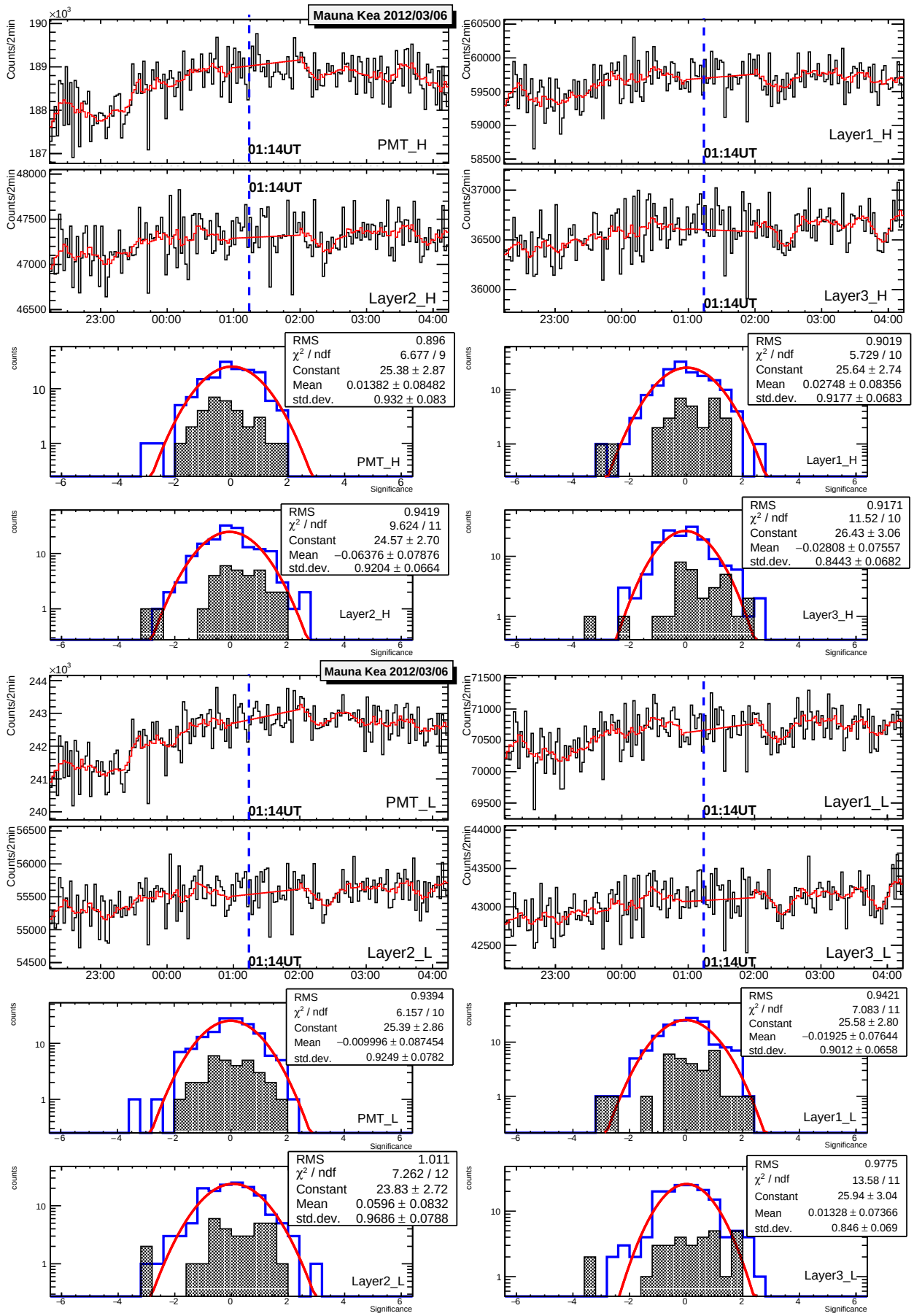

Figure C.12: 2-min time profiles and statistical significances for the eight different channels of MKUS for the X1.3-class flare on 2012 March 7. The top 8 panels correspond to the highest energy threshold (>20 MeV). The bottom 8 panels correspond to the threshold energy of >12 MeV.

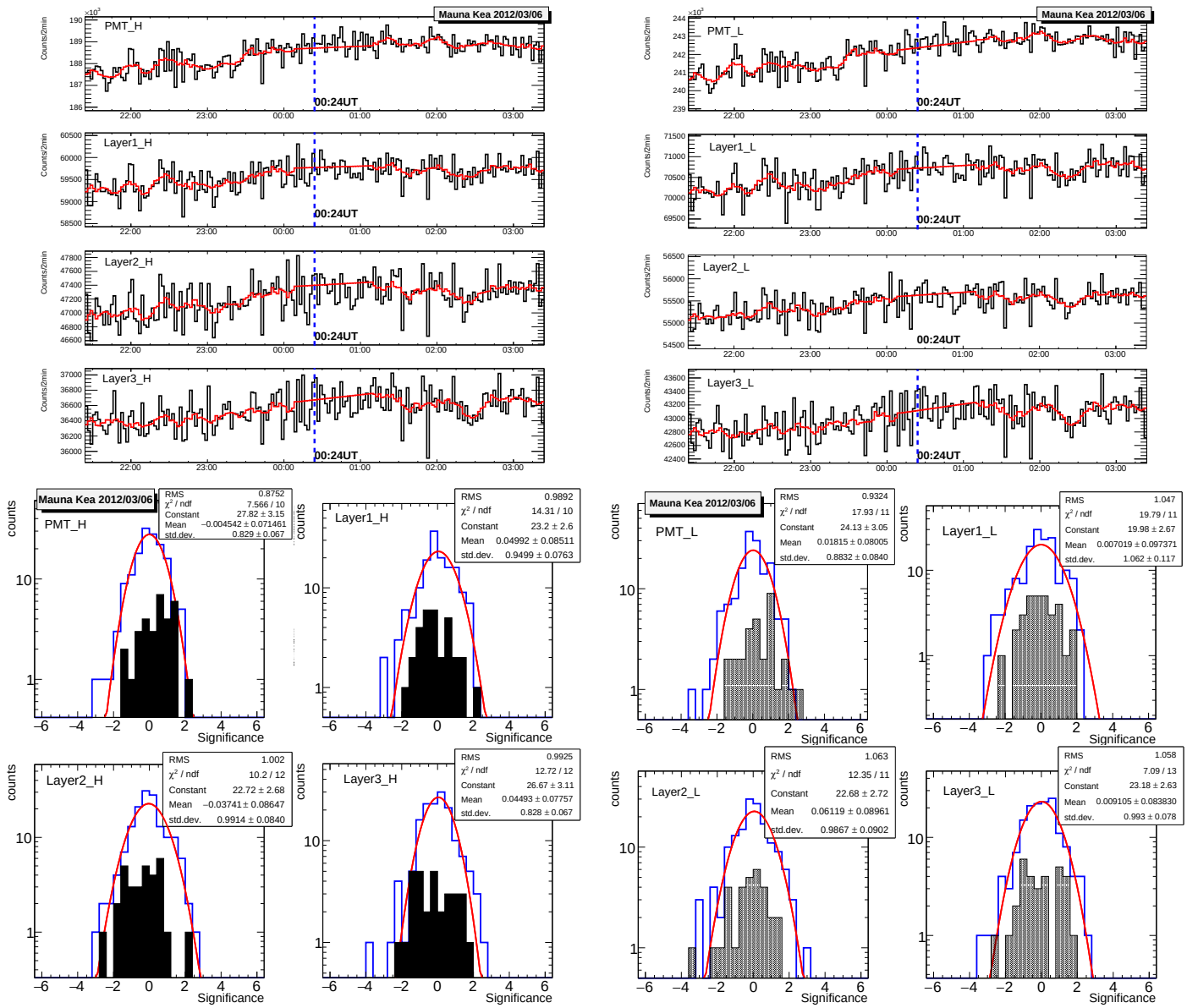

Figure C.13: 2-min time profiles for the MKUS detector on 2012 March 7

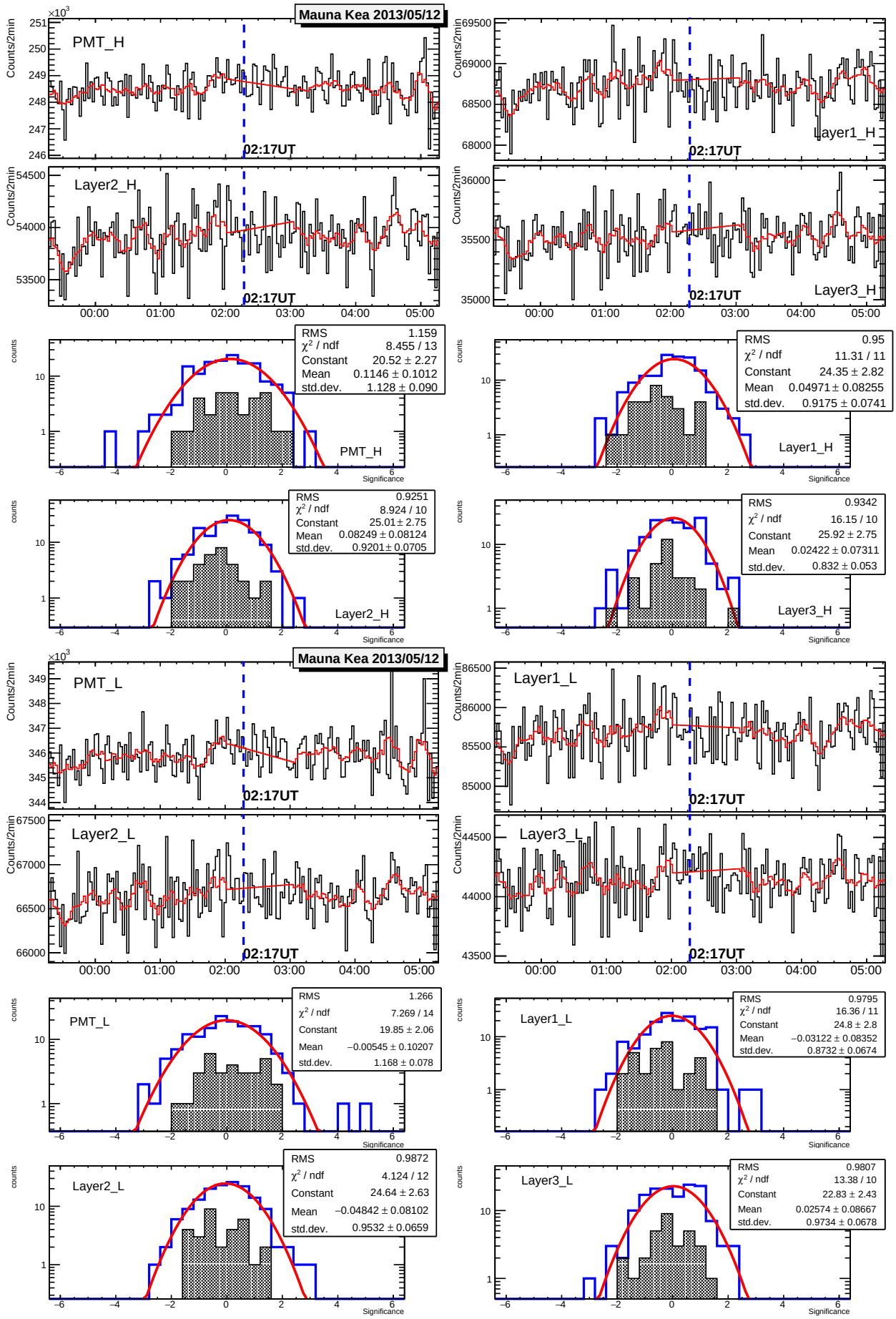

Figure C.14: 2-min time profiles and statistical significances for the eight different channels of MKUS for the X1.7-class flare on 2013 May 13. The top 8 panels correspond to the highest energy threshold (>20 MeV). The bottom 8 panels correspond to the threshold energy of >12 MeV.

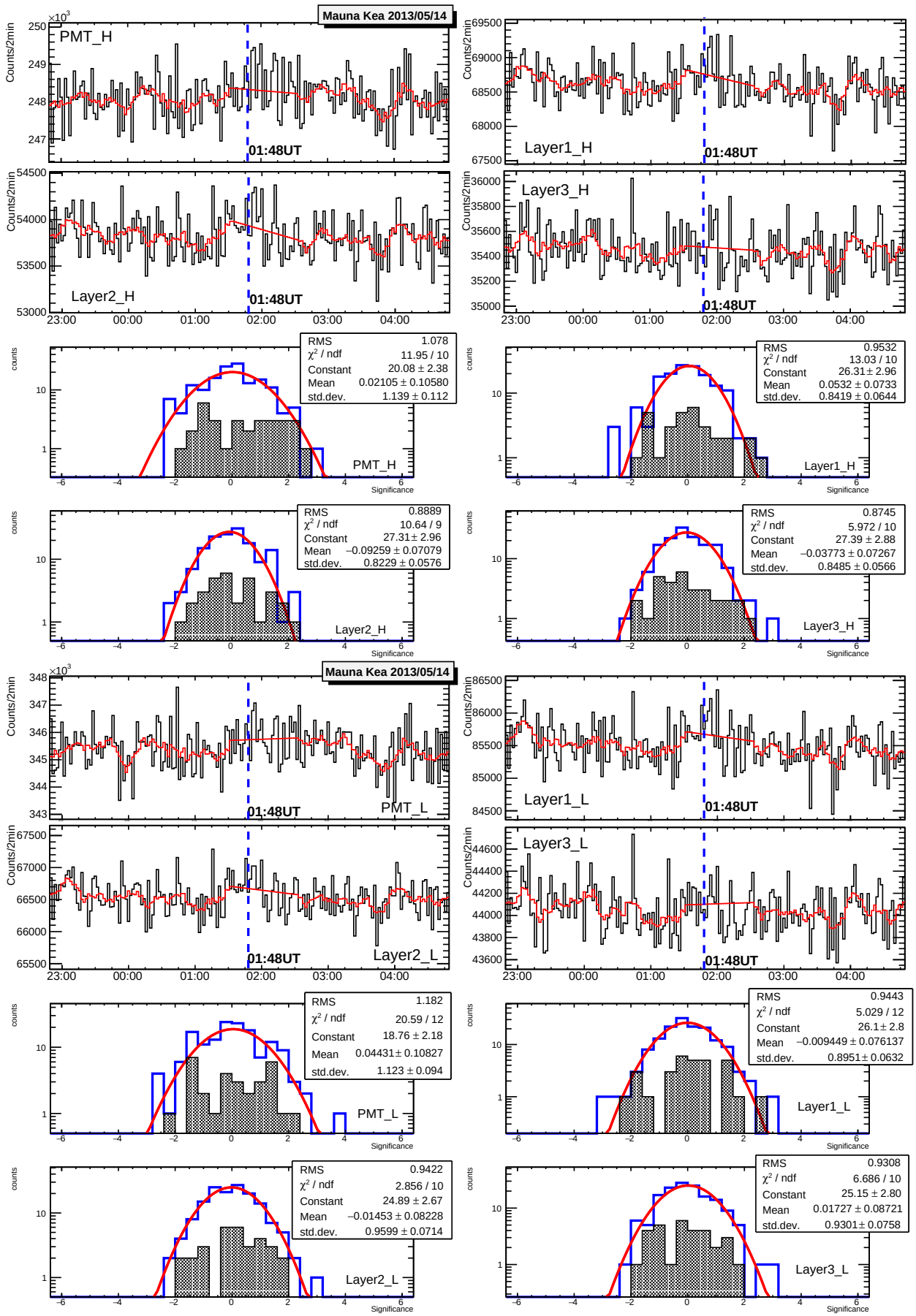

Figure C.15: 2-min time profiles and statistical significances for the eight different channels of MKUS for the X1.2-class flare on 2013 May 15. The top 8 panels correspond to the highest energy threshold (>20 MeV). The bottom 8 panels correspond to the threshold energy of >12 MeV.

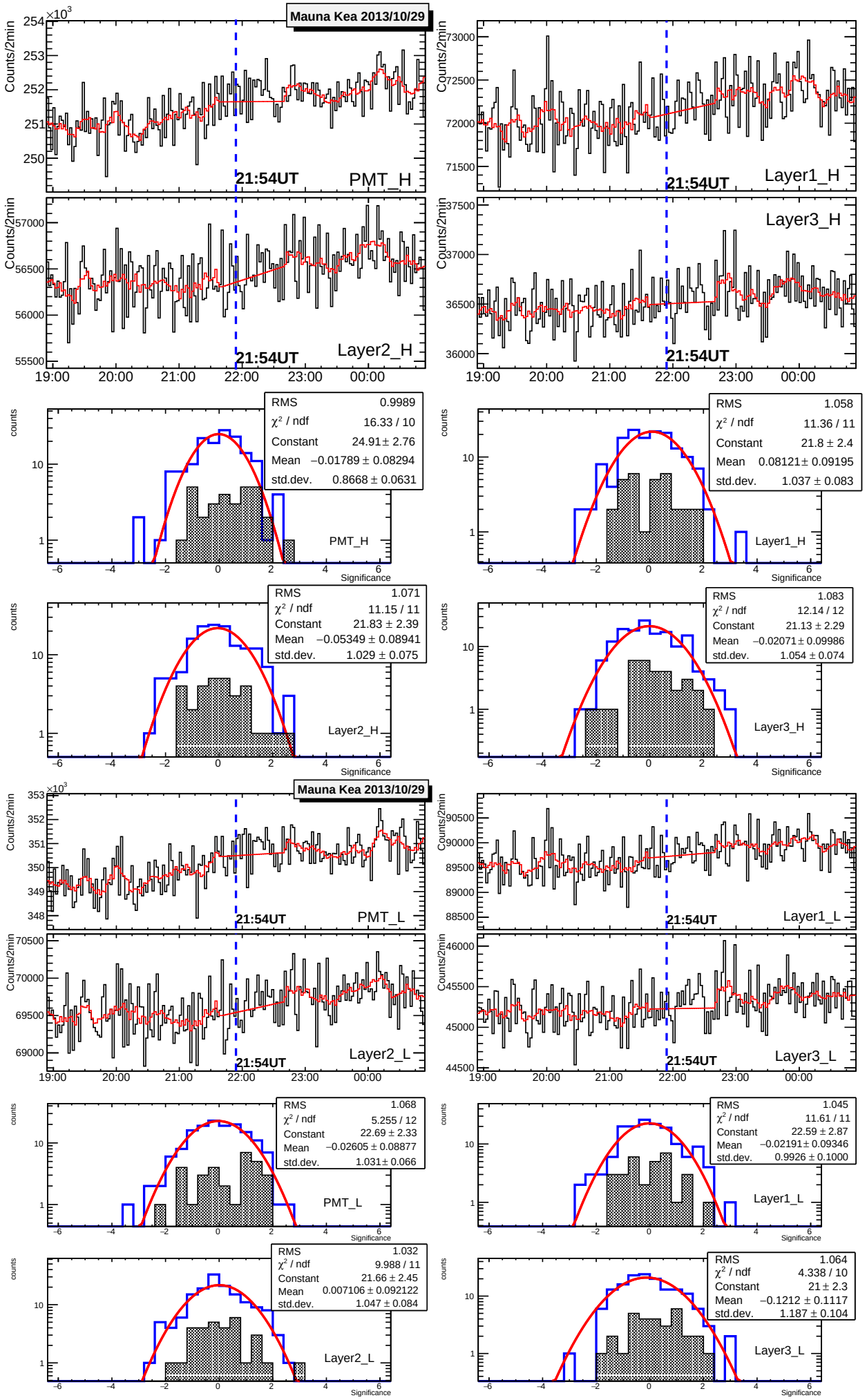
Mauna Kea 2013/10/29
Counts/2min
21:54UT
PMT_H
Layer1_H
Layer2_H
Layer3_H
19:00
20:00
21:00
22:00
23:00
00:00
counts
Significance
RMS 0.9989
χ² / ndf 16.33 / 10
Constant 24.91 ± 2.76
Mean −0.01789 ± 0.08294
std.dev. 0.8668 ± 0.0631
RMS 1.058
χ² / ndf 11.36 / 11
Constant 21.8 ± 2.4
Mean 0.08121 ± 0.09195
std.dev. 1.037 ± 0.083
RMS 1.071
χ² / ndf 11.15 / 11
Constant 21.83 ± 2.39
Mean −0.05349 ± 0.08941
std.dev. 1.029 ± 0.075
RMS 1.083
χ² / ndf 12.14 / 12
Constant 21.13 ± 2.29
Mean −0.02071 ± 0.09986
std.dev. 1.054 ± 0.074
PMT_L
Layer1_L
Layer2_L
Layer3_L
RMS 1.068
χ² / ndf 5.255 / 12
Constant 22.69 ± 2.33
Mean −0.02605 ± 0.08877
std.dev. 1.031 ± 0.066
RMS 1.045
χ² / ndf 11.61 / 11
Constant 22.59 ± 2.87
Mean −0.02191 ± 0.09346
std.dev. 0.9926 ± 0.1000
RMS 1.032
χ² / ndf 9.988 / 11
Constant 21.66 ± 2.45
Mean 0.007106 ± 0.092122
std.dev. 1.047 ± 0.084
RMS 1.064
χ² / ndf 4.338 / 10
Constant 21 ± 2.3
Mean −0.1212 ± 0.1117
std.dev. 1.187 ± 0.104

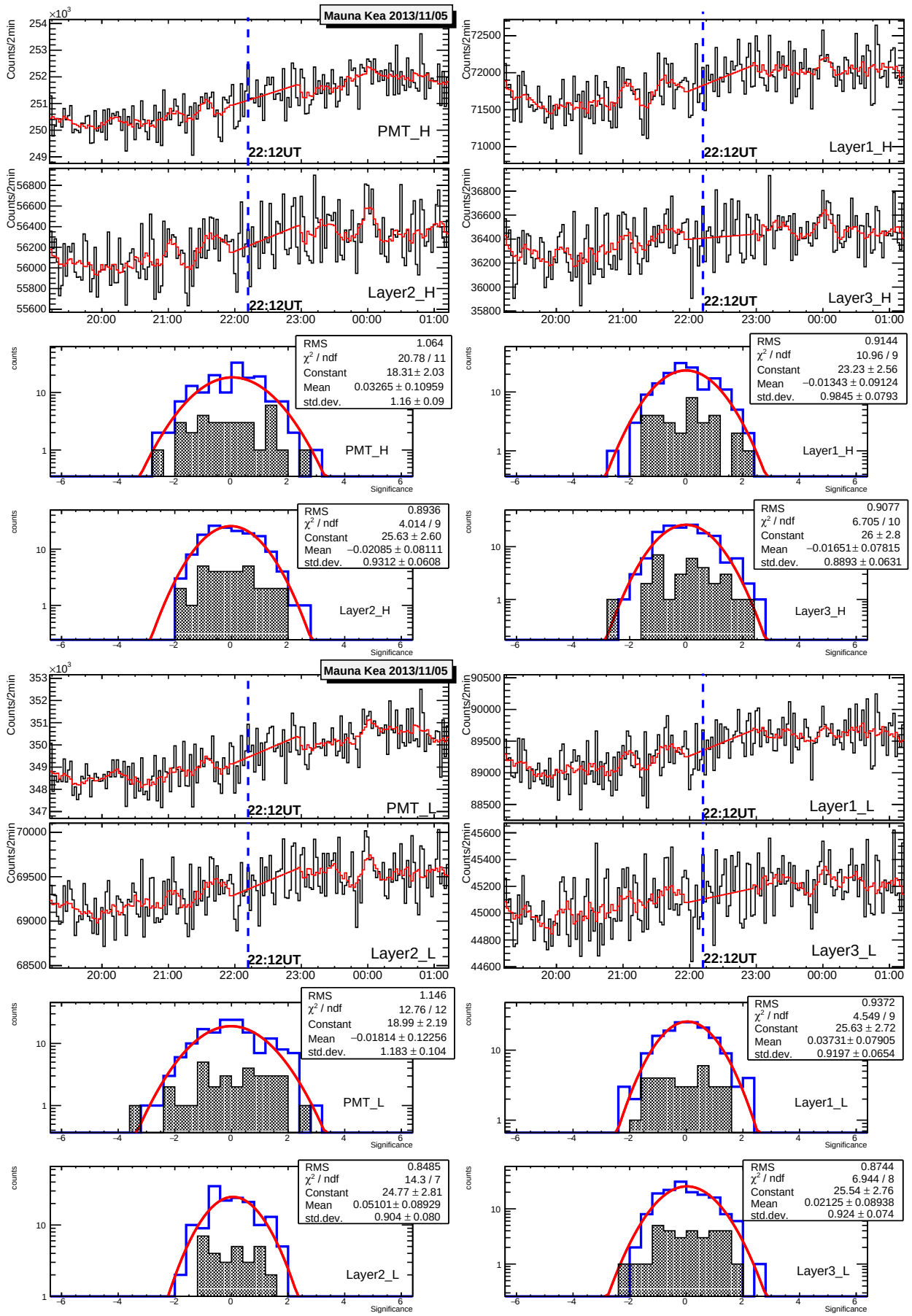

Figure C.17: 2-min time profiles and statistical significances for the eight different channels of MKUS for the X3.3-class flare on 2013 November 5. The top 8 panels correspond to the highest energy threshold (>20 MeV). The bottom 8 panels correspond to the threshold energy of >12 MeV.

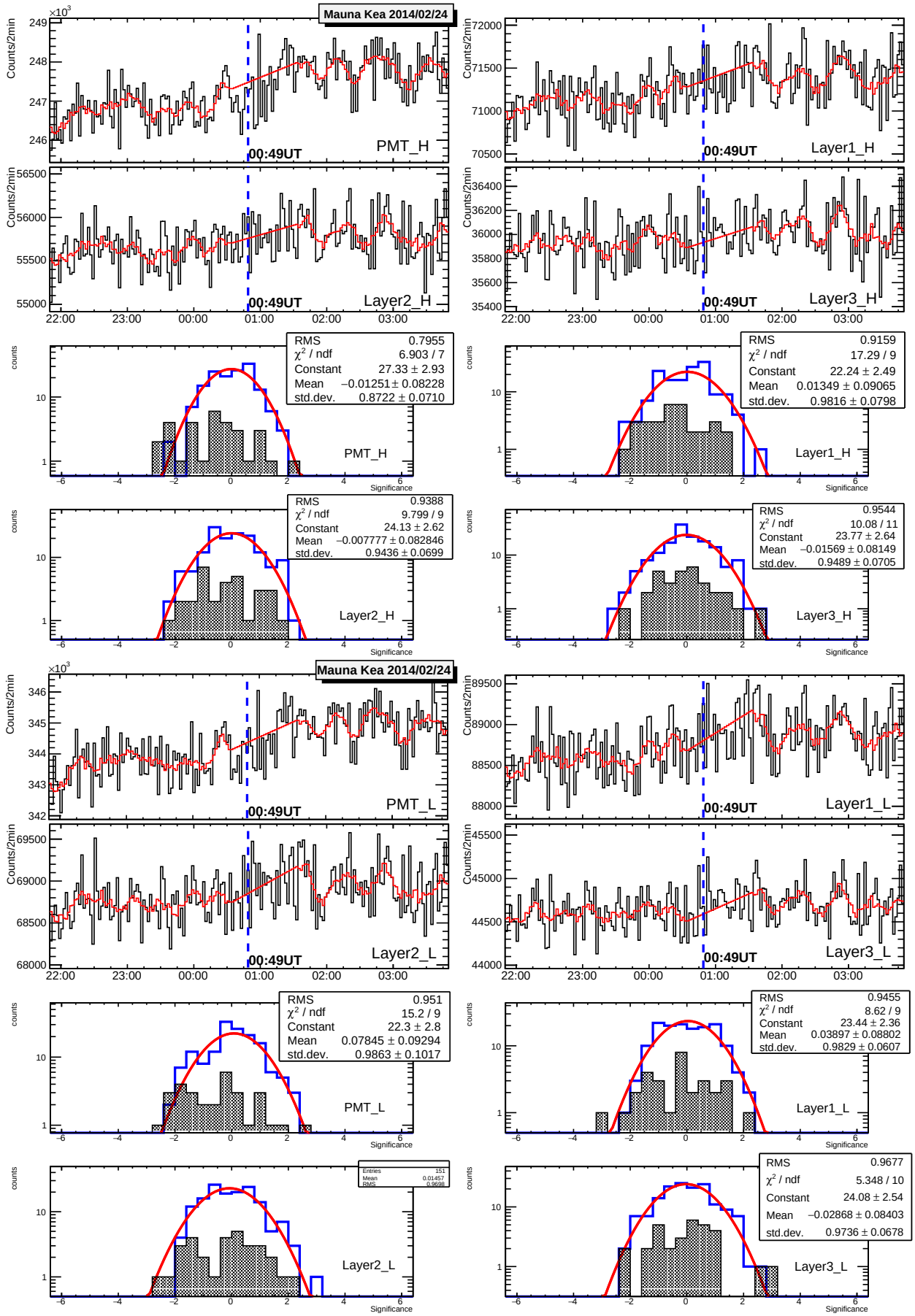

Figure C.18: 2-min time profiles and statistical significances for the eight different channels of MKUS for the X4.9-class flare on 2014 February 25. The top 8 panels correspond to the highest energy threshold (>20 MeV). The bottom 8 panels correspond to the threshold energy of >12 MeV.

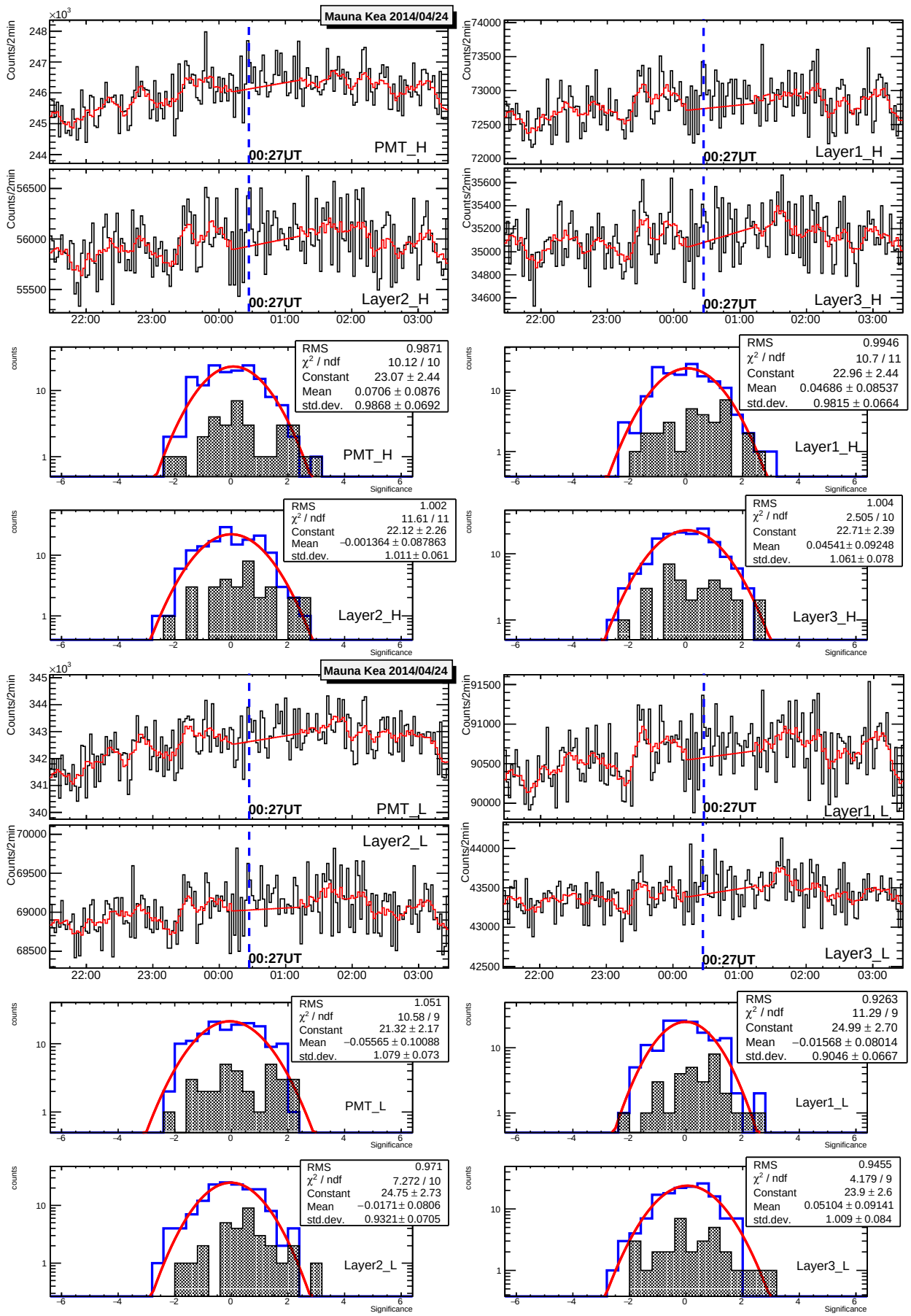

Figure C.19: 2-min time profiles and statistical significances for the eight different channels of MKUS for the X1.3-class flare on 2014 April 25. The top 8 panels correspond to the highest energy threshold (>20 MeV). The bottom 8 panels correspond to the threshold energy of >12 MeV.

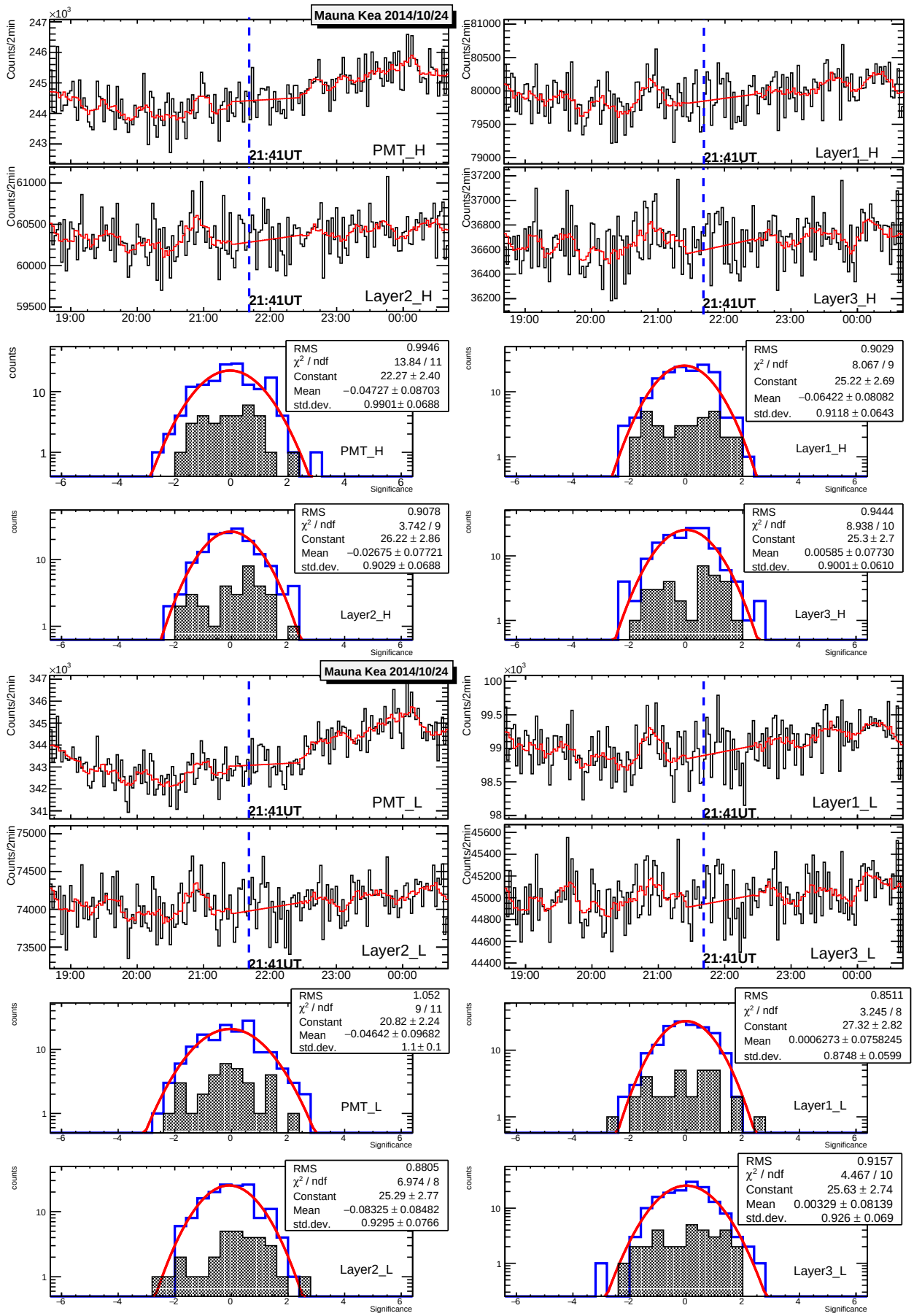

Figure C.20: 2-min time profiles and statistical significances for the eight different channels of MKUS for the X3.1-class flare on 2014 October 24. The top 8 panels correspond to the highest energy threshold (>20 MeV). The bottom 8 panels correspond to the threshold energy of >12 MeV.

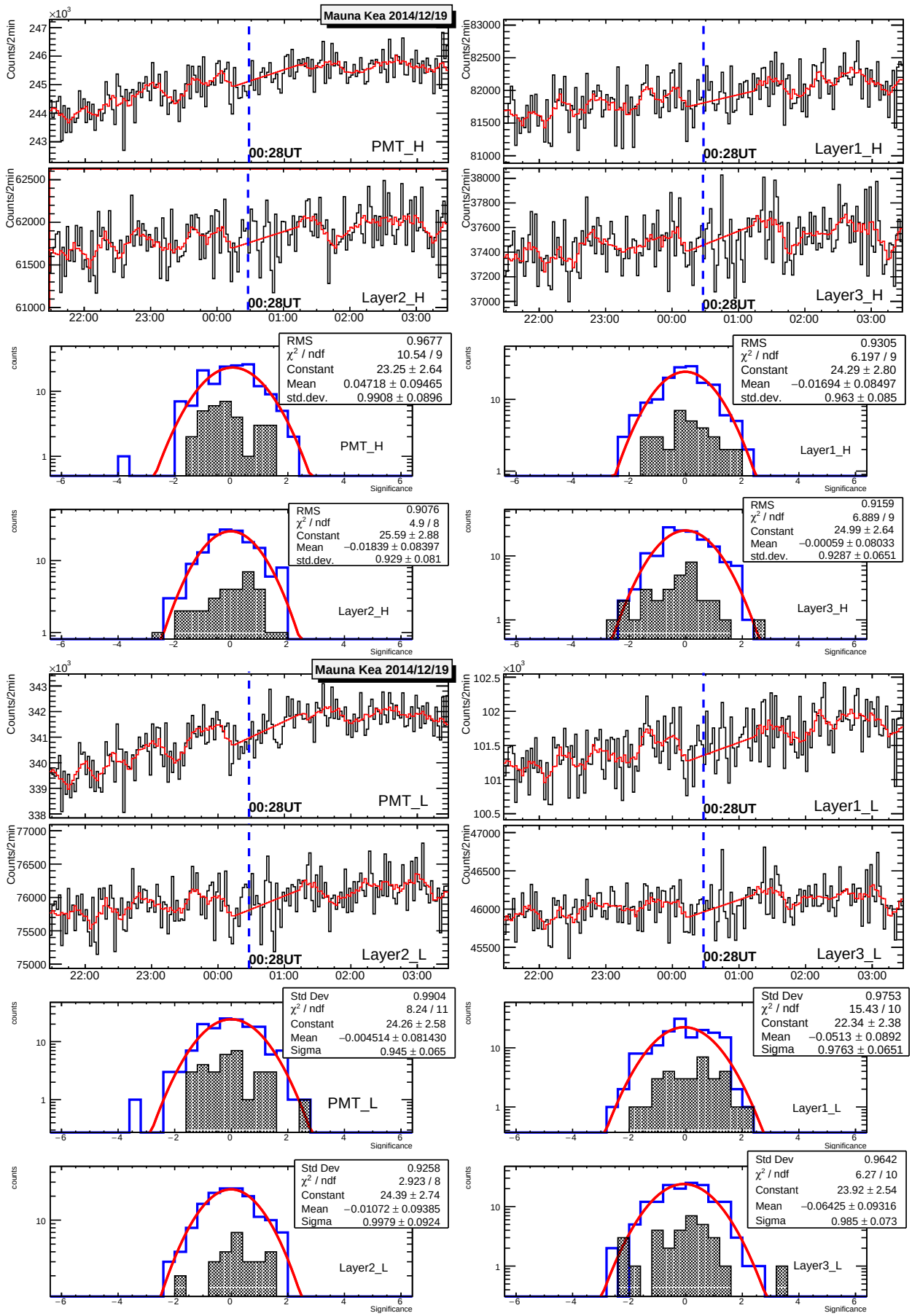

Figure C.21: 2-min time profiles and statistical significances for the eight different channels of MKUS for the X1.8-class flare on 2014 December 20. The top 8 panels correspond to the highest energy threshold (>20 MeV). The bottom 8 panels correspond to the threshold energy of >12 MeV.

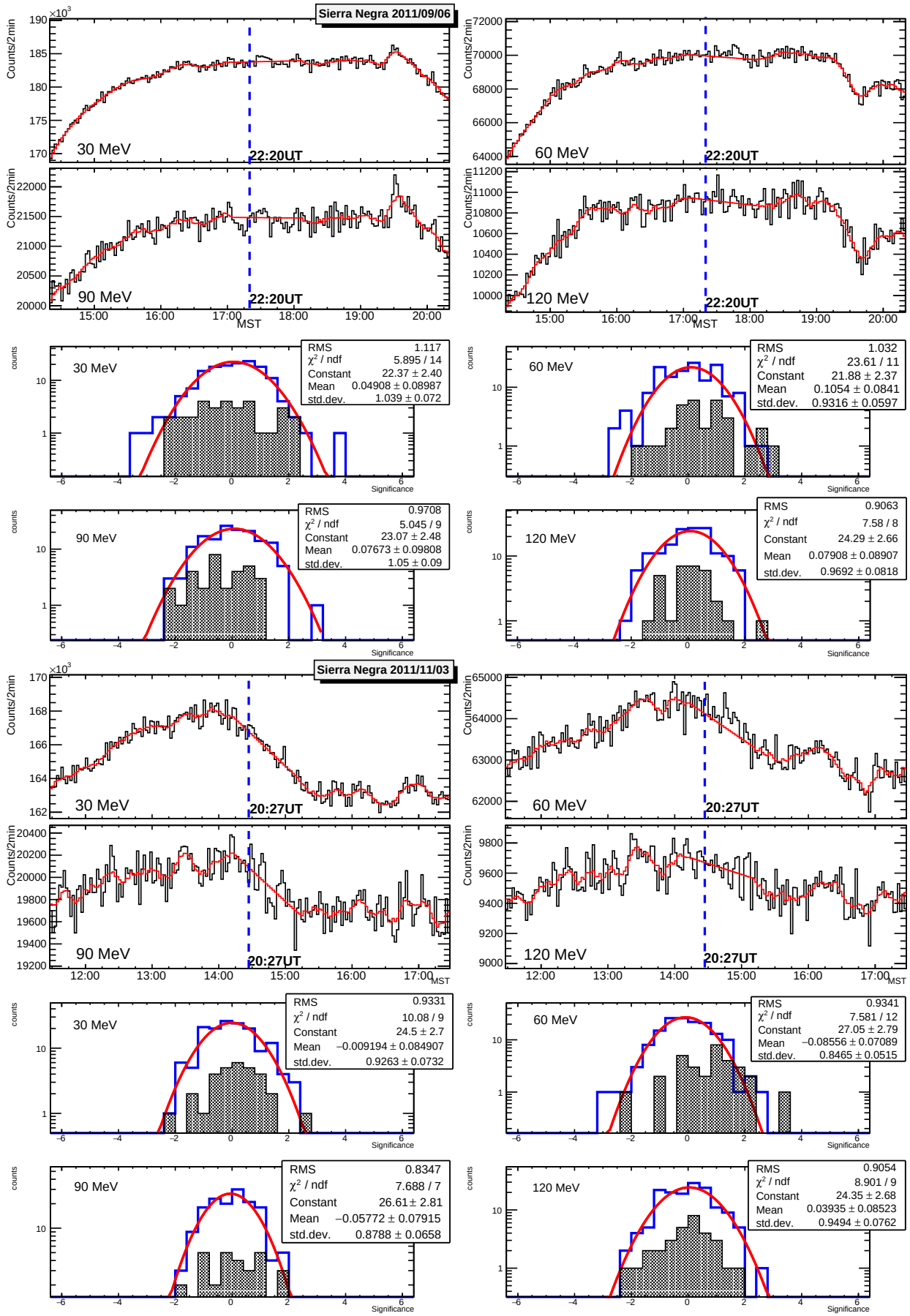

Figure C.22: 2-min time profiles and statistical significances for the four different channels of SNMX for the X2.1 (2011/09/06) and X1.9 (2011/11/03) flares.

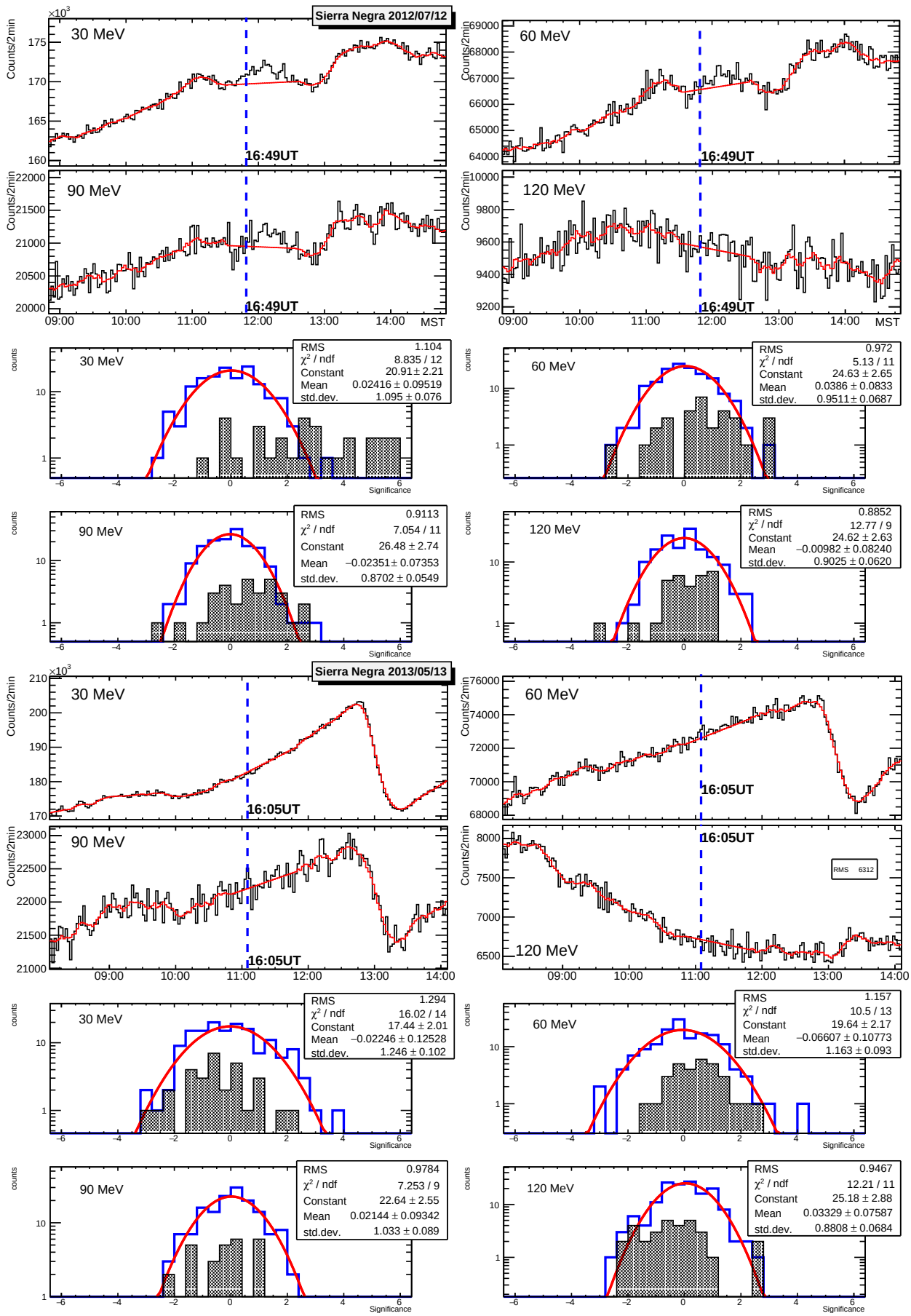

Figure C.23: 2-min time profiles and statistical significances for the four different channels of SNMX for the X1.4 (2012/07/12) and X2.8 (2013/05/13) flares.

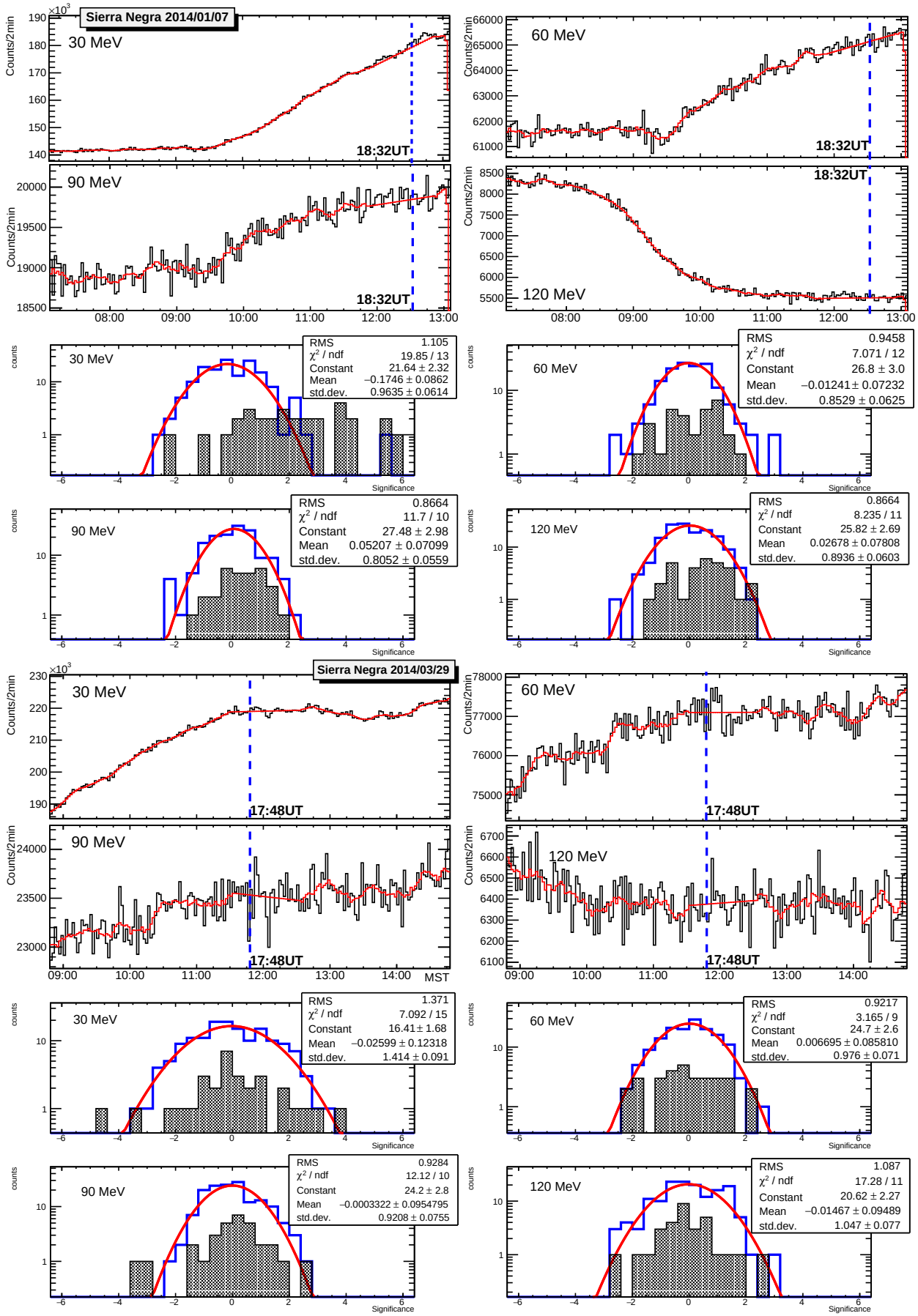

Figure C.24: 2-min time profiles and statistical significances for the four different channels of SNMX for the X1.2 (2014/01/07) and X1.0 (2014/03/29) flares.

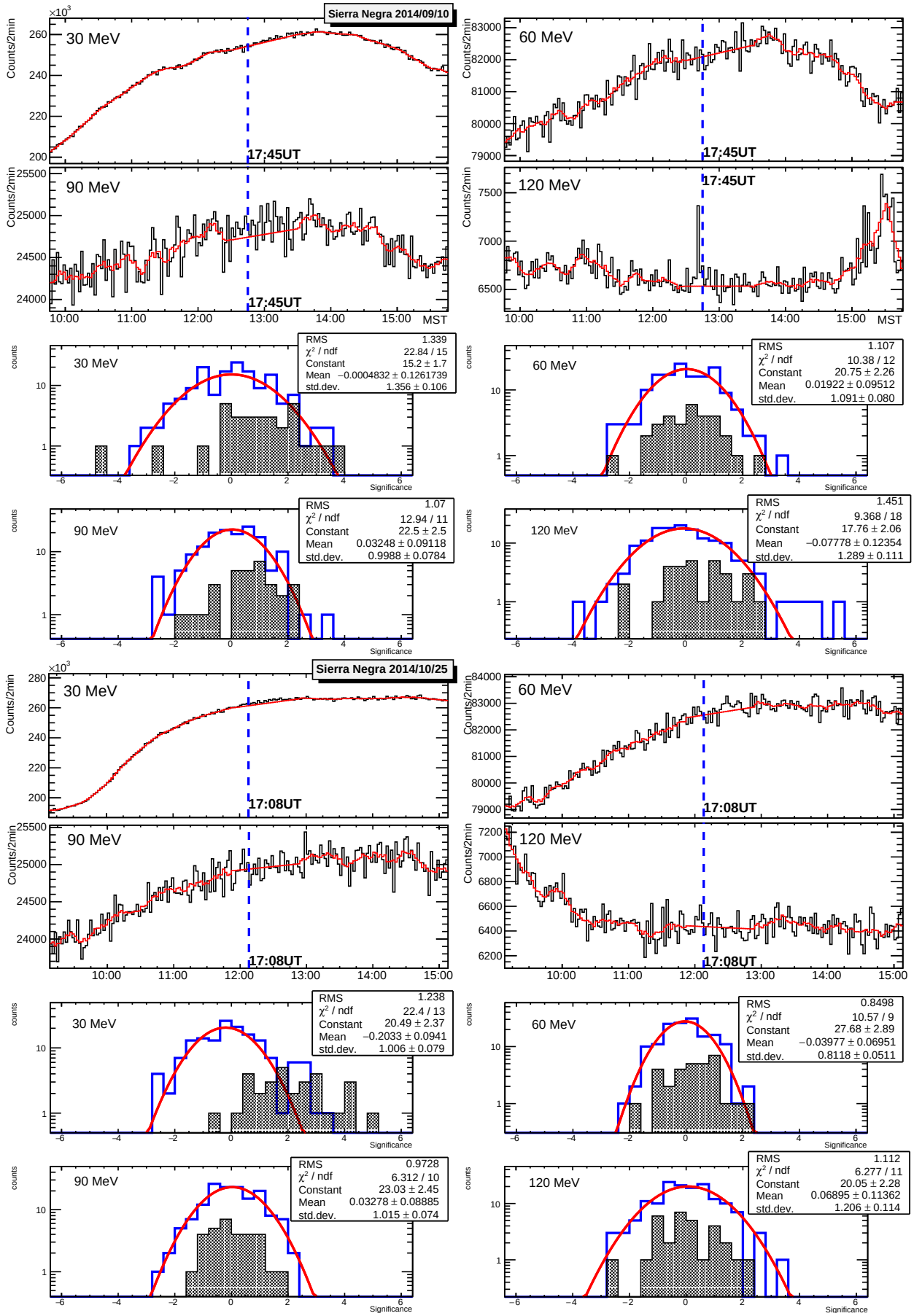

Figure C.25: 2-min time profiles and statistical significances for the four different channels of SNMX for the X1.6 (2014/09/10) and X1.0 (2014/10/25) flares.

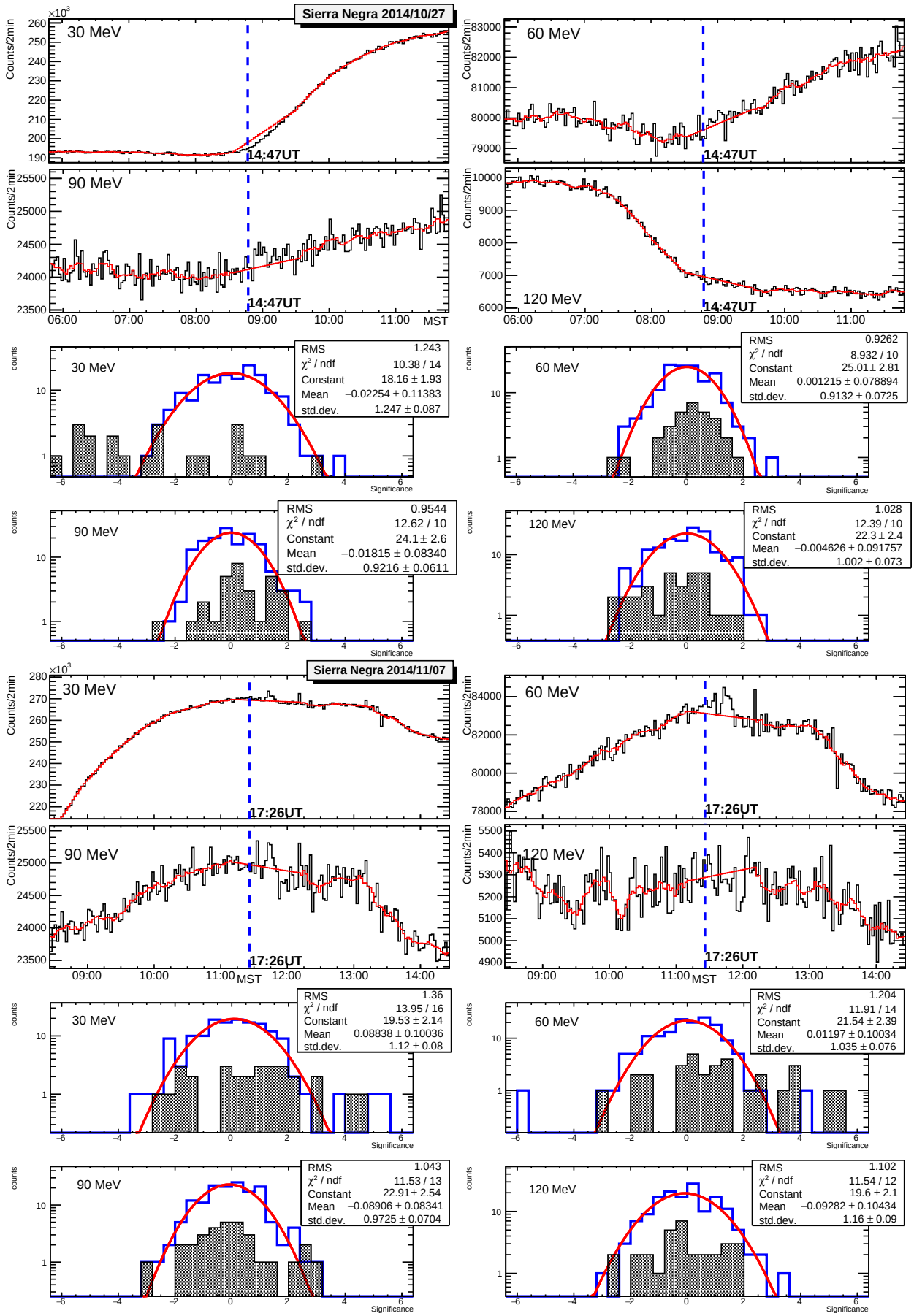

Figure C.26: 2-min time profiles and statistical significances for the four different channels of SNMX for the X2.0 (2014/10/27) and X1.6 (2014/11/07) flares.

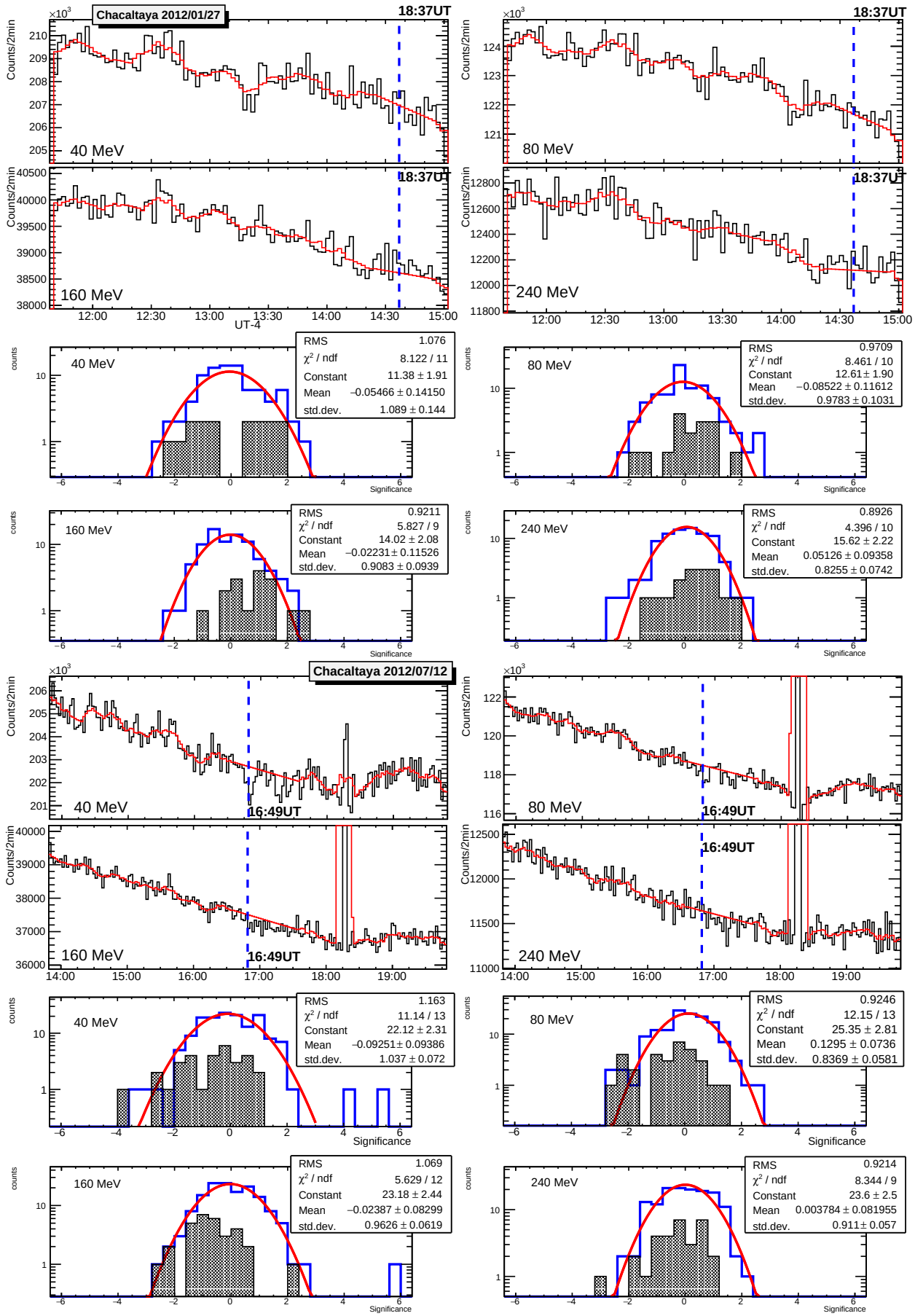

Figure C.27: 2-min time profiles and statistical significances for the four different channels of CHBO for the X1.7 (2012/01/27) and X1.4 (2012/07/12) flares.

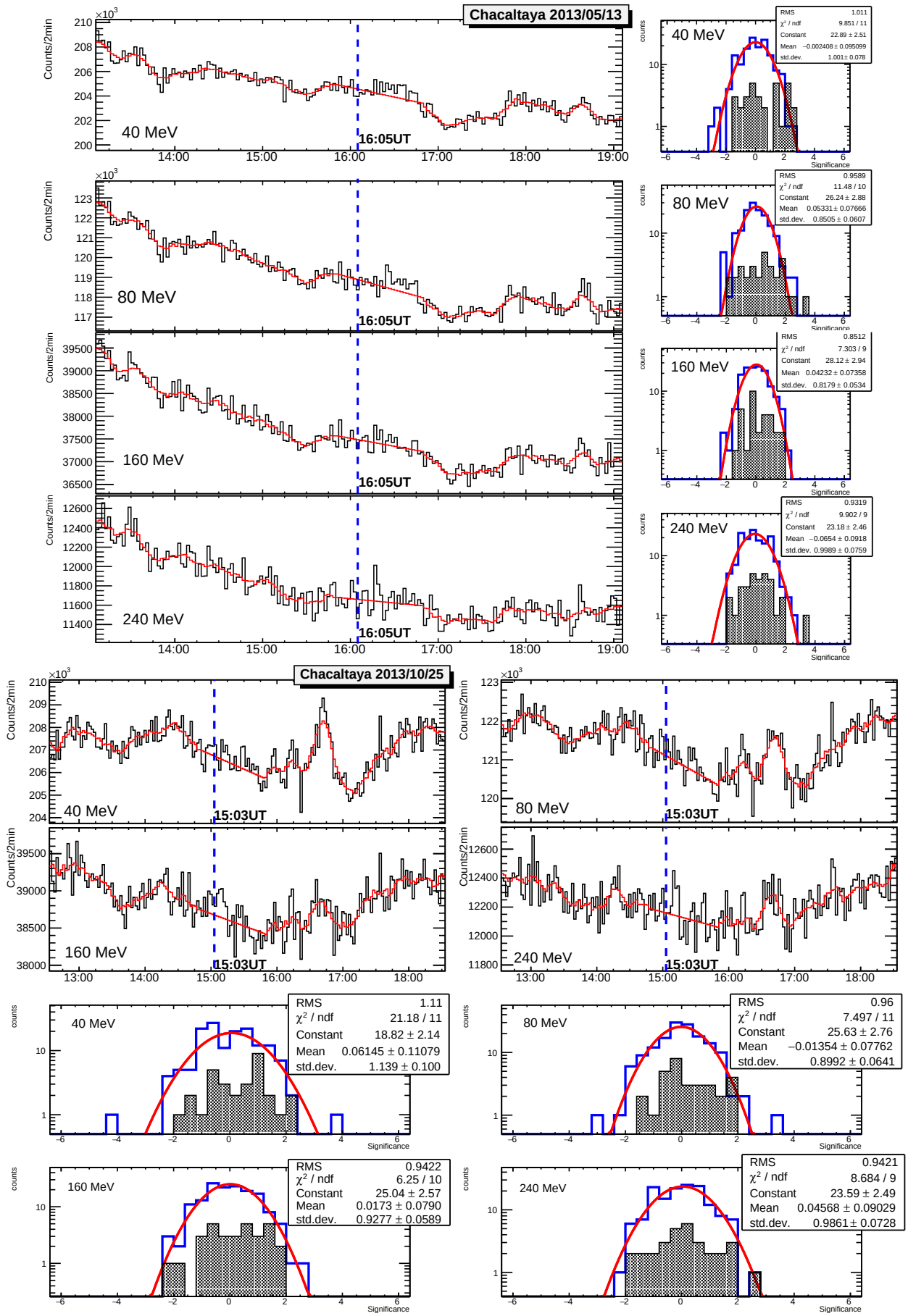

Figure C.28: 2-min time profiles and statistical significances for the four different channels of CHBO for the X2.8 (2013/05/13) and X2.1 (2013/10/25) flares.

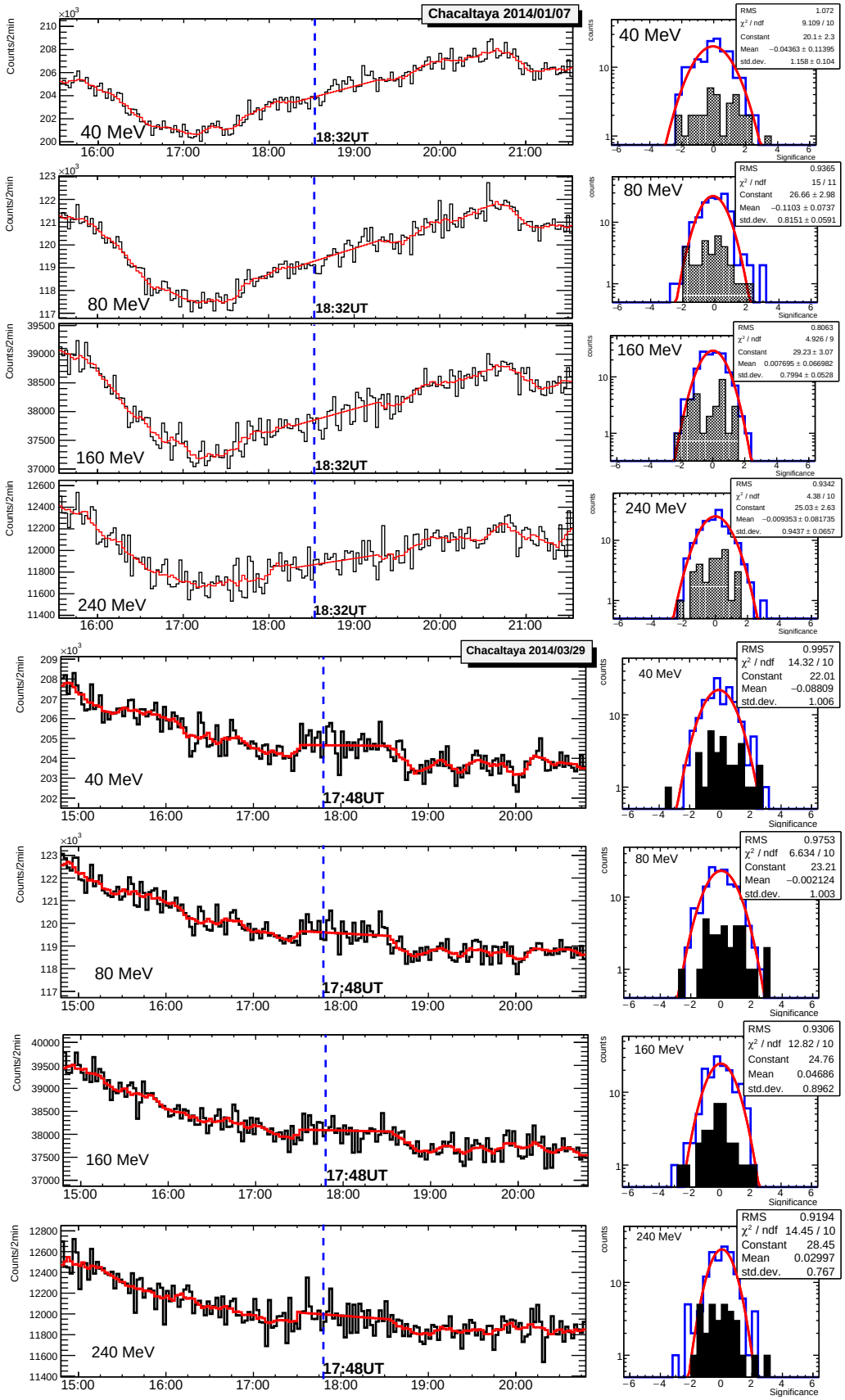

Figure C.29: 2-min time profiles and statistical significances for the four different channels of CHBO for the X1.2 (2014/01/07) and X1.0 (2014/03/29) flares.

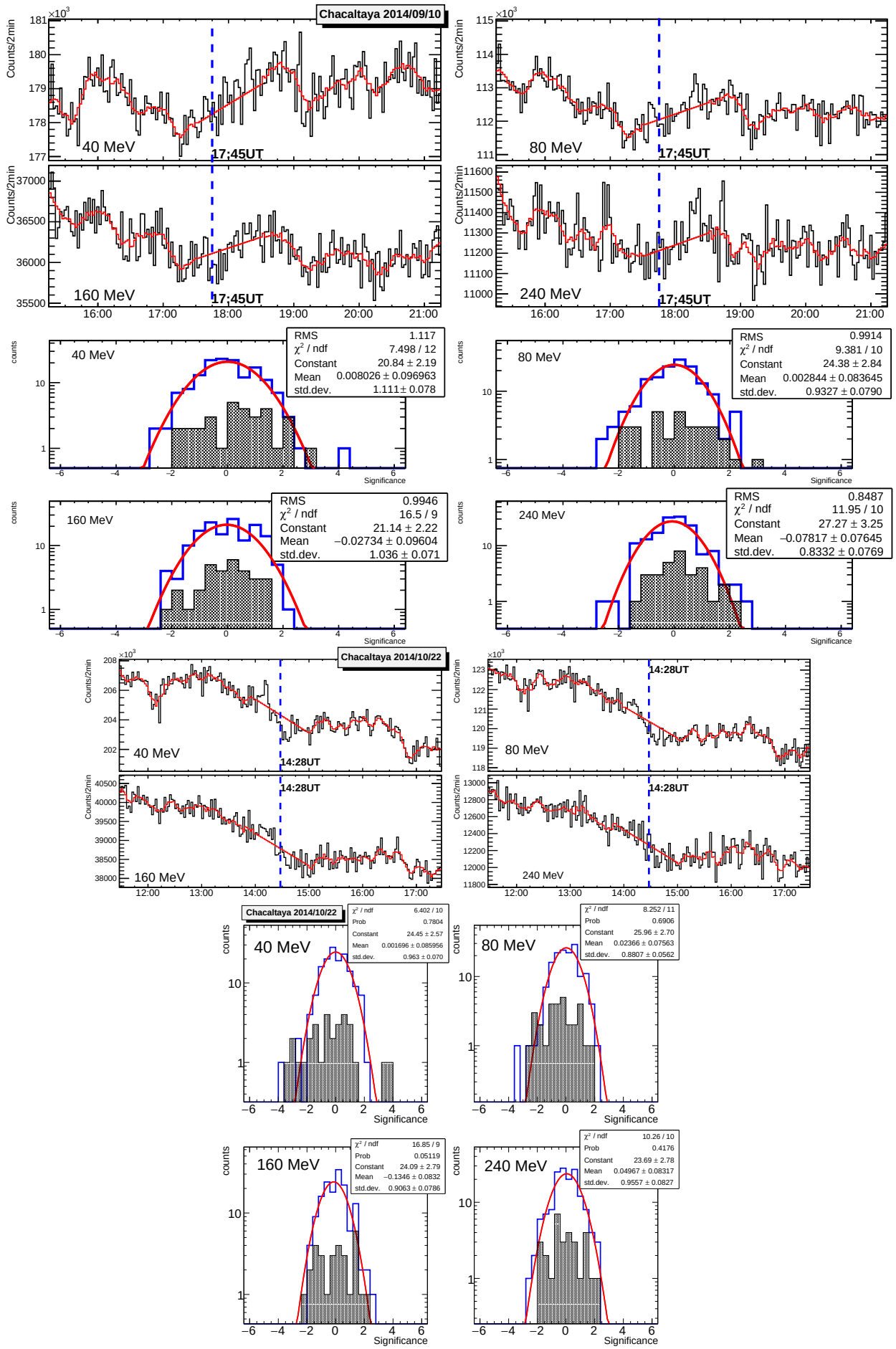

Figure C.30: 2-min time profiles and statistical significances for the four different channels of CHBO for the X1.6 (2014/09/10) and X1.6 (2014/10/22) flares.

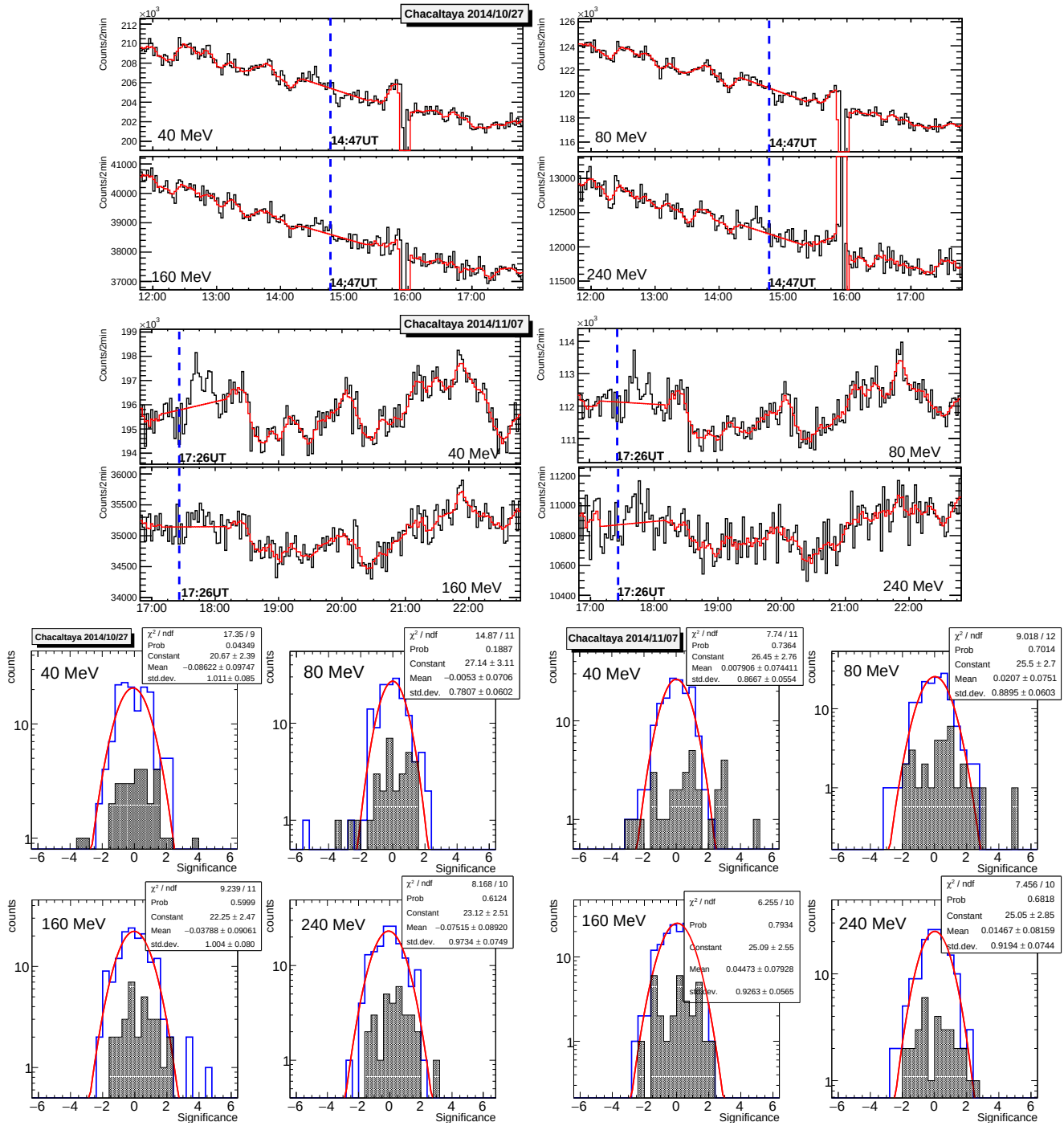

Figure C.31: 2-min time profiles and statistical significances for the four different channels of CHBO for the X2.0 (2014/10/27) and X1.6 (2014/11/07) flares.

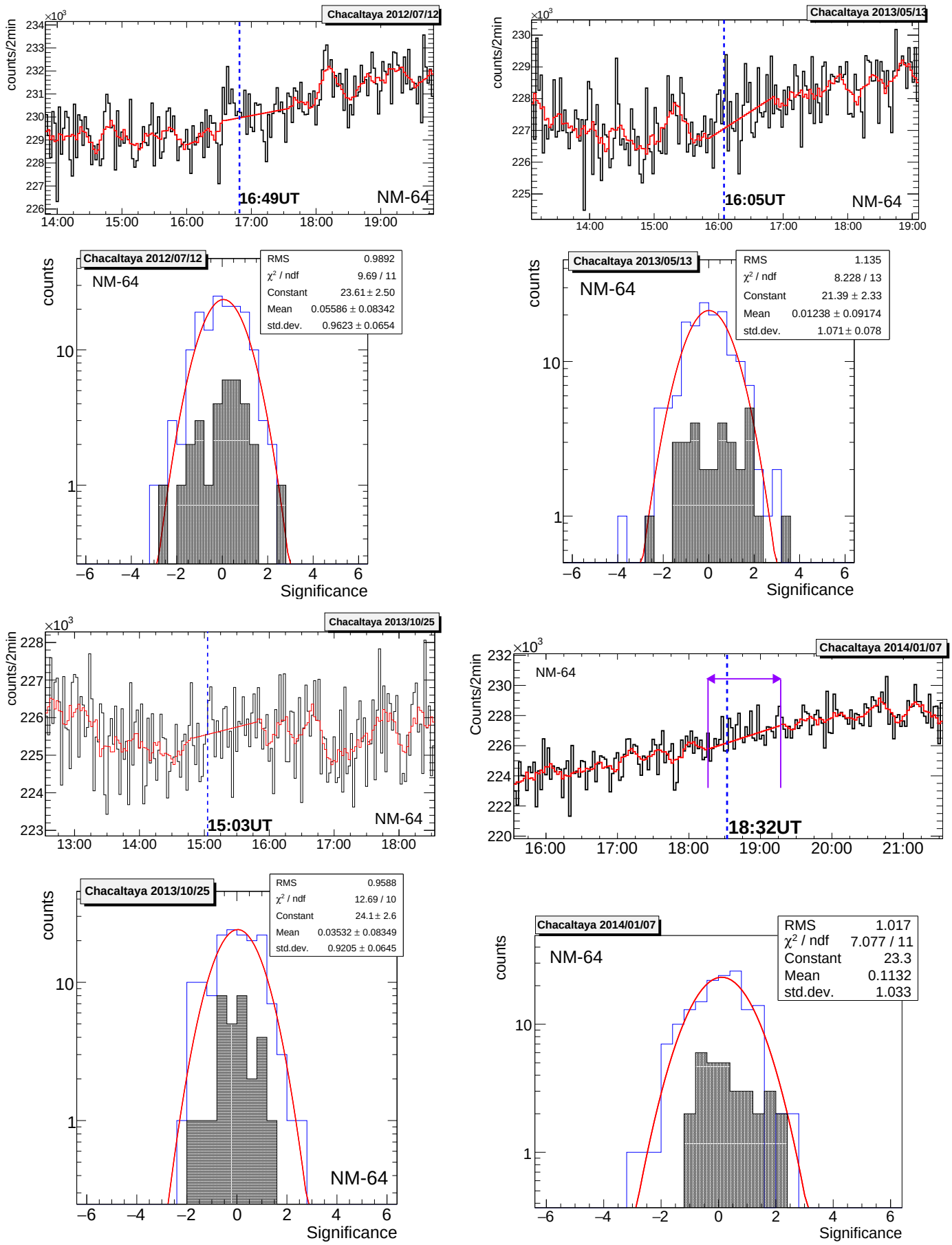

Figure C.32: Neutron monitor 2-min time profile and statistical distributions.

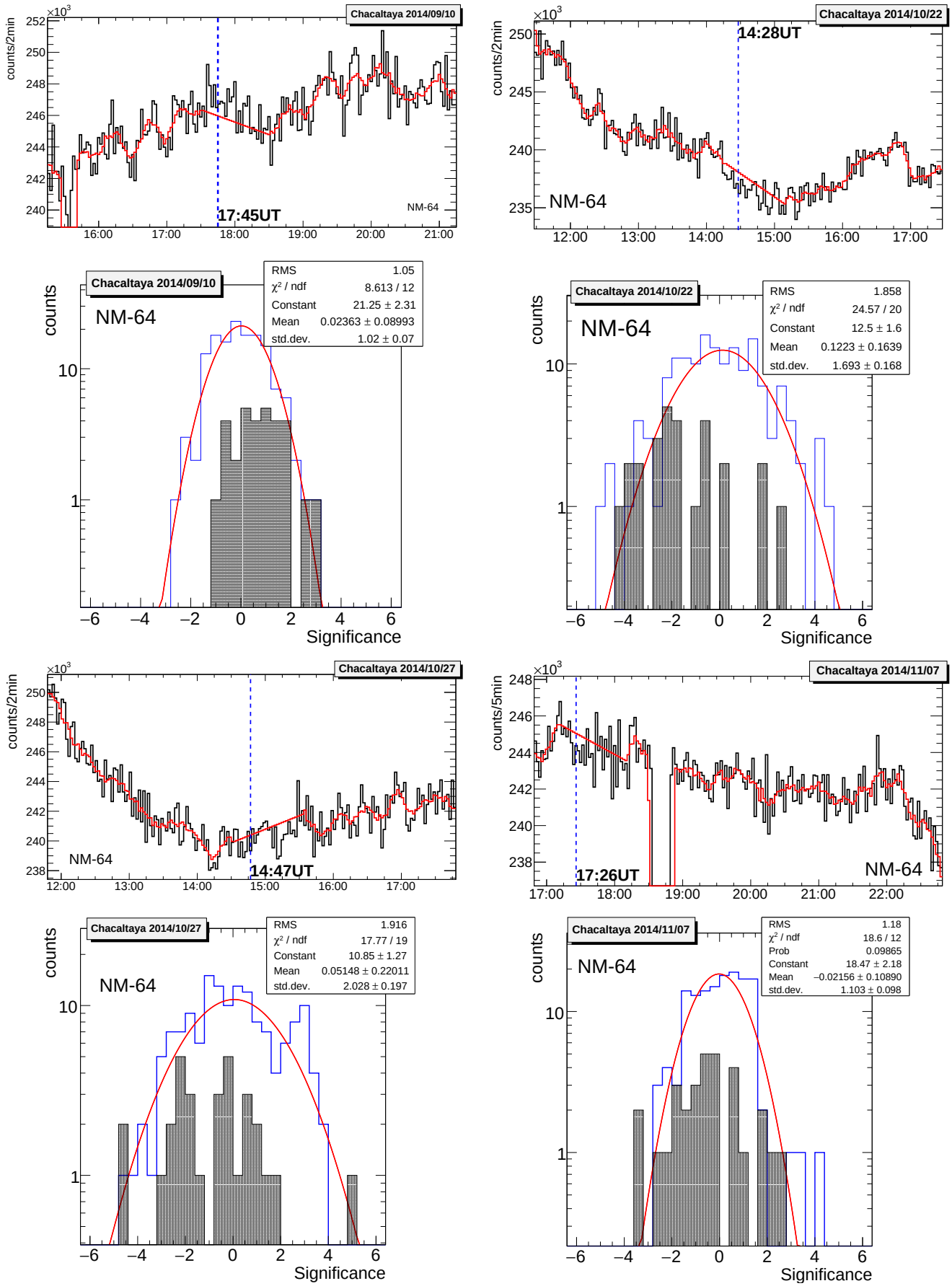

Figure C.33: Neutron monitor 2-min time profile and statistical distributions.

Bibliography

L. Bierman, O. Haxel, A. Schlüter, Neutrale Ultrastrahlung von der Sonne. Z. Naturforsch **6a**, 47 (1951)

H. Carmichael, Cosmic Rays (Instruments), in *Annals of the IQSY*, vol. 1, 1968, pp. 178–197

R. Carrington, Description of a singular appearance seen in the Sun on September 1, 1859. Mon. Not. R. Astron. Soc. **20**(13) (1859)

E.L. Chupp, et al., A direct observation of solar neutrons following the 0118ut fare on 1980 June 21. ApJ **263**, 95–99 (1982)

E.L. Chupp, et al., Solar neutron emissivity during the large flare on 1982 June 3. ApJ **318**, 913–925 (1987)

J.M. Clem, L.I. Dorman, Neutron monitor response functions. Space Sci. Rev. **93**, 335–359 (2000)

H. Debrunner, E.O. Flückiger, E.L. Chupp, D.J. Forrest, The solar cosmic ray neutron event on June 3, 1982, in *Proc. of the 18th ICRC in Bangalore*, vol. 4, 1983, pp. 75–78

L. Dorman, *Solar Neutrons and Related Phenomena* (Springer, Heidelberg, 2010), p. 912

H. Dreicer, Electron and ion runaway in a fully ionized gas. ii. Phys. Rev. **117**, 329–342 (1960)

E. Fermi, On the origin of the cosmic ray radiation. Phys. Rev. **75**, 1169–1174 (1949)

E.O. Flückiger, et al., in *Proc. 16th European Cosmic Ray Simposium*, 1998, p. 219

E.O. Flückiger, et al., Solar neutron events that have been found in solar cycle 23. Int. J. Mod. Phys. A **20**(29), 6646–6649 (2005)

M.A. Forman, R. Ramaty, E.G. Zweibel, *The Physics of the Sun*, vol. 2 (Reidel, Dordrecht, 1986), p. 249

D.J. Forrest, E.L. Chupp, Upper limit for the solar neutron flux in the energy interval 20-120 MeV. Solar Physics **6**, 339–350 (1969)

J.O. Goldstein, et al., The MESSENGER Gamma-Ray and Neutron Spectrometer. Space Sci. Rev. **131**, 339–391 (2007)

L.X. González, et al., Re-evaluation of the neutron emission from the solar flare of September 07, detected by the solar neutron telescope at Sierra Negra. ApJ **814**(2), 1–7 (2015). doi:10.1088/0004-637X/814/2/136

N. Gopalswamy, P. Mäkela, S. Yashiro, H. Xie, S. Akiyama, N. Thakur, *High-energy solar particle events in cycle 24*, 2015. `http://arxiv.org/pdf/1507.06162.pdf`

C.J. Hatton, The Neutron Monitor. Progress in Elementary Particle and Cosmic Ray Physics **X**, 1–100 (1971)

X.-M. Hua, et al., Angular and energy-dependent neutron emission from solar flare magnetic loops. ApJS **140**(2), 563 (2002)

X.-M. Hua, R.E. Lingenfelter, Solar flare neutron and accelerated ion angular distributions. ApJ **323**, 779–794 (1987)

H.S. Hudson, Global properties of solar flares. Space Sci. Rev. **158**, 5–41 (2011)

I. Imada, Y. Muraki, Y. Matsubara, et al., A new tracking satellite-borne solar neutron detector. Nucl. Instr. and Meth. A **421**, 99–112 (1999)

Y. Katayose, et al., A solar neutron telescope in Tibet, in *Proc. 26th ICRC in Salt Lake*, vol. 6, 1999, pp. 58–61

E. Kirsch, Estimation of an upper limit for the solar neutron emission during large flares. Solar Physics **28**, 233–246 (1973)

K. Koga, et al., Measurement of high-energy neutrons at ISS by SEDA-AP. Astrophys. Spa. Sci. Trans. **7**, 411–416 (2011)

D. Lario, Estimation of the solar flare neutron worst-case fluxes and fluences for missions traveling close to the sun. Space Weather **10**, 11 (2012)

D.J. Lawrence, W.C. Feldman, J.O. Goldstein, P.N. Peplowski, D.J. Rodgers, S.C. Solomon, Detection and characterization of 0.5-8 MeV solar neutrons near Mercury. JGR Space Physics **119**, 1–22 (2014). doi:10.1002/2013JA019037

R.E. Lingenfelter, E.J. Flamm, E.H. Canfield, S. Kellman, High-energy solar neutrons: 1. production in flares. J. Geophys. Res. **70**(17), 4077 (1965)

D. Lopez, Particle Identification with the mini-SciCR detector at Mount Sierra Negra in Mexico, M.Sc. thesis, Nagoya University, 2012

D. Lopez, Y. Matsubara, Search for solar neutrons at Mount Chacaltaya associated with M- and X-class flares during the rising period of solar cycle 24. Earth, Planets and Space **67**, 54 (2015). doi:10.1186/s40623-015-0222-2

N. Martinic, M. Kusunose, F. Osco, N. Ohmori, S. Callejas, R. Choque, H. Sasaki, V. Tarquino, J. Mariscal, Search for solar neutrons using NM-64 equipment, in *Proceedings of the 19th ICRC La Jolla, CA*, vol. 4, 1985

Y. Matsubara, et al., New Bolivia solar neutron telescope, in *Proceedings of the 23rd ICRC in Calgary*, vol. 3, 1993, pp. 139–142

Y. Matsubara, et al., A new solar neutron telescope in Hawaii, in *Proceedings of the 25th ICRC in Durban*, vol. 1, 1997, pp. 37–40

H. Mavromichalaki, et al., Applications and usage of the real-time Neutron Monitor Database. Adv. Space Res. **47**, 2210 (2011)

L. Miroshnichenko, *Solar Cosmic Rays: Fundamentals and Applications*, 2nd edn. (Springer, Heidelberg, 2015), pp. 1–521. ISBN 9783319094281

M. Moser, Solar neutron telescope Gornergrat Montecarlo simulation of detector properties, Diplomarbeit (M.Sc. Thesis), Physikalisches Institut, Universität Bern, 2002

Y. Muraki, et al., Observation of solar neutrons associated with the large flare on 1991 June 4. ApJ **400**, 75–78 (1992)

Y. Muraki, et al., The 64m^2 Solar Neutron Telescope at Norikura, in *Proceedings of the 25th ICRC in Durban*, vol. 1, 1997, pp. 53–56

Y. Muraki, et al., A solar neutron telescope in Tibet and its capability examined by the 1998 November 28th event. Astropart. Phys. **28**, 119–131 (2007)

Y. Muraki, D. Lopez, et al., Simultaneous observation of solar neutrons from the ISS and high mountain observatories in association with a flare on July 8, 2014. Sol. Phys. (2016). (Accepted)

Y. Muraki, K. Koga, H. Matsumoto, O. Okudaira, S. Shibata, T. Goka, T. Obara, T. Yamamoto, Measurement of high-energy solar neutrons with SEDA-FIB onboard the ISS, in *Proceedings of the 33rd ICRC Rio de Janeiro*, 2013

R.J. Murphy, B. Kozlovsky, G.H. Share, The Production of low-energy neutrons in the solar flares and the importance of their detection in the inner heliosphere. ApJS **202**(3), 1–32 (2012)

Y. Nagai, M.Sc. thesis (in japanese), Nagoya University, 2011

Y. Nagai, Observation of cosmic rays by the new solar neutron telescope, SciCRT, PhD thesis, Department of Physics, Nagoya University, 2014

K. Nitta, et al., The k2k scibar detector. Nucl. Instr. and Meth. A **535**, 147–151 (2004)

R. Ramaty, N. Manzhavidze, Solar Flares: Gamma Rays. In Press: Encyclopedya for Astronomy (1998). `arxiv:astro-ph/9810089v1`

R. Ramaty, R.J. Murphy, Nuclear processes and accelerated particles in solar flares. Space Sci. Rev. **45**, 213–268 (1987)

T. Sako, et al., Super Solar Neutron Telescope for the Next Solar Maximum, in *Proc. of the 28th ICRC in Tsukuba*, vol. 6, 2003, pp. 3437–3440

T. Sako, et al., Long-lived solar neutron emission in comparison with electron-produced radiation in the 2005 September 7 solar flare. ApJ **651**, 69–72 (2006)

S. Shibata, Propagation of solar neutrons through the atmosphere of the Earth. J. Geophys. R. **99**, 6651–6665 (1994)

J.A. Simpson, W. Fonger, S.B. Treiman, Cosmic radiation intensity-time variation and their origin. 1. Neutron intensity variation method and meteorological factors. Phys. Rev. **90**, 934–950 (1953)

P.H. Stoker, The IGY and beyond: A brief history of ground-based cosmic-ray detectors. Adv. Spa. Res. **44**, 1081–1095 (2009)

X. Sun, M.G. Bobra, J.T. Hoeksema, Y. Liu, Y. Li, C. Shen, S. Couvidat, A.A. Norton, G.H. Fisher, Why is the great solar active region 12192 flare-rich but CME-poor? ApJ **804**, 28 (2015). doi:10.1088/2041-8205/804/2/L28

H. Tsuchiya, et al., Detection efficiency of a new type of solar neutron detector calibrated by an accelerator neutron beam. Nucl. Instr. and Meth. A **463**, 183–193 (2001)

H. Tsuchiya, et al., Upper limits on the solar-neutron flux at the Yangbajing neutron monitor from BATSE-detected solar flares. A&A **468**, 1089–1097 (2007)

J.F. Valdés-Galicia, et al., An improved solar neutron telescope installed at a very high altitude in Mexico. Nucl. Instr. and Meth. A **535**, 656–664 (2004)

L. Vlahos, Particle acceleration in solar flares. Sol. Phys. **121**, 431–447 (1989)

K. Watanabe, Solar neutron events in association with large solar flares in solar cycle 23, PhD thesis, Department of Physics, Nagoya University, 2005

K. Watanabe, et al., Highly significant detection of solar neutrons on 2005 September 7. Adv. in Spa. Res. **39**, 1462–1466 (2007)

K. Watanabe, et al., Physics of ion acceleration in the solar flare on 2005 September 7 determines γ-ray and neutron production. Adv. in Spa. Res. **44**, 789–793 (2009)

K. Watanabe, et al., G-band and hard X-ray emissions of the 2006 December 14 flare observed by Hinode/SOT and RHESSI. ApJ **715**(1) (2010)